CRANFIELD UNIVERSITY

Yuzhi CHEN

Operation Optimisation Study for CCGT Power Plant

SCHOOL OF ENGINEERING
PhD in Aerospace

PhD
Academic Year: 2015 - 2018

Primary Supervisor: Dr Yiguang Li
Associate Supervisor: Dr Devaiah Nalianda
Industry Supervisor: Mr Mike Newby
10 2018

CRANFIELD UNIVERSITY

SCHOOL OF ENGINEERING
PhD in Aerospace

PhD

Academic Year 2015 - 2018

Yuzhi CHEN

Operation Optimisation Study for CCGT Power Plant

Primary Supervisor: Dr Yiguang Li
Associate Supervisor: Dr Devaiah Nalianda
Industry Supervisor: Mr Mike Newby
10 2018

This thesis is submitted in partial fulfilment of the requirements for the degree of PhD

ABSTRACT

A major concern for the power generation industry is to obtain a maximum economic benefit without over-consuming the remaining life of the gas turbine hot section. This study explored a methodology to support decision making for operational optimisation of a combined cycle gas turbine (CCGT) power plant. There is no published algorithm for modelling a parallel dual pressure, once-through steam generator (OTSG), nor any proposed method for OTSG degradation diagnosis and how the degradation affects OTSG performance. What is more, few publications were found for optimisation existing power plant operation considering gas turbine creep life.

This study presents a new thermodynamic algorithm to simulate the thermodynamic performance of parallel dual pressure OTSG. In this study, a novel gas path diagnostic method for an OTSG based on the Newton-Raphson method was developed to predict the OTSG degradation caused by fouling. A daily operation decision support platform for this existing power plant is proposed that models CCGT performance, creep life, emissions, economics, and provides a basis for decision-making based optimised results.

The OTSG performance model is applied to an OTSG operating in a CCGT power plant at Manx Utilities on the Isle of Man, United Kingdom to demonstrate the effectiveness of the simulation method. A comparison between predicted OTSG performance and OTSG field data showed that the proposed model offers good prediction accuracy when simulating OTSG performance for both design and off-design points.

The OTSG diagnostic system was applied to a model OTSG to test its effectiveness. The impact of measurement noise on the diagnostic accuracy was also analysed and discussed. A comparison between predicted and implanted degradation of a model OTSG demonstrated that the results were satisfactory, and the method is promising. Moreover, the diagnostic analysis of an OTSG based on real measurement has further proved that the proposed diagnostic method works well.

This simulation will recommend to the plant operator optimal operation schedules taking into consideration thermo-economics and lifing, under conditions of variation of power demand, electricity price, ambient conditions and gas turbine engine health states. It will suggest the more severely degraded engine should run at a relatively lower power setting to decrease creep life consumption. The established power plant optimisation framework will assist power plant operators to decide the total power output and power split between generators based on an optimisation system that considers both immediate economic benefit and life considerations. It will help existing power plant to adjust daily operation to achieve better thermoeconomic and lifing benefits. The outcome of this research will be useful for industrial CCGT power generation.

Keywords:

Creep Life, Decision-Making, Diagnostic, Economics, Emission, Gas Turbine, Once-through Steam Generator, Optimisation, Performance, Simulation, Steam Turbine, Thermoeconomic

ACKNOWLEDGEMENTS

It is a great pleasure to thank my research supervisor, Dr Yiguang Li, for his suggestions and supervision during the preparation and proceeding of the project. Meanwhile, I really appreciate his support while preparing the publications.

I want to express my appreciation to Dr Devaiah Nalianda for his valuable and constructive suggestions during the study here.

I would sincerely thank my sponsor, Manx Utilities (MU), who offer me this research project with funding which is eligibility for an international student. Moreover, I am thankful for my industrial supervisor, Mr Mike Newby, who kindly help with power plant knowledge. I am also very thankful to the Mr Graham Stigant and other MU staffs for preparing the filed data for OTSG performance model validation and power plant operation optimisation.

I acknowledge gratefully to Dr Zhitao Wang from the Harbin Engineering University for his suggestions, supporting and encouraging during the tough moments.

I feel very grateful to those who helped me during my PhD study here, those who gave me suggestions and those who encouraged me. These people are including some academic and administrative staffs, PhD researchers, and MSc students at Cranfield University. Especially appreciate to the graduated PhD students Dr Chen Wang, and Dr Zhuo Li for their advice, guidance, and encouragement.

Most of all, I am heartily obliged and grateful to my family members, for their encouragement, support, and dedication to my studies here which offered the foundation of the work.

TABLE OF CONTENTS

ABSTRACT i
ACKNOWLEDGEMENTS iii
LIST OF FIGURES viii
LIST OF TABLES xii
LIST OF EQUATIONS xiii
LIST OF ABBREVIATIONS xix
GREEK LETTERS xxvi
SUBSCRIPTS xxviii
SUPERSCRIPTS xxxi
1 Introduction 1
  1.1 Preamble 1
    1.1.1 Background 1
    1.1.2 Importance of This Research 2
  1.2 Aim and Objectives 3
    1.2.1 Aim 3
    1.2.2 Objectives 3
  1.3 Contribution to Knowledge 4
    1.3.1 Key Findings 4
    1.3.2 Potential Impact of Findings 4
  1.4 Thesis Outline 5
  1.5 Methodology Outline 5
2 Literature Review 9
  2.1 Gas Turbine Performance 9
    2.1.1 Gas Turbine Simulation Platform 9
  2.2 Gas Turbine Emissions 10
    2.2.1 Carbon Dioxides 10
    2.2.2 Adiabatic Flame Temperature 11
    2.2.3 Nitrogen Oxides 11
    2.2.4 Carbon Monoxide 13
    2.2.5 Conclusion 14
  2.3 High-pressure Turbine Creep Life 15
  2.4 OTSG Performance 16
  2.5 OTSG Performance Diagnosis 16
  2.6 Steam Turbine Performance 18
  2.7 Economics of Electricity Generation 19
  2.8 Optimiser 20
    2.8.1 Genetic Algorithm 20
    2.8.2 Simulated Annealing 20
    2.8.3 Ant Colony Optimisation 21
    2.8.4 Particle Swarm Optimisation 21

2.8.5 Differential Evolution 22
2.8.6 Gradient Descent 22
2.8.7 Tabu Search 23
2.8.8 Comparison between Single Criterion Optimisation and Multiple Criteria Optimisation 23
2.9 Multi-Criteria Decision Making 24
2.9.1 Technique for Order Preference by Similarity to Ideal Solution 24
2.9.2 Eigenvector Weighting Method 25
2.9.3 Concordance and Discordance Analyses by Similarity to Ideal Designs 25
2.10 Power Plant Optimisation 25
3 Methodology 27
3.1 Gas Turbine Performance Model 27
3.1.1 Design Point Performance Simulation 28
3.1.2 Off-design Point Performance Simulation 34
3.2 Gas Turbine Emissions Model 41
3.2.1 Carbon Dioxides 41
3.2.2 Adiabatic Flame Temperature 43
3.2.3 Nitrogen Oxides 50
3.2.4 Carbon Monoxide 50
3.3 High-pressure Turbine Creep Life Model 51
3.3.1 Blade Thermal Model 51
3.3.2 Blade Stress Model 54
3.3.3 Creep Model 57
3.4 OTSG Performance Model 58
3.4.1 Geometry Structure and Temperature Profiles 58
3.4.2 Basic Concepts and Definitions 60
3.4.3 Design Point Performance Simulation 62
3.4.4 Off-design Performance Simulation under Dual-pressure Operation 68
3.4.5 Off-design Performance Simulation under Single-pressure Operation 72
3.5 OTSG Performance Diagnosis Model 75
3.5.1 Cleanliness Factor of OTSG 75
3.5.2 Gas Path Analysis 75
3.5.3 Measurement Noise 79
3.6 Steam Turbine Performance Model 81
3.6.1 Steam Turbine Power Output 83
3.6.2 Steam Turbine Thermal Efficiency 83
3.7 Economic Model for CCGT Operation 83
3.7.1 Maintenance and Staff Cost 85
3.7.2 Fuel Cost 85

3.7.3 Emission Cost ... 86
3.7.4 Income through Selling Electricity ... 86
3.7.5 Spark Spread ... 87
3.8 Optimiser ... 87
3.8.1 Genetic Algorithm ... 87
3.9 Multi-Criteria Decision Making Model ... 94
3.9.1 Filter Undesired Results ... 94
3.9.2 TOPSIS ... 95
3.9.3 Adapted TOPSIS ... 96
3.10 Power Plant Decision Support System ... 97
3.10.1 CCGT Performance System ... 98
3.10.2 Optimisation Variables ... 100
3.10.3 Objective Function ... 101
3.10.4 Weighted Factor ... 101
3.10.5 Constraint and Penalty Function ... 101
3.10.6 Implementation of Decision Support for Optimisation System ... 102
4 Application, Results, and Analysis ... 105
4.1 OTSG Performance Simulation ... 105
4.1.1 OTSG Specification and Measurement ... 105
4.1.2 Design Point Performance Calculation and Validation ... 106
4.1.3 Off-design Performance Simulation and Validation under Dual-pressure Operation ... 106
4.1.4 Off-design Performance Simulation and Validation under Single-pressure Operation ... 109
4.1.5 Impact of Gas Turbine Power Setting and Steam Turbine Erosion 112
4.2 OTSG Performance Diagnosis ... 119
4.2.1 Effect of Fouling Resistance on OTSG Performance ... 119
4.2.2 Diagnostic System Testing ... 123
4.2.3 Effect of Measurement Noise ... 126
4.2.4 Diagnostic Analysis Applied to Real Power Plant Measurements .. 130
4.3 Decision Support of CCGT Power Plant ... 136
4.3.1 CCGT Specification ... 136
4.3.2 Typical Day Operation ... 137
4.3.3 Gas Turbine Engine without Degradation ... 139
4.3.4 Gas Turbine Engine under Degradation ... 147
4.3.5 Comparison between Optimised and Original Operations ... 152
4.3.6 Conclusions ... 153
5 Conclusions ... 157
5.1 Once-through Steam Generator Performance Simulation ... 157
5.2 OTSG Performance Diagnosis ... 158
5.3 Operation Optimisation of CCGT Power Plant ... 158
5.4 Overall Conclusion ... 159

6 Future Work 161
  6.1 Dynamic Model for the CCGT 161
  6.2 Adiabatic Flame Temperature Calculation 161
  6.3 Lifing Model 161
  6.4 OTSG Leakage Prediction 161
  6.5 Optimal Cleaning Schedules 162
  6.6 CCGT Cooling Cycle Optimisation 162
  6.7 Integration Heat Pump for Natural Gas De-icing 162
  6.8 Steam Turbine Corrosion 163
REFERENCES 164
APPENDICES 180
  Appendix A Pythia-Turbomatch Bricks 180
  Appendix B Sensitivity Analysis 181
  Appendix C Optimisation Results without Degradation 185
  Appendix D Optimisation Results under Degradation 189
  Appendix E Main Interfaces 193

LIST OF FIGURES

Figure 2-1 Comparison between Single Criterion Optimisation and Multiple Criteria Optimisation 24

Figure 3-1 Scheme of Dual Shaft Gas Turbine (GT). 27

Figure 3-2 Compressor Map [5]... 35

Figure 3-3 Burner Map [5]. 36

Figure 3-4 Turbine Map [5]. 37

Figure 3-5 Schematic of Standard Molar Enthalpies of Formation $\Delta\mathrm{Hfo}$ and Reaction $\Delta\mathrm{Hro}$ [8]. 44

Figure 3-6 Dissociated Flame Temperature Flowchart. 48

Figure 3-7 Creep Life Prediction Model. 51

Figure 3-8 Turbine Inlet Temperature Distribution along Span [173]. 52

Figure 3-9 One Dimensional HPT Blade Section. 52

Figure 3-10 Bending Moments of Turbine Blade [11]. 56

Figure 3-11 Schematic of Once-through Steam Generator (OTSG) [175]. 59

Figure 3-12 OTSG Temperature Profiles along OTSG Gas Path. 60

Figure 3-13 OTSG Design Point (DP) Performance Calculation. 63

Figure 3-14 OTSG Off-Design (OD) Performance Calculation with Dual-pressure. 69

Figure 3-15 OTSG OD Performance Calculation with Single-pressure. 73

Figure 3-16 Nonlinear Gas Path Analysis based on Newton-Rapson Method [31]. 78

Figure 3-17 Steam Turbine Schematic. 81

Figure 3-18 T-S Diagram of Ideal and Actual Steam Cycle. 81

Figure 3-19 Typical Daily Load Profile for Isle of Man, January 2005 [189]. 84

Figure 3-20 Single Criterion Genetic Algorithm Module Flowchart. 88

Figure 3-21 Relation between Real and Binary Numbers [142]........................ 89

Figure 3-22 Cumulative Percentage for Roulette Wheel Selection [192].......... 89

Figure 3-23 Ranking Method [16,194,195]. 92

Figure 3-24 MCGA Module Flowchart. 93

Figure 3-25 Niche by Project Pareto Front (PF) onto Criterion Axes [16]. 93

Figure 3-26 Criteria Constraints. 94

Figure 3-27 Example of Normalised PF. 97

Figure 3-28 Power Plant Schematic. 99

Figure 3-29 Percentage Reduction in Life due to Low Cycle Fatigue Interaction with Creep [198]. 100

Figure 3-30 Architecture of Decision Support System. 104

Figure 4-1 Comparison between Measured and Predicted Results (WHP and WLP). 108

Figure 4-2 Comparison between Measured and Predicted Results (Pa and Pe). 108

Figure 4-3 Comparison between Measured and Predicted Results ($\mathrm{T8}$ and Te). 108

Figure 4-4 Average Relative Errors of 292 Test Points. 109

Figure 4-5 Comparison between Measured and Predicted Results (WHP). ... 110

Figure 4-6 Comparison between Measured and Predicted Results (Pa). 111

Figure 4-7 Comparison between Measured and Predicted Results ($\mathrm{T8}$). 111

Figure 4-8 Average Relative Errors of 13 Test Points. 112

Figure 4-9 Effect of GT Power on Exhaust Gas $\mathrm{T1}$ and Wexh. 113

Figure 4-10 Effect of GT Power on OTSG $\mathrm{T8}$ and η. 113

Figure 4-11 Effect of GT Power on OTSG WHP and WLP. 114

Figure 4-12 Effect of GT Power on OTSG Pa and Pe. 114

Figure 4-13 Effect of GT Power on OTSG Ta and Te. 115

Figure 4-14 Effect of GT Power on OTSG High Pressure (HP) Heat Transfer Areas. 115

Figure 4-15 Effect of GT Power on OTSG Low Pressure (LP) Heat Transfer Areas. 116

Figure 4-16 Effect of EFST on OTSG $\mathrm{T8}$ and η. 117

Figure 4-17 Effect of EFST on OTSG WHP and WLP. 117

Figure 4-18 Effect of EFST on OTSG Pa and Pe. 118

Figure 4-19 Effect of EFST on OTSG Ta and Te. 118

Figure 4-20 Effect of EFST on OTSG HP Heat Transfer Areas. 119

Figure 4-21 Effect of EFST on OTSG LP Heat Transfer Areas. 119

Figure 4-22 Effect of Cleanliness Factor (CF) on OTSG $\mathrm{T8}$ and η. 120

Figure 4-23 Effect of CF on WHP and WLP. 121

Figure 4-24 Effect of CF on Pa and Pe. 121

Figure 4-25 Effect of CF on OTSG HP Heat Transfer Area............................ 122

Figure 4-26 Effect of CF on OTSG LP Heat Transfer Area. 122

Figure 4-27 Relative Error of CF. 124

Figure 4-28 Convergence Procedure of Three Diagnostic Cases. 126

Figure 4-29 Measurement Samples of $\mathrm{T8}$ with Measurement Noise, Post-filtered Measurement and True Value. 127

Figure 4-30 Diagnostic Results CF using Noisy Measurements. 128

Figure 4-31 Relative Error of CF. 128

Figure 4-32 Comparison of Relative Error between Ten Noisy Measurement and Post-filtering Measurement. 129

Figure 4-33 Convergence Processes of 11 Diagnostic Points........................ 130

Figure 4-34 Predicted CF and Averaged Value.. 132

Figure 4-35 Relative Prediction Error of WHP with and without Implanted Degradation. 132

Figure 4-36 Relative Prediction Error of WLP with and without Implanted Degradation. 133

Figure 4-37 Relative Prediction Error of Pa with and without Implanted Degradation. 133

Figure 4-38 Relative Prediction Error of Pe with and without Implanted Degradation. 134

Figure 4-39 Relative Prediction Error of $\mathrm{T8}$ with and without Implanted Degradation. 134

Figure 4-40 Relative Prediction Error of Te with and without Implanted Degradation. 135

Figure 4-41 Comparison of Relative Errors with and without Implanted Predicted Fouling. 135

Figure 4-42 Typical Day Load Profile. 137

Figure 4-43 Typical Day System Buying (SSP) and Ambient Temperature (Tamb) Profile. 138

Figure 4-44 PF Searched by MCGA. 140

Figure 4-45 Normalised PF (PFN) and Final Operating Point (FOP). 141

Figure 4-46 PF Searched by MCGA. 143

Figure 4-47 PFN and FOP. 144

Figure 4-48 Suggested Trading Schedule without Degradation. 145

Figure 4-49 SSEq for Typical Day Operation. 146

Figure 4-50 LCFEq for Typical Day Operation. 146

Figure 4-51 Effect on Creep Factor of GT Degradation Factor. 147

Figure 4-52 PF Found by MCGA Search. 149

Figure 4-53 FOP Selection from PFN. 150

Figure 4-54 Suggested Trading Schedule under Degradation. 150

Figure 4-55 SSEq under Suggested Typical Day Operation. 151

Figure 4-56 LCFEq under Suggested Typical Day Operation. 151

Figure 4-57 Comparison between Optimised and Original Operation in LCFEq. 152

Figure 4-58 Enhancement of LCFEq in Percentage. 153

LIST OF TABLES

Table 3-1 Dry Air Composition [116]. 42

Table 3-2 Natural Gas Composition [169]. 42

Table 3-3 Total Thermochemical Enthalpy Levels for Gases [10]. 45

Table 3-4 Partial-pressure Equilibrium Constants [170]. 48

Table 3-5 Measurement of Noise Magnitude [186]... 80

Table 3-6 Parent Strings.. 90

Table 3-7 Offspring Strings.. 90

Table 3-8 String before and after Mutation.. 90

Table 3-9 Example of Decision-Making... 97

Table 4-1 OTSG DP Performance Specification [175,199]. 105

Table 4-2 Results Comparison at DP [175,199,200]. 106

Table 4-3 Iteration Variables for DP Performance Calculation. 106

Table 4-4 Range of Operating Conditions for 292 Off-Design (OD) Points. ... 107

Table 4-5 Range of Operating Conditions for 13 OD Points.......................... 109

Table 4-6 OTSG Measurement Set z. 123

Table 4-7 Diagnostic Results of Measurements for Case 1. 124

Table 4-8 Diagnostic Results of Measurements for Case 2. 124

Table 4-9 Diagnostic Results of Measurements for Case 3. 125

Table 4-10 Comparison of Implanted and Predicted Degradations for Three Diagnostic Test Cases.. 125

Table 4-11 Range of Operating Conditions for 10 OD Points........................ 131

Table 4-12 GT DP Specification [175].. 136

Table 4-13 Steam Turbine DP Specification [175]... 136

Table 4-14 Operation Condition between 00:00 and 00:30. 140

Table 4-15 Operation Condition between 11:30 and 12:00. 142

Table 4-16 Case Study of Different Operating Conditions............................. 143

Table 4-17 Assumed GT6 Engine Degradation... 148

LIST OF EQUATIONS

(3-1) 29
(3-2) 29
(3-3) 29
(3-4) 30
(3-5) 30
(3-6) 30
(3-7) 30
(3-8) 30
(3-9) 31
(3-10) 31
(3-11) 31
(3-12) 31
(3-13) 32
(3-14) 32
(3-15) 32
(3-16) 32
(3-17) 33
(3-18) 33
(3-19) 33
(3-20) 33
(3-21) 33
(3-22) 35
(3-23) 36
(3-24) 36
(3-25) 37
(3-26) 37
(3-27) 37
(3-28) 37

(3-29).. 39

(3-30).. 39

(3-31).. 39

(3-32).. 39

(3-33).. 40

(3-34).. 40

(3-35).. 40

(3-36).. 40

(3-37).. 40

(3-38).. 41

(3-39).. 41

(3-40).. 42

(3-41).. 43

(3-42).. 43

(3-43).. 44

(3-44).. 44

(3-45).. 44

(3-46).. 45

(3-47).. 46

(3-48).. 46

(3-49).. 46

(3-50).. 46

(3-51).. 46

(3-52).. 47

(3-53).. 47

(3-54).. 47

(3-55).. 47

(3-56).. 49

(3-57).. 49

(3-58).. 50
(3-59).. 50
(3-60).. 50
(3-61).. 53
(3-62).. 53
(3-63).. 53
(3-64).. 53
(3-65).. 53
(3-66).. 54
(3-67).. 54
(3-68).. 55
(3-69).. 55
(3-70).. 55
(3-71).. 55
(3-72).. 56
(3-73).. 56
(3-74).. 56
(3-75).. 57
(3-76).. 57
(3-77).. 57
(3-78).. 57
(3-79).. 58
(3-80).. 58
(3-81).. 60
(3-82).. 61
(3-83).. 61
(3-84).. 61
(3-85).. 62
(3-86).. 62

(3-87) 62
(3-88) 64
(3-89) 64
(3-90) 65
(3-91) 65
(3-92) 66
(3-93) 66
(3-94) 66
(3-95) 66
(3-96) 66
(3-97) 67
(3-98) 67
(3-99) 67
(3-100) 67
(3-101) 70
(3-102) 70
(3-103) 72
(3-104) 75
(3-105) 75
(3-106) 76
(3-107) 76
(3-108) 76
(3-109) 76
(3-110) 76
(3-111) 77
(3-112) 77
(3-113) 77
(3-114) 77
(3-115) 77

(3-116).. 78
(3-117).. 79
(3-118).. 79
(3-119).. 79
(3-120).. 79
(3-121).. 80
(3-122).. 80
(3-123).. 82
(3-124).. 82
(3-125).. 82
(3-126).. 82
(3-127).. 82
(3-128).. 83
(3-129).. 83
(3-130).. 83
(3-131).. 83
(3-132).. 85
(3-133).. 86
(3-134).. 86
(3-135).. 86
(3-136).. 87
(3-137).. 92
(3-138).. 92
(3-139).. 95
(3-140).. 95
(3-141).. 95
(3-142).. 95
(3-143).. 95
(3-144).. 96

(3-145).. 96
(3-146).. 101
(3-147).. 101

LIST OF ABBREVIATIONS

For Gas Turbine Performance Model

A	Nozzle Area
$BRatio$	Bleed ratio
C^*	Heat capacity rate ratio
C	heat capacity
CM	Corrected mass flow rate
CN	Shaft Corrected Rotational Speed
Cp	Specific heat at constant pressure
CW	Compressor work
Dh	Enthalpy drop
FF	Fuel flow rate
h	Specific enthalpy
H	Total Enthalpy
LHV	Low heating value
MN	Mach number
n	Iteration step
NTU	Number of transfer unit
p	Static pressure
P	Total Pressure
PCN	Shaft relative rotational speed
PO	Power output
PR	Pressure ratio
R_g	Gas constant
RMS	Root mean square
t	Static temperature
T	Total temperature
TET	Turbine entry temperature
TW	Turbine work
UA	Overall conductance
UW	Turbine useful work
V	Velocity

W	Mass flow rate
$\varDelta P$	Pressure drop

For Gas Turbine Emission Model

ΔH_f^o	Enthalpy of formation at standard state
ΔH_r^o	Enthalpy of reaction at standard state
ΔH_a	Atomisation enthalpy
H^{T^*}	Sensible enthalpy
$H_t^{T^*}$	Total enthalpy at specified temperature
$(\Delta H^T)_{air}$	Air sensible enthalpy at specified temperature
$D(X-Y)$	Released enthalpy for bond dissociation
FAR	Fuel-air ratio
EQR	Equivalence ratio
K_{co_2}	CO_2 equilibrium constants
K_{H_2O}	H_2O equilibrium constants
$\dot{m}_A$	Combustor airflow rate
$\dot{m}_{pz}$	Primary zone airflow rate
P	Pressure
T	Temperature
V_c	Combustion volume
V_c	Evaporation volume
W_{CO}	Amount of carbon monoxide
W_{NO_x}	Amount of nitrogen oxides

For High-Pressure Turbine Creep Life Model

$A_{CS,sp}$	Cross-sectional area of a specified location along the blade span
$A_{An,sec}$	Blade section annulus area
C	Constant
CF	Centrifugal force
CS	Centrifugal stress
d_{sp}	Distance between the section CG to the respective specified location along the blade span

I_X	Second moment of area at a specified location along the blade span
I_Y	Second moment of area at a specified location along the blade span
LF	Life fraction
LMP	Larson-Miller Parameter
m	Mass
$M_{X,sp}$	Resulting bending moment about the $X-X$ direction at a specified location along the blade span
$M_{Y,sp}$	Resulting bending moment about the $Y-Y$ direction at a specified location along the blade span
MBM_{sp}	Momentum bending moment about the specified location along the blade span
MF	Momentum force
NoB	Number of blade
OT	Operating time
P	Pressure
PBM_{sp}	Pressure bending moment about the specified location along the blade span
PF_{sec}	Pressure force acting on the blade section
r_{CG}	Radius between the rotation axis and the blade section or the shroud centre of gravity
$RTDF$	Radial temperature distribution factor
t_f	Time to failure
t_{ref}	Reference time to failure
T	Temperature
TS_{sp}	Total stress
X_L	X distance between the corresponding chord-wise location to the blade CG
Y_L	Y distance between the corresponding chord-wise location to the blade CG
ΔP_{sec}	Average static pressure difference for each section
ΔVel	Average velocity difference for each section

For OTSG Performance Model

A	Heat transfer area
$CA_{[\cdot]/[\cdot]}$	Ratio of heat transfer area
$Cf_{[\cdot]/[\cdot]}$	Heat transfer ratio
d	Diameter of tube
EF_{ST}	Steam turbine erosion factor
$f(\cdot)$	OTSG system function
G	Number of convergence check (DP: $G = 2$; OD: $G = 6$)
h	Specific enthalpy
$LMTD$	Logarithmic mean temperature difference
n	Iteration step
N	Number of prediction points
P	Pressure
PP	Pinch point
q	Specific heat rate
Q	Heat rate
RMS	Root mean square
T	Temperature
U	Overall heat transfer coefficient
W	Mass flow rate
X	Iteration variable matrix
ΔY	The total iterative error
$\bar{Z}$	Measured parameter
Z	Simulated parameter

For OTSG Diagnostic Model

a	Number of cases
CF	Cleanliness factor
FCM	Fault coefficient matrix
h	Nonlinear vector-valued function
H	Influence coefficient matrix (ICM)

k	Number of datum for average
M	Number of measurements
N	Number of degradation factors
$o[]$	Higher order term
P	Pressure
PP	Pinch point temperature difference
RMS	Root mean square
T	Temperature
U	Overall heat transfer coefficient
W	Mass flow rate
$\vec{x}$	Degradation factor matrix
$\vec{x}$	Measurement parameter matrix

For Steam Turbine Performance Model

h	Enthalpy
P	Pressure
PO	Power output
S	Entropy
W	Mass flow rate
x	Steam content of the wet steam

For Economic Model

EC	Emission cost
FC	Fuel cost
FF	Fuel flow rate
$Income$	Income from selling electricity
LHV	Low heating value
MC	Maintenance cost
MSC	Maintenance and staff cost
OT	Operating time
PO_{CCGT}	Power output from CCGT power station

Pri_{FF}	Fuel price
SC	Staff cost
SS	Spark spread
SSP	System selling price
$Taxes$	Emission taxes of CO_2
W_{CO_2}	Mass flow rate of CO_2

For Optimiser Model

a	Control coefficient
FN	Fitness
FN_s	Fitness sharing
N_{Niche}	Number of Niches
PS	Population size
RANK(i)	Rank ith population

For Multi-Criteria Decision Making Model

$\bar{w}$	Normalised weight factor
D	Relative distance to the ideal best and ideal worst
y	Initial decision matrix
z	Normalised decision matrix
S^b	Distance to ideal best
S^w	Distance to ideal worst
V	Weighted normalised decision matrix
V^b	Ideal best value for the weighted normalised decision matrix
V^w	Ideal worst value for the weighted normalised decision matrix
w	Weight vector

For Power Plant Optimisation System

DM_{island}	Island power demand

DM_{total}	Total power demand (island and cable)
LF	Life fraction
LCF_{Eq}	Equivalent Life consumption factor
LCF_{Ref}	Reference Life consumption factor
PO_{CCGT}	CCGT power output
SS	Spark spread
SS_{Eq}	Equivalent spark spread
SS_{Ref}	Reference spark spread

GREEK LETTERS

For Gas Turbine Performance Model

η	Efficiency
ε_{HE}	Heat exchanger effectiveness
δ	Global error
γ	Heat capacity ratio
ρ	Gas density

For Gas Turbine Emission Model

ε_{blade}	Blade effectiveness
η_{conv}	Convection efficiency
ω	Angular velocity
ρ_{pz}	Primary zone airflow density
λ_{eff}	Evaporation constant

For OTSG Performance Model

α	Heat transfer coefficient
λ	Thermal conductivity
η	OTSG efficiency
$\bar{\gamma}_i$	Average prediction error of ith measurement parameter
σ	Convergence threshold (1E-05)

For OTSG Diagnostic Model

α	Constant weight
σ	GPA convergence threshold
$\vec{v}$	Zero-mean measurement noise vector
ω	Under-relaxation factor
γ	Prediction error of cleanliness factor
$\bar{\varepsilon}$	Average difference of cleanliness factor

ϕ	Prediction error of measurement parameter
$\bar{\phi}$	Average prediction error of measurement parameter

For Steam Turbine Performance Model

$\eta_{ST,pol}$	Steam turbine actual polytrophic efficiency
$\eta_{ST,pol,dry}$	Steam turbine polytrophic efficiency at dry condition
$\eta_{ST,is}$	Steam turbine isentropic efficiency
η_{m}	Steam turbine mechanical efficiency
η_{th}	Steam turbine thermal efficiency

SUBSCRIPTS

For Gas Turbine Performance Model

act	Actual value
bur	Burner
cal	calculated
co	Cold flow
$comp$	Compressor
cri	Critical condition
DP	Design point
Duc	Duct
gue	Guessed value
GT	Gas turbine
ho	Hot flow
$HETCOL$	Cold side of heat exchanger
$HETHOT$	Hot side of heat exchanger
HP	High-pressure
HPT	High-pressure turbine
in	Inlet
LP	Low-pressure
LPT	Low-pressure turbine
max	Maximum value
min	Minimum value
Noz	Nozzle
OD	Off-design point
out	Outlet
P	Pressure
req	Required value
sn	Sonic condition
st	Static condition
$stag$	Stagnation condition
tt	Total
$turb$	Turbine

W	Mass flow rate

For Gas Turbine Emission Model

P	Products
pz	Primary zone adiabatic flame temperature
R	Reacts
st	Stoichiometric flame temperature

For High-Pressure Turbine Creep Life Model

$axial$	Axial direction
bur	Burner
$cool$	Colling flow
g	Gas
in	Inlet
m	Metal
max	Maximum
min	Minimum
out	Outlet
Ref	Reference value
tan	Tangential direction

For OTSG Performance Model

amb	Ambient
DP	Design point
exh	Exhaust
HP	High-pressure
in	Inlet
inn	Inner side of tubes
LP	Low-pressure
o	Outer (fume) side of tubes

OD	Off-design point
out	Outlet
TOT	Total outer tube surface

For OTSG Diagnostic Model

amb	Ambient
C	Clean state
exh	Exhaust
F	Fouling state
HP	High-pressure
LP	Low-pressure
m	Iteration step
o	Taylor series about given operation point

For Steam Turbine Performance Model

HP	High-pressure
in	Inlet
LP	Low-pressure
out	Outlet
ST	Steam turbine

For Power Plant Optimisation System

cle	Gas turbine under clean state
deg	Gas turbine under degradation state
$GT6$	Specified gas turbine engine 6 in Figure 3-28
$GT7$	Specified gas turbine engine 7 in Figure 3-28

SUPERSCRIPTS

For OTSG Performance Model

$'$	Function's derivative

For OTSG Diagnostic Model

$Predict$	Predicted measurement parameter
T	Transpose
$True$	Measured measurement parameters
-1	Inverse
$\#$	Pseudoinverse

For Multi-Criteria Decision Making Model

b	Ideal best
w	Ideal worst

1 Introduction

1.1 Preamble

1.1.1 Background

The increasing demand for electricity and simultaneous concern about global warming has meant that there is now a demand for electric power generation to be more efficient, cleaner, and cost-effective. An annual increase of around 1.8% in the world's energy production is predicted for the next 30 years [1].

With traditional power generation configurations, such as coal-fired boilers, it was difficult to achieve high efficiency. However there are many sources of energy that can be used for power generation, these include wind power, solar, nuclear, tide energy, and fuel. It has been demonstrated that alternative sources could supply most of the energy produced by the burning the fossil fuel [2].

Today power generation is usually by burning fuel in diesel, gas turbine, and fired steam generators with steam turbine engines, and one of the most attractive arrangements for a power plant is the combined cycle gas turbine (CCGT) that can recover approximately two-thirds of the heat from the gas turbine exhaust flow [3].

There is a growing body of literature that recognises the importance of running a power plant with advanced efficiency, high economic benefit, low emission and extended operating hours between failures. The power plant thermodynamic model has a pivotal role in the design and operation of power generating systems. Meanwhile, economic benefit plays the vital role for the potential power plant investor and power plant holder.

The gas turbine hot section working life has a considerable impact on power plant availability and safety considerations. To acquire high revenue and prevent over-consumption of the gas turbine hot section life when generating electricity, operation optimisation is an urgent consideration. This project will include an investigation of CCGT performance, gas turbine gas turbine hot section creep life analysis, economic analysis, emission analysis, optimisation, and decision-making. The project develops a suitable decision support framework for optimising CCGT operation under different conditions which include variations of ambient temperature, pressure, humidity, engine health state, electricity price, and power demand. The optimisation algorithm will consider the different constraints including gas turbine low-pressure turbine inlet temperature, once-through steam generator (OTSG) stack temperature, steam quality at the steam turbine exit and grid power demand.

1.1.2 Importance of This Research

- There has been a growing body of literature concerning OTSGs, but no previous publication has reported an investigated of the parallel dual pressure OTSG. For example, no simulation algorithm is available for the OTSG at Manx Utilities, Isle of Man, UK. It is worthwhile to develop an OTSG thermodynamic model for predicting OTSG characteristics under both design point and off-design conditions.
- In addition, no research has been found concerning OTSG degradation diagnostics to quantify fouling during operation. The power plant could use thermal shock (dry running) to mitigate tube outer side fouling. However, the relative short-time intervals used for fouling mitigation will over-consume the OTSG tube life but the longer time intervals will have a more adverse effect on OTSG performance. Hence, it is necessary to develop an OTSG diagnostic to quantify the fouling level for condition-based maintenance rather than time-based maintenance.
- Attempts have been made to develop an optimisation system for deciding configuration, capacity, and thermodynamic cycle parameters of a new power plant. Existing power plant operation optimisation has frequently focused only on the thermodynamic and thermoeconomic parameters and gas turbine hot section lifing has been combined with a thermoeconomic model to optimise the maintenance schedule for medium/long-term operation. However, lifing assessment for maintenance strategies is typically based on the gas turbine design point condition, as it is not possible to accurately represent the real ever-changing electricity demand.

Up to now, no attention has been paid to produce a guide for an existing CCGT power plant to decide all power setting for the plant, including the power split between different engine units taking into account both thermoeconomic parameters and gas turbine lifing considerations. In daily operations, it is especially tricky for power plant operators to decide total power output and power allocation between engine units when different engine health conditions exist. It is worth mentioning that degraded gas turbine will have higher hot section temperatures than healthy engines at the same power setting. Additionally, the life consumption rate increases exponentially with more severe degradation levels, so it is necessary to develop a decision support framework to guide the power plant’s daily operation that not only considers thermoeconomic parameters but also prevents over-consumption of the gas turbine hot section life.

1.2 Aim and Objectives

1.2.1 Aim

The power plant operator does not have a decision support tool to decide the total power output under different conditions. Moreover, there is no decision support for power split between different engine units that the health state of gas turbine engines tends to be different with time. The main aim of this study is to develop a techno-economic methodology for the optimise operation schedules of a CCGT power plant taking into account gas turbine life consumption and economic benefits that the CCGT power plant includes two gas turbines and two parallel dual pressure OTSGs, and a steam turbine.

1.2.2 Objectives

There are three primary objectives of this study to achieve the above aim:

- To develop a methodology that correctly predicts parallel dual pressure OTSG performance.
- To develop a diagnostic system for OTSG which quantifies the fouling level.
- To develop a decision support platform for operation optimisation of CCGT power plant.

1.3 Contribution to Knowledge

1.3.1 Key Findings

- An algorithm suitable for simulating OTSG performance has been developed with high precision and the model developed for OTSG performance could include the impact of degradation on OTSG performance as well.
- The results show that the proposed diagnostic system is able to produce satisfactory results even when the simulated measurements contain noise. Additionally, using measured field data for performance diagnostic also demonstrated the effectiveness of the proposed system.
- The proposed decision support platform could be helpful for an existing power plant to schedule the daily operation to achieve high economic benefit without over consuming the gas turbine hot section life. It is particularly useful when the engines' health states are different.

1.3.2 Potential Impact of Findings

- The newly developed OTSG thermodynamic model could be applied to simulate the performance of an existing OTSG to obtain its operating characteristic. The proposed method also could be used to assist in the design of a new OTSG. Meanwhile, the plant manager could input degradation factors into the OTSG performance model for it to provide an intuitive view of degraded OTSG performance.
- The proposed OTSG diagnostic system could help the power plant to track OTSG degradation and schedule condition-based maintenance. It should significantly benefit the plant manager to determine the timeline for fouling mitigation by thermal shock.
- The developed decision-support tool for power plant optimisation could guide the power plant operator in deciding the preferred operating condition for the CCGT based on any preference between economic benefits and life consideration. It will also reduce the risk of overrunning the gas turbine engine lifing while meeting economic benefits considerations.

1.4 Thesis Outline

- Chapter 1 – This chapter presents an overview of research background, motivation, aims, objectives, contribution to knowledge, thesis outline, and methodology outline.
- Chapter 2 – The pertinent literature were browsed, and the related state of art methods are discussed.
- Chapter 3 – The detailed algorithms for different models are introduced.
- Chapter 4 – Discusses the results obtained for the three major contributions.
- Chapter 5 – Conclusions are presented as are the major contributions to knowledge made by this study.
- Chapter 6 – The limitations of this work are presented, and future work is suggested.

1.5 Methodology Outline

The methodologies for the involved models could be divided into two parts without and with innovation:

1) Without innovation
    - The gas turbine performance model is based on Pythia-Turbomatch developed by the Propulsion Engineering Centre, Cranfield University [4,5].
    - The carbon dioxide emission model has been developed based on chemical equilibrium [6]. The emissions of carbon monoxide and nitrogen oxides are based on the empirical correlation suggested by Lefebvre (2010) [7], and the flame temperature as referred to [8–10].
    - The gas turbine hot section creep life was recoded in C sharp based on the existing algorithm [11].
    - The steam turbine performance model is a development based on the method suggested by [12–14].

- The economic model is based on the four elements of concern to power plant operators: maintenance and staff cost, fuel cost, emission cost, and revenue obtained by the sale of electricity [15].
- The Genetic Algorithm optimiser is based on the work of Todd (1997) [16].
- The multi-criteria decision-making model is adapted from the Technique for Order Preference by Similarity to Ideal Solution [17].

2) With innovation
    - The novel thermodynamic performance model of OTSG is derived from the continuity of mass and energy, and the fundamental laws of thermodynamics. The most challenging part of modelling parallel dual pressure OTSGs are the moving boundaries, and multi-pressure circuits in parallel. The proposed performance simulation algorithm is validated against field data of an OTSG installed and operated at Manx Utilities in the Isle of Man, United Kingdom.
    - This study introduces a nonlinear gas path method to diagnose the fouling of an OTSG, this is based on the Newton Raphson method and gas path measurements. The method has been applied to a model OTSG implanted with typical fouling degradation to test the effectiveness of the diagnostic method. In addition, the diagnostic analysis has been applied to an OTSG of a CCGT power plant operated at Manx Utilities using real power plant measured data to demonstrate the applicability of the method.
    - The decision support framework is designed to optimise the CCGT power plant daily generation schedule. When considering the thermoeconomic of the CCGT, and gas turbine hot section lifing, the framework of the decision-support model is based on a CCGT thermoeconomic and lifing, multi-criteria Genetic Algorithm, and multi-criteria decision-making. Management of the power generation from an operational plant for a typical day has been analysed using model-based operations to instead experience-based that include engine health condition, electricity price, fuel

price, emission tax, gas turbine hot section lifing, and power demand simultaneously.

2 Literature Review

2.1 Gas Turbine Performance

The gas turbine (GT) engine simulation model for the top cycle of a combined cycle power plant is the foundation of this work. To reduce the cost of engine design, Pilidis (1983) [18] proposed an engine simulation model for both steady state and transient conditions. Sugiyama (1990) [19] introduced a universal GT model for real-time simulation of aero, industrial and marine engine performance. Sanghi et al. (1998) [20] proposed a steady state simulation model for military engines, considering control of the early design stage. Wang (2016) [21] introduced a GT transient simulation model which combined the fuel and control systems.

Several widely used GT performance simulation software are introduced below.

2.1.1 Gas Turbine Simulation Platform

2.1.1.1 GasTurb

The Kurzke (1995) [22] first proposed a model of a GT which included design point (DP), off-design (OD) and transient simulations. However, this model could only cope with engines available in the engine library that reduced its flexibility and generality. More detail can be found on the GasTurb official website [23].

2.1.1.2 Modular Aero-Propulsion System Simulation (MAPSS)

NASA develops the MAPSS for simulating turbofan engines with a graphical user interface. Parker and Guo (2003) [24] first developed MAPSS for a turbofan simulation using Simulink after which MAPSS was extended and commercial versions published; C-MAPSS and C-MAPSS40k [25]. Demonstrations of the MPSS and C-MPSS software can be found in [25,26], with detailed information in [27].

2.1.1.3 Gas Turbine Simulation Program (GSP)

GSP was developed for simulating the performance of any GT engine under both steady-state and transient conditions [28]. The GPS offers the engine configuration in two-dimensions and can cope with installation performance loss and system failure. Based on GSP, the Netherlands Aerospace Centre has developed an online tool called Turbine Engine Real-Time Simulator (TERTS) to support the aerospace industry.

2.1.1.4 Pythia-Turbomatch

Turbomatch is a modular GT engine simulation software that was first developed by MacMillan (1974) [4]. Since then, the platform has been developed more than fourth years at Centre for Propulsion Engineering, Cranfield University. Today, Turbomatch is able to simulate civil, military, industrial, and marine engines. It has been used successfully to simulate the performance of single and multiple shaft engines with different heat exchanger configurations [29]. Additionally, a web-based engine performance simulation model has been developed by Apostolidis et al. (2013) [30], the core of which is based on Turbomatch. The diagnostic system Pythia, which is also based on Turbomatch can now address the performance adaptation to GT, component degradation diagnostics and prognostics, and the life consumption prediction of high-pressure turbine blades [5,31,32].

2.2 Gas Turbine Emissions

The world’s ever-increasing demand for power generation has resulted in significant regulation of power plant emissions so that one of the driving factors in modern GT design is to reduce emissions and avoid emission taxes. Generally speaking, there are five major emissions from GT engines: smoke (particulate matter), carbon dioxide (CO_2), carbon monoxide (CO), unburned hydrocarbons (UHC), and nitrogen oxides (NOx) [1]. There is a direct and substantial correlation between unburned hydrocarbon (UHC) and carbon monoxide (CO) emissions [1]. UHCs are, essentially, the fuel that was not completely combusted, and are mostly produced at low power levels [1].

2.2.1 Carbon Dioxides

2.2.1.1 Carbon Dioxides Equivalents Value

The US Environmental Protection Agency (EPA) has suggested a method of calculating a carbon dioxide equivalence value (2016) [33]. The equivalencies calculator uses the fuel consumed (e.g., natural gas) and/or the heat output (combustion energy) to calculate the mass of carbon dioxide produced.

2.2.1.2 Carbon Dioxides Prediction based on Stoichiometric Balance

The second method for predicting the amount of carbon dioxide produced by combustion is to assume a stoichiometric balance. In most modern industrial GT engines, the combustor efficiency is around 0.999 for a broad power setting [1], and it is acceptable to assume the complete combustion of the natural gas when calculating the carbon dioxide produced. Mohamed (2013) [34] streamlined these calculations by the simplifying assumption that natural gas was methane.

2.2.1.3 Stirred Reactor model

The reactor model was developed to predict the nitrogen oxides, and carbon monoxide produced by a GT engine and is capable of determining the carbon dioxide present by considering it as an extraneous product [35].

2.2.2 Adiabatic Flame Temperature

The nitrogen oxides, carbon monoxide, and UHC are all related to the primary temperature that is the adiabatic flame temperature located at the combustor primary zone. Hence, in this thesis, the primary temperature calculation will be introduced before considering these emissions. Spakovszky et al. (2006) [36] defined adiabatic flame temperature as the final product temperature of two reacting gases under a specific pressure, incomplete combustion or dissociation, but without any heat loss. There are three solutions for the calculated adiabatic flame temperature; for constant specific heat, for variable specific heat with temperature, and for temperature related to enthalpy [37–40].

2.2.3 Nitrogen Oxides

There are three main techniques applied to predict nitrogen oxides emission.

2.2.3.1 Nitrogen Oxides Correlation

There are five widely-used correlations developed by previous researchers for predicting nitrogen oxide emission from traditional combustors [7,41–44]. All the relationships show satisfactory accurate results for the given combustors.

Tsalavoutas et al. (2007) [45] suggested a method for extending the existing correlations to an industrial GT and a military turbojet that obtained good agreement when compared with measurement data. Nalianda and Dahlquist (2015) [46] have developed a new relation, which has shown satisfactory results when correlating nitrogen oxides produced by rich-burn, quick-mix, and lean-burn combustors.

2.2.3.2 Stirred Reactor Model

Samaras (2010) [47] developed an emission model for industrial GTs based on perfectly-stirred reactors, a series of perfectly-stirred reactors (PSRS), and partially-stirred reactors (PaSR), all of which have shown adequately accurate results. Cesar (2010) [48] proposed a reactor model for prediction the emissions tends of both existed and future GT combustors. Pervier (2013) [35] offered reactor models for aero engine root optimisation by considering nitrogen oxide emissions.

2.2.3.3 Computational Fluid Dynamics

Usually, Reynolds Averaged Navier Stokes (RANS), Large Eddy Simulation (LES), Detached Eddy Simulation (DES), and Direct Numerical Simulation (DNS) are used for emission calculations [49]. Maidhof and Janicka (1993) [50] simulated the turbulence swirling flow effect within a combustor to predict the production of nitrogen oxides. However, the predicted primary temperature was higher than the experimental data that cause higher nitrogen oxides when comparing with measurement data. Alizadeh (1993) [51] developed a nitrogen oxides prediction method based on a laminar flamelet approach. Marini, Bucchieri, and Peschiulli 2010 [52] proposed a computational fluid dynamics (CFD) simulation for nitrogen oxides production based on a shear stress transport turbulence model. Meloni (2013) [53] suggested CFD modelling of emissions for industrial GTs using 35 chemical species and 177 reactions, and which showed a high level of accuracy when compared to measured nitrogen oxides. Pierre (2016) [54] indicated that the flame lengths could be over-predicted using RANS simulation which should thus apply DES or LES to increase the accuracy of the result. The flame lengths will directly affect flame temperature, and too long a flame will tend to overestimate the nitrogen oxides produced.

2.2.4 Carbon Monoxide

2.2.4.1 Carbon Monoxide Correlation

Two widely used correlations have been developed for carbon monoxide [7,44]. These two correlations have proved to be sufficiently accurate to be used with the proposed GT engines.

2.2.4.2 Stirred Reactor Model

Rizk and Mongia (1993) [55] sub-divided an annular combustor into several separate reactors to predict the CO produced with an accurate prediction. Allaire (2006) [56] further developed the physic based emissions model for policy-making that estimate the effect design and operation condition on emissions and the predicted results showed good agreement with five industry combustors. Marchand (2013) [57] suggested a reactor network method for predicting carbon monoxide and tested his hypothesis with four combustors. This model considered the effects of fuel drop size and evaporation, combustor flow field and combustion chemistry on CO emissions. Cold flow CFD calculations and idealised reactors were used to estimate droplet size and evaporation rates. The model predictions were tested against measured CO emissions from four real turbojet engines, and it is claimed that the results were a significant improvement on previous methods. These results are expected to help define the equivalence ratios for different sections in the reactor. It is admitted that the CO will be overestimated under lower power, but the model showed better results when compared to previous work.

2.2.4.3 Computational Fluid Dynamics

McGuirk (1988) [58] estimate GT CO emission through the laminar flamelet method. The conclusion was drawn that the flame temperature is lower when compared to the equilibrium method. Frassoldati et al. (2010) [59] proposed a three-dimensional CFD for a new aero engine which showed good accuracy when predicting carbon monoxide. Pierre (2016) [54] indicated that carbon dioxide formation from carbon monoxide is a slow process which could be affected by turbulent diffusion.

2.2.5 Conclusion

This project is focused only on stationary GTs burning natural gas, so the emissions of unburned hydrocarbon, particulate matter, and sulfoxide will be negligibly small; only carbon dioxide, carbon monoxide, and nitric oxides will be considered. Sometimes, carbon dioxide is not considered as a pollutant as it is a natural component of air [60]. However, carbon dioxide is a significant contributor to global warming, and its output from the turbines will be proportional to fuel consumption. Thus, higher combustion efficiencies will reduce both fuel costs and the production of carbon dioxide. The combustion efficiency is suggested to be higher than 99% based on current emission regulations [1]. Industrial GT engines typically have a larger combustor chamber than aero engines. In such conditions, there is a longer residence time and lower flow velocity which means more complete combustion and a lower pressure loss [1].

The CFD models require details of the combustor geometry that the original equipment manufacturer may not be prepared to provide and in those circumstances, these methods are more suitable for the design of new combustors. Moreover, the computational time is enormous, which is not appropriate for operational optimisation. Reactor models are one of the most widely used physics-based models. The initial purpose of the reactor model as developed was for governing pollutants formation; then the model was extended to predict emissions. However, the equivalence ratios for the different parts in the reactor were difficult to obtain.

Correlations obtained from the regression equations for measured emission data, as a function of the engine performance, require knowledge of fewer parameters and geometric data. Frequently, semi-empirical correlations can generally apply to the different engine when considering emissions [61–65]. Because these correlation methods require minimum geometric information and the least computation time, it is this method which this project will be based on.

2.3 High-pressure Turbine Creep Life

The surface-related failure mechanism of GTs is a function of fatigue, corrosion, oxidation and creep [66]. Creep is a critical failure mechanism for the hot sections of a stationary GT [67]. Larson and Miller (1952) [68] proposed the Larson-Miller Parameter (LMP) for rupture and creep analysis under temperature and time variation. The proposed method is based on extensive experimental work conducted by Jaffe and Swartz (1944) [69]. Bueno et al. (2005) [70] have summarised a master curve for 2.25Cr-1Mo steel over the temperature range of 600 °C to 700 °C experimentally. Based on LMP method, Oluyede and Phillips (2007) [71] investigated the different creep life remaining when using natural gas and syngas as fuels for a heavy-duty GT. It was found that for the same metal temperature the power output could be increased by as much as 25% when fired with syngas rather than natural gas. Mohammad and Masoud (2009) [72] applied LMP to predict the remaining life of a GT blade and found reasonably good agreement with the manufacturer’s support documentation.

Research has also analysed the degradation of material under high temperatures and its effect on creep life. Using a single spool turboshaft engine, Ghafir et al. (2010) [73] investigated high-pressure blade creep life under OD and degradation conditions based on the LMP approach. It was found that the rotational speed could have a significant effect on creep life, and the creep factor is a suitable metric for indicating creep life consumption. Mohamed et al. (2011) [67] evaluated the effect of the GT power setting on high-pressure turbine life, but only considered the centrifugal stress. Eshati (2013) [74] demonstrated the positive impact of increasing water-air ratio (WAR) on GT blade creep life. The variation in gas properties caused by changing WAR included specific heat of the gases, gas constant R, density, Nusselt number and so forth. Ogiriki et al. (2015) [75] analysed the impact of thermal barrier coating (TBC) on a turbine blade creep life and summarised the relative longer life in percentage for four seasons respectively. Sahoo et al. (2017) [76] using a military aircraft engine and low-pressure turbine, demonstrated the creep life degradation of the blades was combined with microstructure degeneration. Schmidt et al. (2018) [77] investigated the turbine creep life based on three-dimensional thermal and stress model for turbine blade pre-design that could be considered the effect of mechanical and aerodynamic changing on creep life.

2.4 OTSG Performance

A heat recovery steam generator (HRSG) is a device that uses the exhaust heat energy from topping cycle as the source of energy to generate steam with high pressure and temperature for driving an ST and process [78]. Its performance is determined by the thermodynamic conditions of the hot gas and steam flows. The combined-cycle power plant contains three primary units: the GT, steam generator, and ST [79]. There are two kinds of steam generators: the conventional drum-type steam generator, and the OTSG without a drum. Many performance simulation models have been successfully developed for the traditional drum-type steam generator [80–84], and are not discussed in this thesis.

Research on OTSG performance simulation has been carried out and results published. Bayless (1979) [85] introduced a performance simulation method for a helically coiled single-pressure OTSG for marine application where the whole tube is split into equidistant parts, where each section is checked against phase change to determine the rough position of the boundaries between economiser, evaporator, and superheater. Several single-pressure OTSG performance simulation methods have been proposed for the nuclear power generation industry where moving boundaries are considered [86–88]. Dumont and Heyen (2004) [89] suggested a simulation method for single-pressure OTSG performance prediction. Ngoma et al. (2003) [90] developed a performance simulation algorithm for sequential dual-pressure OTSG. In summary, all the simulation methods published so far are limited to either relatively simple single-pressure OTSG or multi-pressure OTSG with circuits in sequence.

2.5 OTSG Performance Diagnosis

During the operation of the OTSG, one of the significant degradations that occur is fouling. Fouling is a universal phenomenon that has to be considered in designs and operations for heat exchangers with fluid-solid surfaces [91–94]. The different types of fouling of heat transfer surfaces include particulate, crystallisation/precipitation, chemical reactions (including corrosion), biological, and solidification/freezing [95]. Walker et al. (2012) [96] suggested a method of quantifying the economic effect of condenser fouling. In some highly developed nations, it was found that the financial loss due to fouling of heat exchangers accounts for about 0.15–0.25% of the gross national product (GNP) [97,98]. Belmiloudi [95] demonstrated that the fouling layer has a relatively low thermal conductivity compared with tube material, which raised the operating cost and decreased the performance of heat exchangers, and therefore, increased the maintenance cost.

OTSG degradation due to fouling may be represented by fouling resistance that is not only related to the thickness of fouling but also closely related to the thickness and mechanisms of the fouling [99]. This means that the visual access of an OTSG by power plant engineers may not be able to quantify the fouling resistance by measuring only the fouling thickness. Meanwhile, the thickness of fouling inside a tube cannot, generally, be measured without cutting the tube. Many researchers have mentioned the Wilson Method [100,101], which can be used to determine the fouling resistance by measuring the total resistance [102] and, knowing the initial thermal resistance of the tube, assess the dependence of the convective thermal resistance on the fluid velocity. The method was initially developed for a condenser, but it is difficult to measure the total resistance of tubes in an OTSG for each section, the geometry of which is more complicated than that of a condenser. It is worth mentioning that the higher the temperature in the OTSG, the faster the fouling will form and the more difficult it is to remove [103]. Some researchers proposed time-dependent or measurement correlation fouling models based on previous experimental data, or historical experience, to obtain the changing fouling resistance and overall heat transfer coefficient, but the accuracy of the method may not be satisfactory due to changing operating conditions [104–107]. Bishara et al. (2015) [108] suggested thermal shock could be used for fouling mitigation. However, the dry-run operation for a steam generator is limited by specific hours for the whole lifetime, and accurate fouling diagnostics are necessary for optimising such cleaning schedules.

2.6 Steam Turbine Performance

The steam turbine (ST) may be classified into two categories: condensing and non-condensing [109]. The condensing ST has a condenser pressure less than atmospheric which increases the work done by the expansion of the steam. A non-condensing ST is normally combined with other processes that require steam. The power generation industry will usually select the condensing ST [110]. The ST power output could be obtained knowing inlet steam conditions, condenser pressure, and isentropic efficiency. However, the ST's isentropic efficiency cannot be measured directly but is derived from the inlet steam condition, outlet steam pressure, and outlet steam moisture content.

However, exhaust steam moisture is typically difficult to measure accurately [111,112]. For zero-dimensional ST performance modelling, the greatest challenge is to obtain the correct isentropic efficiency. The total ST efficiency is determined by the efficiency of each stage, though multi-stage blades can be considered as a group when obtaining the overall efficiency. ST power plants run at a constant speed that corresponds to grid frequency, so the efficiency is only related to the enthalpy released through turbine blades [111].

Kehlhofer et al. (2009) [14] indicated no apparent change in performance for those stages where the moisture is equal to zero. This means the isentropic efficiency changes happen mostly at the last stage of the ST where the moisture content is greatest. Hence, the ST efficiency prediction could be separated into two parts: constant efficiency for the dry stage and variable efficiency for the last stage [14].

Bahadori and Vuthaluru (2010) [113] proposed an ST performance prediction method by polynomial correction based on steam rate, and nozzle diameters (inlet and outlet). Medina-Flores, and Picon-Nunez (2010) [114] proposed a regression algorithm for ST efficiency with steam extraction, suggesting that the temperature and enthalpy are correlated with extraction pressure. Forsthoffer (2011) [111] presented universal efficiency curves for both multistage and single stage ST for efficiency estimation purpose. All the methods mentioned above could obtain accurate results but requires the measurement to adapt their correlation for a specific ST. In addition, an empirical correction between mass flow rate and efficiency is suggested by commercial software Epsilon 11 [115].

2.7 Economics of Electricity Generation

The economic study of the power plant has been carried out in different domains to reduce the risk and enhance the profitability of a project for plant investors. Research into the financial aspect of constructing a new power plant has a long history [14,116–119]. The concerns include the Net Present Value (NPV), worst annual negative cash flow (WANCF), break-even time (BVT), return on equity (ROE), internal rate of return (IRR) and so on. Mohamed et al. (2012) [120] proposed an economic evaluation for assessing the worth of a GT project for the power generation industry. Four typical economic appraisal methods for evaluating investment were summarised: discounted cash flow rate, investment pay-back, minimum revenue requirement, and net present value [120].

Nasir et al. (2012) [121,122] investigated the emission-related economic analysis for selecting a GT for natural gas pipeline transportation. Walsh and Fletcher (2004) [116] presented an example based on NPV assessment for establishing a new CCGT power plant. The spark spread (gross margin) is applied to combine the electricity price, fuel price, and heat rate for the financial industry [123].

A negative value of spark spread means the power plant is losing money rather than generating profit [124,125]. Hence, spark spread could provide useful information for potential power plant investors in terms of the valuation of power generation assets [126,127]. The economics of power generation will affect not only the industry’s investors but also the customers. Design failures in the power generation industry can possibly cause electricity price fluctuations and spikes, and even power shortages. Woo (2001) [128] detailed reasons for the power market reform failure in California. Woo et al. (2003) [129] summarised failures to reform the electricity market at UK, Norway, Alberta, and California that resulted in high and unstable electricity prices. The fuel price and power demand mostly affect the payback for the heat engine power plant. Some researchers have demonstrated forecasting models for fuel price and power demand that may possibly reduce the risk of investment in power plant [130,131].

2.8 Optimiser

2.8.1 Genetic Algorithm

Genetic Algorithm (GA) is based on the theory of natural selection developed to explain biological evolution, and have been used to search for the optimum solutions to both constrained and unconstrained problems [132].

The GA operators (Selection, Crossover and Mutation) are used to improve the fitness of “individuals” within a population, generation by generation. Each iteration of the algorithm represents a new generation.

The algorithm will produce a new generation of individual samples from the search space via the use of genetic operators. The new generation is then assessed according to the defined objective function, and the generation repeated [3]. The selection process, iterations, will continue until the next generation produces no better solution than the previous, or the number of iterations is equal to a pre-set maximum, at which point the process ceases. GA is suitable for complex problems which Newton’s method, the simplex method and least meant squares are not able to solve. Comparison with the fitness function of the GA will remove less efficient individuals and progress towards a final global maximum/minimum solution.

2.8.2 Simulated Annealing

Metropolis, et al., (1953) [133] proposed an important sampling method which means the new state will be accepted based on probability. In such conditions, the computational resources required are a lot less than for the Monte Carlo method. Kirkpatrick, Gelatt and Vecchi (1983) [134] proposed Simulated Annealing (SA) based on the physical process of annealing in solids for optimisation problems that if new fitness value is less than the last one, the new solution will be accepted or based on Metropolis principle to decide accepting or abandon. The initial temperature should be determined and generate a random solution to start the calculation. The higher the initial temperature, the more possible it is to achieve an excellent quality in the result but at the cost of increasing total computing time. The terminal condition of SA could be based on annealing temperature, the iteration step and the energy value does not change for several series of iterations. One of the distinct advantages of SA is that multi-target optimisation will not generally increase the computation time. However, the optimal local phenomenon will still exist.

2.8.3 Ant Colony Optimisation

Dorigo, Maniezzo and Colorni (1991) [135] proposed an optimising method called Ant Colony Optimisation (ACO) for the well-known travelling salesman problem. Ants lay a trail of pheromones from a food source back to the nest. So the shorter the distance and the more recent the find, the higher the pheromone intensity. Other ants will be most likely to select the trail with the highest pheromone intensity, which is positive feedback.

This method has been applied to vehicle routing problems, job-shop problems, graph colouring problems and quadratic assignment problems [136]. The advantages of ACO are its robustness, and the ease with which it can be combined with other methods. The main drawback of ACO is that the convergence rate is slow and it is easy to get a local maximum/minimum solution.

2.8.4 Particle Swarm Optimisation

Particle Swarm Optimisation (PSO) is also an inspired derivative-free optimisation algorithm which was developed for studying the behaviour of bird flocks and fish schools [137]. PSO has lost similarities with other evolutionary methods which generator random solutions and then search for best solutions. The main differences are that PSO does not use crossover and mutation to explore the best solution. One distinct advantage of PSO, when compared to GA, is that the PSO does not ignore low fitness particles, but moves all the particles toward the best solution that makes it possible to avoid local maximum and minimum points when the number of particles is large enough. However, the larger the number of particles, the longer the computation time.

Two classifications of PSO, global and local-oriented have been developed by Eberhart and Kennedy (1995) [137]. The local-oriented is faster when compared to the global-oriented, but is highly likely to reach a local optimum solution. The global-oriented is slower but is less likely to achieve a local maximum/minimum solution. The most attractive method is to combine using global-oriented to start a quick iteration, and then using local-oriented to validate it.

2.8.5 Differential Evolution

Storn and Price (1995) [138] indicated a new evolutionary algorithm based on GA. Differential Evolution (DE) computational procedure with crossover is analogous to GA, with the main difference being that the process of mutation is based on a different strategy which increases the search capability when compared to the GA. The robustness and global convergence behaviour of DE have been demonstrated by numerical optimisation.

The evolution of the optimisation system is the same as for the GA; that of repeating the evolution iteration until the global optimisation solution is found. The control parameters of the DE are the number of the population, the scaling factor and crossover probability. Selection of suitable control parameters will increase the iteration speed and raise the possibility of finding the optimal solution. Researchers have combined DE with other algorithms such as SA, PSO and ACO. Most of the combined work has been focused on mutation [139].

2.8.6 Gradient Descent

Gradient Descent (GD), also called method of steepest descent, was proposed by Curry (1944) [140]. The underlying theory is derived from the Taylor first-order approximation with Peano type remainder. If one is looking for a minimum value, the negative gradient direction will be selected every time, and this algorithm becomes a search for a minimum optimisation point. If searching for a maximum, the function needs to be negatively transformed and then explored for a minimum point.

The advantage of GD is that there is no particular requirement for the initial search value. Nevertheless, it is apparent the GD can easily become “locked into” a local minimum point, so it is necessary to add a reverse search or to combine GD with another method. For example, coupled with the SA by applying reverse lookup based on a random number or combined with GA by crossover or mutation.

Regarding computation time, if the objective function has only slight gradient changes across the domain, GD will only slow progress towards the best solution, and vice versa.

2.8.7 Tabu Search

Glover (1986) [141] suggested Tabu Search (TS) which has proved able to determine the global optimum. TS has been widely applied for combinatorial optimisation, production scheduling, machine learning, neural networks, and circuit design. TS simulated memory storage structure by introducing a taboo list to avoid another search that is the basic idea.

The iteration-stopping criterion is much the same as with other evolutionary algorithms and could including a maximum number of iteration steps, and a solution that remains constant after several iterations. There are two searching strategies for TS: diversification and intensification. Diversification searches seek possible solutions in the whole domain. Intensification searches hunt regions known to have better solutions based on previous searches. However, the algorithm cannot guarantee an optimal result.

2.8.8 Comparison between Single Criterion Optimisation and Multiple Criteria Optimisation

The single criterion optimisation is applied to address the extreme problem that only has a single solution. In this kind of problem, it may have several local extrema, but only one global extreme. Figure 2-1 (a) [16] show a function includes two local maximum. The global maximum is easy to find by a sophisticated multi-point optimisation algorithm. For multiple criteria optimisation, the algorithm is looking to find the Pareto Front (dominant solutions) that is set of optimal results. Figure 2-1 (b) [142] showed several different types of aircraft fuel pumps candidates that two conflict criteria are pump cost and mass. The higher the cost, the less the weight. However, lower cost and less mass are preferred for selecting the pump. Hence, the multiple criteria optimisation is proposed to find the boundary (red dotted line) and an example is showed in Figure 2-1 (b). It is clear to see that the optimal results are not a single solution that has five options available. Hence, the number of conflict criteria will decide the type of optimisation system to be selected. More criteria scenario requires multiple criteria optimisation methods.

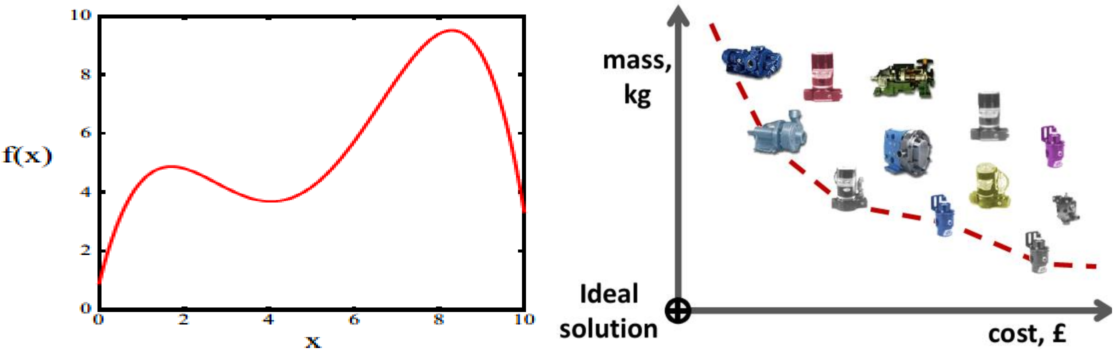

(a) [16]

(b) [142]

Figure 2-1 Comparison between Single Criterion Optimisation and Multiple Criteria Optimisation

2.9 Multi-Criteria Decision Making

The power plant operation optimisation for this study includes two conflicting criteria, so the multiple criteria optimiser is required to approximate the Pareto Front. The approximated Pareto Front is a group of optimal or efficient results, but not able to suggest the final decision [142]. In such condition, it may be difficult for the decision maker to find a candidate from the set of results directly. It is necessary to develop an algorithm for finding the final preferred solution from the optimal solutions. Three widely used Multi-Criteria Decision Marking (MCDM) methods will be introduced: Technique for Order Preference by Similarity to Ideal Solution (TOPSIS), Eigenvector Weighting Method (EWM), and Concordance and Discordance Analyses by Similarity to Ideal Designs (CODASID).

2.9.1 Technique for Order Preference by Similarity to Ideal Solution

TOPSIS is one of the most popular methods of decision making [17]. The ideal best and worst possible solutions are assumed by comparison with calculated Pareto Front. The best candidate is the candidate geometrically nearest the perfect best solution [17]. However, the distances are affected by the weighted by preference weights according to each criterion. Thus, the distance is sensitive to the weighting factors may be chosen according to subjective criteria.

2.9.2 Eigenvector Weighting Method

EWM decided the weighting matrix through pairwise comparison and Eigenvector methods [143]. The pairwise comparison is superior to TOPSIS when the number of attributes is more than two. Meanwhile, only two attributes need to be decided each time when comparing between disparate attributes [142]. However, consistency should be checked after the weighting matrix is calculated, with problems of inconsistency solved by iteration.

2.9.3 Concordance and Discordance Analyses by Similarity to Ideal Designs

CODASID is based on a preferred decision matrix to rank the Pareto Front [144]. The method requires calculating three index matrixes: the evaluation concordance index matrix, preference concordance index matrix, and combined discordance index matrix; which is more complicated than the TOPSIS or EWM. After the three index matrixes have been obtained, the judgement-evaluation matrix may be calculated. Finally, TOPSIS is applied to the judgement evaluation matrix to decide the final rank.

The Multi-Criteria Genetic Algorithm (MCGA) is one of the algorithms capable of dealing with multiple criteria optimisation for complex models. However, the results from the MCGA should not be used directly; a final decision needs compromises between different criteria. Thus, MCDM is necessary for post-processing the raw MCGA results. For more details about MCDM refer to the relevant publications [145–147].

2.10 Power Plant Optimisation

Much research has focused on the selection of power generating equipment and could be considered as plant concept design [148–152]. The selection criteria have included the number of the heat engines, the configuration of the heat engines, the capacity of individual engine/equipment, renewable electricity equipment, and so on. The power plants supplying to the grid will highly possibly affect by the following aspects: peak lopping engines, based load power plant, and mid-merit power plant. For example, the peak load operation will prefer to select the low capital cost with costly fuels and base load operation will select the opposite [14]. Attala et al. (2001) [153], have suggested a design tool for steam cycle optimisation by minimising the purchase cost of CCGT power plant. Pelster et al. (2001) [154], suggested an optimisation system for power plant configuration using design parameter selection. Optimisation systems for the steam generator in a CCGT power plant generally propose considering the two objectives separately for optimum design [13,155]. Möller et al. (2004) [156] optimised DP parameters for a humid air turbine for the efficiency of production and cost of electricity respectively. Casarosa et al. (2004) [157] suggested an optimisation system through hierarchical objectives to minimise both exergy losses and total cost of a steam cycle for a CCGT power plant. Aref et al. (2010) [158] suggested a thermoeconomic optimisation to minimise the cost of a power plant, considering capital cost, resource costs, and emission costs. Brighenti et al. (2017) [159] proposed a single objective optimisation system for a humid air turbine power plant DP performance to maximise the plant thermal efficiency.

Some researchers have investigated the combined heat and power (CHP) optimisation to determine the operation of each item of equipment to minimise energy expense [160–162]. Optimal studies for a gas turbine cogeneration plant have suggested a possible way to reduce the annual cost for the changing of energy demand [160]. However, the elements of concern are limited to the operation cost and power-heat production.

3 Methodology

3.1 Gas Turbine Performance Model

Figure 3-1 presents a schematic of a dual shaft GT in concern that including a heat exchanger. The bricks shown in Figure 3-1 are explained in Appendix A, for a more detailed explanation see [163]. The numbers, 1, 2, 3, etc., shown in the figure are used to describe the GT brick number.

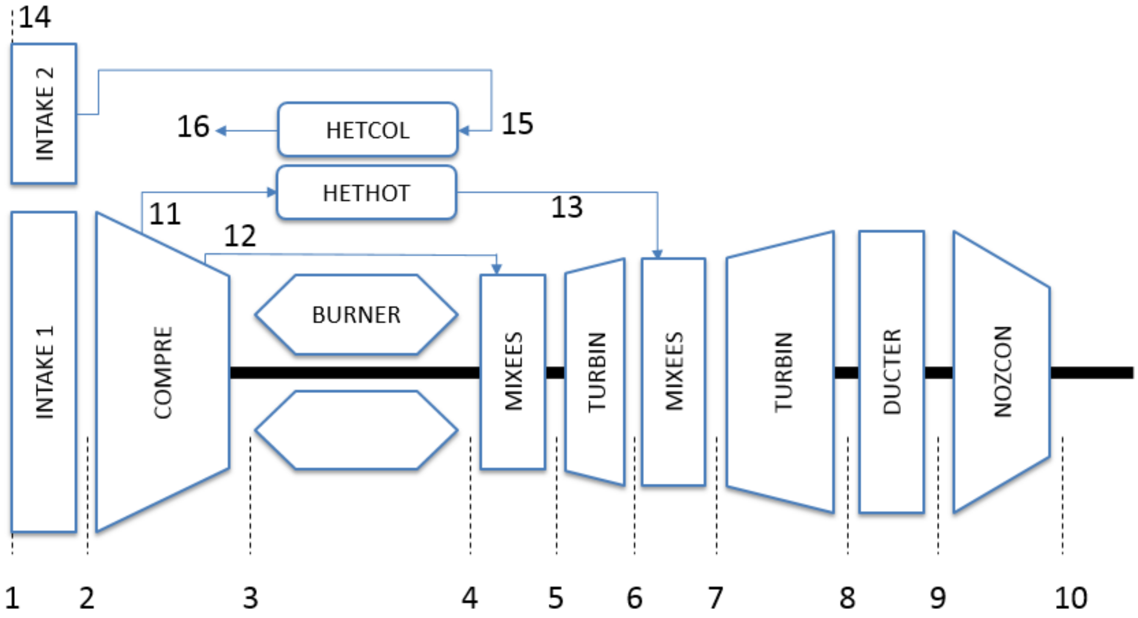

Figure 3-1 Scheme of Dual Shaft Gas Turbine (GT).

As mentioned previously, in this study the Pythia based version of Turbomatch [4,5] will be used to simulate engine performance. The interpolation table for gas properties (i.e. specific heat at constant pressure, the specific heat of gases, gas constant R, density, enthalpy) is generated using NASA CEA [164] and integrated into the performance program using the TRM function [15]. When the fuel-air ratio (FAR), the water-air ratio (WAR), and any two of pressure, temperature, enthalpy, entropy and so on, are known, the remaining gas properties can be obtained.

The detailed algorithm for brick calculation is explained as follows. It is necessary to mention that the GT performance calculation involves both global and local iterations of variables/errors. The global variables/errors are applied to the whole performance simulation, while the local iteration variables/errors are applied only within each brick.

The global iteration is based on the Newton-Rapson method [21]. Local iterations are based on the Air Force Quadratic Interpolation Routine (AFQUIR), for details refer to [165,166]. The universal engine component map can be adapted for performance simulation. For details of the DP adaptation refer to [167] and OD map adaptation is based on the Genetic Algorithm presented in Section 3.8.1.1, also see [168]. It is assumed the compressor, burner and turbine maps are obtained from the OEM rig test. Hence, the following demonstration will not cover compressor surge margin calculations, nor the scaling factor of maps by DP, and DP/OD adaptation.

3.1.1 Design Point Performance Simulation

3.1.1.1 Inputs for Design Point

The inputs for the GT DP performance calculation is showed as follows.

- Intake 1 mass flow rate: W_1
- Intake 2 mass flow rate: W_{14}
- Compressor relative rotational speed: PCN_{comp}
- Compressor pressure ratio: PR_{comp}
- Compressor isentropic efficiency: η_{comp}
- Bleed 1 pressure ratio coefficient: $BRatio_{P,11}$
- Bleed 1 mass ratio coefficient: $BRatio_{W,11}$
- Bleed 2 pressure ratio coefficient: $BRatio_{P,12}$
- Bleed 2 mass ratio coefficient: $BRatio_{W,12}$
- HETCOL pressure drop: ΔP_{HETCOL}
- HETHOT pressure drop: ΔP_{HETHOT}
- Effectiveness for HETCOL and HETHOT: ε_{HE}
- Burner pressure drop: ΔP_{bur}
- Combustion efficiency: η_{bur}
- Turbine entry temperature: TET

- Low heating value: LHV
- High pressure (HP) turbine isentropic efficiency: η_{HPT}
- Low pressure (LP) turbine power output: PO_{GT}
- LP turbine relative rotational speed: PCN_{LPT}
- LP turbine isentropic efficiency: η_{LPT}
- DUCTER pressure drop: ΔP_{Duc}

3.1.1.2 Design Performance Calculation

3.1.1.2.1 Intake

For a stationary GT, the flight Mach Number (MN) is zero and it is assumed the engine is installed at sea level with no pressure loss at the intake. Hence, the two intake bricks only need to determine the WAR and FAR for calculating the gas properties at the following bricks. For the intake brick, the FAR equals to zero.

3.1.1.2.2 Compressor

The compressor outlet pressure, P_3, can be obtained as:

$$P_3 = PR_{comp} \cdot P_2 \tag{3-1}$$

Figure 3-1 showed two bleeding paths in the compressor so that the compressor may be separated into three sections (2–11, 11–12, and 12–3). P_{11} the first bleeding pressure could be obtained as:

$$P_{11} = BRatio_{P,11} \cdot PR_{comp} \cdot P_2 \tag{3-2}$$

The bleed mass flow rate, W_{11}, for the first bleed can be obtained as:

$$W_{11} = BRatio_{W,11} \cdot W_{in} \tag{3-3}$$

where W_{in} varies for each compressor section.

The bleed pressure, P_{12}, and mass flow rate, W_{12}, for the second bleed are obtained in the same way as P_{11} and W_{11} when $BRatio_{P,12}$ and $BRatio_{W,12}$ are given.

It is assumed the compressor isentropic efficiency, η_{comp}, is constant for the whole compressor. So, the outlet temperature, T_{out} , for each section of compressor can be obtained from:

$$\left(\frac{P_{out}}{P_{in}}\right)^{\frac{\gamma-1}{\gamma}} - 1 = \eta_{comp}\left(\frac{T_{out}}{T_{in}} - 1\right) \tag{3-4}$$

where γ is the heat capacity ratio.

The compressor work, CW_i, for ith section can be obtained as follows.

$$CW_i = W_{in} \cdot (h_{i,out} - h_{i,in}) \tag{3-5}$$

The total compressor work, CW, accumulated across all three sections that could be obtained as follows.

$$CW = \sum_{i=1}^{3} CW_i \tag{3-6}$$

3.1.1.2.3 Burner

The burner outlet pressure, P_{out}, can be calculated based on the pressure loss (ΔP) as follows.

$$P_{out} = P_{in} \cdot \Delta P \tag{3-7}$$

As the combustion efficiency, η_{bur} , is known, the enthalpy released from combustion can be calculated based on the assumed fuel flow rate (FF) as:

$$\Delta H = FF \cdot LHV \cdot \eta_{bur} \tag{3-8}$$

Then, the outlet enthalpy, h_4, and temperature, T_4, can be obtained in sequence. When, the calculated T_4 is close to the TET, the iteration of local variable FF will stop. It is necessary to mention that the FAR should be updated by calculating the gas properties at the burner outlet.

3.1.1.2.4 First MIXEES

For MIXEES brick, it is assumed the pressure remains the same as for the core flow. The outlet enthalpy, h_5, at Section 5 is easily calculated using Eq. (3-9). And, the temperature could be known when the outlet enthalpy, and pressure are known.

$$h_5 = \frac{W_{4}h_4 + W_{12}h_{12}}{W_5} \tag{3-9}$$

3.1.1.2.5 High-pressure Turbine

The high-pressure (HP) turbine outlet temperature, T_{out}, and pressure, P_{out}, can be estimated using local iterations. Then, the HP turbine isentropic efficiency η_{cal} can be calculated as follows.

$$\eta_{cal} = \frac{1 - \frac{T_{out}}{T_{in}}}{1 - \left(\frac{P_{out}}{P_{in}}\right)^{\frac{\gamma-1}{\gamma}}} \tag{3-10}$$

Meanwhile, the total outlet enthalpy for the outlet condition is estimated. Thus, the turbine work could be obtained as follows.

$$TW = W_{in} \cdot (h_{in} - h_{out}) \tag{3-11}$$

The two-convergence criteria are explained as follows. If mechanical losses are ignored, the HP turbine work TW should be close to the compressor work CW within the pre-set threshold. Meanwhile, the calculated η_{cal} should be close to the input turbine efficiency η_{HPT} , also within a pre-set threshold. When the convergence criteria are satisfied, the appropriate turbine outlet temperature and pressure are obtained and the local iteration will stop.

3.1.1.2.6 HETHOT and HETCOL

The HETHOT and HETCOL represent the hot and cold sides of the heat exchanger respectively. The HETCOL outlet flow temperature, $T_{co,out}$, can be obtained from [93].

$$\varepsilon_{HE} = \frac{T_{co,out} - T_{co,in}}{T_{ho,in} - T_{co,in}} \tag{3-12}$$

where the subscripts co and ho mean the cold and hot flows respectively.

The pressure drop for both cold and hot sides are obtained by Eq. (3-7). As the cold side inlet and outlet conditions are known, the enthalpy increase can be identified. Based on the heat balance between cold and hot flows, the hot side enthalpy drop is calculated as follows [93].

$$\Delta h_{HETHOT} = \frac{W_{co}(h_{co,out} - h_{co,in})}{W_{ho}} \tag{3-13}$$

Hence, the hot side outlet enthalpy can be found, and then the hot side outlet temperature found from the hot side outlet pressure and enthalpy. The average specific heat at constant pressure for both sides, Cp_{ho} and Cp_{co}, respectively, can be obtained, by multiplying by the respective hot and cold side mass flow rates, and the respective heat capacities, C_{ho} and C_{co}, can be derived. The smallest heat capacity is denoted C_{min}, and the largest, C_{max}.

The heat capacity rate ratio C^* is defined as follows [93].

$$C^* = \frac{C_{min}}{C_{max}} \tag{3-14}$$

As shown in Figure 3-1, the configuration of the heat exchanger (11–13 and 15–16) is counter flow, and the number of transfer unit (NTU) can be obtained as [93].

$$NTU = \frac{\ln\left(\frac{1 - C^* \times \varepsilon_{HE}}{1 - \varepsilon_{HE}}\right)}{1 - C^*} \tag{3-15}$$

It is assumed the overall conductance, UA, of the heat exchanger is constant and can be obtained as follows [93].

$$UA = NTU \cdot C^* \tag{3-16}$$

3.1.1.2.7 Second MIXEES

For the second MIXEES, the calculation could follow the same steps as first.

3.1.1.2.8 Low-pressure Turbine

For the low-pressure (LP) turbine, the turbine outlet temperature T_{out} and pressure P_{out} can be estimated as two local iteration variables in much the same way as the calculations for the HP turbine. The only difference is that the turbine work should equal the specified GT power output PO_{GT}, because the power turbine needs to drive an electricity generator, rather than a compressor. PO_{GT} is known as DP input.

3.1.1.2.9 DUCTER

It is assumed that only pressure loss occurs in the DUCTER, that the outlet temperature and mass flow rate remain the same as at the inlet. Therefore, the outlet pressure can be obtained using Eq. (3-7).

3.1.1.2.10 NOZCON

For an industrial GT, the convergent nozzle is assumed and is choked at the DP; $MN = 1$. Thus, the outlet static temperature, t_{10}, can be obtained as follows.

$$\frac{T_{10}}{t_{10}} = 1 + \frac{\gamma - 1}{2} \cdot MN^2 \qquad \textbf{(3-17)}$$

And the static outlet pressure, p_{10}, can be obtained as follows.

$$\left(\frac{P_{10}}{p_{10}}\right)^{\frac{\gamma-1}{\gamma}} = 1 + \frac{\gamma - 1}{2} \cdot MN^2 \qquad \textbf{(3-18)}$$

The nozzle jet velocity, V_{10}, can be calculated as follows.

$$V_{10} = \sqrt{\gamma \cdot R_g \cdot t_{10}} \qquad \textbf{(3-19)}$$

where R_g is the gas constant.

Then, the exit gas density, ρ_{10}, can be obtained as follows.

$$\rho_{10} = \frac{101325 \cdot p_{10}}{R_g \cdot t_{10}} \qquad \textbf{(3-20)}$$

Finally, the nozzle area, A_{10}, can be calculated as follows.

$$A_{10} = \frac{W_{10}}{\rho_{10} \cdot V_{10}} \qquad \textbf{(3-21)}$$

Stationary GTs produce thrust which is offset by the foundation bed. Hence, the thrust calculation will not be included here.

3.1.2 Off-design Point Performance Simulation

3.1.2.1 Input Parameters

- Power setting: PO_{GT}

3.1.2.2 Global Iteration Variables

The performance simulation of the dual-shaft industrial engine needs five global iteration variables, as listed below.

- Compressor pressure ratio: PR_{comp}
- Compressor relative rotational speed: PCN_{comp}
- Turbine entry temperature: TET
- Guessed HP turbine inlet corrected mass flow rate: $CM_{HPT,gue}$
- Guessed LP turbine inlet corrected mass flow rate: $CM_{LPT,gue}$

3.1.2.3 Global Iteration Errors

Both turbine inlet flows are obtained from previous bricks that are able to calculate the CM from the known inlet parameters. Meanwhile, both HP and LP turbine CM values are estimated by global iteration, so two global errors are possible. Meanwhile, the turbine work is calculated based on estimated CM and turbine map. For the HP turbine, work should be equal to the work done by the compressor, and the LP turbine work should be equal to the specified GT power output (OD input). For industrial GT, a convergent nozzle is used and the nozzle area is fixed, so the total pressure is required to expand the flow based on the specified nozzle area that obtained by DP. Hence, the final global error is the difference between the required total pressure for the nozzle and actual outlet total pressure. Therefore, the five global iteration errors are identified:

- Global Error 1: $(CM_{HPT,in} - CM_{HPT,gue})/CM_{HPT,in}$
- Global Error 2: $(CW - TW_{HPT})/CW$
- Global Error 3: $(CM_{LPT,in} - CM_{LPT,gue})/CM_{LPT,in}$
- Global Error 4: $(PO_{GT} - TW_{LPT})/PO_{GT}$
- Global Error 5: $(P_{Noz,act} - P_{Noz,req})/P_{Noz,act}$

3.1.2.4 Off-design Performance Calculation

3.1.2.4.1 Intake

The brick intake calculations are the same as for the DP in Section 3.1.1.2.1.

3.1.2.4.2 Compressor

As mention in Section 3.1.2.2, PR_{comp} and PCN_{comp} are estimated and then the inlet ND mass flow rate CM_{in} and isentropic efficiency η_{comp} (ETA) can be found using the compressor map, Figure 3-2 [5].

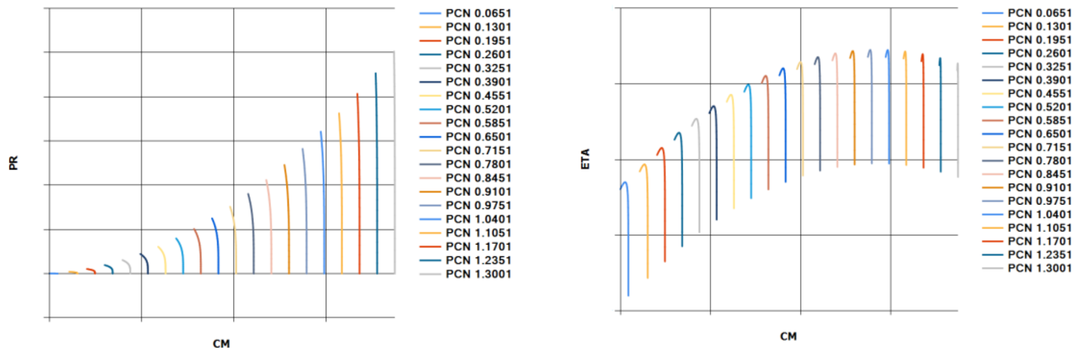

Figure 3-2 Compressor Map [5].

The inlet air mass flow, W_{in}, for the compressor could be obtained from Eq. (3-22).

$$CM_{in} = \frac{W_{in} \cdot P_{in}}{\sqrt{T_{in}/288.15}} \qquad \textbf{(3-22)}$$

After the mass flow rate has been found, the remaining parameters are the same as for the DP calculation in Section 3.1.1.2.2.

3.1.2.4.3 Burner

The burner inlet conditions are now known, and the TET is assumed as a global variable so that the increase in combustor temperature (DT in the map) can be determined. Then, the burner OD combustion efficiency (ETA) can be obtained using the burner map, Figure 3-3.

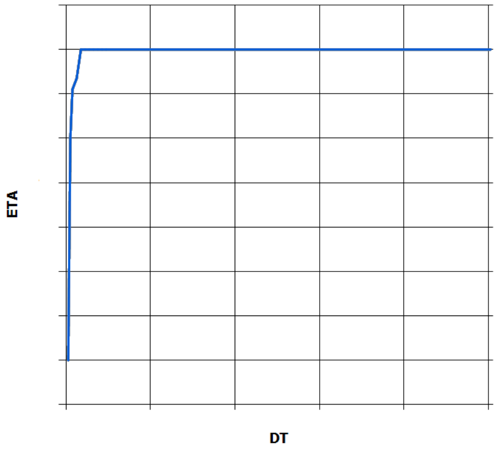

Figure 3-3 Burner Map [5]**.**

Meanwhile, the pressure drop along the combustor is considering to be proportion to the kinetic head at the burner inlet as [4].

$$\frac{\Delta P_{DP}}{\Delta P_{OD}} = \left(\frac{W_{in}^2 \cdot T_{in}}{P_{in}}\right)_{DP} \Bigg/ \left(\frac{W_{in}^2 \cdot T_{in}}{P_{in}}\right)_{OD} \tag{3-23}$$

Then, the burner OD calculation is the same as that shown in Section 3.1.1.2.3.

3.1.2.4.4 First MIXEES

For the first MIXEES brick, the calculation is the same as shown in Section 3.1.1.2.4.

3.1.2.4.5 High-pressure Turbine

The HP turbine is co-shafted with the compressor, so the PCN_{comp} is the same as the HP turbine. For reading the turbine map, Figure 3-4, the shaft corrected rotational speed, CN, should be calculated using Eq. (3-24).

$$CN = \frac{PCN \cdot \sqrt{T_{in,DP}}}{\sqrt{T_{in,OD}}} \tag{3-24}$$

Meanwhile, the $CM_{HPT,gue}$ is estimated, so the turbine isentropic efficiency η_{gue} (ETA) and relative enthalpy drop $\left({}^{Dh}/_{T}\right)$ may be obtained from the turbine map. The HP turbine enthalpy drop can be obtained as follows.

$$\Delta h = T_{in} \cdot \left({}^{Dh}\!/_{T} \right) \tag{3-25}$$

Hence, the turbine useful work (UW) is given by;

$$UW = W_{in} \cdot \Delta h \tag{3-26}$$

The turbine outlet temperature and pressure are estimated as two local variables, then η_{cal} and TW can be found from Eqs. (3-10) and (3-11). Finally, η_{cal} should be close to the η_{gue} from turbine map with a pre-set threshold criterion for halting the local iteration process for the HP turbine brick when the TW is close to the UW, so that suitable outlet temperature and pressure are found when the local iterations converge.

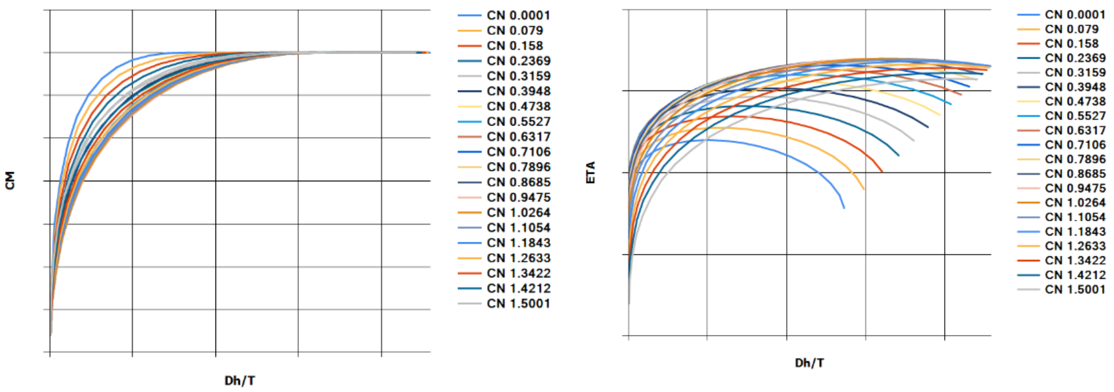

Figure 3-4 Turbine Map [5]**.**

The value of CM_{in} for the HP turbine can be calculated from the previous brick by Eq. (3-22). Then, the two global iteration errors for the HP turbine can be shown to be:

Global error 1:

$$\delta_1 = \frac{CM_{HPT,in} - CM_{HPT,gue}}{CM_{HPT,in}} \tag{3-27}$$

Global error 2:

$$\delta_2 = \frac{CW - TW_{HPT}}{CW} \tag{3-28}$$

3.1.2.4.6 HETHOT and HETCOL

The pressure drop at the OD condition for both HETHOT and HETCOL can be obtained from Eq. (3-23). As stated above, the UA is considered as constant, so C^* can be calculated initially on the basis of the inlet condition as given by Eq. (3-14). The NTU can be found using Eq. (3-16) and ε_{HE} from Eq. (3-15). Finally, the $T_{co,out}$ and $T_{ho,out}$ can be found from Eqs. (3-12) and (3-13) respectively. After both cold side and hot side outlet temperatures are known, the C^* can be updated using the average temperature of inlet and outlet and the calculation repeated until the change of C^* is small enough to be ignored.

3.1.2.4.7 Second MIXEES

For the second MIXEES brick, the calculations could follow the same steps as for the first MIXEES brick.

3.1.2.4.8 Low-pressure Turbine

The LP turbine is running at fixed rotation speed to satisfy the electricity phase control, so the PCN_{LPT} is a constant value. The CN_{LPT} can be found from Eq. (3-24) with $CM_{LPT,gue}$ is estimated, so the LP turbine isentropic efficiency η_{gue} and relative enthalpy drop $\left({}^{Dh}/_{T}\right)$ obtained from the turbine map. The LP turbine enthalpy drop can be obtained from Eq. (3-25), and the LP turbine UW from Eq. (3-26).

The turbine outlet temperature and pressure are estimated as two local variables and the η_{cal} and TW can be calculated using Eqs. (3-10) and (3-11). The value of η_{cal} should be close to that of $\eta_{LPT,gue}$ from turbine map. TW should be close to UW within a pre-set threshold for stopping the local iteration for the LP turbine brick, given that the correct outlet temperature and pressure are found when the local iterations converge.

CM_{in} could be obtained from (3-22) and the two global iteration errors for LP turbine would be obtained as;

Global error 3:

$$\delta_3 = \frac{CM_{LPT,in} - CM_{LPT,gue}}{CM_{LPT,in}} \tag{3-29}$$

Global error 4:

$$\delta_4 = \frac{PO_{GT} - TW_{LPT}}{PO_{GT}} \tag{3-30}$$

3.1.2.4.9 DUCTER

The DUCTER brick considers only pressure loss. For OD calculation, the pressure loss is determined according to Eq. (3-23). Then the outlet pressure can be found, see Section 3.1.1.2.9.

3.1.2.4.10 NOZCON

3.1.2.4.10.1 Sonic Condition

It is assumed the entropy for the sonic state is the same as for the stagnation condition. Two local variables (static temperature t_{sn} and static pressure p_{sn}) are estimated in order to calculate the sonic condition.

For sonic temperature, t_{sn}, is guessed, the estimated speed of sound can be obtained [116].

$$V_{sn} = \sqrt{\gamma \cdot R_g \cdot t_{sn}} \tag{3-31}$$

Meanwhile, based on the estimated values of t_{sn} and p_{sn} the static enthalpy h_{sn} and entropy s_{sn} can be found in gas properties table. The total enthalpy h_{tt} would then be given by Eq. (3-32).

$$h_{tt} = h_{sn} + 0.5 \cdot V_{sn}^2 \tag{3-32}$$

Based on the total temperature T_9 and pressure P_9 from NOZCON inlet, the stagnation enthalpy h_{stag} and entropy s_{stag} can be found. When the values of h_{stag} and s_{stag} are close to h_{tt} and s_{sn} respectively, and within the pre-set threshold, the calculation is considered to have converged, and the sonic condition is obtained.

3.1.2.4.10.2 Critical Nozzle Area

The required nozzle area A_{cri} for the critical condition can be obtained from:

$$A_{cri} = \frac{W_{10}}{\rho_{sn} \cdot V_{sn}} \tag{3-33}$$

When the DP nozzle area A_{10} is larger than A_{cri}, the nozzle flow is sub-critical. Here introduced only the sub-critical condition since that is the common case for industrial GTs under OD conditions.

3.1.2.4.10.3 Sub-critical Condition

For the sub-critical condition, the static outlet pressure p_{10} is equal to the ambient pressure. The outlet static temperature t_{10} is estimated as a local iteration variable. Then, the gas density ρ_{10} can be obtained from Eq. (3-34).

$$\rho_{10} = \frac{101325 \cdot p_{10}}{R_g \cdot t_{10}} \tag{3-34}$$

The velocity can be found from:

$$V_{10} = \frac{W_{10}}{\rho_{10} \cdot A_{10}} \tag{3-35}$$

Then, the total enthalpy can be obtained from Eq. (3-36).

$$h_{tt} = h_{10,st} + 0.5 \cdot V_{10}^2 \tag{3-36}$$

The calculated total enthalpy h_{tt} should be close to h_{stag} within a pre-set threshold that is the convergence criterion. This is taken to be a sufficiently correct t_{10} and the local iteration ends.

The values t_{10}, p_{10}, and T_{10} are known at this stage, and the required outlet total pressure, P_{10}, is calculated using:

$$\frac{P_{10}}{p_{10}} = \left(\frac{T_{10}}{t_{10}}\right)^{\frac{\gamma}{\gamma-1}} \tag{3-37}$$

The calculated P_{10} is the required total pressure $P_{Noz,req}$ for expansive flow through the nozzle, and P_9 is the actual nozzle total pressure $P_{Noz,act}$. It follows that global error 5 is:

Global error 5:

$$\delta_5 = \frac{P_{Noz,act} - P_{Noz,req}}{P_{Noz,act}} \tag{3-38}$$

3.1.2.4.11 Global Iteration

The RMS value for the five global errors, RMS_{GT} for use with the GT OD performance calculation is obtained using the standard formula:

$$RMS_{GT} = \sqrt{\frac{1}{5}\sum_{i}^{5}\delta_i^2} \tag{3-39}$$

The RMS_{GT} should less than the specified threshold of 1E-5, until that is reached the Newton-Raphson iteration continues updating the five global variables.

3.2 Gas Turbine Emissions Model

3.2.1 Carbon Dioxides

The calculation of carbon dioxides is based on the assumption of chemical equilibrium and complete combustion in the combustor. The model applies the fuel composition method which calculates both carbon dioxides and water vapour. The dry air composition is listed in Table 3-1 [116] and is used to determine the carbon dioxide present after combustion.

It is also necessary to define the composition of natural gas for proposed GT combustion, see Table 3-2 [169]. The chemical composition will be slightly different for different oil fields and batches, so the chemical composition percentages are required as input data for emission prediction. In Table 3-2, the percentage of C_4H_{10} includes both normal butane and iso-butane, because, the chemical composition is the same, and both consume the same amount of oxygen and produce the same amounts of water and carbon dioxide on combustion.

Table 3-1 Dry Air Composition [116].

Air	Chemical Formula	Molecular Weight (g/mole)	by Mass (%)	by Mole or Volume (%)
Nitrogen	N_2	28.103	75.52	78.08
Oxygen	O_2	31.999	23.14	20.95
Argon	Ar	39.948	1.28	0.93
Carbon Dioxide	CO_2	44.01	0.05	0.03
Neon	Ne	20.183	0.001	0.002
Total		164.243	99.99	99.99

Table 3-2 Natural Gas Composition [169].

Natural Gas	Chemical Formula	Molecular Weight (g/mole)	by Mole or Volume (%)
Methane	CH_4	16.04246	94.9
Ethane	C_2H_6	30.06904	2.5
Propane	C_3H_8	44.09562	0.2
Butane	C_4H_{10}	58.1222	0.06
Pentane	C_5H_{12}	72.14878	0.02
Nitrogen	N_2	28.103	1.6
Carbon Dioxide	CO_2	44.01	0.7
Oxygen	O_2	31.999	0.02
Total		324.5901	100

The hydrocarbon stoichiometric combustion reaction is as follows:

$$C_aH_b + (a + 0.25b)O_2 \rightarrow aCO_2 + 0.5bH_2O \qquad \textbf{(3-40)}$$

Based on Eq. (3-40), the production of CO_2 and H_2O can be calculated for the specific mass of any hydrocarbon in the natural gas. With a fuel mass flow rate of known molar composition, the total production rates of CO_2 and H_2O for each hydrocarbon can be calculated. Since the composition and mass flow rate of the GT intake air are known, the CO_2 and H_2O in the air intake are also known. The GT exhaust gas includes both the CO_2 from the air intake and the CO_2 generated by burning the fuel.

Perfect combustion is assumed, but this is reasonable as the real combustion efficiency is close to 100% for the DP and should higher than 96% for all normal engine operating conditions [1].

3.2.2 Adiabatic Flame Temperature

3.2.2.1 Enthalpy of Formation and Reaction

To calculate the flame temperature, it is necessary to know the value of enthalpy of formation ΔH_f^o. Here, this is the enthalpy difference between the production and reactants (elemental molecules) under the standard state when formation 1 mole production. Standard values for typical gaseous fuels are given in [10] and are represented by a superscript '^{o}'. The standard state is refereed as under 1 atmosphere, and 298.15 Kelvin.

It is necessary to emphasise that the ΔH_f^o for elemental molecules is zero. Figure 3-5 showed the formation process, and the formula expressing of ΔH_f^o is as follows [8].

$$\Delta H_f^o = \Delta H_a - D(X - Y) \tag{3-41}$$

where ΔH_a is the atomisation enthalpy, and $D(X - Y)$ is the energy (enthalpy) released from chemical bond.

The enthalpy of reaction ΔH_r^o is defined by the following equation representing the enthalpy difference between reactant (elemental molecules) and product molecules. Meanwhile, Figure 3-5 also shows the relation expressed in the following equation.

$$\Delta H_r^o = \sum (\Delta H_f^o)_P - \sum (\Delta H_f^o)_R \tag{3-42}$$

where subscript P refers to products and R refers to reactants.

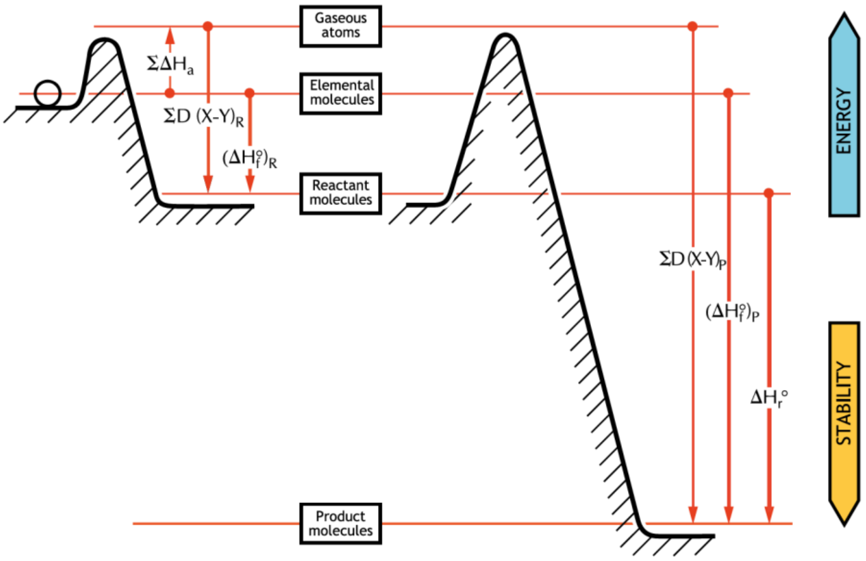

Figure 3-5 Schematic of Standard Molar Enthalpies of Formation ΔH_f^o and Reaction ΔH_r^o [8].

When fuel and oxygen are involved in the combustion process, the Eq. (3-42) is modified as follows.

$$\Delta H_r^o = \sum (\Delta H_f^o)_P - (\Delta H_f^o)_{fuel} \tag{3-43}$$

where $(\Delta H_f^o)_{fuel}$ is enthalpy formation of fuel, and ΔH_f^o for oxygen is zero.

Then, the Eq. (3-43) can be rearranged as follows.

$$(\Delta H_f^o)_{fuel} = \Delta H_r^o + \sum (\Delta H_f^o)_P \tag{3-44}$$

For adiabatic conditions, the ΔH_r^o is absorbed by the product molecules and that causes the temperature to rise to the adiabatic flame temperature T^*. The increase compared with standard state enthalpy, and is defined by the sensible enthalpy H^{T^*}. Then, Eq. (3-44) can be re-written as follows.

$$(\Delta H_f^o)_{fuel} = \sum (H^{T^*})_P + \sum (\Delta H_f^o)_P = \sum (H_t^{T^*})_P \tag{3-45}$$

where $H_t^{T^*}$ is the total enthalpy of each product.

The total thermochemical enthalpy levels for common gases and temperature relation with $H_t^{T^*}$ are shown in Table 3-3 [10]. Hence, the T^* could be known when $H_t^{T^*}((\Delta H_f^o)_{fuel})$ is known, using the method of similar triangles [8].

$$T^* = T_1 + (T_2 - T_1)\frac{\sum H_t^{T_1} - (\Delta H_f^o)_{fuel}}{\sum H_t^{T_1} - \sum H_t^{T_2}} \tag{3-46}$$

where subscripts “1” and “2” refers to the available data from $T - H_t^{T^*}$ in Table 3-3 that the enthalpies for two states are closed to $(\Delta H_f^o)_{fuel}$.

Table 3-3 Total Thermochemical Enthalpy Levels for Gases [10]**.**

T (K)	$H_t^T = H^T + \Delta H_f^o$			$H_t^T = H^T$		
	CO_2	H_2O	CO	H_2	O_2	N_2
298.15	-393.52	-241.83	-110.53	0	0	0
300	-393.46	-241.76	-110.47	0.05	0.05	0.05
500	-385.21	-234.91	-104.60	5.88	6.09	5.91
1000	-360.12	-215.85	-88.84	20.69	22.71	21.46
1500	-331.81	-193.73	-71.68	36.27	40.61	38.41
2000	-302.07	-169.14	-53.79	52.93	59.20	56.14
2100	-296.02	-164.00	-50.15	56.38	62.99	59.75
2200	-289.95	-158.79	-46.51	59.86	66.80	63.37
2300	-283.85	-153.53	-42.85	63.37	70.63	67.01
2400	-277.73	-148.22	-39.18	66.92	74.49	70.65
2500	-271.60	-142.86	-35.51	70.49	78.38	74.31
2700	-259.27	-132.01	-28.12	77.72	86.20	81.66
3000	-240.66	-115.47	-16.99	88.74	98.10	92.74

3.2.2.2 Alkanes Fuel

The combustion equation for alkane fuels is shown as in Eq. (3-47) assuming the inlet air comprise only O_2 and N_2, and the dissociations considered are CO, H_2, and O_2. Non-dissociated adiabatic flame temperature is not considered here, for that refer to [8].

$$C_aH_b + m(O_2 + 3.76N_2) \leftrightharpoons n_1CO_2 + n_2H_2O + n_3CO + n_4H_2 + n_5O_2 + n_6N_2 \quad \textbf{(3-47)}$$

The volume ratio of N_2 and O_2 is assumed to be 3.72, so the mole volume fractions for N_2 and O_2 are 0.79 and 0.21 respectively, and the mole mass for air is 28.96 g/mol.

The equivalence ratio (EQR) is the ratio of actual FAR divide by the stoichiometric FAR. If EQR is less than one, it means the combustion is lean-burn, if the EQR is greater than one, then the combustion is rich-burn. If EQR equals to one, the combustion is stoichiometric. The molar FAR_{sto} is equal to $\frac{1}{4.76\times(a+0.25b)}$ [8]. The actual molar FAR can be determined when fuel and air mass flow rates are known.

$$EQR = \frac{FAR_{actual}}{FAR_{sto}} \quad \textbf{(3-48)}$$

The molar volume of air, m, required for combusiton is obtained as follows.

$$m = (a + 0.25b)/EQR \quad \textbf{(3-49)}$$

The above calculation is universal for all alkanes, but this study considers only methane when calculating the flame temperature. To determine the six independent coefficients ($n_1, \ldots, n_6$) products of combustion needs six independent equation. The first four equations are easy to obtain based on the conservation of mass.

The C balance is as follows:

$$n_1 + n_3 = a \quad \textbf{(3-50)}$$

The H_2 balance is as follows:

$$n_2 + n_4 = 0.5b \quad \textbf{(3-51)}$$

The O_2 balance is as follows:

$$n_1 + 0.5n_2 + 0.5n_3 + n_5 = m \tag{3-52}$$

$$n_5 = m - n_1 - 0.5n_2 - 0.5n_3$$

The N2 balance is as follows:

$$n_6 = 3.76m \tag{3-53}$$

The two remaining independent equations are obtained based on the equilibrium constants for CO_2, and H_2O. The derivation of these constants, K_{CO_2} and K_{H_2O}, is given in [8] as Eqs (3-54) and (3-55).

$$\frac{n_1}{n_3\sqrt{P\cdot(\frac{n_5}{n_t})}} = K_{co_2} \tag{3-54}$$

$$\frac{n_2}{n_1\sqrt{P\cdot(\frac{n_5}{n_t})}} = K_{H_2O} \tag{3-55}$$

which P is inlet air pressure (atm). For the standard state, the $P = 1\ atm$.

The available flame temperature is selected by traversing from Table 3-4 [170] and determining the appropriate values of K_{co_2}, and K_{H_2O} for the selected flame temperature in the first column of Table 3-4 [170].

n_T is defined as the total molar mass of the products of combustion, summed from n_1 to n_6. An iterative procedure is carried out on n_5/n_T to get sufficiently close to the total mole number. The flowchart for the calculation algorithm is showed in Figure 3-6. After the iteration has converged, H_t^T could be obtained from Table 3-3 [10], and then multiplied in turn by each of the six values listed for each product respectively. Finally, the $\sum H_t^T$ is found by selecting the two values of $\sum H_t^T$ that are nearest the $(\Delta H_f^o)_{fuel}$ and then, based on Eq. (3-46), the final adiabatic flame temperature can be obtained.

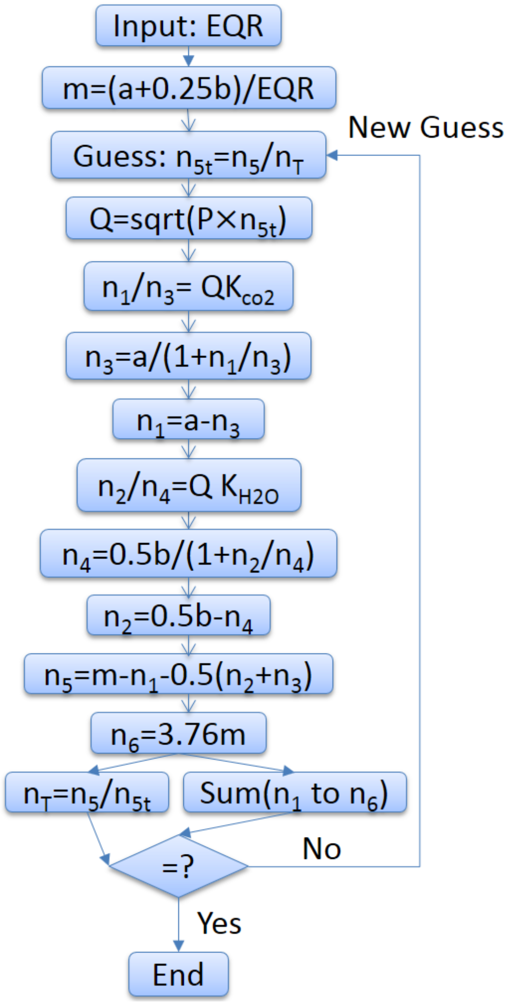

Figure 3-6 Dissociated Flame Temperature Flowchart.

Table 3-4 Partial-pressure Equilibrium Constants [170]**.**

T (K)	K_{co_2}	K_{H_2O}
298.15	1.1641 x 10^{45}	11.169 x 10^{39}
300	575.44 x 10^{42}	6.1094 x 10^{39}
500	10.593 x 10^{24}	76.913 x 10^{21}
1000	16.634 x 10^{9}	11.535 x 10^{9}
1500	207.01 x 10^{3}	530.88 x 10^{3}
2000	765.60	3.4670 x 10^{3}

2100	345.94	1.6866×10^3
2200	168.27	874.98
2300	87.097	480.84
2400	47.753	277.43
2500	27.543	167.49
2700	10.351	68.077
3000	3.0549	22.029

3.2.2.3 Effects of Flame Temperature

As mentioned above, the standard condition is under 1 atmosphere and 298.15 Kelvin, but that it is not aligned with the combustor inlet condition and the adiabatic flame temperature will be different when considering the influence of initial air temperature and pressure [8].

3.2.2.3.1 Influence of Initial Air Temperature

The variation of air temperature could be considered using sensible enthalpy, H_{air}^T, where the sensible enthalpy is the difference between the actual enthalpy and enthalpy at standard conditions. Thus, the total enthalpy difference is as follows [10]:

$$(\Delta H^T)_{air} = 4.76 \cdot m \cdot H_{air}^T \tag{3-56}$$

Then, the Eq. (3-43) will become Eq. (3-57), and Eqs. (3-45) and (3-46) should be updated accordingly.

$$\Delta H_r^o = \sum (\Delta H_f^o)_P - [\left(\Delta H_f^o\right)_{fuel} + (\Delta H^T)_{air}] \tag{3-57}$$

3.2.2.3.2 Influence of Air Pressure

The impact of inlet air pressure will change the flame temperature only under dissociated conditions. The effect could be considered during the calculation of K_{co_2} and K_{H_2O} using Eqs. (3-54) and (3-55) respectively.

3.2.3 Nitrogen Oxides

Industrial GTs emit nitrogen oxides which are a health and environmental hazard. The predominant compound of NO_x is NO which is related to both photochemical smog and acid rain [1]. Lefebvre (1984) [7] presented the following correlation between the mass flow rate of NO_x (W_{NO_x}) produced, and the system parameters.

$$W_{NO_x} = \frac{9 \cdot 10^{-8} \cdot P^{1.25} \cdot V_c \cdot e^{0.01T_{st}}}{\dot{m}_A \cdot T_{pz}} \quad \textbf{(3-58)}$$

where P is combustor inlet pressure (kPa), $\dot{m}_A$ is combustor airflow rate (kg/s), V_c is the volume of the combustion chamber (m^3), T_{pz} is primary zone adiabatic flame temperature (K), T_{st} is stoichiometric flame temperature (k).

3.2.4 Carbon Monoxide

Generally, the less oxygen to fuel the combustion, the more of CO will be formed, rather than complete the reaction to CO_2. Moreover, dissociation of CO_2 under stoichiometric or moderately fuel-lean conditions will also contribute a significant amount of CO. Lefebvre and Ballal (2010) [1] demonstrated that the amount of carbon monoxide is affected by FAR, residence time, mixture strength of air and fuel, and equivalence ratio.

According to Lefebvre (1984) [7], one correlation for the mass flow rate of carbon monoxide, W_{CO}, produced is as follows:

$$W_{CO} = \frac{86\dot{m}_A T_{pz} e^{-(0.00345T_{pz})}}{(V_c - V_e)(\frac{\Delta P}{P})^{0.5} P^{1.5}} \quad \textbf{(3-59)}$$

which V_e is the volume employed in fuel evaporation, calculated as follows.

$$V_e = \frac{0.55\dot{m}_{PZ} D_0^2}{\rho_{pz}\lambda_{eff}} \quad \textbf{(3-60)}$$

where D_0 is Sauter mean diameter (m), $\dot{m}_A$ is combustor airflow rate (kg/s), T_{pz} is primary zone adiabatic flame temperature, V_c is the volume of the combustion chamber (m^3), V_e is volume occupied in evaporation (m^3), $\frac{\Delta P}{P}$ is non-dimensional pressure drop, P is combustor inlet pressure (kPa), $\dot{m}_{PZ}$ is the primary zone airflow rate (kg/s), ρ_{pz} is primary zone airflow density, and λ_{eff} is evaporation constant (m^2/s).

3.3 High-pressure Turbine Creep Life Model

It is assumed that the high-pressure turbine (HPT) creep life can represent the hot section lifing of the GT that the turbine blades normally suffer the worst operating conditions [171]. Fatigue, hot corrosion and other failure models are not covered in this study. The GT performance and blade data are the inputs to the lifing model, see the flowchart of the HPT lifing model presented in Figure 3-7. The detailed algorithm of HPT creep life prediction is in [11,172].

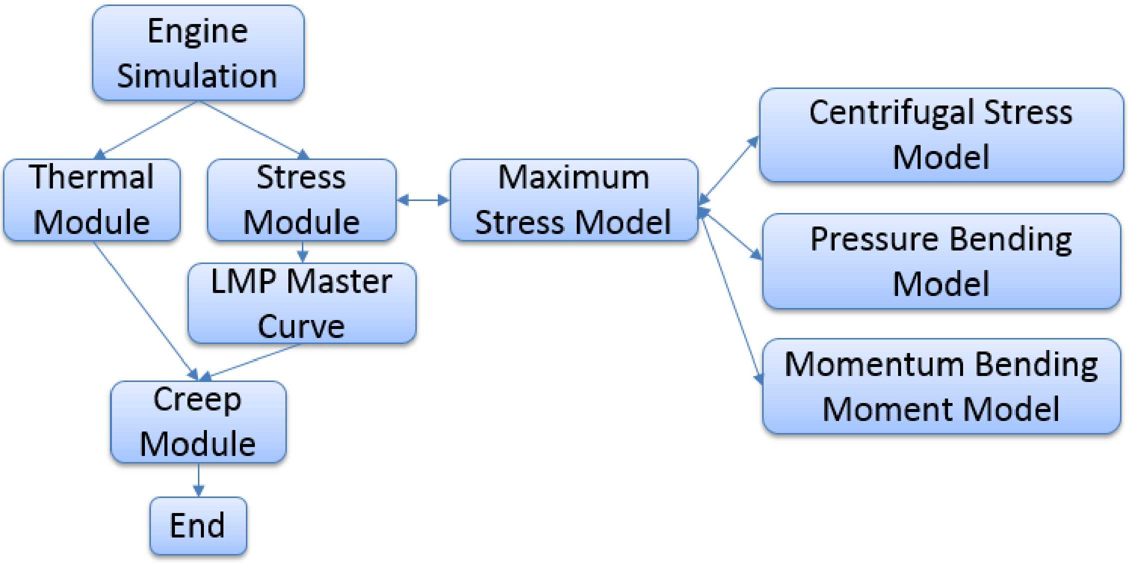

Figure 3-7 Creep Life Prediction Model.

3.3.1 Blade Thermal Model

The blade thermal model is applied to calculate the blade metal temperature. As can be seen in Figure 3-8, the temperature varies along the entire span and is related to the radial temperature distribution factor ($RTDF$). Here, the blade is divided into four sections with five nodes, see Figure 3-9. It is assumed the maximum gas temperature is located at 75% of the blade length from the root [173], see Figure 3-8. Moreover, the tip and root gas temperatures are assumed the same that is the minimum gas temperature. The radial temperature distributions between root and 75% along the blade, and from 75% along the blade to the tip are both assumed to be a linear.

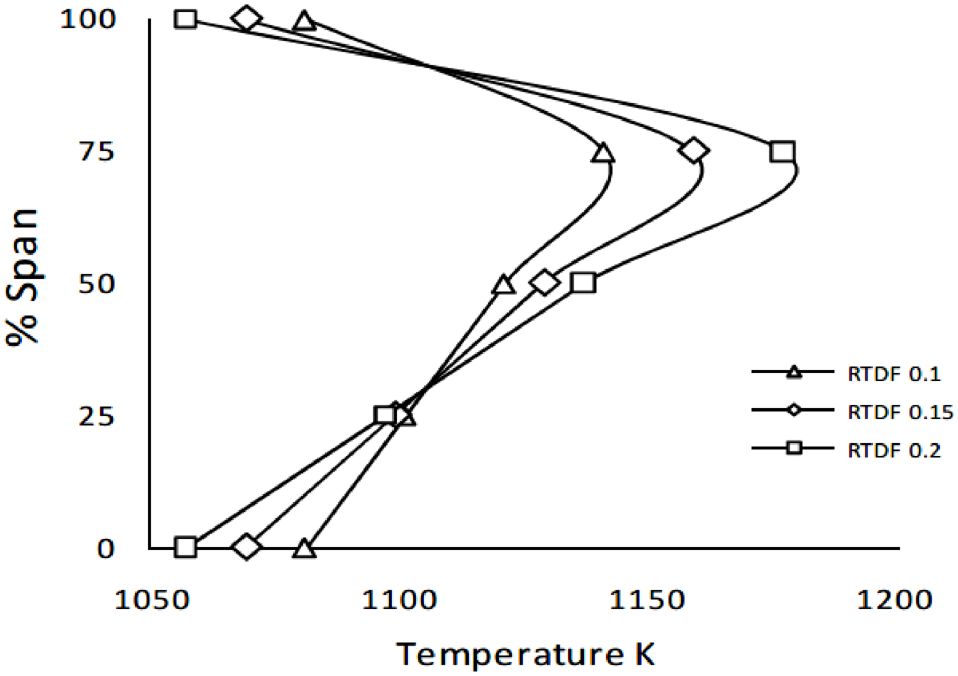

Figure 3-8 Turbine Inlet Temperature Distribution along Span [173]**.**

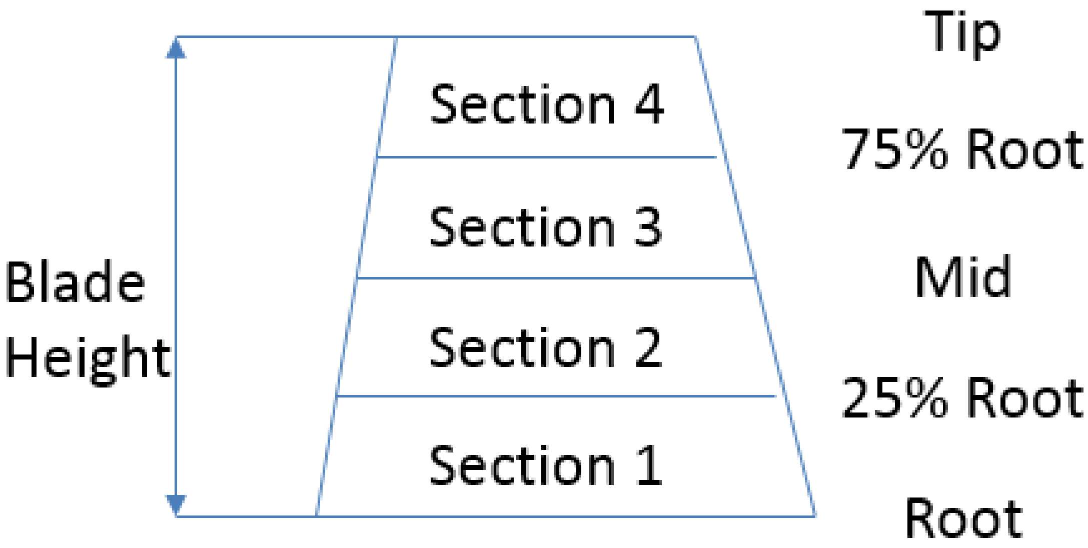

Figure 3-9 One Dimensional HPT Blade Section.

3.3.1.1 Gas Radial Temperature Distribution

The reference temperature, T_{Ref}, is calculated using Eq. (3-61), which follows that is temperature rise in combustor [11]. The burner inlet temperature, $T_{Bur,in}$, and outlet temperature, $T_{Bur,out}$, are obtained based on the zero dimensional GT performance model [4].

$$T_{Ref} = T_{Bur,out} - T_{Bur,in} \tag{3-61}$$

The maximum temperature is obtained from Eq. (3-62) [11].

$$T_{max} = T_{Bur,out} + T_{Ref} \cdot RTDF \tag{3-62}$$

Thus, the minimum gas temperature at the tip and root may be obtained from Eq. (3-63), assuming the temperature gradients between the maximum temperature and both minimums are linear [11].

$$T_{min} = \frac{(5 \cdot T_{Bur,out} - 2 \cdot T_{max})}{3} \tag{3-63}$$

The gas temperatures for blade mid-point and 25% along the length of the blade from the root and can be obtained using linear interpolation. The gas temperature of five nodes will be mentioned as gas temperature T_g while their value vary for different locations among span.

3.3.1.2 Blade Metal Temperature

The blade metal temperature, T_m, for each subsection of the blade is found following [11,174], where ε_{blade} is the cooling effectiveness:

$$\varepsilon_{blade} = \frac{T_g - T_m}{T_g - T_{cool,in}} \tag{3-64}$$

The exit temperature of the coolant gas, $T_{cool,out}$, is obtained as follows for each subsection of the blade [11].

$$\eta_{conv} = \frac{T_{cool,out} - T_{cool,in}}{T_m - T_{cool,in}} \tag{3-65}$$

where η_{conv} is convection efficiency, $T_{cool,in}$ is inlet coolant gas temperature.

3.3.2 Blade Stress Model

The blade stress model includes centrifugal stress and gas bending moment, which require knowledge of the rotational speed of the HPT, and the differences in gas properties between the inlet and outlet of the turbine blades. The stress-predicting algorithm is a pseudo-2D approach that considered the stress distribution for both span and chord directions. The span distribution includes five locations at root, 25% along the blade from the root, middle of the blade, 75% along the blade from the root, and blade tip. Meanwhile, the chord distribution will consider the leading edge, trailing edge, and the farthest point at the back of the blade. For more details of the following models for blade stress calculation algorithm refer to [11].

3.3.2.1 Centrifugal Stress Model

The centrifugal force, CF_{sec}, along span for each section is calculated based on Eq. (3-66). It is assumed that the centrifugal force acts through the centre of gravity (CG) of each section.

$$CF_{sp} = m \cdot \omega^2 \cdot r_{CG} \tag{3-66}$$

where m is mass of the section being considered, ω is the angular velocity of the HPT, r_{CG} is the distance between the centre of gravity of the section and the centre line of the turbine shaft.

The centrifugal stress, CS_{sp}, of each subsections can be calculated from (3-67).

$$CS_{sp} = \frac{CF_{sp}}{A_{CS,sp}} \tag{3-67}$$

where $A_{CS,sp}$ is the cross sectional area for each section in Figure 3-9.

3.3.2.2 Pressure Bending Moment Model

The static pressure will decrease as the gas passes past the turbine blades [116]. Meanwhile, the resultant pressure is due to the static pressure difference between inlet and outlet. The pressure force PF_{sec} on each section can be obtained from Eq. (3-68). The PF_{sec} is assumed to act on the centre of gravity (CG) of each section.

$$PF_{sec} = \frac{A_{An,sec} \cdot \Delta P_{sec}}{NoB} \tag{3-68}$$

where $A_{An,sec}$ is the blade section annulus area, ΔP_{sec} is the decrease of gas static pressure across the blade, NoB is the number of blades at each turbine stage.

The pressure bending moment can be obtained based on Eq. (3-69).

$$PBM_{sp} = \sum (PF_{sec} \cdot d_{sp}) \tag{3-69}$$

where d_{sp} is the distance between the central of the section being considered and the root of the section.

3.3.2.3 Momentum Bending Moment Model

The gas velocity will change as the gas flows across the turbine blades, the change in momentum will result in forces acting on the turbine blades. The absolute velocity of the gas flow may be presented as a combination of axial and tangential velocities, so the momentum bending force can be calculated separately for these two directions. The axial momentum force, $MF_{axial,sec}$, and tangential momentum force, $MF_{tan,sec}$, are calculated based on Eqs. (3-70) and (3-71) respectively.

$$MF_{axial,sec} = \frac{\dot{W}_{area} \cdot A_{An,sec} \cdot \Delta Vel_{axial}}{NoB} \tag{3-70}$$

$$MF_{tan,sec} = \frac{\dot{W}_{area} \cdot A_{An,sec} \cdot \Delta Vel_{tan}}{NoB} \tag{3-71}$$

where $\dot{W}_{area}$ is the mass flow rate per unit area, ΔVel_{axial} is the axial velocity difference, $VF_{tan,sec}$ is the tangential velocity difference.

The momentum bending moment for axial and tangential directions can now be calculated based on Eqs. (3-72) and (3-73) respectively.

$$MBM_{axial,sp} = \sum (MF_{axial,sec} \cdot d_{sp}) \tag{3-72}$$

$$MBM_{tan,sp} = \sum (MF_{tan,sec} \cdot d_{sp}) \tag{3-73}$$

3.3.2.4 Maximum Stress Model

The bending moments of the turbine blade are shown in Figure 3-10 [11]. It is assumed blade density is uniform, so the CG, the centre of mass, and centroid are at the same point. Hence, the neutral axis, X-X in the figure, will across the CG point that θ is the angle between the neutral line and turbine axial direction.

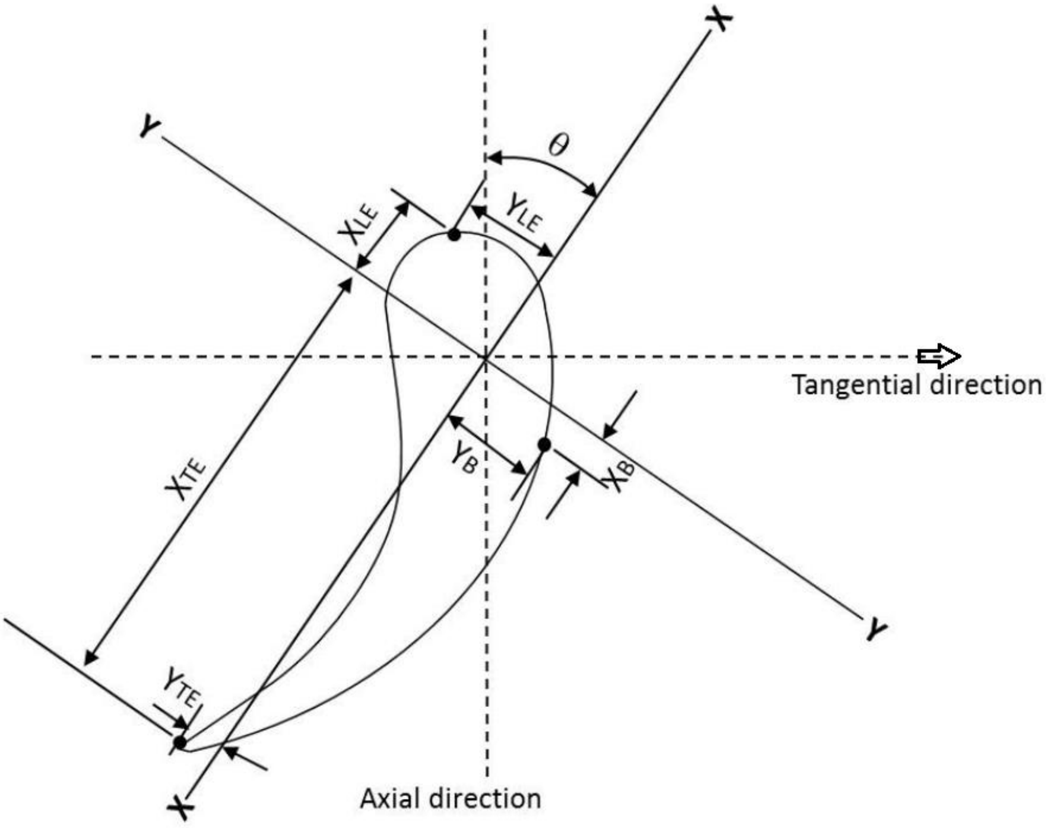

Figure 3-10 Bending Moments of Turbine Blade [11].

$$M_{X,sp} = \left(PBM_{sp} + MBM_{axial,sp}\right) sin\theta_{sp} + MBM_{tan,sp} cos\theta_{sp} \tag{3-74}$$

$$M_{Y,sp} = \left(PBM_{sp} + MBM_{axial,sp}\right)cos\theta_{sp} - MBM_{tan,sp}sin\theta_{sp} \tag{3-75}$$

where $M_{X,sp}$ and $M_{Y,sp}$ are the resulting bending moments at the X-X and Y-Y directions respectively.

For calculating the resulting bending moment stress $RBMS_{sp}$ at three different locations (leading edge, trailing edge, and farthest location), the coordinate system is transferred from turbine direction (axial and tangential direction) to blade direction (X-Y) [11]. The maximum $RBMS_{sp}$ is obtained as follows.

$$RBMS_{sp} = \frac{M_{X,sp}Y_L}{I_X} + \frac{M_{Y,sp}X_L}{I_Y} \tag{3-76}$$

where Y_L and X_L are the perpendicular distances to the neutral axis that are differ for different locations (leading edge, trailing edge, and farthest location), I_X and I_Y are the second moment of area about the neutral axes X and Y respectively.

The total stress, TS_{sp}, at the three different chord-wised locations can be obtained by Eq. (3-77).

$$TS_{sp} = CS_{sp} + RBMS_{sp} \tag{3-77}$$

After TS_{sp} has been calculated for the different locations, the maximum TS_{sp} will be obtained for each section.

3.3.3 Creep Model

The time to failure, t_f, can be obtained based on the Larson-Miller parameter method as follows by Eq. (3-78).

$$t_f = 10^{\left(\frac{1000 \cdot LMP}{T_m} - C\right)} \tag{3-78}$$

where C is constant (typically about 20), LMP is the blade LMP master curve (TS_{sp} VS LMP).

The creep factor, CF, could be obtained from Eq. (3-79) as follows.

$$CF = \frac{t_f}{t_{ref}} \tag{3-79}$$

where t_{ref} is reference time to failure.

The life fraction, LF, can be calculated based on Eq. (3-80) representing the ratio of operating time at the specific condition to the total creep life at this condition.

$$LF = \frac{OT}{t_f} \tag{3-80}$$

where OT is operating time.

It is clear that the lower the value of LF, the less life has been consumed and the longer remaining life until failure. When the accumulated value of LF for all previous operation equals unity, the blade failure is likely occur. For the same GT engine power setting, a degraded engine will run at a higher TET and that consumes more blade life per unit operating time compared with a new engine.

3.4 OTSG Performance Model

The performance calculation of a parallel dual-pressure OTSG can be divided into two steps as follows:

- DP performance calculation, where the OTSG's performance at a specified DP is calculated and critical heat transfer areas are determined;
- OD performance calculation, where the performance of an OTSG under changing exhaust gas and operating conditions is calculated. When the OTSG is operating at OD condition, the LP feed water could be none and only HP route in operation. So, the OD algorithm will have two parts.

3.4.1 Geometry Structure and Temperature Profiles

Figure 3-11 [175] shows a typical dual-pressure OTSG, and Figure 3-12 shows its temperature profiles along the OTSG gas path, where T_1 is the OTSG inlet gas temperature, T_8 is the stack temperature, T_j is the HP circuit feed water temperature, and T_h is the LP circuit feed water temperature. The HP circuit is divided into three sections, namely (a–d) or (a–b–c–d), (d–i) or (d–m–n–i), and (i–j), where the HP circuit (d–i) is parallel to the LP circuit (e–h). The location of the inlets (i.e., ‘1, j and h’) and the outlets (i.e., ‘8, a and e’) of the gas and steam circuits remain unchanged during operation. As points h and e (inlet and outlet of the LP circuit) are fixed, the four points (i.e., ‘7, i, 4, and d’) in the exhaust gas path and HP circuit are unchanged for all conditions. Therefore, the heat transfer areas of the HP sections (a–d), (d–i), and (i–j) are unchanged, and their relative positions to the LP circuits are also unchanged. Meanwhile, the heat transfer areas of sections (e–h) and (a–j) are the total heat transfer areas of the LP and HP circuits, respectively, and they are unchanged. Hence, even when the boundaries between the economizer, evaporator, and superheater in the OTSG are moving, the heat transfer areas of sections (a–d), (d–i), (i–j), and (e–h) are unchanged. The heat transfer is balanced between the exhaust gas side and the water-steam side between any two vertical dash lines, as shown in Figure 3-12.

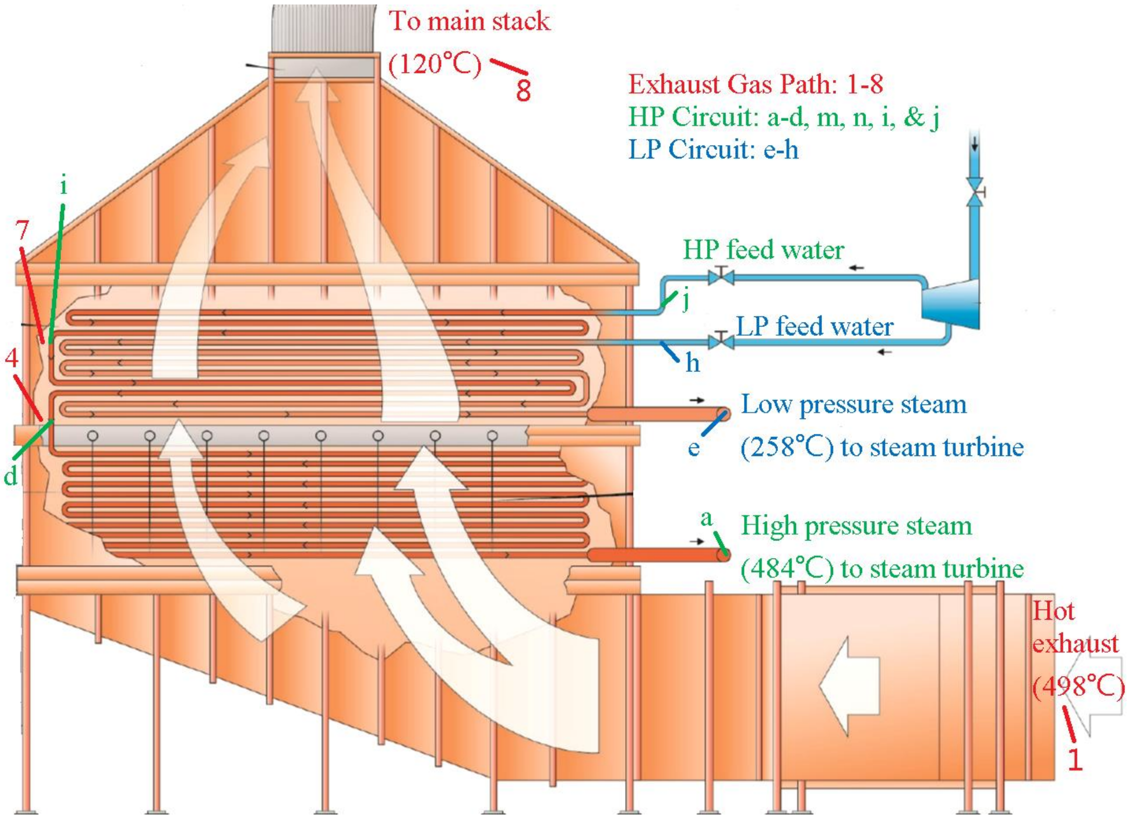

Figure 3-11 Schematic of Once-through Steam Generator (OTSG) [175]**.**

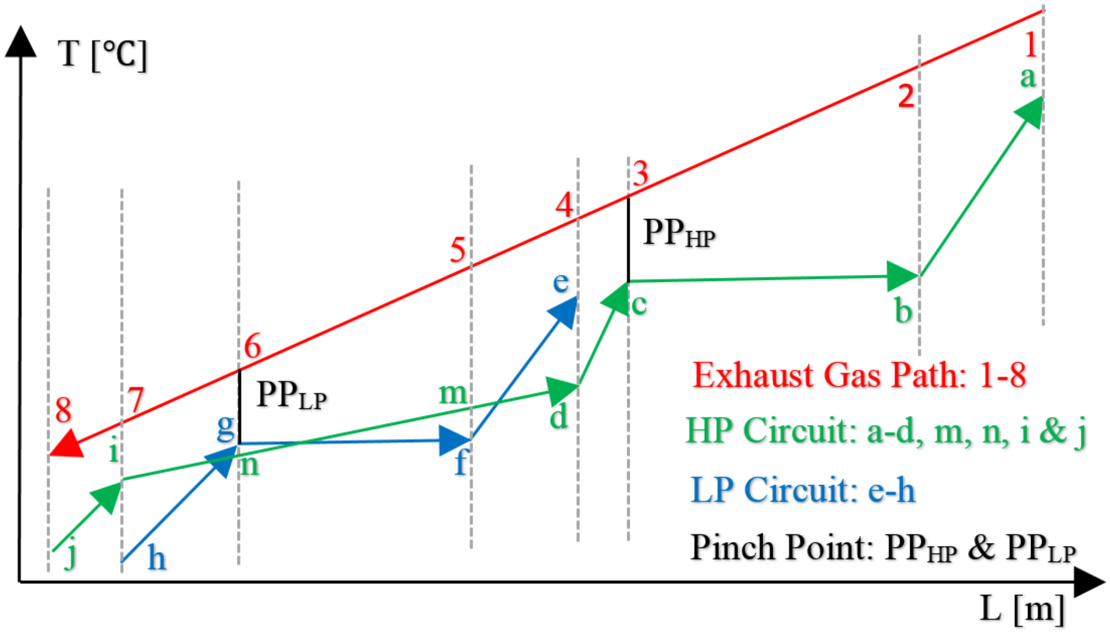

Figure 3-12 OTSG Temperature Profiles along OTSG Gas Path.

3.4.2 Basic Concepts and Definitions

3.4.2.1.1 Overall Heat Transfer Coefficient

The finned tube geometry, α_{inn}, α_o, and λ determines the overall heat transfer coefficient U for calculating the rate of heat transfer as follows [95,98,176].

$$\frac{1}{U} = \frac{1}{\alpha_o} + \frac{A_{TOT}}{A_{inn}}\left(\frac{1}{\alpha_{inn}} + \frac{d_o - d_{inn}}{2\lambda}\right) \tag{3-81}$$

where α_{inn} is the heat transfer coefficient in the inner tube, α_o is the virtual heat transfer coefficient (considering the fin efficiency) at fume side, λ is the thermal conductivity, d_{inn} is tube inner diameter, d_o is tube outer diameter, A_{inn} is tube inner surface area, and A_{TOT} is the total outer surface area. The heat transfer coefficient at the fume side α_o for cross-flow configuration is estimated using the method in [89,176,177].

The heat transfer coefficient of the tube side α_{inn} is divided into two parts—a single-phase flow (economizer and superheater) and dual-phase flow (evaporator):

1) The calculation of heat transfer coefficient of turbulent, hydrodynamically developed and forced single-phase internal flows refers [89,178];
2) In an evaporator, the heat transfer coefficient at the tube side varies with the flow pressure and internal flow conditions. The perimeter-averaged heat transfer coefficient that considers the convective and nucleate boiling for mixed flow inside the tubes refers to [179].

The properties of water or steam were calculated based on the method proposed by Wagner [180]. The properties of the GT exhaust gas were calculated by NASA CEA programme [164].

3.4.2.2 Heat Balance

It is essential to quantify the heat transfer Q between the OTSG inlet gas and water-steam flows in OTSG circuits, represented by the specific enthalpy h and mass flow rate W in Eq. (3-82):

$$Q = W \cdot q = W \cdot |h_{in} - h_{out}| \tag{3-82}$$

where h_{in} and h_{out} are the inlet and outlet specific enthalpy of either the hot side or cold side of a heat transfer circuit, while q is the specific heat transfer rate.

The heat transfer in an OTSG section is driven by a logarithmic mean temperature difference ($LMTD$) [93], defined by Eq. (3-83):

$$LMTD = (\Delta T_I - \Delta T_{II})/(\ln(\Delta T_I/\Delta T_{II})) \tag{3-83}$$

where $\Delta T_I = T_{hot,in} - T_{cold,out}$, and $\Delta T_{II} = T_{hot,out} - T_{cold,in}$. Equation (3-84) [93] represents the heat transfer rate of any OTSG sections:

$$Q = U \cdot A \cdot LMTD \tag{3-84}$$

where A is the heat transfer area and U is the overall heat transfer coefficient. The value of U varies at different parts of the OTSG that decided by Eq. (3-81).

3.4.2.3 Once-through Steam Generator Efficiency

The efficiency of an OTSG is defined by Eq. (3-85), where T_1 is the OTSG inlet gas temperature, T_8 is the stack temperature, and T_{amb} is the ambient temperature:

$$\eta = (T_1 - T_8)/(T_1 - T_{amb}) \tag{3-85}$$

3.4.2.4 Heat Transfer Ratio

The heat transfer ratio defined by Eq. (3-86) represents the ratio between the heat transfer of section (x–y) and that of section (u–v), where the former is a subsection of the latter:

$$Cf_{xy/uv} = Q_{xy}/Q_{uv} = q_{xy}/q_{uv} \tag{3-86}$$

3.4.2.5 Ratio of Heat Transfer Areas

Equation (3-87) defines the ratio between the heat transfer area of section (x–y) and that of section (u–v); the former is a subsection of the latter:

$$CA_{xy/uv} = A_{xy}/A_{uv} \tag{3-87}$$

3.4.3 Design Point Performance Simulation

3.4.3.1 Input Parameters

Figure 3-13 shows the simulation flowchart of a parallel dual-pressure OTSG at the DP where the following gas path input parameters are given:

- Gas inlet temperature: T_1
- Gas mass flow rate: W_{exh}
- Ambient temperature: T_{amb}
- HP circuit live steam temperature: T_a
- HP live steam pressure: P_a
- HP pinch point temperature difference: PP_{HP}
- HP feed water temperature: T_j
- LP circuit live steam temperature: T_e
- LP circuit live steam pressure: P_e

- LP pinch point temperature difference: PP_{LP}
- LP feed water temperature: T_h
- Heat transfer ratio of section (d–i) over (c–j): $Cf_{di/cj}$
- Heat transfer ratio of section (i–j) over (c–j): $Cf_{ij/cj}$

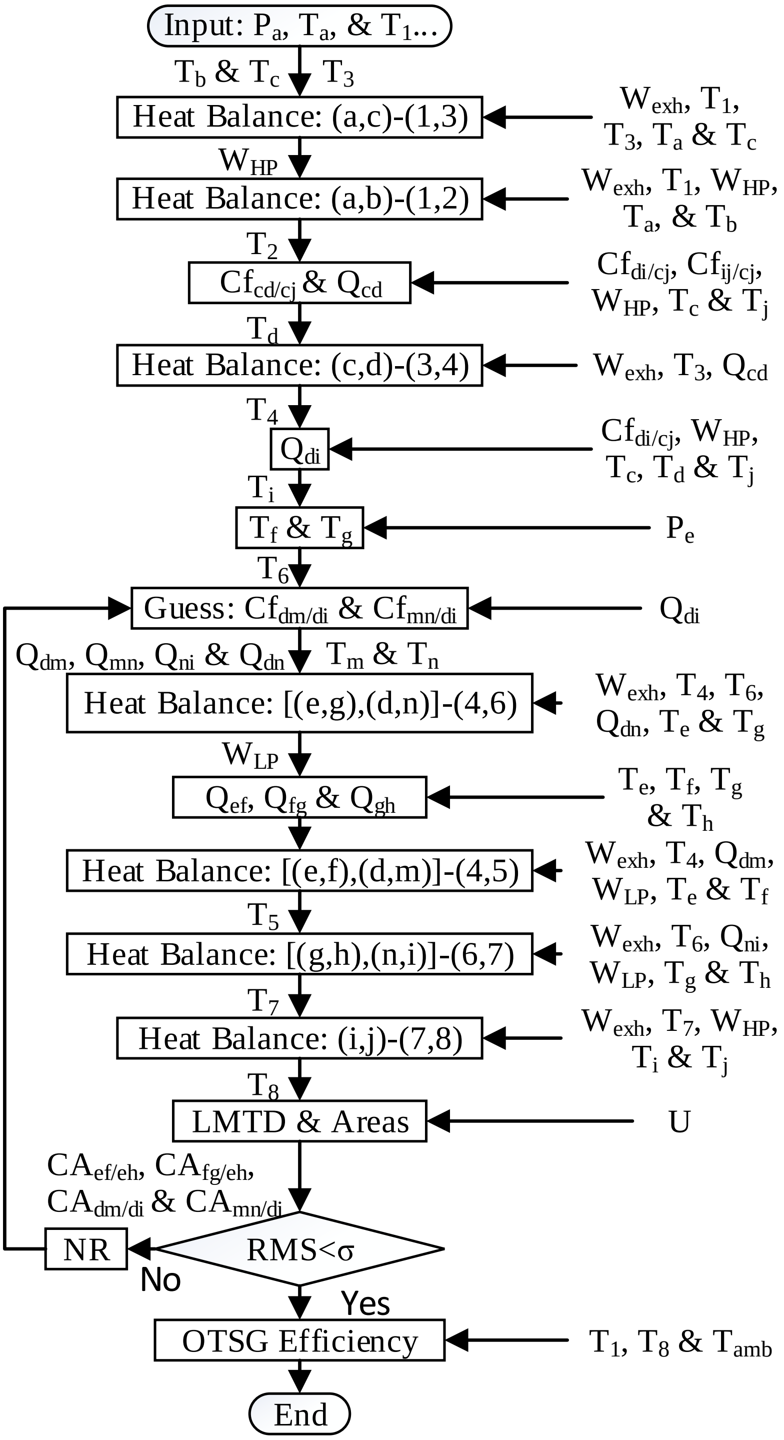

Figure 3-13 OTSG Design Point (DP) Performance Calculation.

3.4.3.2 State Variables

To quantify the heat transfer (Q_{dm}, Q_{mn}, and Q_{ni}) within subsection (d–i) that is in parallel with the LP circuit and obtain a DP solution, two iteration variables are selected, as defined by Eq. (3-86), as follows:

- Heat transfer ratio between section (d–m) and section (d–i): $Cf_{dm/di}$
- Heat transfer ratio between section (m–n) and section (d–i): $Cf_{mn/di}$

3.4.3.3 Errors and Root Mean Square Error

The heat transfer area is proportional to the length of the tube when the tube cross-section diameter is constant. Meanwhile, it is assumed that the tube length is proportional to the X-axis in Figure 3-12, so the heat transfer area is proportional to the X-axis. It can be seen in Figure 3-12 that points d and e, m and f, n and g, and i and h have the same flow path locations on the X-axis, respectively. Therefore, $CA_{ef/eh}$ should equal to $CA_{dm/di}$, and $CA_{fg/eh}$ should equal to $CA_{mn/di}$. Thus, two errors are defined as follows:

- $\Delta Y_1 = (CA_{ef/eh} - CA_{dm/di})/CA_{dm/di}$
- $\Delta Y_2 = (CA_{fg/eh} - CA_{mn/di})/CA_{mn/di}$

The Root Mean Square (RMS) of the errors is defined by Eq. (3-88), required to be less than a threshold σ (1E-05) as convergence criteria.

$$RMS = \sqrt{\frac{1}{G}\sum_{k=1}^{G}(\Delta Y_k)^2} < \sigma \tag{3-88}$$

where G is the number of the errors; for DP calculations $G = 2$.

3.4.3.4 Newton Raphson Method

To satisfy the above convergence criteria, Newton Raphson (NR) iteration method [181] was used to search for an optimal solution of the variables ($Cf_{dm/di}$ and $Cf_{mn/di}$) by Eq. (3-89) until the RMS of the errors defined by Eq. (3-88) is less than a threshold σ.

$$X_{n+1} = X_n - f(X_n)/f'(X_n) \tag{3-89}$$

where X is an iteraiton variable , n is the number of iterations, $f(\cdot)$ is the OTSG system function that represents an implicit functional relationship between the variables and errors, and $f'(\cdot)$ is the function's derivative that could be obtained through Jacobian matrix.

3.4.3.5 Design Point Performance Calculation Algorithm

Figure 3-13 shows the simulation flowchart for a parallel dual-pressure OTSG DP performance simulation. The calculation for each section of the OTSG and the iterative process are explained as follows:

(1) The initial values of the two variables $Cf_{dm/di}$ and $Cf_{mn/di}$ are guessed based on experience.

(2) Section (a–b–c–d) and Section (1–2–3–4)

The T_b = T_c is the saturated temperature in the HP circuit that can be calculated once P_a is given. Therefore, temperature T_3 is determined by Eq. (3-90):

$$T_3 = T_c + PP_{HP} \tag{3-90}$$

Among the points indicated in Figure 3-12, the temperature at positions 1, 3, a, and c are known. Based on the heat balance between the hot side (1–3) and cold side (a–c), the HP circuit mass flow rate W_{HP} can be calculated by Eq. (3-82). Therefore, T_2 can be obtained based on the heat balance between the hot side (1–2) and cold side (a–b). Q_{cj} can be decided by W_{HP}, T_c, and T_j. Then, the heat transfer Q_{cd} can be calculated by Eq. (3-91).

$$Q_{cd} = Cf_{cd/cj} \cdot Q_{cj} = (1 - Cf_{di/cj} - Cf_{ij/cj}) \cdot Q_{cj} \tag{3-91}$$

As W_{HP}, T_c, and Q_{cd} have already been determined, T_d can be calculated by Eq. (3-82) at the HP water circuit (c–d). Based on the heat balance between sections (c–d) and (3–4), T_4 can be determined by Eq. (3-82).

(3) Section (d–m–n–i), Section (e–f–g–h) and Section (4–5–6–7)

$Cf_{di/cj}$ is known as an input parameter and Q_{di} can be obtained by Eq. (3-86). Therefore, T_i can be obtained based on Q_{di}, W_{HP}, and T_d.

The T_f = T_g is the saturated temperature in the LP circuit that can be obtained once P_e is given. Then, the temperature T_6 could be obtained by Eq. (3-92).

$$T_6 = T_g + PP_{LP} \tag{3-92}$$

Section (d–i) is divided into three sections, (d–m), (m–n) and (n–i). The variables $Cf_{dm/di}$ and $Cf_{mn/di}$ are guessed in iterations where Q_{dm}, Q_{mn} and Q_{ni} can be calculated respectively by Eq. (3-86) and Q_{dn}, can be calculated by Eq. (3-93).

$$Q_{dn} = (Cf_{dm/di} + Cf_{mn/di}) \cdot Q_{di} \tag{3-93}$$

Therefore, T_m can be obtained based on Q_{dm}, W_{HP} and T_d. Similarly, T_n can be calculated. As the temperature at points 4, 6, e, and g are known, the heat transfer rate at the cold side between (e–g) and (d–n) and at the hot side (4–6) can be obtained based on heat balance shown by Eq. (3-94):

$$W_{LP} \cdot \left(h_e - h_g\right) = Q_{eg} = Q_{46} - Q_{dn} \tag{3-94}$$

Hence, the LP circuit mass flow rate W_{LP} can be determined, and this is then used to derive the heat transfer rates Q_{ef}, Q_{fg}, Q_{gh} and Q_{eh} by Eq. (3-82). T_5 can be calculated via the heat balance between the hot section (4–5) and cold sections (d–m) and (e–f) by Eq. (3-95) combined with Eq. (3-82). Similarly, T_7 can be calculated based on the heat balance between the hot section (6–7) and cold sections (g–h) and (n–i) by Eqs. (3-96) and (3-82):

$$Q_{ef} + Q_{dm} = Q_{45} = W_{exh} \cdot (h_4 - h_5) \tag{3-95}$$

$$Q_{gh} + Q_{ni} = Q_{67} = W_{exh} \cdot (h_6 - h_7) \tag{3-96}$$

(4) Section (i–j) and Section (7–8)

As the $Cf_{ij/cj}$ is known, so the Q_{ij} could be obtained based on $Cf_{ij/cj}$ and Q_{cj} by Eq. (3-86). Hence, the OTSG stack temperature T_8 can be obtain when h_8 is calculated by Eq. (3-97).

$$Q_{ij} = Q_{78} = W_{exh} \cdot (h_7 - h_8) \tag{3-97}$$

(5) Heat Transfer Areas

From the results of the above calculations, the DP performance of the OTSG is obtained provisionally, and the LMTD and the heat transfer areas for each section (A_{ab}, A_{bc}, A_{cd}, A_{dm}, A_{mn}, A_{ni}, A_{ij}, A_{ef}, A_{fg}, and A_{gh}) can be calculated based on the continuation of energy by Eq. (3-84). Therefore, the heat transfer areas of the whole HP and LP steam circuits can be calculated by Eq. (3-98) and (3-99):

$$A_{aj} = A_{ab} + A_{bc} + A_{cd} + A_{dm} + A_{mn} + A_{ni} + A_{ij} \tag{3-98}$$

$$A_{eh} = A_{ef} + A_{fg} + A_{gh} \tag{3-99}$$

(6) Iterations and Convergence

At this point, $CA_{ef/eh}$ can be calculated by Eq. (3-100). Similarly, $CA_{fg/eh}$ $CA_{dm/di}$, and $CA_{mn/di}$ can be determined.

$$CA_{ef/eh} = A_{ef}/A_{eh} \tag{3-100}$$

Therefore, ΔY_1 and ΔY_2 are calculated and the RMS can be obtained by Eq. (3-88). If the RMS is less than the threshold, the iteration will be terminated and the OTSG efficiency will be obtained by Eq. (3-85). Meanwhile, the non-dimensional steam flow capacity at OTSG outlets can be obtained. If the convergence criteria is not satisfied, the two iteration variables will be updated by Eq. (3-89) and the calculations will be repeated from Step (2) using the Newton-Raphson method.

The above calculation process may be used for the preliminary design of a new OTSG where the heat transfer ratios $Cf_{di/cj}$ and $Cf_{ij/cj}$ are specified and the heat transfer areas and OTSG performance are calculated.

3.4.4 Off-design Performance Simulation under Dual-pressure Operation

3.4.4.1 Input Parameters

The OD performance of an OTSG refers to an existing OTSG operating at different ambient and operating conditions. The input parameters for the OTSG at dual-pressure OD operating conditions are as follows:

- Gas inlet temperature: T_1
- Gas mass flow rate: W_{exh}
- ST Erosion Factor: EF_{ST}
- Ambient temperature: T_{amb}
- HP feed water temperature: T_j
- LP feed water temperature: T_h

3.4.4.2 Iteration Variables

The following six parameters in an OTSG system are selected as variables that determine the status of the OTSG:

- HP circuit mass flow rate: W_{HP}
- LP circuit mass flow rate: W_{LP}
- Heat transfer ratio of section d–i over c–j: $Cf_{di/cj}$
- Heat transfer ratio of section i–j over c–j: $Cf_{ij/cj}$
- Heat transfer ratio of section d–m over d–i: $Cf_{dm/di}$
- Heat transfer ratio of section m–n over d–i: $Cf_{mn/di}$

3.4.4.3 Iteration Errors

As mentioned already, A_{ad}, A_{di}, A_{ij}, and A_{eh} are constant under all conditions and they are used as OD convergence criteria. In addition, the two DP convergence criteria also need to be satisfied under OD conditions. Therefore, the following six iteration errors are identified:

- $\Delta Y_1 = (A_{ad\_OD} - A_{ad})/A_{ad}$
- $\Delta Y_2 = (A_{di\_OD} - A_{di})/A_{di}$

- $\Delta Y_3 = (A_{ij\_OD} - A_{ij})/A_{ij}$
- $\Delta Y_4 = (A_{eh\_OD} - A_{eh})/A_{eh}$
- $\Delta Y_5 = (CA_{ef/eh} - CA_{dm/di})/CA_{dm/di}$
- $\Delta Y_6 = (CA_{fg/eh} - CA_{mn/di})/CA_{mn/di}$

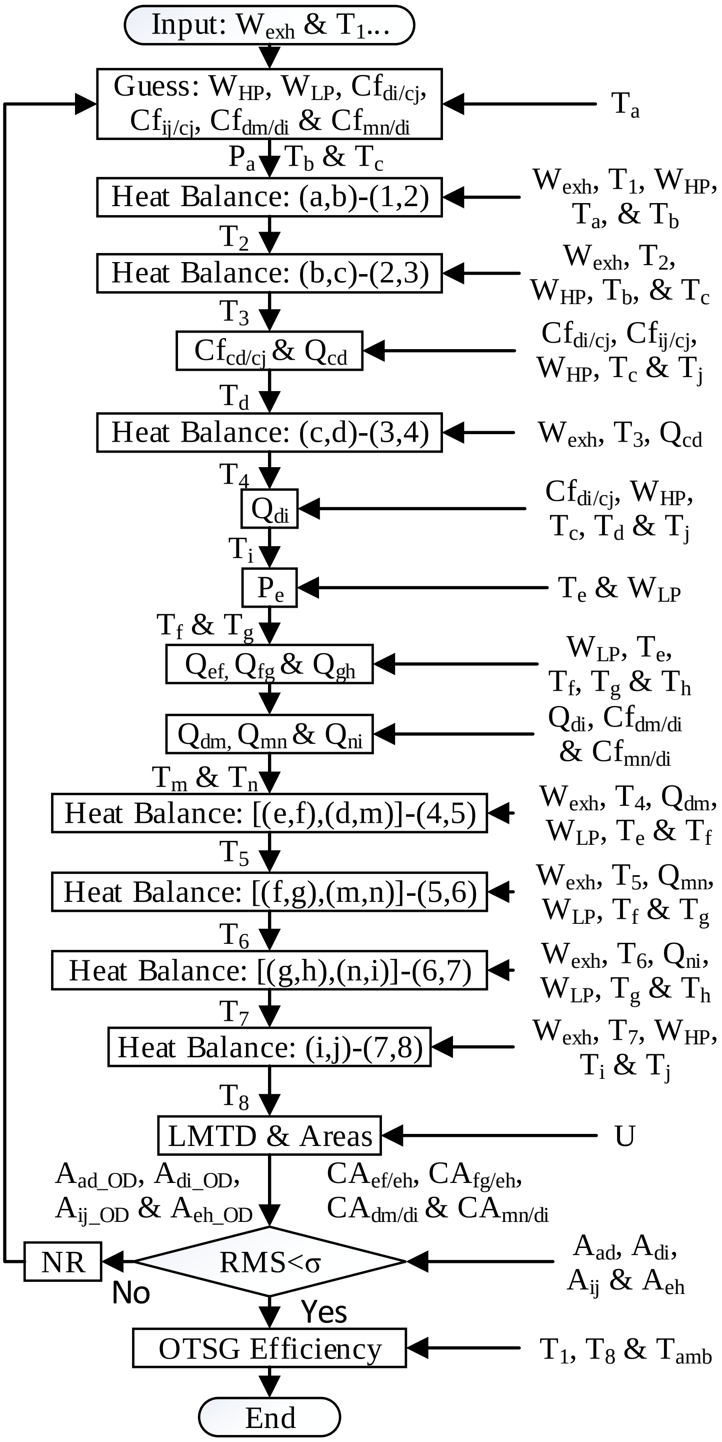

Figure 3-14 OTSG Off-Design (OD) Performance Calculation with Dual-pressure.

3.4.4.4 Off-design Performance Calculation Algorithm with Dual-pressure

Figure 3-14 illustrates the calculation flowchart of the OD performance calculation of a parallel dual-pressure OTSG with detailed description given as follows:

(1) The initial values of the six variables W_{HP}, W_{LP}, $Cf_{di/cj}$, $Cf_{ij/cj}$,$Cf_{dm/di}$, and $Cf_{mn/di}$ take their values at DP point to start the calculation.

(2) *Sections (a–b–c–d) and (1–2–3–4)*

At a changing OD condition, the desired HP steam temperature T_a is determined by Eq. (3-101). The value of the controlled temperature "484 ºC" is case specific and may be different for different power plants. If such a desired value of T_a is not satisfied, the feed water mass flow rate will be adjusted by a feedback control to obtain such T_a.

$$\begin{cases} T_a = T_1 - 14 & T_1 \leq 500℃ \\ T_a = 484 & T_1 > 500℃ \end{cases} \qquad \textbf{(3-101)}$$

If an OTSG inlet gas flow rate drops due to the reduction of upstream GT load, less steam will be generated by the OTSG, and consequently the steam pressure has to respond for keeping the same steam flow capacity represented by Eq. (3-102) [182]. This refers to sliding control that is widely used for steam cycle OD control [14].

$$\frac{W \cdot \sqrt{T}}{P} = \frac{W_{DP} \cdot \sqrt{T_{DP}}}{P_{DP}} \cdot EF_{ST} \qquad \textbf{(3-102)}$$

where W is the live steam mass flow rate, T is the live steam temperature, P is the live steam pressure, and EF_{ST} is the erosion factor of downstream ST non-dimensional flow capacity [183]. The increasing of EF_{ST} represents ST erosion regarded as degradation. Lakshminarasimha et al. [183] demonstrated erosion could cause an increase in ST flow capacity and a decrease in ST isentropic efficiency. As this study focuses on OTSG performance simulation, only the ST flow capacity is relevant.

The HP steam pressure P_a can be determined if T_a and W_{HP} are available in Eq. (3-102). Once the steam pressure is known, the saturation temperature at points b, and c can be calculated. Based on the heat balance between the hot side (1–2) and cold side (a–b), T_2 can be obtained by Eq. (3-82).

Following the same procedure, T_3 can be determined based on the heat balance between the hot side (2-3) and cold side (b-c).

Since the OTSG inlet feed water temperature is given, the Q_{cj} needed for the HP economizer can be calculated by T_c, T_j, and W_{HP}. Hence, the Q_{cd} can be obtained by Eq. (3-86). Then, T_d, and T_4 are determined in the same way as that in the DP performance calculation.

(3) *Sections (d–m–n–i), (e–f–g–h) and (4–5–6–7)*

Q_{di} and T_i can be obtained in the same way as that in DP calculation. The LP steam temperature T_e is obtained by setting the constant difference between T_4 and T_e . Then P_e can be decided by Eq. (3-102). Correspondingly, saturation temperature T_f and T_g can be easily obtained. Based on the known temperature (i.e. T_e, T_f, T_g, and T_h) and the guessed value of W_{LP}, the value of Q_{ef}, Q_{fg}, and Q_{gh} can be determined by Eq. (3-82). Based on the guessed $Cf_{dm/di}$ and $Cf_{mn/di}$, Q_{dm}, Q_{mn}, Q_{ni}, T_m and T_n are obtained. T_5 can be calculated based on Eq. (3-95). Similarly, T_6 is obtained via the heat balance between the hot section (5–6) and cold sections (f–g) and (m–n). In addition, T_7 can be obtained by Eq. (3-96).

(4) *Sections (i–j) and (7–8)*

Q_{ij} can be obtained by using Q_{cj} and guessed $Cf_{ij/cj}$. Then, the T_8 can be calculated by Eq. (3-97).

(5) *Heat Transfer Areas*

At the end of the above calculations, the heat transfer areas (i.e. A_{ad_OD}, A_{di_OD}, A_{ij_OD}, A_{eh_OD}), and the ratios of heat transfer areas (i.e. $CA_{ef/eh}$, $CA_{dm/di}$, $CA_{fg/eh}$, and $CA_{mn/di}$) can be calculated.

(6) *Iteration Errors, Convergence Criteria and Iterations*

Following the above calculations, the six OD errors ΔY_k (Section 3.4.4.3) and the corresponding RMS can be calculated by Eq. (3-88). If the RMS is less than the threshold, the OD calculation finishes and the OTSG efficiency will be obtained by Eq. (3-85). Otherwise, the six iteration variables will be updated by Eq. (3-89) and the calculation will be repeated from Step (2) following the Newton Raphson method.

To assess the quality of the final solutions, an average prediction error $\bar{\gamma}_i$ for each measurement parameter at multiple OD points is defined by Eq. (3-103).

$$\bar{\gamma}_i = \frac{1}{N}\sum_{j=1}^{N}\left|\frac{\bar{Z}_i - Z_i}{\bar{Z}_i}\right| \cdot 100\% \quad \textbf{(3-103)}$$

where N is the number of OD points, $\bar{Z}_i$ is the measured parameter, and Z_i is the simulated value of the same parameter.

3.4.5 Off-design Performance Simulation under Single-pressure Operation

The OTSG is rarely operated at the single-pressure (HP only) condition that most of the time happens at starting up and shutting down. It may also occur when the OTSG LP tube has a leakage problem. There is no doubt the OTSG efficiency will be decreased under single-pressure operation that the LP heat transfer surface is wasted, and the stack temperature will be increased.

3.4.5.1 Input Parameters

The input parameters for the OTSG at single-pressure OD operating conditions are as follows:

- Gas inlet temperature: T_1
- Gas mass flow rate: W_{exh}
- ST Erosion Factor: EF_{ST}
- Ambient temperature: T_{amb}
- HP feed water temperature: T_j

3.4.5.2 Iteration Variables

The following three parameters in an OTSG system are selected as variables that determine the status of the OTSG:

- HP circuit mass flow rate: W_{HP}
- Heat transfer ratio of section d–i over c–j: $Cf_{di/cj}$
- Heat transfer ratio of section i–j over c–j: $Cf_{ij/cj}$

3.4.5.3 Iteration Errors

As mentioned already, A_{ad}, A_{di}, and A_{ij} are constant under all conditions and they are used as OD convergence criteria. Therefore, the following three iteration errors are identified:

- $\Delta Y_1 = (A_{ad\_OD} - A_{ad})/A_{ad}$
- $\Delta Y_2 = (A_{di\_OD} - A_{di})/A_{di}$
- $\Delta Y_3 = (A_{ij\_OD} - A_{ij})/A_{ij}$

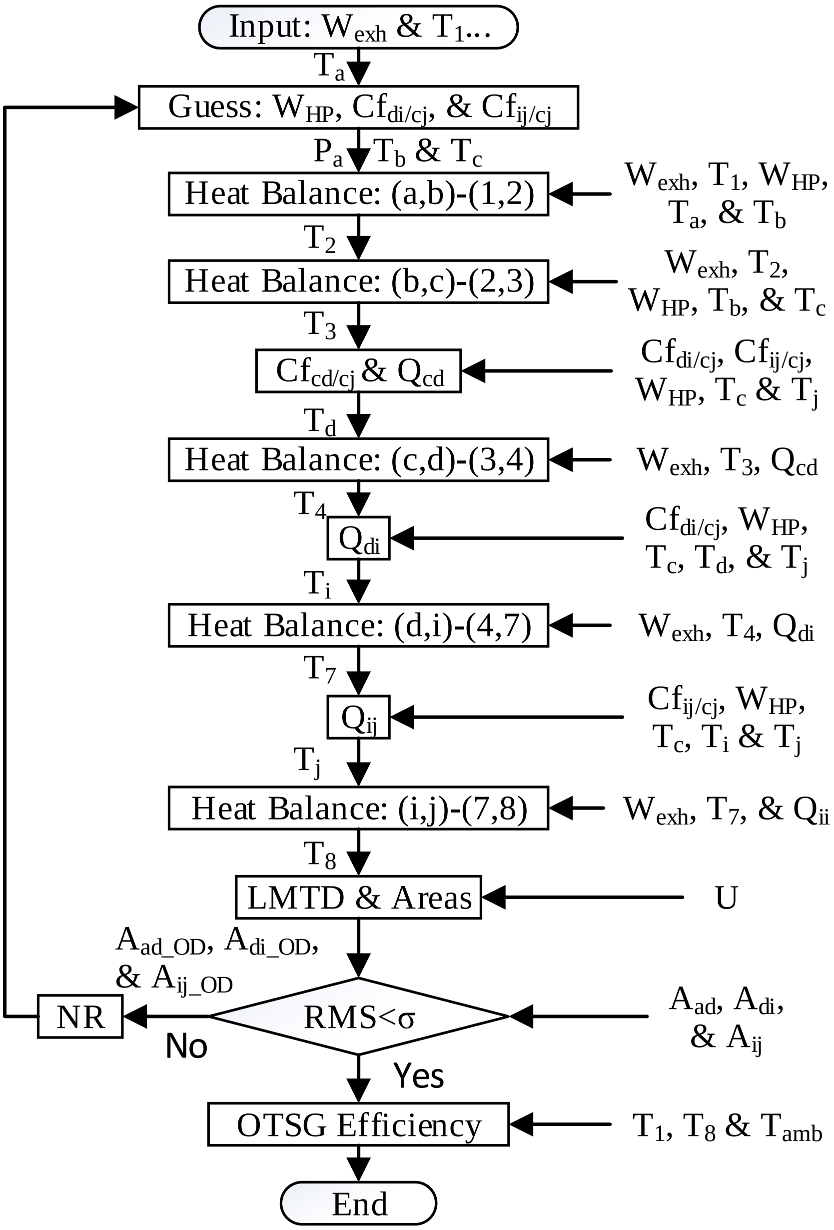

Figure 3-15 OTSG OD Performance Calculation with Single-pressure.

3.4.5.4 Off-design Performance Calculation Algorithm with Single-pressure

Figure 3-15 illustrates the calculation flowchart of the OD performance calculation of a parallel dual-pressure OTSG operated at a single pressure condition with detailed description given as follows:

(1) *The initial values of the three variables W_{HP}, $Cf_{di/cj}$, and $Cf_{ij/cj}$ take their values at DP point to start the calculation.*

(2) *Sections (a–b–c–d) and (1–2–3–4)*

The OTSG HP steam temperature T_a is decided by Eq. (3-101) and steam pressure is decided by Eq. (3-102). Once the steam pressure is known, the saturation temperature at points b, and c can be calculated. Based on the heat balance between the hot side (1–2) and cold side (a–b), temperature T_2 can be obtained by Eq. (3-82). Following the same procedure, temperature T_3 can be determined.

Since the OTSG inlet feed water temperature is given, the heat Q_{cj} needed for the HP economizer can be calculated by T_c, T_j, and W_{HP}. Hence, the Q_{cd} can be obtained by Eq. (3-86). Then, T_d, and T_4 are determined in the same way as that in the DP performance calculation.

(3) *Sections (d–i) and (4–7)*

The point 5, 6, m, n could be ignored as the LP does not have flow at this condition. Q_{di} could be obtained by Q_{cj} and guessed value of $Cf_{di/cj}$. Then, T_i can be determined in the same way as that in DP calculation. In addition, T_7 can be obtained based on the heat balance between the hot side (4-7) and cold side (d-i).

(4) *Sections (i–j) and (7–8)*

Q_{ij} can be obtained by using Q_{cj} and guessed $Cf_{ij/cj}$. Then, the stack temperature T_8 can be calculated by Eq. (3-97).

(5) *Heat Transfer Areas*

At the end of the above calculations, the heat transfer areas (i.e. A_{ad_OD}, A_{di_OD}, A_{ij_OD}) can be calculated.

(6) *Iteration Errors, Convergence Criteria and Iterations*

Following the above calculations, the three OD errors ΔY_k (Section 3.4.5.3) and the corresponding RMS can be calculated by Eq. (3-88). If the RMS is less than the threshold, the OD calculation finishes and the OTSG efficiency will be obtained by Eq. (3-85). Otherwise, the three iteration variables will be updated by Eq. (3-89) and the calculation will be repeated from Step (2) following the Newton Raphson method.

3.5 OTSG Performance Diagnosis Model

3.5.1 Cleanliness Factor of OTSG

For the utility industry, Cleanliness Factor (CF) defined by Eq. (3-104) is widely used for heat exchangers to represent the effect of fouling resistance on the overall heat transfer coefficient [98].

$$CF = \frac{U_F}{U_C} \tag{3-104}$$

where U_C and U_F are the overall heat transfer coefficients under clean and fouling state respectively. In other words, the Cleanliness Factor is used as the health parameter of OTSG and its variation represents the fouling of OTSG. As fouling is sensitive to temperature, different CF may be used for different sections of OTSG. In this study, three CF are applied to sections (a–d), (d–j), and (e–h), respectively (Figure 3-12).

3.5.2 Gas Path Analysis

3.5.2.1 Linear Gas Path Analysis

In this study, the Gas Path Analysis (GPA) method by Escher and Singh [31] has been extended to the gas path diagnostics of parallel dual-pressure OTSG, and the details of the method are described below.

It is assumed that the measurable performance parameters $\vec{z}$ of an OTSG are a thermodynamic function of the health parameters $\vec{x}$ (i.e. CF) of the OTSG represented by Eq. (3-105):

$$\vec{z} = h(\vec{x}) \tag{3-105}$$

where h is a nonlinear vector-valued function.

It is worth mentioning that the number of measurement parameters should be equal to or greater than the number of health parameters to ensure a unique solution of the health parameters [184]. A Taylor series expansion may be applied to Eq. (3-105) at a nominal operating point for diagnostic analysis represented by subscript “0” and the expansion may be shown by Eq. (3-106):

$$\vec{z} = h(\vec{x}_0) + \left.\frac{\partial h(\vec{x})}{\partial \vec{x}}\right|_0 (\vec{x} - \vec{x}_0) + o[(\vec{x} - \vec{x}_0)^1] \tag{3-106}$$

where $o[(\vec{x} - \vec{x}_0)^1]$ is a higher order term that can be ignored, resulting in Eqs. (3-107) or (3-108):

$$\vec{z} = \vec{z}_0 + \left.\frac{\partial \vec{z}}{\partial \vec{x}}\right|_0 (\vec{x} - \vec{x}_0) \tag{3-107}$$

$$\Delta\vec{z} = H \cdot \Delta\vec{x} \tag{3-108}$$

Here, $\Delta\vec{z}$ is the measurement deviation vector, $\Delta\vec{x}$ is the health parameter deviation vector and H is the influence coefficient matrix (ICM); they are represented by Eq. (3-109) to Eq. (3-111) respectively.

$$\Delta\vec{z} = \vec{z} - \vec{z}_0 = \begin{pmatrix} \Delta z_1 \\ \Delta z_2 \\ \cdots \\ \Delta z_M \end{pmatrix} \tag{3-109}$$

$$\Delta\vec{x} = \vec{x} - \vec{x}_0 = \begin{pmatrix} \Delta x \\ \Delta x_2 \\ \cdots \\ \Delta x_N \end{pmatrix} \tag{3-110}$$

$$H = \frac{\partial \vec{z}}{\partial \vec{x}}\bigg|_0 = \begin{pmatrix} \frac{\partial h_1(\vec{x})}{\partial x_1} & \cdots & \frac{\partial h_1(\vec{x})}{\partial x_N} \\ \vdots & \ddots & \vdots \\ \frac{\partial h_M(\vec{x})}{\partial x_1} & \cdots & \frac{\partial h_M(\vec{x})}{\partial x_N} \end{pmatrix} \quad \textbf{(3-111)}$$

where M is the number of measurements and N is the number of health parameters.

If H is invertible, the deviation of the health parameters $\Delta\vec{x}$ can be represented by Eq. (3-112):

$$\Delta\vec{x} = H^{-1}\Delta\vec{z} \quad \textbf{(3-112)}$$

where H^{-1} is called a fault coefficient matrix (FCM). If $M \neq N$, H is not a square matrix, so a pseudoinverse matrix of H has to be obtained by either Eq. (3-113) or (3-114):

$$H^{\#} = (H^T H)^{-1} H^T, \quad when\ M > N \quad \textbf{(3-113)}$$

$$H^{\#} = H^T (H H^T)^{-1}, \quad when\ M < N \quad \textbf{(3-114)}$$

3.5.2.2 Nonlinear Gas Path Analysis based on Newton-Rapson Method

The above linear approach may provide good solutions if the linear OTSG model (Eq. (3-112)) is a good representation of OTSG performance behaviour around the normal operating point. However, the prediction errors of the linear GPA can be significant if the OTSG performance is strongly nonlinear. Such a problem can be mitigated by using a Non-linear GPA [5,185] where an iterative process is applied as shown in Figure 3-16 using the Newton–Raphson method [31]. During the iteration process, $\Delta\vec{x}$ is updated by Eq. (3-115) until the iteration is converged.

$$\vec{x}_{m+1} = \vec{x}_m + \omega \cdot \Delta\vec{x} \quad \textbf{(3-115)}$$

where $\vec{x}_m$ and $\vec{x}_{m+1}$ are the health parameter vectors for m and $m+1$ iterative step respectively, ω is the under-relaxation factor taking a value between zero and one for improving the convergence of the iterations.

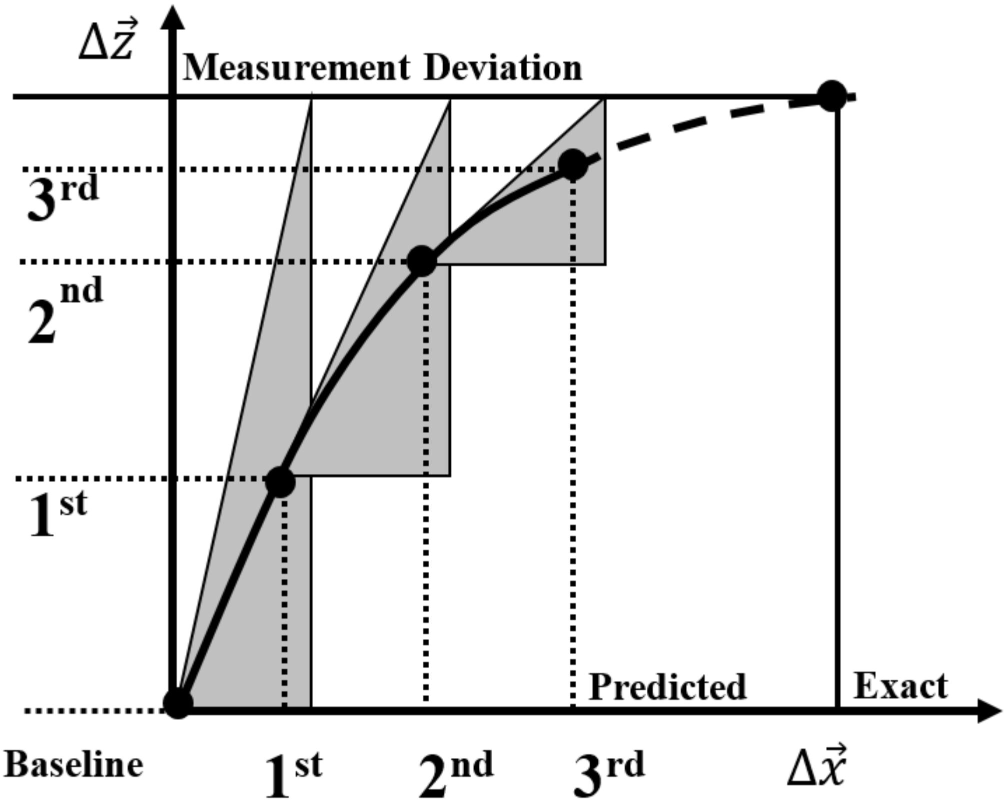

Figure 3-16 Nonlinear Gas Path Analysis based on Newton-Rapson Method [31]**.**

The Root Mean Square (RMS) of the difference Cleanliness Factors at consecutive iterative steps is used as the convergence criteria of the iterations represented by Eq. (3-116). Convergence may be declared if the RMS is lower than a threshold σ (1E-05 is used in this study).

$$RMS = \sqrt{\left[\sum_{i=1}^{N}\left(\frac{\vec{x}_{i,m+1} - \vec{x}_{i,m}}{\vec{x}_{i,m}}\right)^2\right]/N} < \sigma \tag{3-116}$$

The estimation error for each CF is defined as follows, where Eq. (3-117) represents the absolute relative difference between the predicted and implanted Cleanliness Factors:

$$\gamma_i = \left|\frac{x_i^{True} - x_i^{Predict}}{x_i^{True}}\right| \cdot 100\% \tag{3-117}$$

where γ_i is the estimation error of the ith CF.

The average prediction error $\bar{\varepsilon}$ is defined by Eq. (3-118) for multiple cases:

$$\bar{\varepsilon}_i = \left(\sum_{j=0}^{a} \gamma_i^j\right)/K \tag{3-118}$$

where $\bar{\varepsilon}_i$ represents the average prediction error for the ith CF and K is the total number of diagnostic cases.

The prediction error, ϕ, for ith measurement parameter is defined as follows:

$$\phi_i = \left|\frac{\bar{Z}_i - Z_i}{\bar{Z}_i}\right| \cdot 100\% \tag{3-119}$$

where $\bar{Z}_i$ is the measured parameter, and Z_i is the simulated parameter.

The average prediction error, $\bar{\phi}$, for ith measurement parameters of multiple operating points is defined as follows.

$$\bar{\phi}_i = \frac{1}{a}\sum_{j=1}^{a} \phi_i \tag{3-120}$$

3.5.3 Measurement Noise

In real-world, measurement noise for field data is inevitable, and the measurement noise will have a negative impact on diagnostic predictions. It is necessary to conduct a diagnostic test with and without preprocessing noisy measurements to understand the effect of noise on the diagnostic results. As shown in Table 3-5, in the Gaussian-type distribution, noise is generated randomly, with the maximum noise level suggested by [186]. The noise is combined with clean data to obtain the noisy measurement samples for testing the effect of noise on the diagnostic system. To reduce the measurement noise, multiple measurement samples at the same OTSG operating conditions may be collected, and the following algorithm [187,188] may be used.

Table 3-5 Measurement of Noise Magnitude [186].

Measurement	Range	Typical Error
Pressure	0.204–3.06 atm	0.50%
	0.544–1.30 atm	±0.5% or 0.125 atm, whichever is greater
Temperature	–65–290 ℃	±3.3
	290–1000 ℃	$\pm\sqrt{2.5^2 + (0.0075 \times T)^2}$
	1000–1300 ℃	$\pm\sqrt{3.5^2 + (0.0075 \times T)^2}$
Fuel Flow	Up to 250 kg/h	41.5 kg/h
	Up to 450 kg/h	34.3 kg/h
	Up to 900 kg/h	29.4 kg/h
	Up to 1360 kg/h	23.7 kg/h
	Up to 1815 kg/h	20.8 kg/h
	Up to 2270 kg/h	23.0 kg/h
	Up to 2725 kg/h	25.9 kg/h
	Up to 3630 kg/h	36.2 kg/h
	Up to 5450 kg/h	63.4 kg/h
	Up to 12260 kg/h	142.7 kg/h

3.5.3.1 Average Filter

The average filter is one of the most common filters to reduce the random noise that summed all the data and divided by the number of data set. The average for kth data could be obtained as follows:

$$\bar{z}_k = \frac{1}{k}(z_1 + \cdots + z_k) \tag{3-121}$$

where z_k meant the kth measurement data, $\bar{z}_k$ is meant the average of k datum.

The recursive expression is more widely used that considered adding new data to previous data set as follows.

$$\bar{z}_k = \frac{k-1}{k}\bar{z}_{k-1} + \frac{1}{k}z_k \tag{3-122}$$

3.6 Steam Turbine Performance Model

The schematic of the ST, and T-S diagram of the steam cycle are shown in Figure 3-17 and Figure 3-18 respectively. The HP steam flow expands to the LP steam pressure at the LP admission point (point r in Figure 3-18). Then, the HP steam (point r) will be mixed with the LP steam (point e) to obtain a mixed state (point s) that the detailed algorithm is referred to [12]. The mixed steam flow will expand at the ST LP section, and the exhaust steam will pass to the condenser.

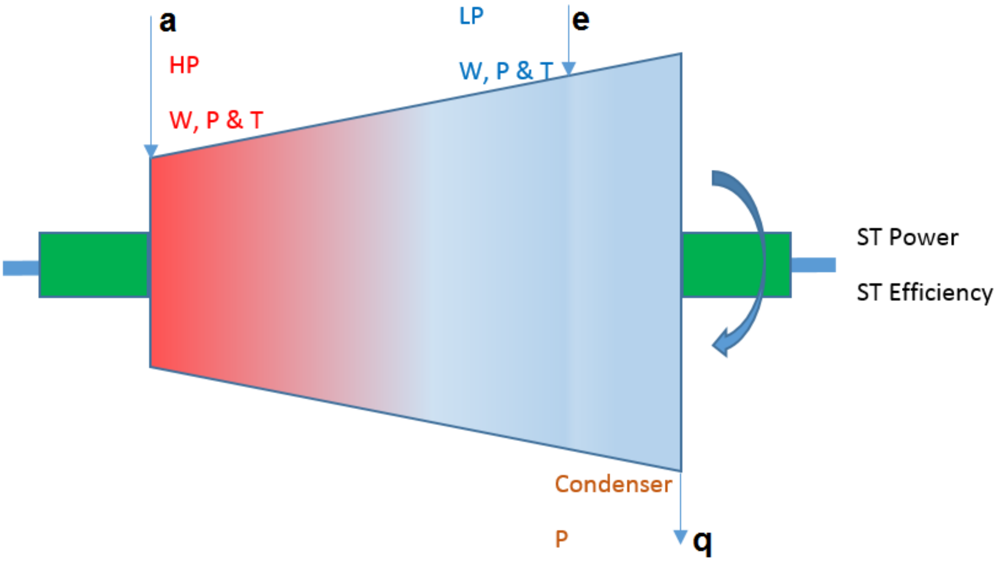

Figure 3-17 Steam Turbine Schematic.

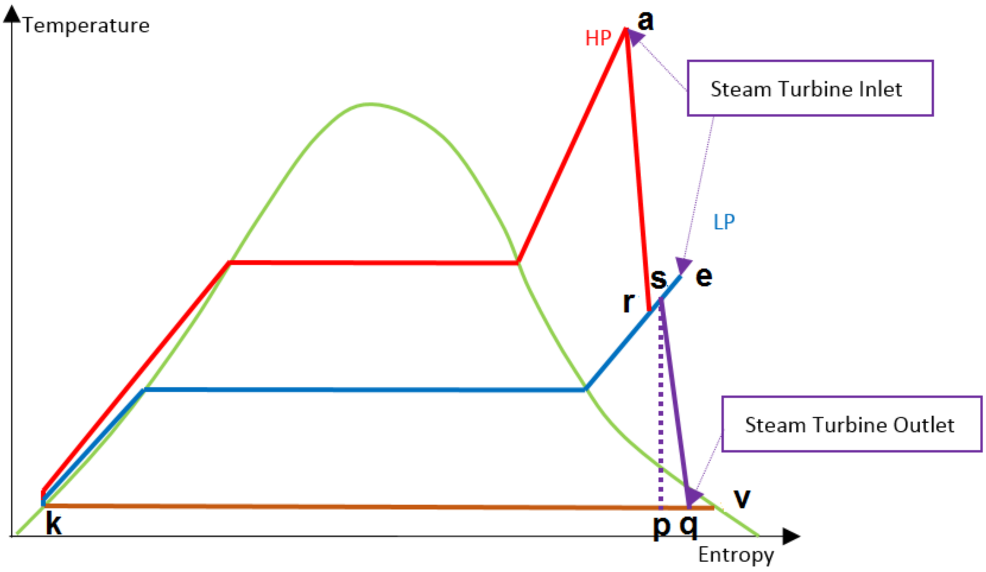

Figure 3-18 T-S Diagram of Ideal and Actual Steam Cycle.

For convenience, the ST is divided into two parts, the HP section and LP section. It is assumed the isentropic efficiency is constant for stages with pure steam and no apparent change in isentropic efficiency before the final stage of the ST even under different operating conditions [14], hence is assumed the isentropic efficiency for the HP section is constant. The LP polytrophic efficiency under dry conditions, $\eta_{ST,pol,dry}$, may also be assumed as constant [14]. Then, the LP isentropic efficiency may be obtained through iteration as described below.

For the LP region, the actual polytrophic efficiency for wet conditions, $\eta_{ST,pol}$, can be obtained by assuming the x_{out} [14].

$$\eta_{ST,pol} = \eta_{ST,pol,dry} - \frac{(1 - x_{in}) - (1 - x_{out})}{2} \tag{3-123}$$

where x_{in} and x_{out} are inlet and outlet steam contents of the steam respectively.

Then, the ST isentropic efficiency, $\eta_{ST,is}$, can be found using Eq. (3-124) [14].

$$\eta_{ST,is} = \frac{1 - \left(\frac{P_{out}}{P_{in}}\right)^{\frac{x_{out}-1}{x_{out}}\eta_{pol}}}{1 - \left(\frac{P_{out}}{P_{in}}\right)^{\frac{x_{out}-1}{x_{out}}}} \tag{3-124}$$

The mixed steam (point s) properties are known, and the entropy for the exhaust steam (point p) is the same as the mixed steam. Thus, the isentropic exhaust steam quality x_p can be found easily from Eq. (3-125):

$$x_p = \frac{S_p - S_k}{S_v - S_k} \tag{3-125}$$

The isentropic enthalpy of exhaust gas could be calculated as follows:

$$h_p = x_p \cdot (h_v - h_k) + h_k \tag{3-126}$$

The actual enthalpy is found using Eq. (3-127).

$$h_q = h_p + (1 - \eta_{ST,is})(h_s - h_p) \tag{3-127}$$

Hence, the actual steam quality, x_q, can be calculated as follows:

$$x_q = \frac{h_q - h_k}{h_v - h_k} \quad \textbf{(3-128)}$$

As x_{out} is assumed for Eq. (3-123), the x_q should close to x_{out}, within a specified threshold to stop the iteration process. After the iteration has converged, the x_q can be applied to the following calculation.

3.6.1 Steam Turbine Power Output

The ST power output for the HP and LP sections can be determined using Eqs. (3-129) and (3-130) respectively. These consider the mechanical efficiency, η_m:

$$PO_{ST,HP} = \eta_m \cdot W_{HP} \cdot (h_a - h_r) \quad \textbf{(3-129)}$$

$$PO_{ST,LP} = \eta_m \cdot (W_{HP} + W_{LP}) \cdot (h_s - h_q) \quad \textbf{(3-130)}$$

3.6.2 Steam Turbine Thermal Efficiency

The ST thermal efficiency can be calculated as follows.

$$\eta_{th} = \frac{PO_{ST,HP} + PO_{ST,LP}}{W_{HP} \cdot (h_a - h_k) + W_{LP} \cdot (h_e - h_k)} \quad \textbf{(3-131)}$$

3.7 Economic Model for CCGT Operation

The economic assessment is quantified by the spark spread (SS) that includes four parts (i.e. Maintenance and staff cost, fuel cost, emission cost, income from selling electricity). The spark spread could be considered as a gross economic margin of power generation [15]. This study is focused on an existing power plant and aims to evaluate CCGT economics for daily operation. Hence, the capital cost, and time related economic parameters (i.e. Discounted Cash Flow (DCF) and Net Present Value (NPV)) are not considered. It is necessary to mention that each operation point is set and maintained for half an hour as that is the fiscal period for electricity pricing at Isle of Man [15].

The power plant being considered needs to cover the power demand of the Isle of Man. Meanwhile, there is an interconnecting electricity cable of capacity 45 MVA between the UK and Isle of Man. It all that follows, the interconnector electricity cable will be termed simply cable. The electricity power demand of the island can be met by the combination of local CCGT power plant and cable. Figure 3-19 showed the cable power PO_{cable} could satisfy the island demand DM_{island} independently from about 23:30 to 07:00 the following morning [189]. No middle price difference will be considered in this study when the power plant brought the electricity from cable to satisfy the island demand. The cable power with respect to demand allow for export and import of electrical power, respectively through the cable.

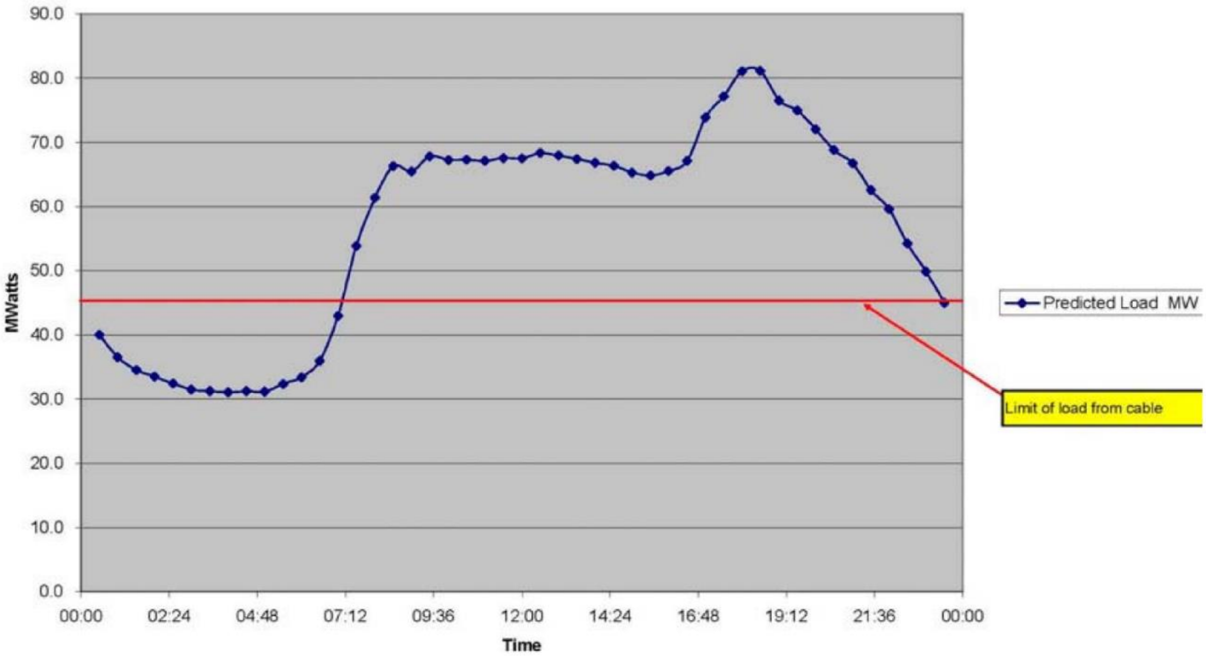

Figure 3-19 Typical Daily Load Profile for Isle of Man, January 2005 [189]**.**

The co-operation between MU power plant and UK grid is a pre-signed contract which assumes the cable is always able to supply a maximum of 45 MVA electricity to the island when the contract is decided in advance. For example, if the island power demand is predicted by the power plant trading team as 60 MW, and the power plant has the capacity to generate 22 MW more power. Meanwhile, the UK cable has the electricity demand to import 20 MW from the MU power plant. Then, the power plant as least need to generate 15 MW to cover the island power demand (60 MW) through cable (45 MW) and generated power (15 MW). Meanwhile, the maximum allowed power generation is 80 MW that is the sum of the island (60 MW) and cable demand (20 MW).

The plant manager must decide how much power to generate at each specific condition. If the electricity price received is quite high, the power plant will produce 80 MW power output itself to help meet the maximum power demand. If the price is relatively low or engine health is poor, the power plant may limit itself to satisfying only the island's electricity demand. In extreme conditions, it may generate only 15 MW and the balance of island's demand will be satisfied by cable. Once the contract is agreed, the power plant must execute the contract for the following half hour as a financial punishment will be applied for default. At the MU power plant, the trading team predicts power demand and system selling price (SSP) with low prediction error but would welcome help in other factors relating to the most efficient and profitable use of plant when deciding the contract with the UK grid [190].

3.7.1 Maintenance and Staff Cost

In MU, the maintenance staffs are responsible for both GT and steam cycle, so staff costs are the same for both closed and open cycle operation. For maintenance cost, MC ($£/(Watt.h)$) referred to [116], and for the specific cost of power plant operation staff, SC ($£/s$), referred to [190]. The sum of maintenance and staff cost (MSC) can be summed as follows.

$$MSC = SC + MC \cdot PO_{CCGT} \cdot \frac{1}{3600} \tag{3-132}$$

where PO_{CCGT} is the power output from CCGT cycle ($Watt$). The coefficient at end of the formula is applied for transfer the unit to ($£/s$).

3.7.2 Fuel Cost

Fuel cost (FC) is one of the major expenditures for power plant operation after the plant has been built. For FC calculations, it is necessary to know the fuel flow rate, fuel price, and LHV. It assumed the gas price is a constant for each day and the unit is pence per therm. The FC can be expressed as follows.

$$FC = FF \cdot Pri_{FF} \cdot LHV \cdot \frac{1}{100 \times 10550558526} \tag{3-133}$$

where FF is the fuel mass flow rate (kg/s), Pri_{FF} is fuel price ($pence/therm$), LHV is low heat value (J/kg). The constant at the end of the formula is applied to transfer the FC to $£/s$.

3.7.3 Emission Cost

The emission tax is based on the state and trends of carbon pricing 2015 which is 28 $ per ton [191]. Based on a selected constant currency rate between the US dollar and the UK pound. For this project, the emission tax cost is taken as 0.0219 $£/kg$. The total amount of carbon dioxide emission cost (EC) is calculated by the emission module and multiplied by the tax as follows.

$$EC = W_{CO_2} \cdot Taxes \tag{3-134}$$

where W_{CO_2} is the amount of carbon dioxide produced by combustion (kg/s), $Taxes$ is the emission taxes ($£/kg$).

3.7.4 Income through Selling Electricity

The revenue income for power plant has two components; sale of electricity to the Isle of Man and sale to the UK through the cable. If the power generation is equal to the power demand of the island, then the only income is from the island. If the power generated is more than the power demand of the island, then extra income is generated by transmission through the cable. It is necessary to mention that the export of electricity through the cable must be within the terms of the contract otherwise the additional power generated will not generate additional income [190].

$$Income = SSP \cdot PO_{CCGT} \cdot \frac{1}{3600000} \tag{3-135}$$

where SSP is the system selling price ($£/(kW.h)$), PO_{CCGT} is the power output from CCGT cycle ($Watt$).

3.7.5 Spark Spread

The SS is the overall economic benefit from plant operation, the higher the income and the lower the cost, the greater the spark spread. The same power output may have a large difference in spark spread when the electricity price is changed substantially. The SS could be calculated as follows.

$$SS = (Income - MSC - FC - EC) \cdot OT \tag{3-136}$$

Positive SS means the income is more than the cost, which is to the benefit of the power plant. If spark spread is negative, it means the plant is operating at a loss and the revenues are not enough to support plant operations.

3.8 Optimiser

3.8.1 Genetic Algorithm

This study needs a multiple criteria optimiser for power plant optimisation, whose foundation is a single-criteria optimiser. Hence, both single and multiple criteria genetic algorithms have been developed for this project, based on open source literature [16]. The main difference between the two algorithms is the fitness calculation. The latter requires the ranking of all the population before the fitness calculation.

3.8.1.1 Single Criterion Genetic Algorithm

Single Criterion Genetic Algorithm (SCGA) could be useful to solve a single objective function with multiple input variables. The flowchart of the SCGA is shown in Figure 3-20; the generation process ceases when a pre-set maximum allowed generation step is achieved. The initial generation of a potential solution randomly generates a set of chromosome strings to represent real values. In biology, the allele information is represented by upper and lower case letters to indicate the dominant gene and recessive genes. Binary numbers can be applied to replace the capital and small letter for the allele by one and zero respectively.

A binary chromosome could including several bits where the bit relates to a single allele. Figure 3-21 indicates how a 10-bit binary chromosome could be associated with a real number between zero and ten [142]. The more bits that are defined for the specified real number filed, the higher the precision.

Three major GA operators (i.e. Selection, Crossover and Mutation) are applied in the search processes [192]. The Selection process selects the strings for the next generation. The Selection operator is based on the roulette wheel selection [192] which normalisation the objective value for all strings, cumulative the normalised objective value (CNOV), and generated a random value $\in [0,1]$ to locate the string with CNOV [192]. Figure 3-22 showed the CNOV for a total population size of five.

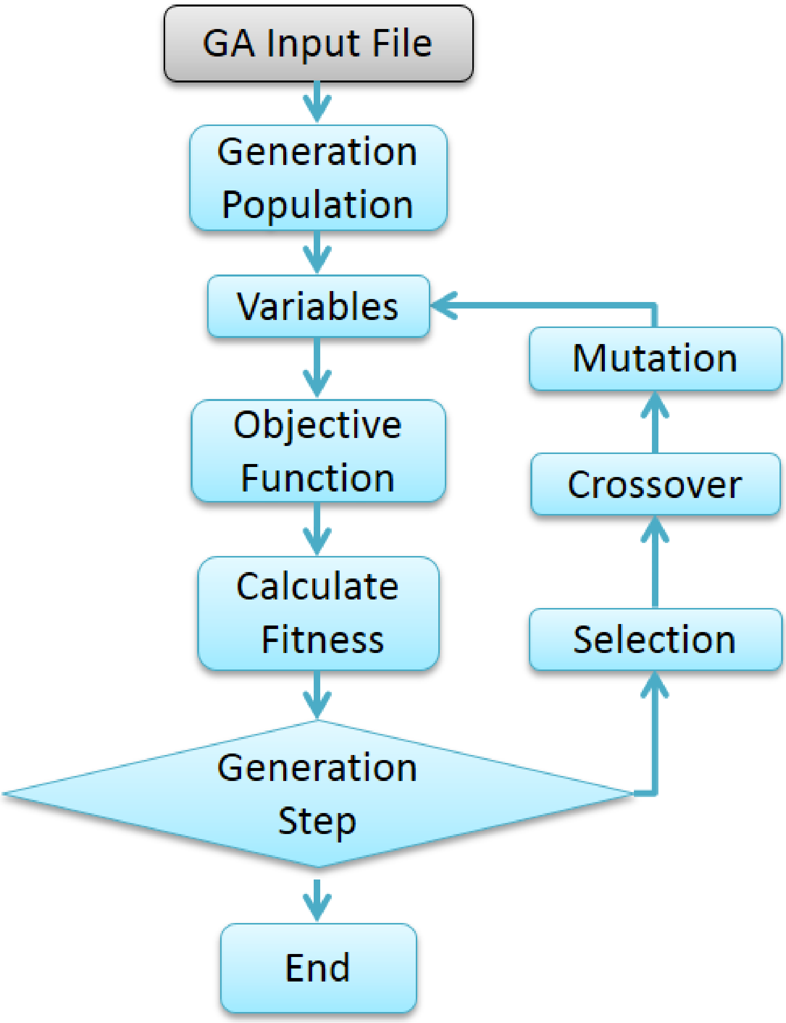

Figure 3-20 Single Criterion Genetic Algorithm Module Flowchart.

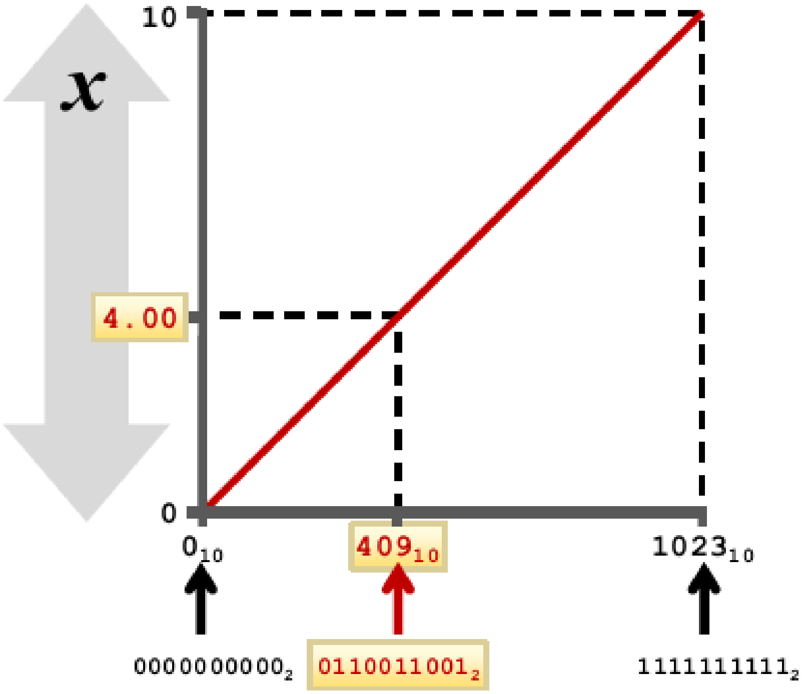

Figure 3-21 Relation between Real and Binary Numbers [142].

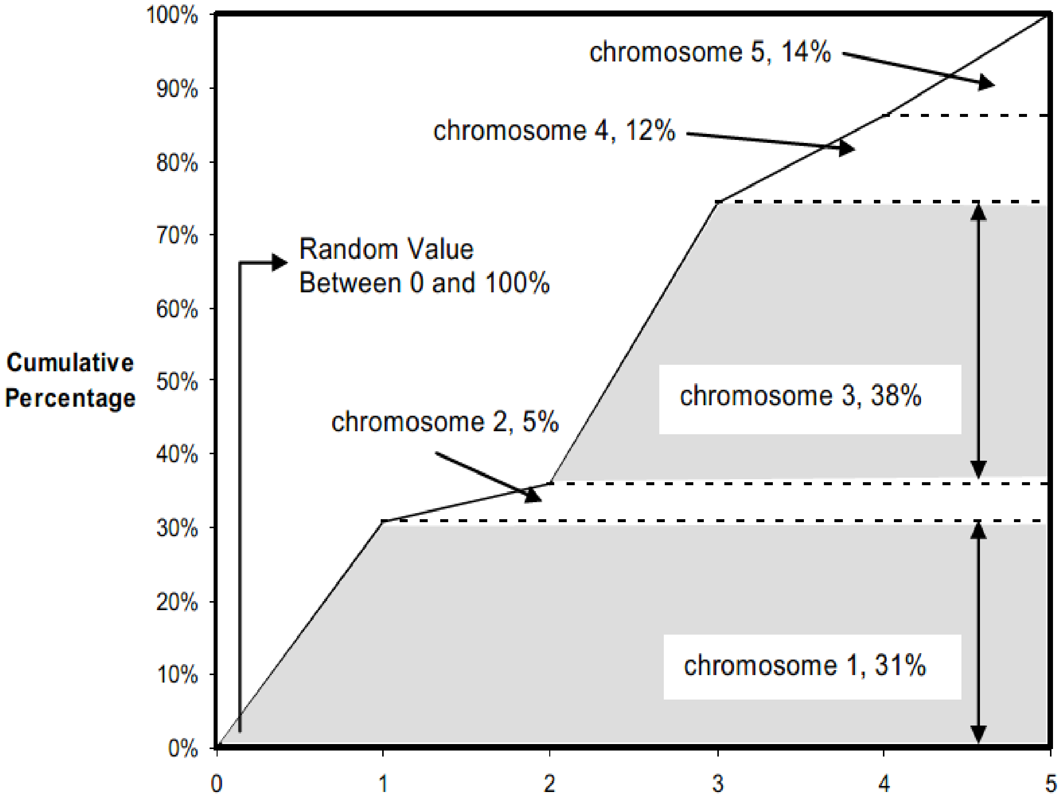

Figure 3-22 Cumulative Percentage for Roulette Wheel Selection [192].

Crossover is the random combination of selected pairs of strings to generate new strings for a new generation. The operator randomly selects the start point and end point along two parent strings and transfers the selected parts from one to the other. The relation between a gene and a binary chromosome is now evident. Table 3-6 shows two examples of parent strings. The green colour indicates the selected regions for crossover. These are swapped, and the remainders remain unchanged, and this process generates the offspring, see Table 3-7. The input variables are changed for each new population.

Table 3-6 Parent Strings.

Parent 1	1	0	1	1	0	1	0	0	0	1
Parent 2	1	1	1	0	0	0	1	0	1	1

Table 3-7 Offspring Strings.

Child 1	1	0	1	0	0	0	1	0	0	1
Child 2	1	1	1	1	0	1	0	0	0	1

Mutation is to randomly invert some of the bits in the selected parent string to generate new strings for the next generation. The mutation operator means the allele will be changed from a dominant gene to recessive gene or vice versa. In binary encoding, it means changing the bit from one to zero or vice versa. Table 3-8 indicates the how mutation happens in binary representation. The upper row is the parent, and the lower row is the offspring. The green coloured column indicates the bit randomly selected for mutation.

Table 3-8 String before and after Mutation.

Parent	0	1	1	0	1	0	0	0	1	0
Child	0	1	1	0	0	0	0	0	1	0

Mutation and crossover are the same in that generating offspring require parent(s). The main difference is that crossover requires two parents and creates two offspring, while mutation needs only one parent and produces one offspring.

GA fitness is defined to assess the quality of the individuals and usually an objective function (OF) representing the distance from the search target.

3.8.1.2 Multiple Criteria Genetic Algorithm

The SCGA can solve many problems; however, some issues cannot be combined into one objective equation. In such circumstances, the Multiple Criteria Genetic Algorithm (MCGA) should be used. It is possible to transfer multiple criteria to a single criterion by a weighted sum of the multiple objectives. However, combining all objectives into one function does not mean it will always be located on the Pareto Front [16]. It means that one objective of the solution obtained from the SCGA can be improved without compromising other objective functions. A Pareto Front represents not able to found a better solution that the one of the objectives progressing in the direction of a better solution and will not direct any of the objectives to a worse course.

The most widely used definition of Pareto Front is referred to [193] as follows:

“Pareto front is a set of nondominated solutions, being chosen as optimal, if no objective can be improved without sacrificing at least one other objective. On the other hand a solution x is referred to as dominated by another solution x if, and only if, x is equally good or better than x* with respect to all objectives.”*

By the definition of the Pareto Front (PF), the ranking method could be applied to calculate the fitness. Two widely used ranking methods, proposed by Goldberg (1989) [194] (left panel) and Fonseca & Fleming (1993) [195] (right panel), are shown in Figure 3-23 [16] respectively. The redeveloped MCGA is based on the second ranking method that ranks the population more easily. For example, both criterion one and criterion two are to be maximised in Figure 3-23 (right panel) that means optimisation direction is the top-right direction. If draw a vertical and horizontal dotted lines through the solid black spot in Figure 3-23 (right panel), then it is easy to find that five points are better than the solid black spot (top-right direction). It means five points is better than its objective values for both criteria, hence, the solid black spot ranked sixth. The points ranked 1 in Figure 3-23 represent the optimised results that is the PF.

Figure 3-24 shows the flowchart of MCGA that the Selection, Crossover, and Mutation operators that are the same as for SCGA and so are not further explained here.

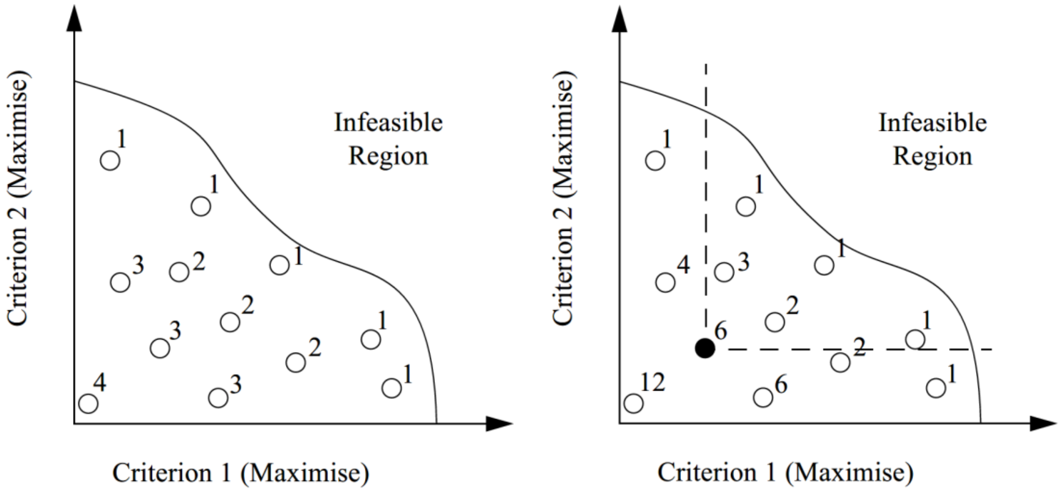

Figure 3-23 Ranking Method [16,194,195]**.**

The fitness (FN) can be calculated using the ranking as follows:

$$FN = (PS + 1 - RANK(i))^a \tag{3-137}$$

where PS is population size, $RANK(i)$ means the ranking for ith population string, a represents a control coefficient.

Fitness sharing (FN_s) is defined as follows to prevent the PF crowding into a small region.

$$FN_s = \frac{FN}{N_{Niche}} \tag{3-138}$$

where N_{Niche} is the number of the population in the specified region, which is termed “Niche”.

Todd (1997) [16] proposed a simple, but sufficient Niche calculation method, see Figure 3-25. The niche is defined by separating each criterion into a designated number of subsections using the maximum and minimum values of each criterion’s objective function value. The niche is a rectangle for two criteria and a cuboid for three criteria. The larger the niche defined, the higher the N_{Niche} and the smaller the FN_s.

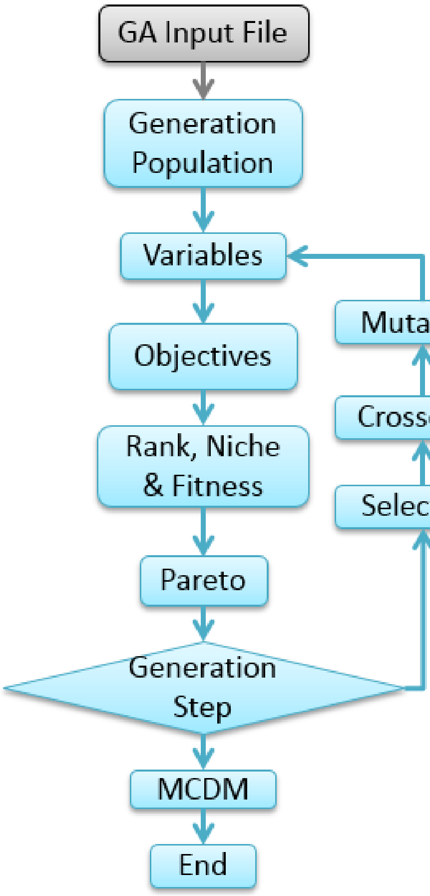

Figure 3-24 MCGA Module Flowchart.

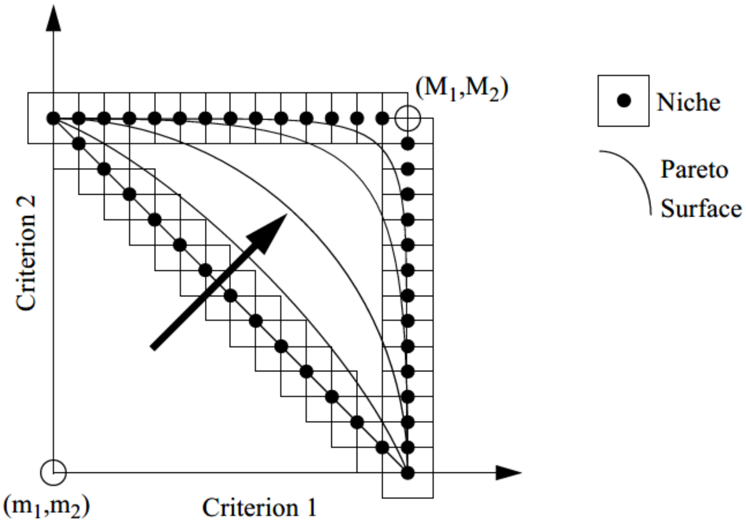

Figure 3-25 Niche by Project Pareto Front (PF) onto Criterion Axes [16].

The main difference between optimisation results between SCGA and MCGA is that the optimisation solution for SCGA is a single result and for MCGA is a PF. For MCGA, the solutions should disperse over the whole PF. Therefore, a memory list for PF needs to be added when comparing to SCGA.

3.9 Multi-Criteria Decision Making Model

As this study only have two criteria for optimisation, the TOPSIS could suggest the final solution from optimal results by MCGA. However, the original TOPSIS is adapted to eliminate the effect of the line shape, offer offering robust decision-making, and a more intuitive view of the impact of the weight matrix on the final decision.

3.9.1 Filter Undesired Results

In some specific situations, the decider could discard some results directly from the larger set of candidates.

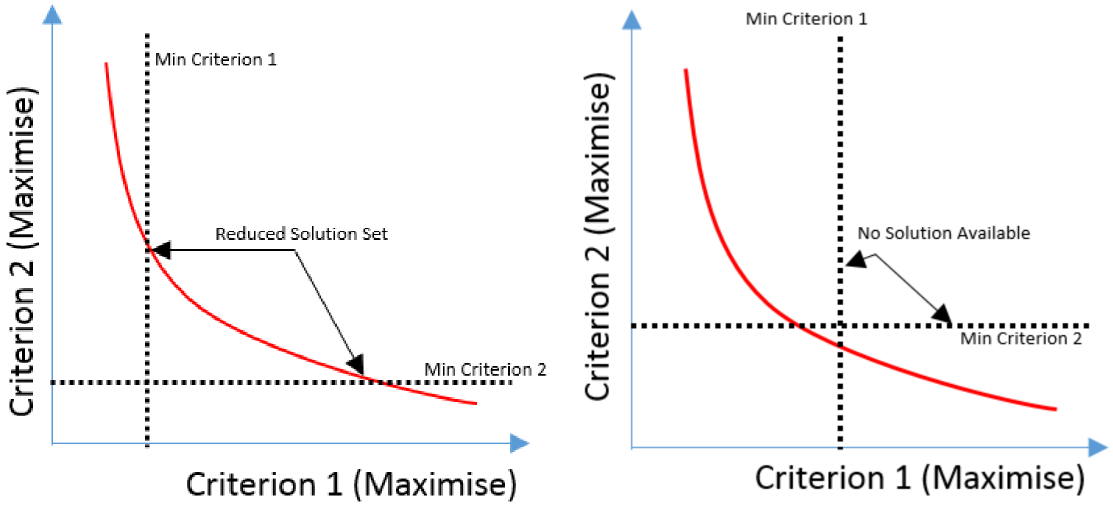

Figure 3-26 Criteria Constraints.

Consider the red line in Figure 3-26, this is the PF found by MCGA. The vertical black dotted line is the minimum acceptable value for criterion 1, and the horizontal black dotted line is the minimum acceptable value for criterion 2. Obviously, the potential solution is reduced to the set of solutions between the two arrows. It is worth to mentioning that the restricting bonds should be set at reasonable values. Alternatively, the PF may have no candidates that satisfy the constraint conditions. This is shown in the right panel of Figure 3-26. More information on reducing candidate sets is given in [196].

3.9.2 TOPSIS

The first step for TOPSIS is to normalise the decision matrix y_{ij}.

$$z_{ij} = \frac{y_{ij}}{\sqrt{\sum_{j=1}^{m} y_{ij}^2}} \tag{3-139}$$

$\forall\ i = 1, \dots, n$, and n is the total criteria of the optimization model. $\forall\ j = 1, \dots, m$ and m is the total number of PF candidates. z_{ij} is the normalised criteria value.

The user should decide the weight vector w for the different criteria:

$$w = [w_1, \dots, w_n] \tag{3-140}$$

Then, the weight vector is normalised as follows:

$$\overline{w}_i = \frac{w_i}{\sum_{i=1}^{n} w_i} \tag{3-141}$$

where $\overline{w}$ is normalised weight vector.

The weighted normalised decision matrix is obtained as follows:

$$V_{ij} = \overline{w}_i \cdot z_{ij} \tag{3-142}$$

Then, the distance between a result and the ideal best solution can be found as follows.

$$S_i^b = \sqrt{\sum_{j=1}^{m} (V_{ij} - V_i^b)^2} \tag{3-143}$$

where V_i^b is the ideal best solution for ith criteria, it could be defined by user.

Meanwhile, the distance between a solution and the ideal worst point could be obtained as follows.

$$S_i^w = \sqrt{\sum_{j=1}^{m} (V_{ij} - V_i^w)^2} \quad \textbf{(3-144)}$$

where V_i^w is the ideal worst solution for ith criteria, it could be defined by user.

Then, the relative distance can be calculated as follows:

$$D_j = \frac{S_i^w}{S_i^b + S_i^w} \quad \textbf{(3-145)}$$

The larger the value of D_j, the closer to the ideal best solution based on the preference weight vector.

3.9.3 Adapted TOPSIS

This study focuses on only two objectives optimisations; hence the PF tends to be a line, the shape of which will affect the final decision by TOPSIS. The TOPSIS is modified to address the oversensitive to line shape for offering robust decision-making. The first two steps of the adapted TOPSIS are the same as for TOPSIS; to normalise the decision matrix y_{ij} and weight matrix w as indicated in Eqs. (3-139) and (3-141). Figure 3-27 shows an example of a normalised PF consisting of five points. Then, the PF is ranked by the selected 1th objective which sorts from smallest to largest. The other objective will automatically rank from biggest to smallest.

The Table 3-9 could represent the last decision-making process. The distance between adjacent points can be obtained after ranking. The dimensionless distance is calculated and the cumulative distance obtained. If the $\overline{w}_i$ is [0.8, 0.2] for the two objectives, e.g. the normalised weight for the first objective is 0.8, and for the second objective 0.2. Clearly, the selection will be between point 4 and point 5, between the cumulative distances (0.75 and 1.0). The final selection is point 4, that 0.8 is closer to 0.75, see the last column of Table 3-9.

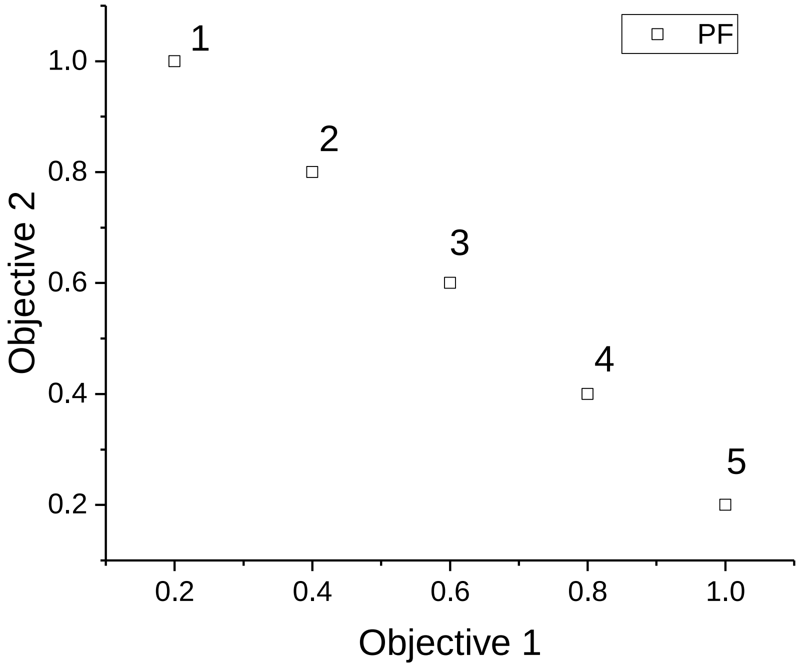

Figure 3-27 Example of Normalised PF.

Table 3-9 Example of Decision-Making.

PF	Objective 1	Objective 2	Distance between Adjacent Points	Dimensionless Distance (%)	Cumulative Distance (%)	Distance to Weight
1	0.2	1	0	0	0	0.8
2	0.4	0.8	0.282842712	0.25	0.25	0.55
3	0.6	0.6	0.282842712	0.25	0.5	0.3
4	0.8	0.4	0.282842712	0.25	0.75	0.05
5	1	0.2	0.282842712	0.25	1	0.2
Sum			1.13137085			

Through adapted TOSIS, the weighted factor will act on the curved line representing the PF, rather than outside the PF so that, the effect of line shape can be eliminated.

3.10 Power Plant Decision Support System

Research into power plant optimisation has a long history. Many optimisation studies have directly addressed how to decide the engine configuration and capacity for a new power plant [148–152]. There has also been an increasing amount of literature on optimising the design parameters of the steam cycle in a power plant [153]. Typically, in previous studies, the total power setting was fixed and thermodynamic, and thermoeconomic optimisation systems were applied to determine only the power distribution between different engine sets [197]. Historically, the research investigated the optimal maintenance schedule based on the GT hot section life consumption using thermoeconomic models. However, the GT hot section life consumption is typically based on DP power setting [171]. Nevertheless, the maintenance cost has been considered by previous research in the thermoeconomic model. However, the maintenance cost ($£/(MW.h)$) was related only to the power output and operating time [116]. Hence, the creep life consumption differences caused by ambient conditions and engine health state was not considered in the maintenance costs. The “clean” state of an engine occupies only a relative short period when comparing to the whole engine life, and GT creep life consumption increases substantially as the state of degradation worsens.

In contrast, the power plant considered in this study has the flexibility to decide its total power output in conditions where the GT power setting and ambient conditions fluctuate during the day. Additionally, the engine health state could be different among the power plant. Thus, it is necessary to develop a decision support framework to optimise the daily operation of the power plant, to decide the total power output and power split between different engine sets and considered both thermo-economics and GT hot section lifing.

3.10.1 CCGT Performance System

Figure 3-28 showed the schematic of a combined-cycle power plant that includes two dual-shaft GTs (GT6 & GT7), two parallel dual-pressure OTSGs (OTSG6 and OTSG7) and an ST (ST8). The GT6 and OTSG6 are parallel with GT7 and OTSG7. When the GT is shut down, the corresponding OTSG will also be shut down not having exhaust gas for energy recovery. The GT exhaust does not have a bypass route, the GT exhaust gas passes through the OTSG from bottom to top even when the OTSG has no feed water (dry-run). This situation typically happens when the GT is starting up and shutting down. The thermal shock (GT at a high power setting) from dry running could be used for OTSG fouling mitigation. However, considering OTSG lifing, the dry-run operation should be operated carefully to avoid unnecessary OTSG life consumption.

The control engineers set the power of the two GTs, and that could decide the whole CCGT performance. The higher the GT power setting, the higher the exhaust gas energy at the GT nozzle outlet for the same ambient conditions and engine health state. Then, the steam cycle performance will be decided automatically when the GT exhaust gas condition is known, see Section 3.4 and 3.6. Changing the GT power setting will cause a corresponding change in the whole CCGT performance. The individual power settings of the two GTs could be different, as determined by the state of health of the individual engines or other factors. Meanwhile, the operation engineer could decide whether to operate one or both GTs and the corresponding steam cycle. One GT and the corresponding OTSG may be shut down for maintenance or due to low power demand. The engine on duty may be called the base load engine set, and the other called the peak load engine set. It is assumed GT6 and OTSG6 is the base load engine set in this study.

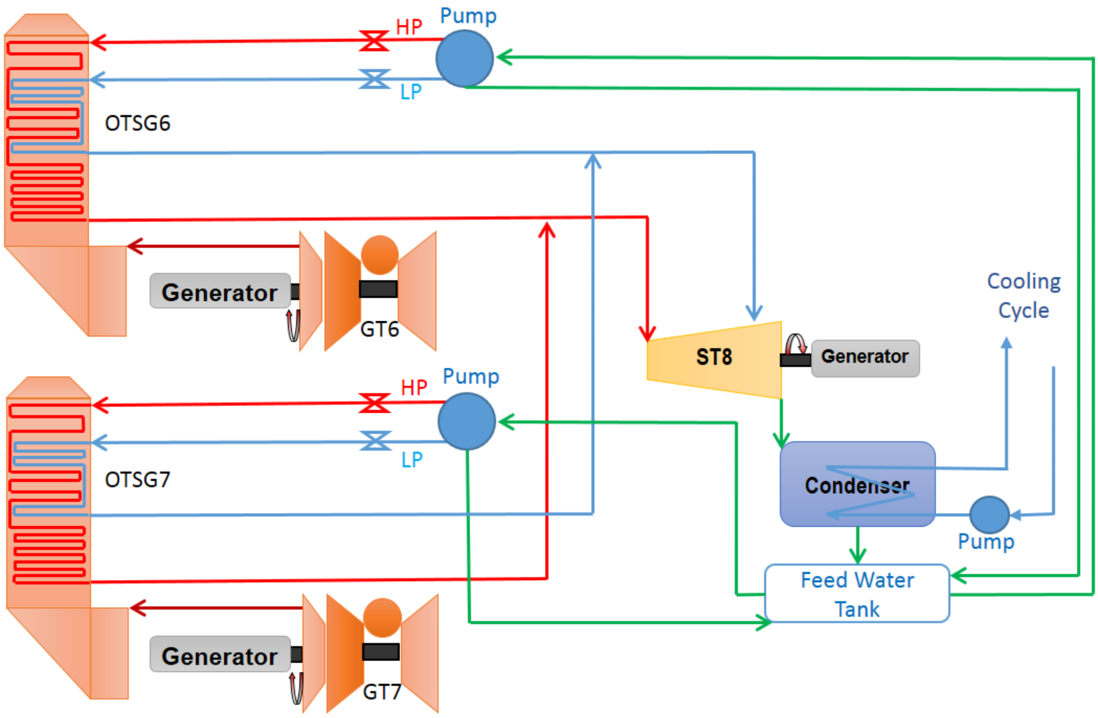

Figure 3-28 Power Plant Schematic.

3.10.2 Optimisation Variables

As mentioned in the previous section, the CCGT control includes the power setting for two GTs respectively. Meanwhile, the number of the GT in operation could be changed with time. Therefore, the variables for optimisation are:

- GT6 power setting
- GT7 power setting
- Number of GT in operation

With only one GT in service, the base load engine set is in operation, and the peak load engine set will be shut down with the GT power set to zero automatically. As mentioned above, the power plant is rarely operated at less than the 22 MW steady state condition. Hence, the boundaries for both GT power settings are between the rated power 32 MW and 22 MW.

As mentioned before, one engine is base load engine set, and the other is peak load engine set. Hence, the low cycle fatigue life consumption for two GTs differ from each other. Figure 3-29 showed the percentage reduction in GT hot section life due to low cycle fatigue interaction with Creep that effect of low cycle fatigue on GT hot section life is less than 15% based on eight-month real engine field data. It is obvious the effect of creep life on GT hot section life is dominant.

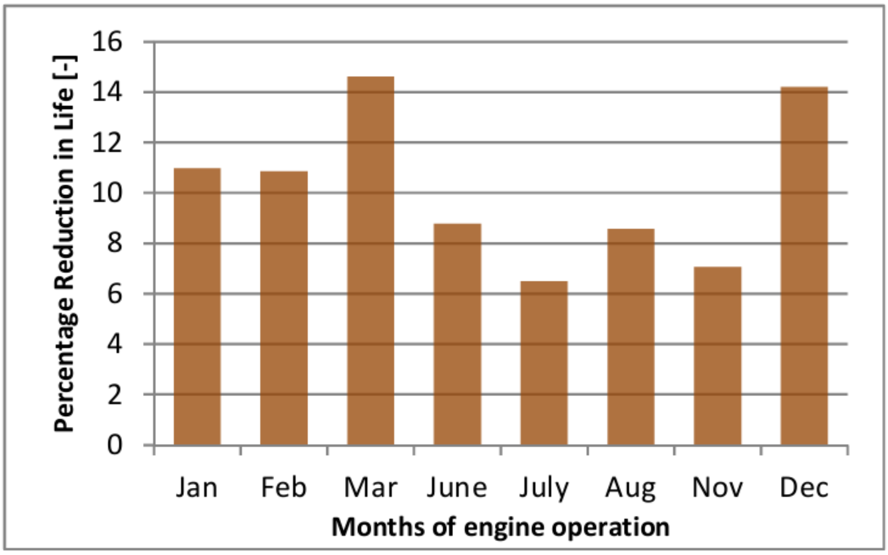

Figure 3-29 Percentage Reduction in Life due to Low Cycle Fatigue Interaction with Creep [198]**.**

3.10.3 Objective Function

The operation optimisation of CCGT power plant involved two objective functions; thermoeconomic and lifing respectively. Here, the thermoeconomic aspect concerns power plant operation and this study quantifies the results by applying spark spread as defined by Eq. (3-136). Thus, the first objective function of the optimisation is represented by the equivalent spark spread SS_{Eq} to represent the thermoeconomic aspect of the power plant according to:

$$SS_{Eq} = \frac{SS}{SS_{Ref}} \tag{3-146}$$

where SS_{Ref} is the dimensionless reference spark spread.

The equivalent creep life consumption factor LCF_{Eq}, representing the lifing consideration that is the second objective function is defined in a way that simultaneously combines the life consumptions of both engines.

$$LCF_{Eq} = \frac{1}{(LF_{GT6} + LF_{GT7}) \cdot LCF_{Ref}} \tag{3-147}$$

where LF_{GT6} and LF_{GT7} represent the life fractions of GT6 and GT7 respectively, as defined by Eq. (3-80), and LCF_{Ref} is the reference value of the life consumption factor.

3.10.4 Weighted Factor

The weighted factor is related to the two objective functions. The higher the relative weight of SS_{Eq} compared with LCF_{Eq} the higher the power setting at which the engine will be operated to obtain more income for the power plant, and this will consume more engine life.

3.10.5 Constraint and Penalty Function

In a real power plant, some constraint conditions need to be satisfied to maintain a safe operation, here these are:

- LP turbine inlet temperature (TET): the GT hot section life usage increases exponentially with HP TET. Hence, it is necessary to have a threshold limit to ensure a long operational life. However, there is no sensor available for TET at the power plant, and the control team uses the LP TET instead

- OTSG stack temperature: the stack temperature should be kept higher than the local dew point temperature to avoid exhaust gas condensation at the exhaust gas outlet which could cause low-temperature corrosion
- ST exhaust steam wetness: the higher the moisture, the greater the potential for last stage blade erosion
- Cable transmission capacity: the electrical equipment limits the maximum permitted power transmission for safety reason, but the transmission is also limited by demand and power supply capacity

3.10.6 Implementation of Decision Support for Optimisation System

Recently, there has been renewed interest in considering both thermoeconomic and lifing for power station daily operation. The electricity price, ambient conditions, and state of engine health could affect the power plant revenue and life consumption of the GT engines, even at the same total power output. Meanwhile, the total power demand for the island also fluctuates during each fiscal period in the day. It is necessary to develop a decision support platform that is able to suggest appropriate operating conditions based on preferences between thermoeconomic and lifing concerns for optimal power operation.

Based on the GT thermodynamic information, the GT HP turbine blade lifing can be found by life model, and GT emission results can also be calculated. GT exhaust information will pass to the steam cycle model to predict OTSG and ST performances. After the ST power is found, the spark spread can be obtained via the economic model. The grid cable transmission load can also be obtained through the CCGT power output and power demand. Hence, the two objective functions are known, and the four constraint parameters can be tested to decide whether a penalty will be applied to the objective functions or not.

The decision support framework architecture is shown in Figure 3-30 and covers the CCGT performance model (GT, OTSG, and ST), GT emission model, GT life model, economic model, optimisation model (MCGA), and MCDM model. The detailed algorithms for the models are presented in Chapter 3. Meanwhile, each sub-model uses module programs to guarantee expansibility and reliability. The green dotted box Figure 3-30 shows the interaction of the models for thermoeconomic and lifing calculations that cover the two objectives for MCGA.

The simulation will start with a randomly generated population of a specified number. Each population will represent three variables (GT6 Power, GT7 Power, number of GTs), and the variables used for simulating the thermoeconomic and lifing of CCGT power plant. After each population of the whole generation has proceeded the thermoeconomic and lifing calculation, the ranking of the population could be processed, and the PF for the current generation could be found. The next generation for MCGA will conduct by Selection, Mutation, and Crossover. The calculation process will be repeated until the total number of PF equal to the specified number. The whole PF will transfer to the MCDM model for decision-making. Then, the final operation point will be suggested based on the pre-defined weighting factor, and the detailed algorithm presented in Section 3.9.

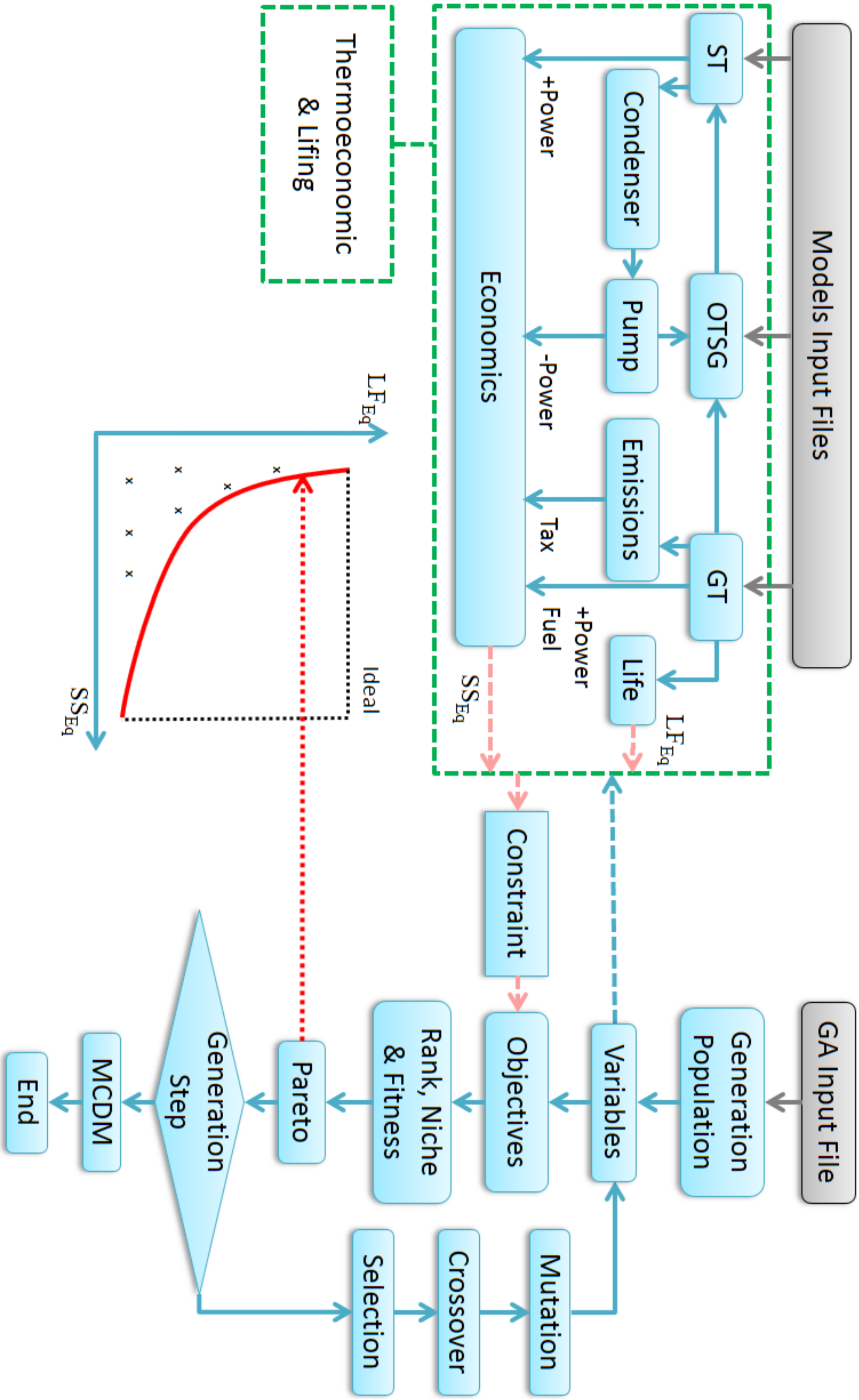

Figure 3-30 Architecture of Decision Support System.

4 Application, Results, and Analysis

4.1 OTSG Performance Simulation

The introduced performance simulation method has been applied to an OTSG installed in a CCGT power plant at Manx Utilities, Isle of Man in the United Kingdom. The power plant has the General Electric LM2500+ aero-derivative GT engine as the prime mover, providing exhaust gas to the OTSG for the generation of high pressure and high-temperature steam driving an ST for electricity generation.

4.1.1 OTSG Specification and Measurement

The boiler in concern is a dual-pressure OTSG manufactured by Innovative Steam Technologies (IST) shown in Figure 3-11 [175]. Table 4-1 shows relevant data [175,199] used as the DP performance specification as input for the OTSG DP performance calculation.

Table 4-1 OTSG DP Performance Specification [175,199]**.**

Parameter	Value	Unit
T_1	498.0	℃
W_{exh}	89.1	kg/s
T_{amb}	13.0	℃
T_a	484.0	℃
P_a	56.81	bar
PP_{HP}	16.0	℃
T_j	36.0	℃
T_e	258.0	℃
P_e	6.89	bar
PP_{LP}	21.0	℃
T_h	36.0	℃
$Cf_{di/cj}$	0.3886	-
$Cf_{ij/cj}$	0.3857	-

4.1.2 Design Point Performance Calculation and Validation

The OTSG DP performance was calculated following the flowchart showed in Figure 3-13. During the DP calculations, the two iteration variables ($Cf_{dm/di}$ and $Cf_{mn/di}$) are searched by Newton Raphson method to reduce the RMS error defined by Eq. (3-88). Table 4-2 shows the simulation results out of the DP performance calculation for the five measurement parameters compared with the data provided by IST and the plant operator [175,199,200]. Meanwhile, the relative error is also demonstrated in Table 4-2 showing that all the prediction errors are quite small, with the maximum error on T_8 being less than 0.8%. It indicates that the DP simulation model and results are satisfactory for the OTSG in concern. The obtained two iteration variables are also showed in Table 4-3.

Table 4-2 Results Comparison at DP [175,199,200]**.**

Parameter	Prediction	Measured Value	Errors (%)
W_{HP}	9.5809	9.58	0.009
W_{LP}	2.2403	2.25	0.431
T_8	119.07	120	0.772
A_{aj}	12500.0	12500	0.000
A_{eh}	3426.03	3426	0.000

Table 4-3 Iteration Variables for DP Performance Calculation.

Parameter	Initial Guess	After Convergence
$Cf_{dm/di}$	0.35	0.4960
$Cf_{mn/di}$	0.35	0.1903

4.1.3 Off-design Performance Simulation and Validation under Dual-pressure Operation

The OD performance was calculated following the flowchart showed in Figure 3-14 where a solution of six state variables are searched by the Newton Raphson method to satisfy the convergence criteria shown in Eq. (3-88). In the calculations, the total heat transfer areas A_{ad}, A_{di}, A_{ij}, and A_{eh} are unchanged at OD operating conditions, although the internal boundaries between the economizer, evaporator, and superheater in both the HP and LP circuits may change. Due to confidentiality reasons, only the range of the OD input parameters are given in Table 4-4.

Table 4-4 Range of Operating Conditions for 292 Off-Design (OD) Points.

Parameter	Unit	Range
T_1	℃	504.5 – 516.5
T_{amb}	℃	14.3 – 17.3
Ambient Pressure	bar	1.00 – 1.02
Relative Humidity	%	58.40 – 88.44
W_{exh}	kg/s	75.49 – 80.44
Gas Turbine Power	MW	26.44 – 29.39
T_j	℃	43.4 – 46.4
T_h	℃	43.4 – 46.4

In this study, 292 sets of OTSG measurements were chosen from three-day steady state OD operations of the plant for the model validation, where the exhaust gas flow rate W_{exh}, exhaust gas temperature T_1, ambient temperature T_{amb}, and feed water temperature varying during the operations. P_{a} and P_{e} are determined by Eq. (3-102) when mass flow rate and steam temperature are available. The desired HP steam temperature are kept by adjusting W_{HP} and W_{LP}. T_8 and T_e are determined for different W_{HP} and W_{LP} values during OD calculations. As the result of OD calculations, the satisfactory consistency between the test data and the simulations of W_{HP}, W_{LP}, P_{a}, P_{e}, T_8, and T_e are demonstrated in Figure 4-1 - Figure 4-3. The maximum average error defined by Eq. (3-103) for individual parameters is less than 1.5% as shown in Figure 4-4 demonstrating good prediction accuracy.

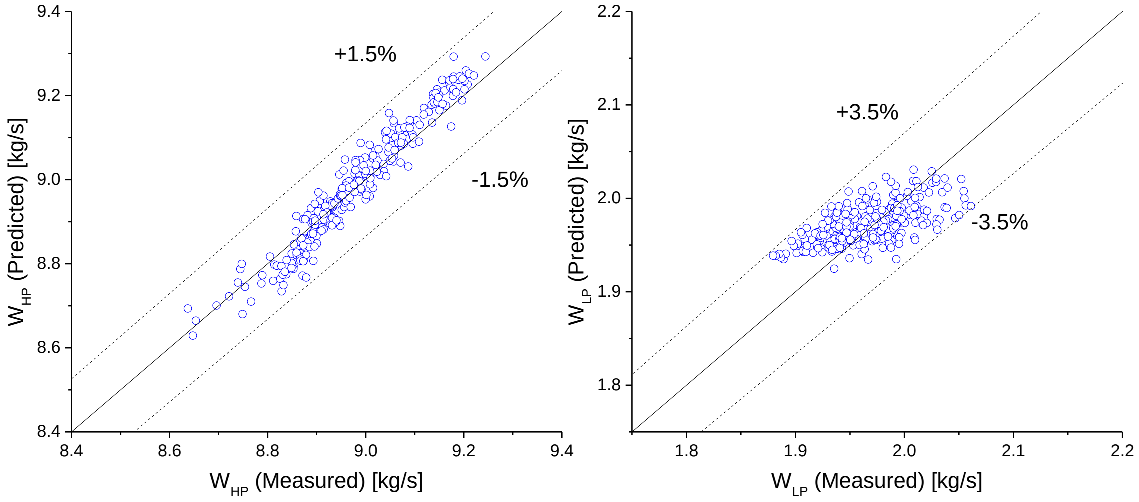

Figure 4-1 Comparison between Measured and Predicted Results (W_{HP} and W_{LP}).

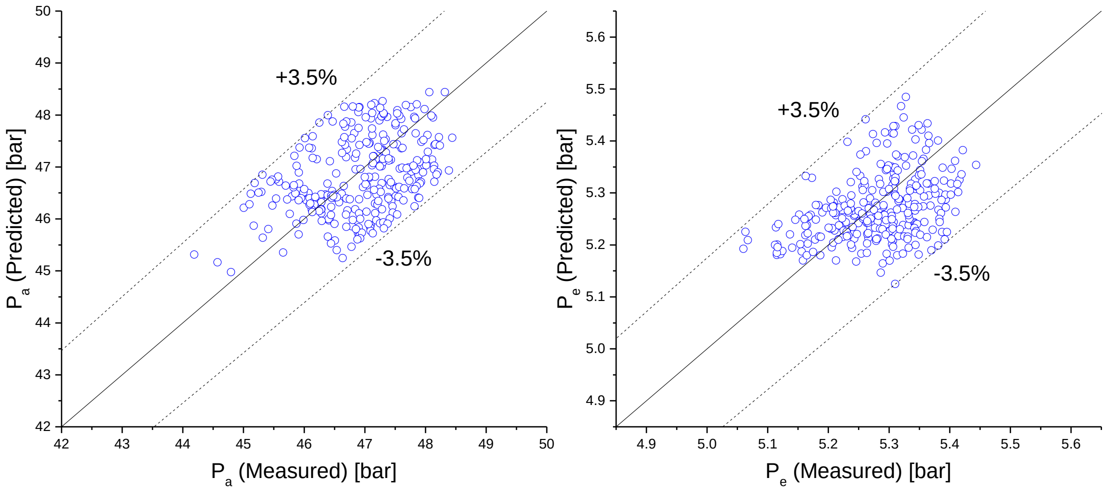

Figure 4-2 Comparison between Measured and Predicted Results (P_a and P_e).

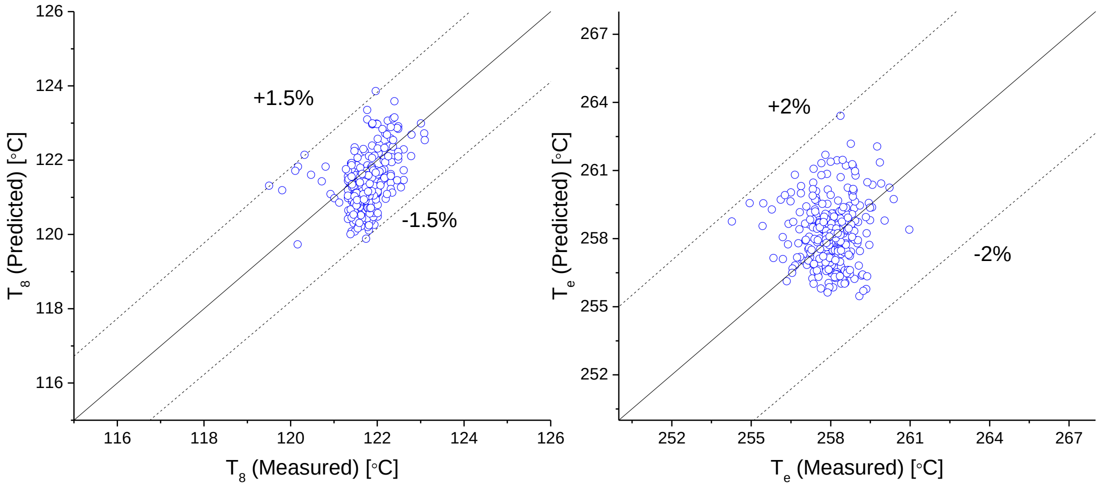

Figure 4-3 Comparison between Measured and Predicted Results (T_8 and T_e).

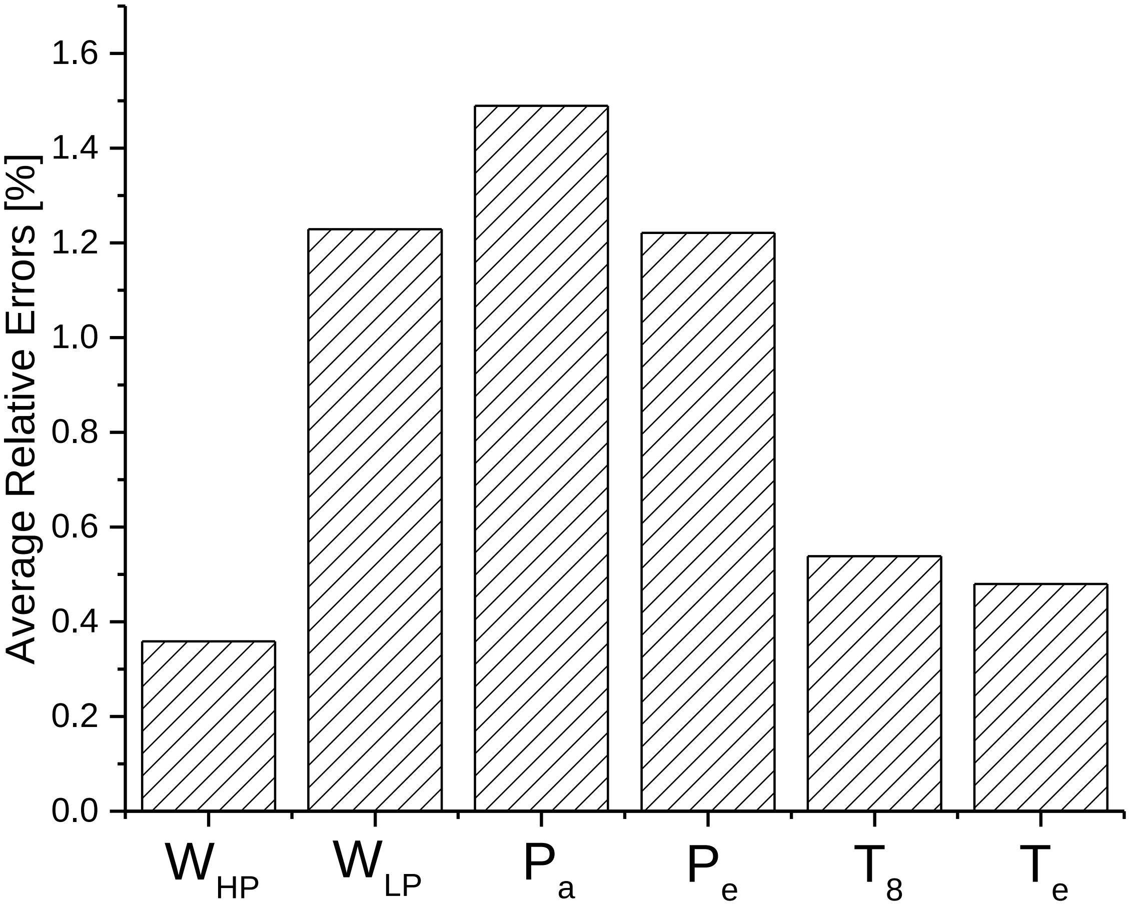

Figure 4-4 Average Relative Errors of 292 Test Points.

4.1.4 Off-design Performance Simulation and Validation under Single-pressure Operation

The OD performance was calculated following the flowchart showed in Figure 3-15 where a solution of three state variables is searched by the Newton Raphson method to satisfy the convergence criteria shown in Eq. (3-88). In the calculations, the total heat transfer areas A_{ad}, A_{di}, and A_{ij} are unchanged at OD operating conditions, although the internal boundaries between the economizer, evaporator, and superheater in the HP circuits may change. Due to confidentiality reasons, only the range of the OD input parameters are given in Table 4-5.

Table 4-5 Range of Operating Conditions for 13 OD Points.

Parameter	Unit	Range
T_1	℃	489.1 – 517.15

T_{ab}	℃	14.59 – 16.56
Ambient Pressure	bar	1.01 – 1.02
Relative Humidity	%	55.8 – 68.65
W_{exh}	kg/s	75.26 – 77.83
Gas Turbine Power	MW	22.04 – 25.10
T_j	℃	41.8 – 43.4

As mentioned before, the OTSG is rarely operated at the single pressure that will recover less heat from exhaust gas. In this study, 13 sets of OTSG measurements were chosen from one-day steady state OD operations of the plant for the model validation, where the gas flow rate W_{exh}, exhaust gas temperature T_1, ambient temperature T_{amb}, and feed water temperature varying during the operations. P_{a} is determined by Eq. (3-102) when mass flow rate and steam temperature are available. The desired HP steam temperature are kept by adjusting W_{HP}. T_8 is determined through the heat balance during OD calculations. As the result of OD calculations, the satisfactory consistency between the test data and the simulations of W_{HP}, P_{a}, T_8 is demonstrated in Figure 4-5-Figure 4-7. The maximum average error defined by Eq. (3-103) for individual parameters is less than 3.2% as shown in Figure 4-8 demonstrating good prediction accuracy.

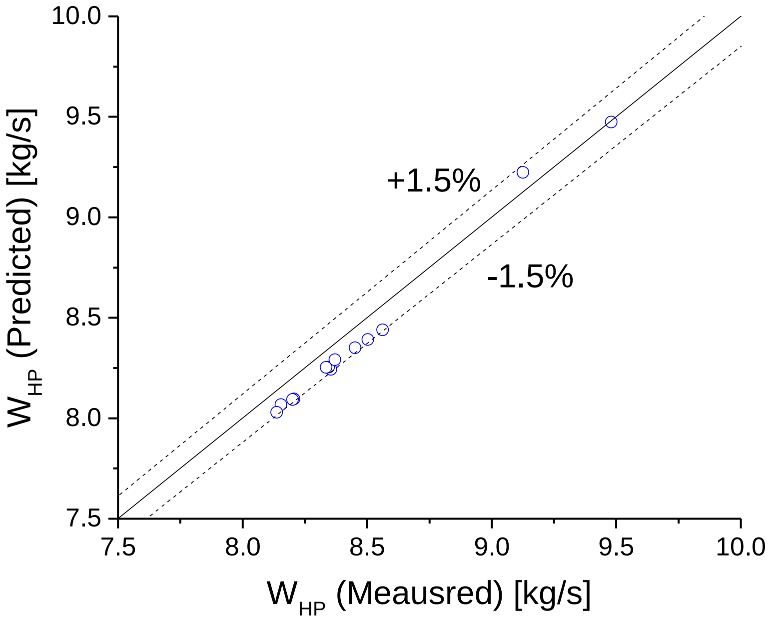

Figure 4-5 Comparison between Measured and Predicted Results (W_{HP}).

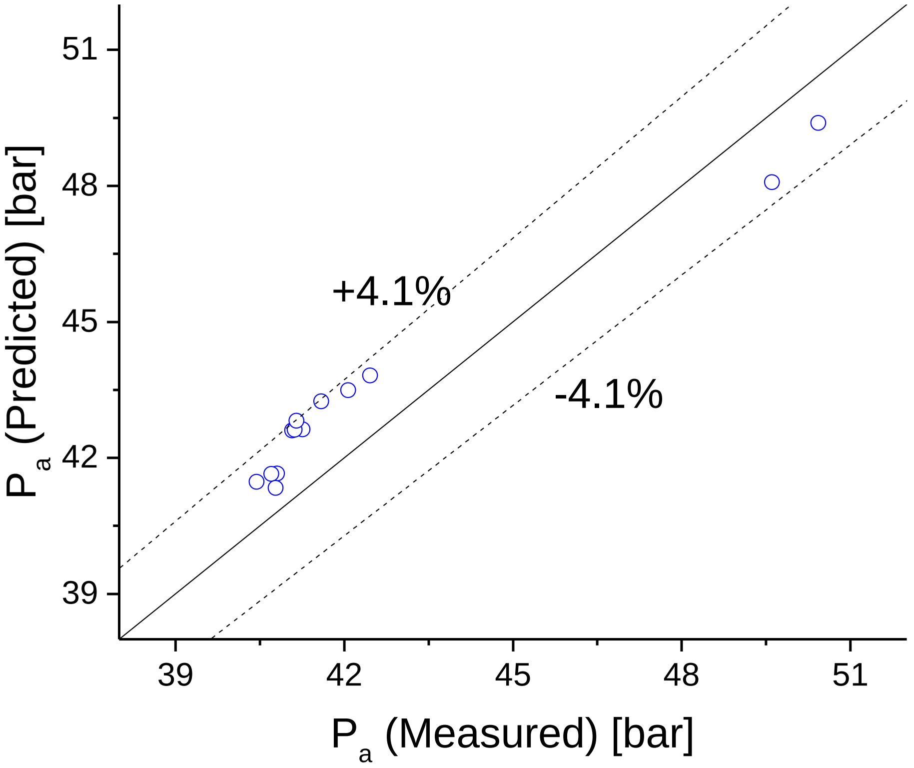

Figure 4-6 Comparison between Measured and Predicted Results (P_a).

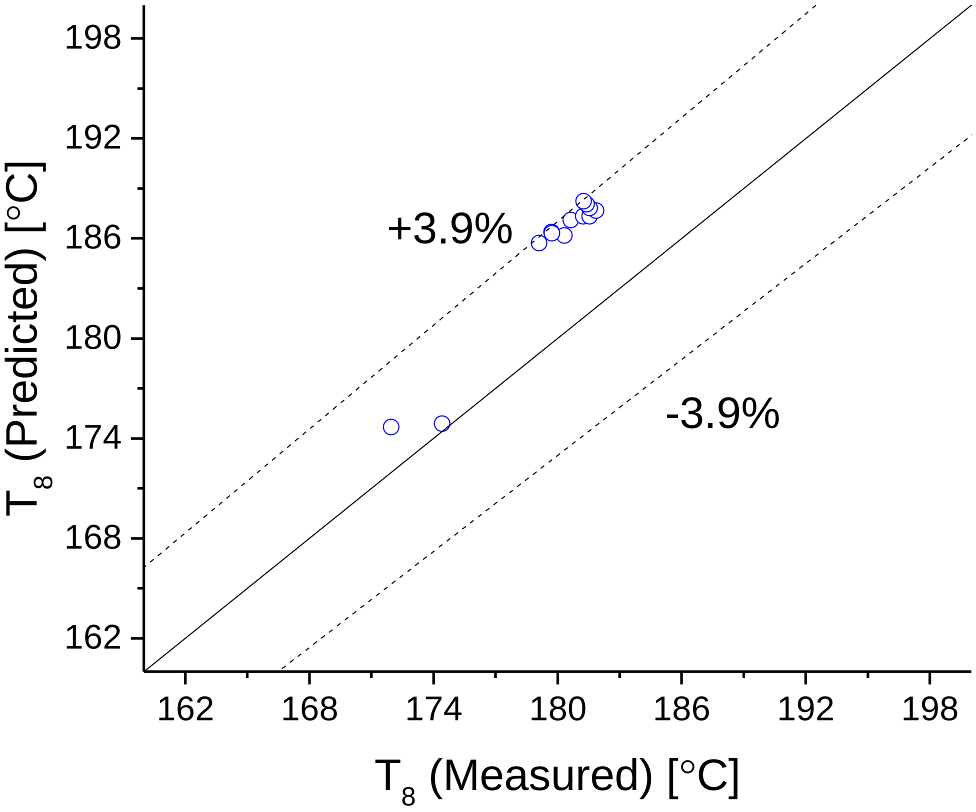

Figure 4-7 Comparison between Measured and Predicted Results (T_8).

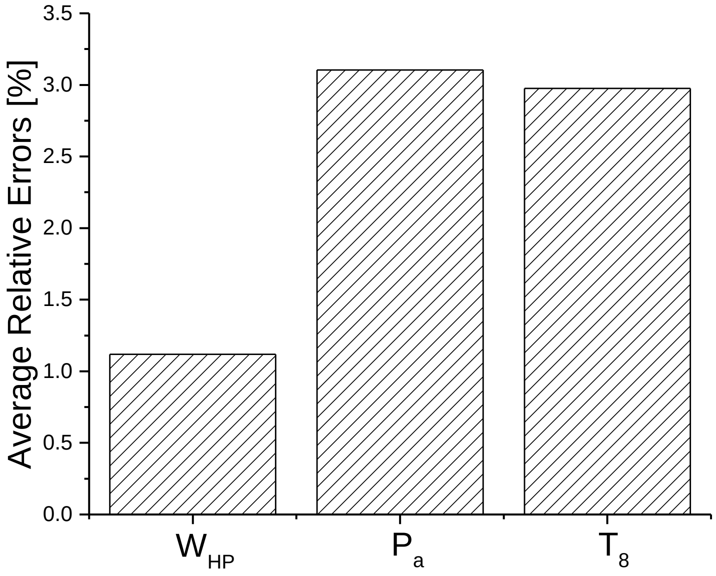

Figure 4-8 Average Relative Errors of 13 Test Points.

4.1.5 Impact of Gas Turbine Power Setting and Steam Turbine Erosion

To illustrate the effect of power plant operating conditions on the performance of the OTSG, changing exhaust gas conditions indicated by dropping the prime mover (i.e. a GT) power output is simulated by PYTHIA [5]. Meanwhile, the GT exhaust results are applied to the input of the OTSG to see the changes in OTSG performance at OD conditions. All the OD calculation is based on the dual-pressure operation that recovery more heat than single pressure operation.

Figure 4-9 shows the impact of GT power drop on exhaust gas temperature and the exhaust gas mass flow rate. It is assumed that the OTSG feed water condition and ST flow capacity maintain the same. Figure 4-10 shows the simulated impact of GT power setting on the OTSG stack temperature T_8 and OTSG efficiency η, where the GT power changes from 32 MW (DP condition) to 22 MW. It can be seen that the OTSG stack temperature, OTSG thermal efficiency and the steam properties such as steam mass flow rate, total pressure and total temperature all decrease with the reduction of GT power illustrated in Figure 4-11 - Figure 4-13. In addition, the moving boundary between the economizer, evaporator and superheater in the OTSG demonstrated by the variations of the heat transfer areas A_{ab}, A_{bc}, A_{cj}, A_{ef}, A_{fg} and A_{gh} are shown in Figure 4-14 and Figure 4-15 respectively while the total heat transfer areas A_{aj} and A_{eh} are unchanged.

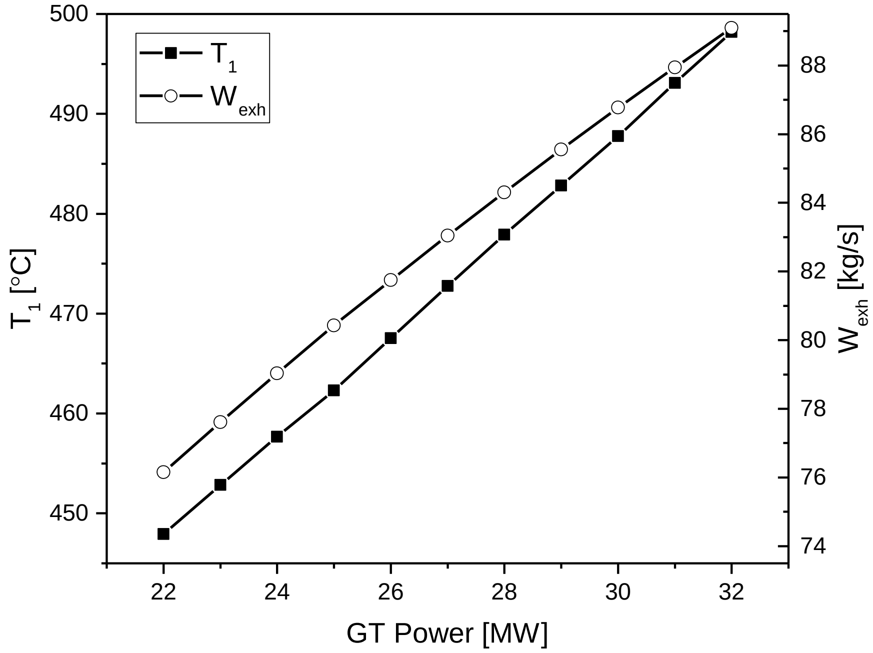

Figure 4-9 Effect of GT Power on Exhaust Gas T_1 and W_{exh}.

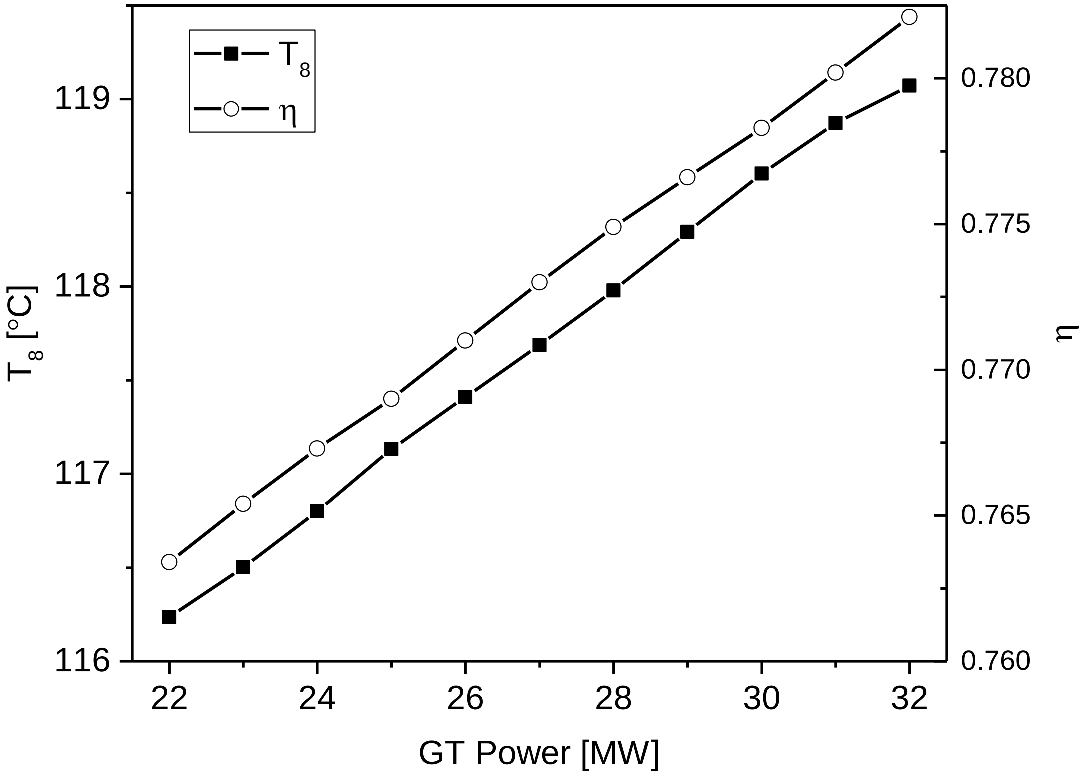

Figure 4-10 Effect of GT Power on OTSG T_8 and η.

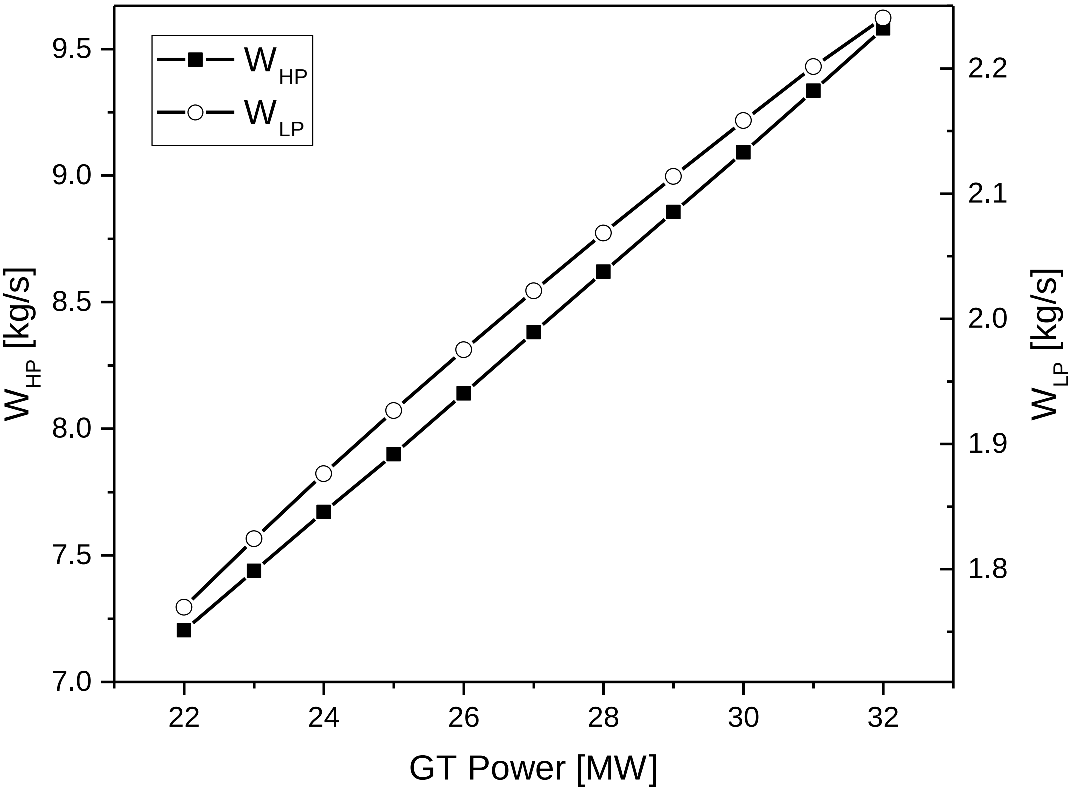

Figure 4-11 Effect of GT Power on OTSG W_{HP} and W_{LP}.

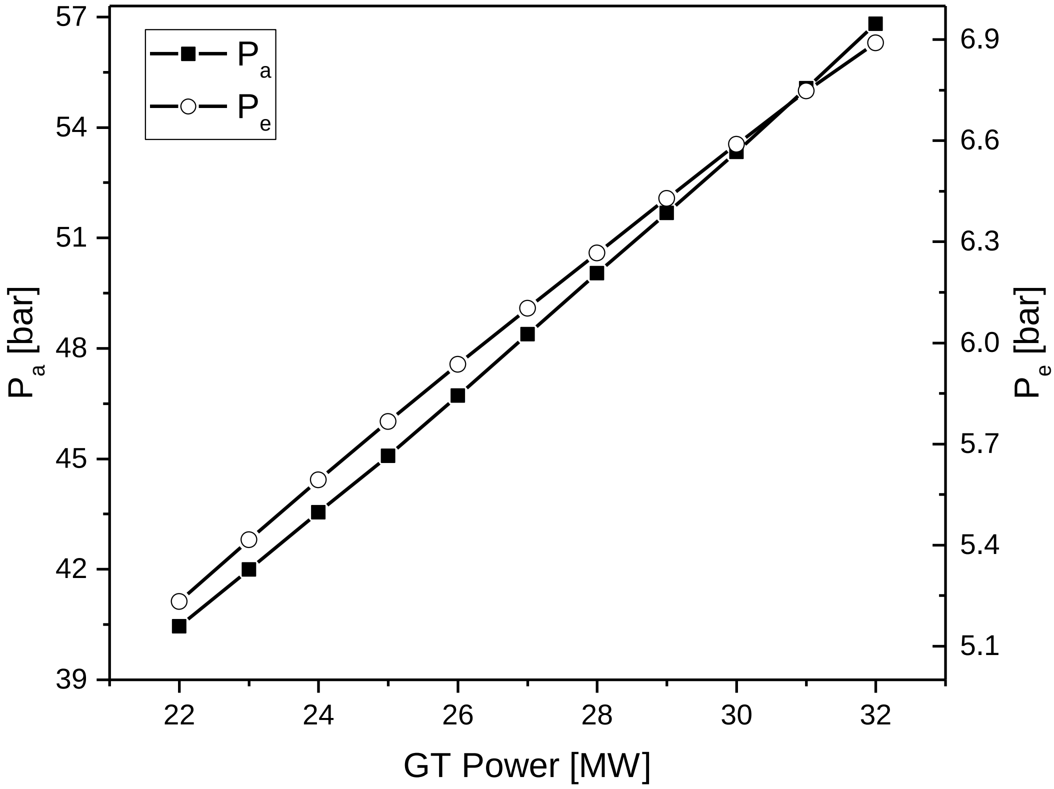

Figure 4-12 Effect of GT Power on OTSG P_a and P_e.

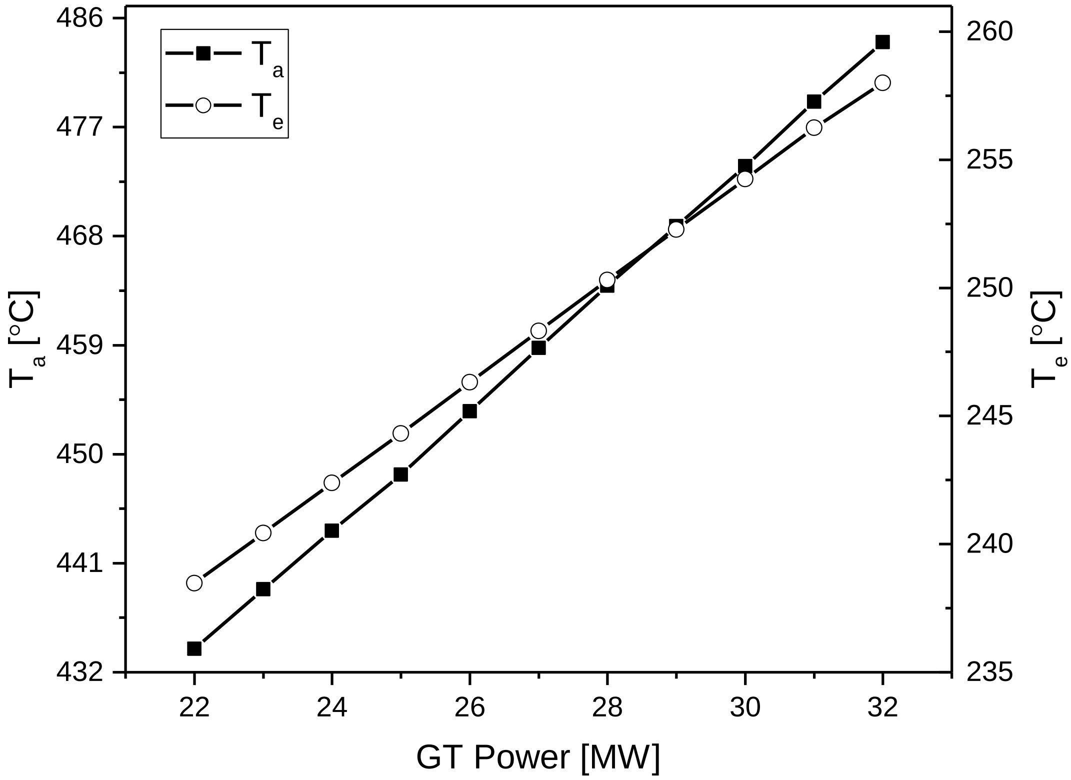

Figure 4-13 Effect of GT Power on OTSG T_a and T_e.

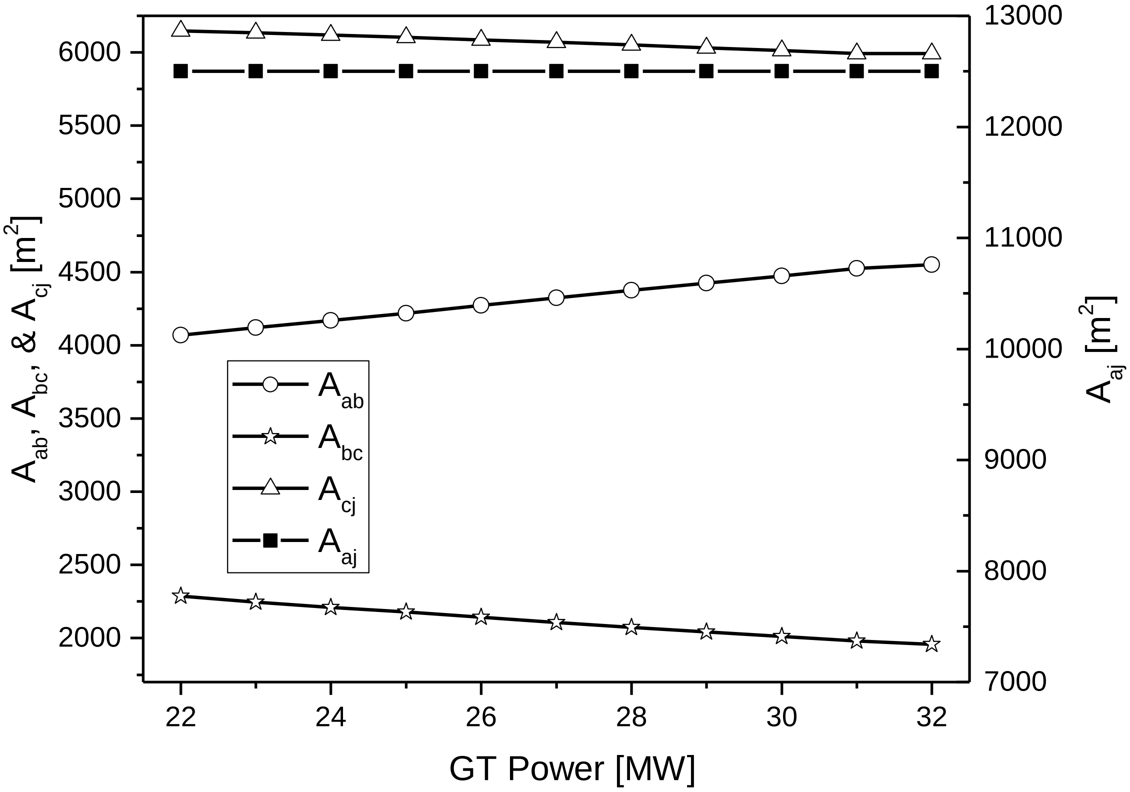

Figure 4-14 Effect of GT Power on OTSG High Pressure (HP) Heat Transfer Areas.

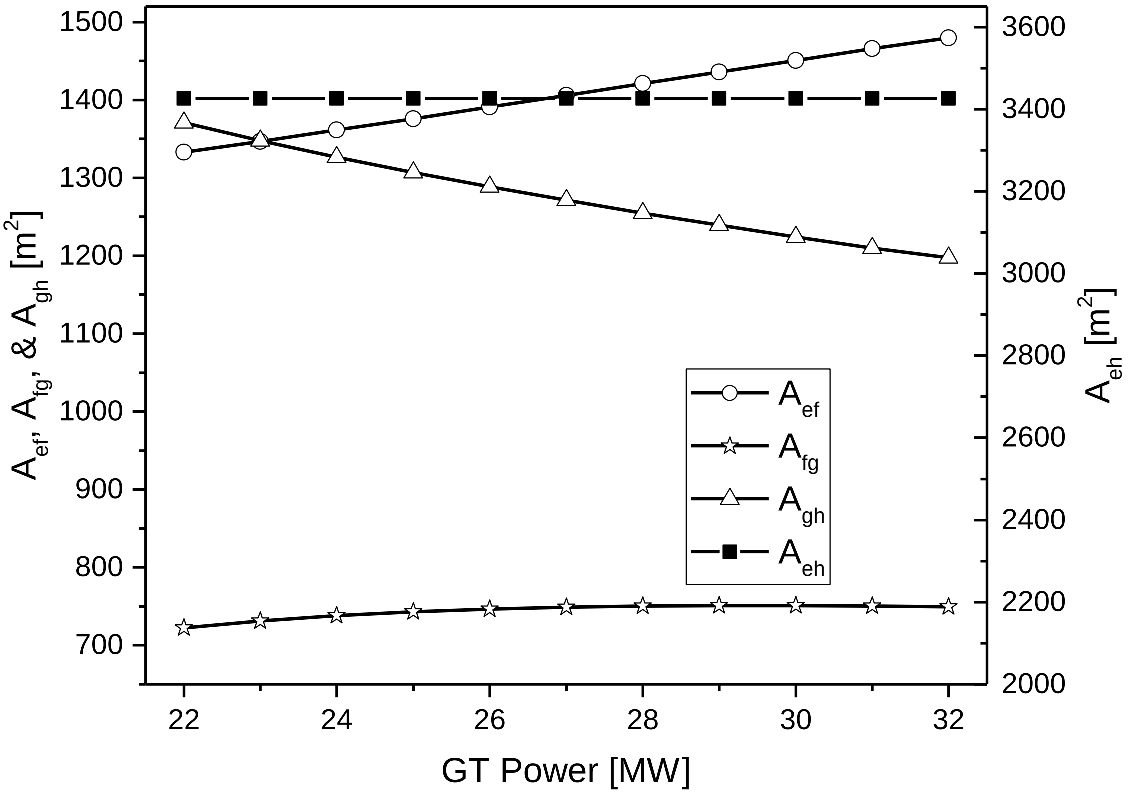

Figure 4-15 Effect of GT Power on OTSG Low Pressure (LP) Heat Transfer Areas.

Erosion is a degradation phenomenon in an ST, and it increases ST flow capacity. Such growth is represented by the change of Erosion factor (EF_{ST}). It is assumed that the EF_{ST} is the same for both the HP and LP circuits of the ST. Figure 4-16 shows the simulated impact of changing EF_{ST} from 1 to 1.1 on the OTSG stack temperature T_8 and OTSG efficiency η. It can be seen that the OTSG stack temperature decreases with erosion when the exhaust gas inlet temperature and mass flow rate are kept unchanged. This means that the erosion results in more heat being recovered by the OTSG due to the decrease of the stack temperature, resulting in higher OTSG efficiency. In addition, the variation of the steam properties is showed in Figure 4-17 - Figure 4-19 and the moving boundaries within the OTSG represented by the changing areas are shown in Figure 4-20 and Figure 4-21.

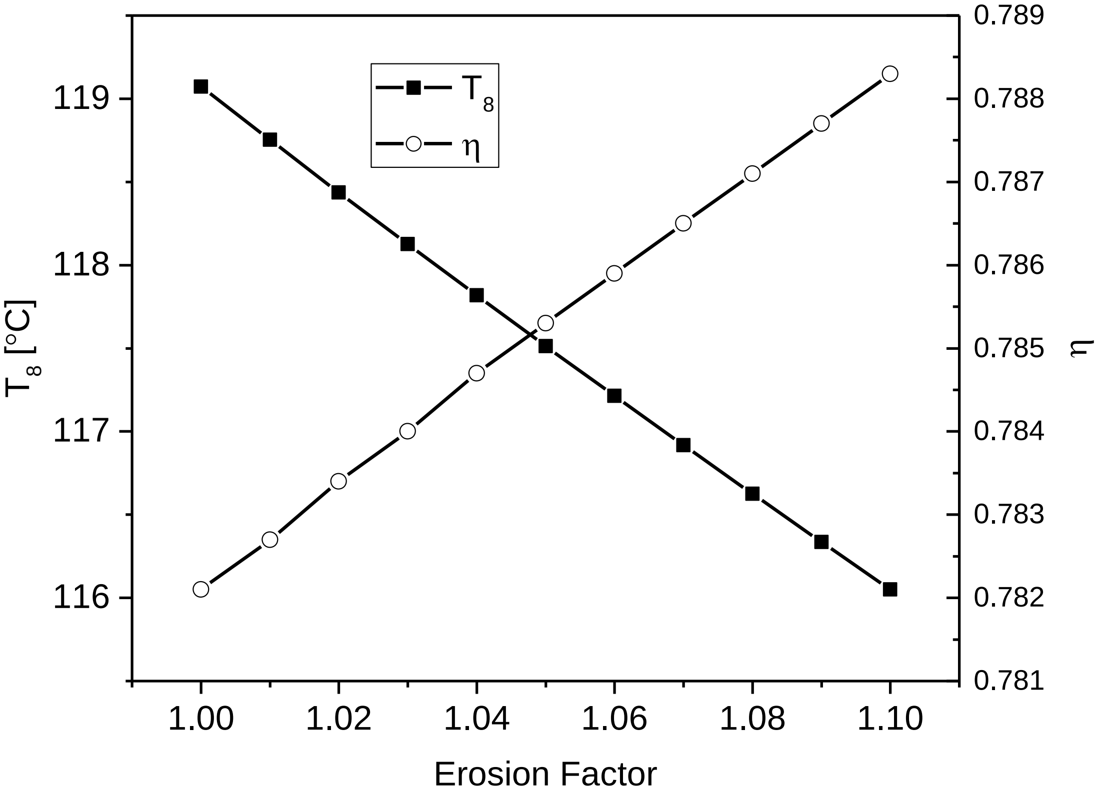

Figure 4-16 Effect of EF_{ST} on OTSG T_8 and η.

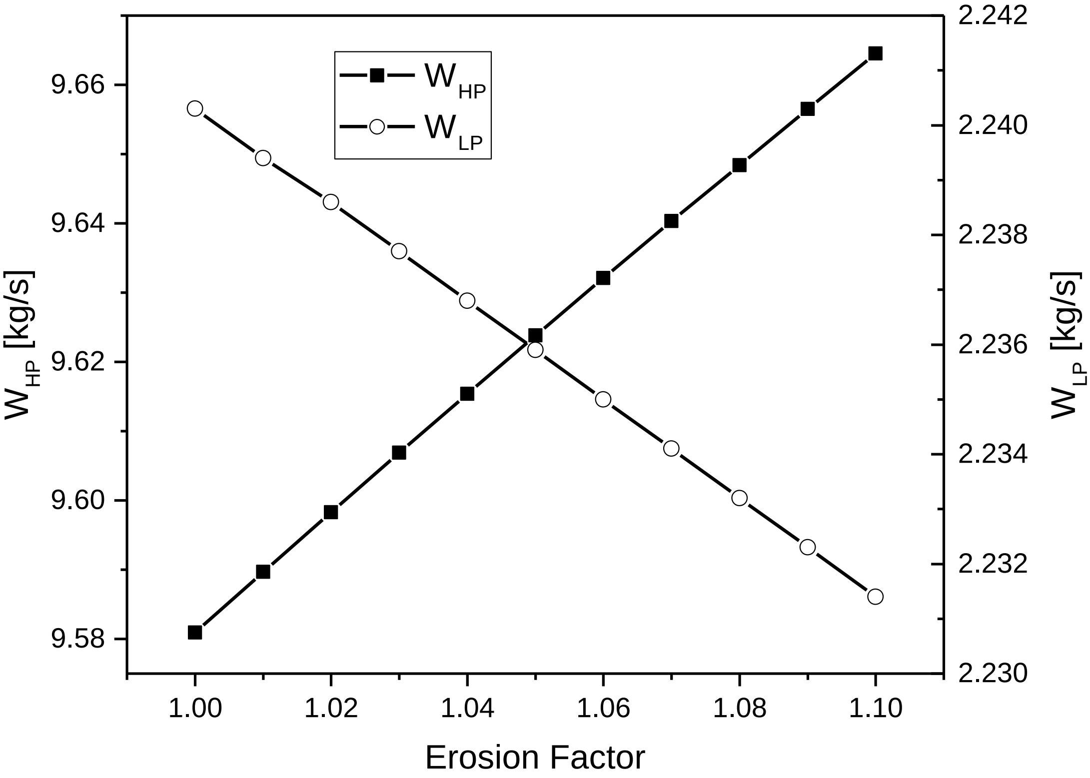

Figure 4-17 Effect of EF_{ST} on OTSG W_{HP} and W_{LP}.

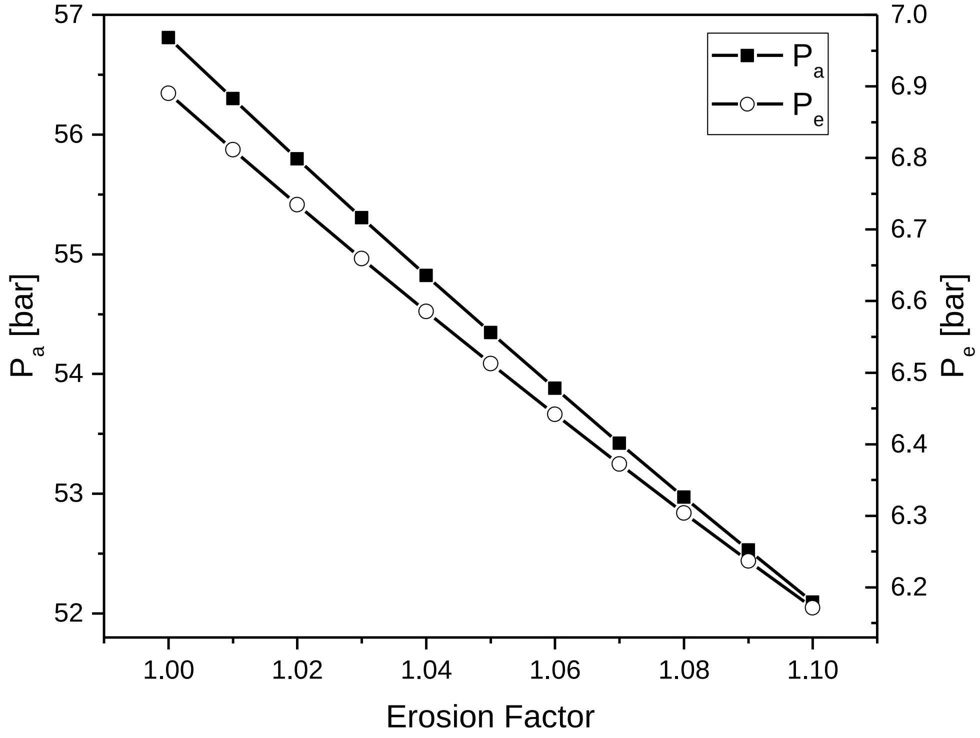

Figure 4-18 Effect of EF_{ST} on OTSG P_a and P_e.

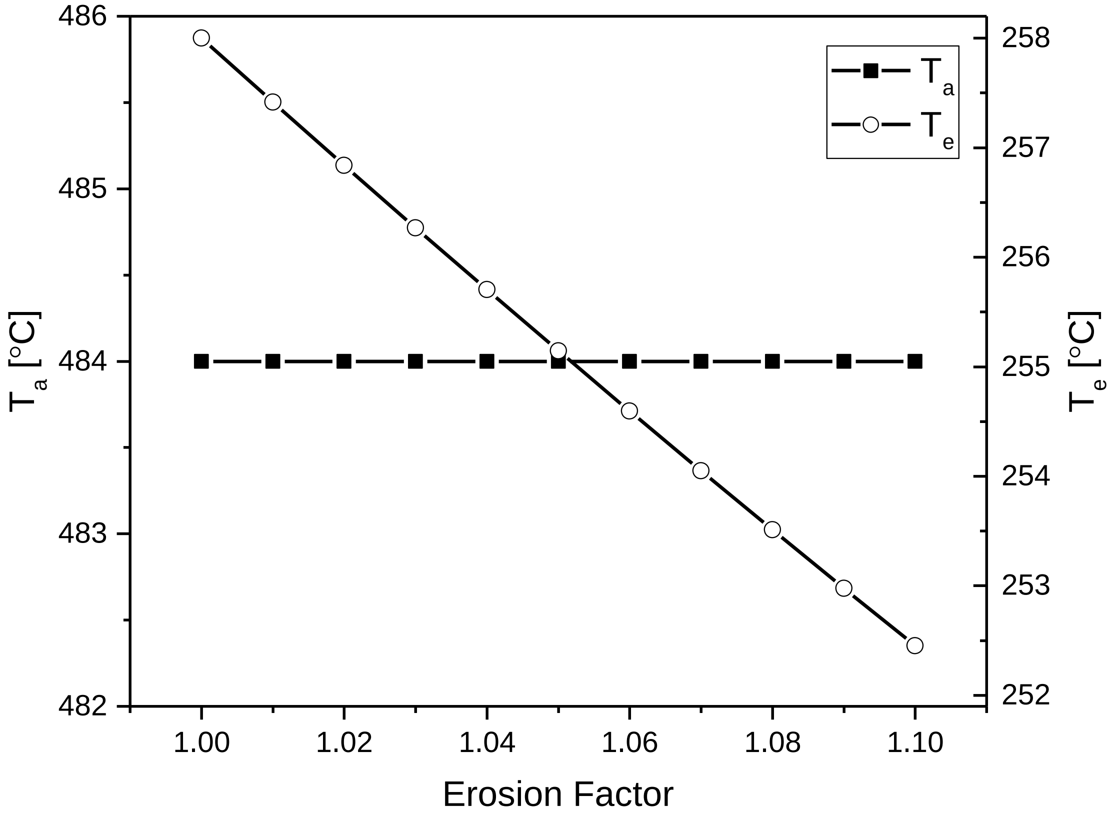

Figure 4-19 Effect of EF_{ST} on OTSG T_a and T_e.

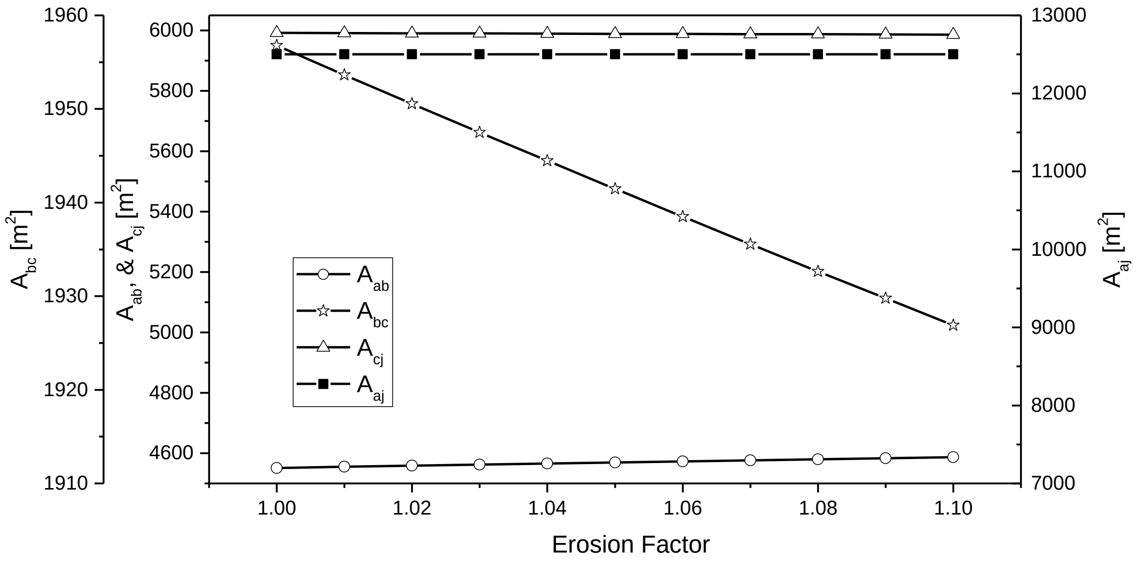

Figure 4-20 Effect of EF_{ST} on OTSG HP Heat Transfer Areas.

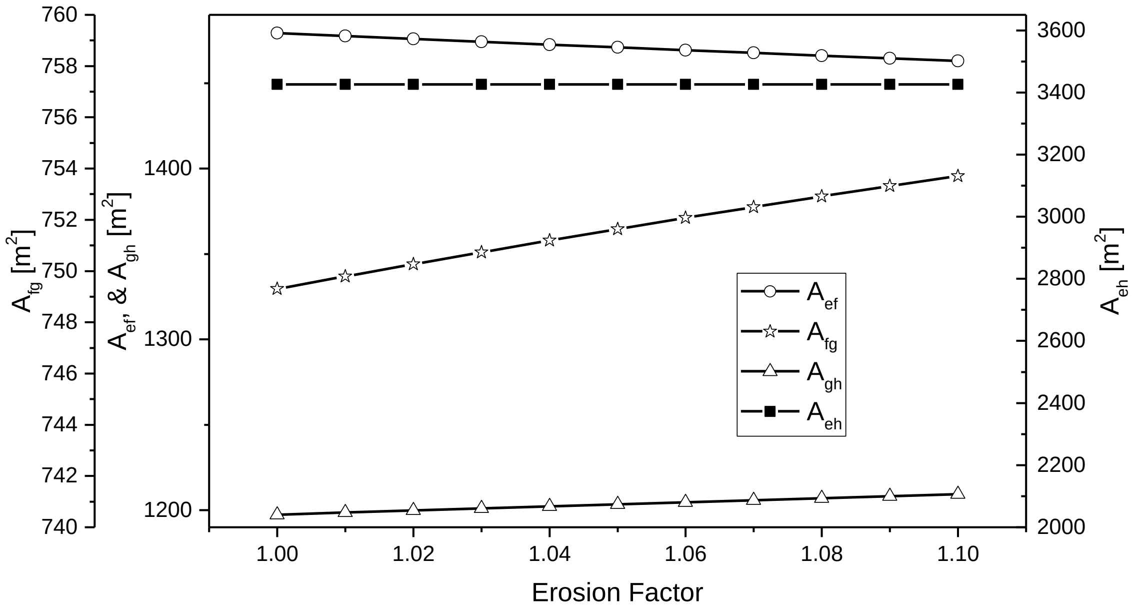

Figure 4-21 Effect of EF_{ST} on OTSG LP Heat Transfer Areas.

4.2 OTSG Performance Diagnosis

4.2.1 Effect of Fouling Resistance on OTSG Performance

The DP of the OTSG is assumed to be the baseline condition of the OTSG. To analyze the effect of fouling degradation on the OTSG performance, ten different degradation levels relative to the baseline OTSG performance are seeded in the OTSG model, and the degraded OTSG performance is calculated with the assumption that all the sections have the same CF. It is also assumed that both the upstream GT exhaust condition and the downstream ST flow capacity are kept the same as that at the DP condition. Meanwhile, the all the cases in diagnostic requires to operate at the dual-pressure condition. Figure 4-22 shows the variation of the OTSG stack temperature and efficiency against the CF changing from 1 to 0.9. It can be seen that the OTSG stack temperature increases with the worsening of the fouling. This indicates that less heat has been recovered by the OTSG. Figure 4-22 also shows the OTSG efficiency decreases when CF decreases.

Figure 4-23 shows the decrease of both the HP and LP mass flow rate with a more severe fouling level. Meanwhile, the HP and LP steam pressure also tend to decrease when fouling develops (Figure 4-24). Figure 4-25 and Figure 4-26 show that the effect of the degradation has changed the boundaries between economiser, evaporator, and superheater of both the LP and HP circuits.

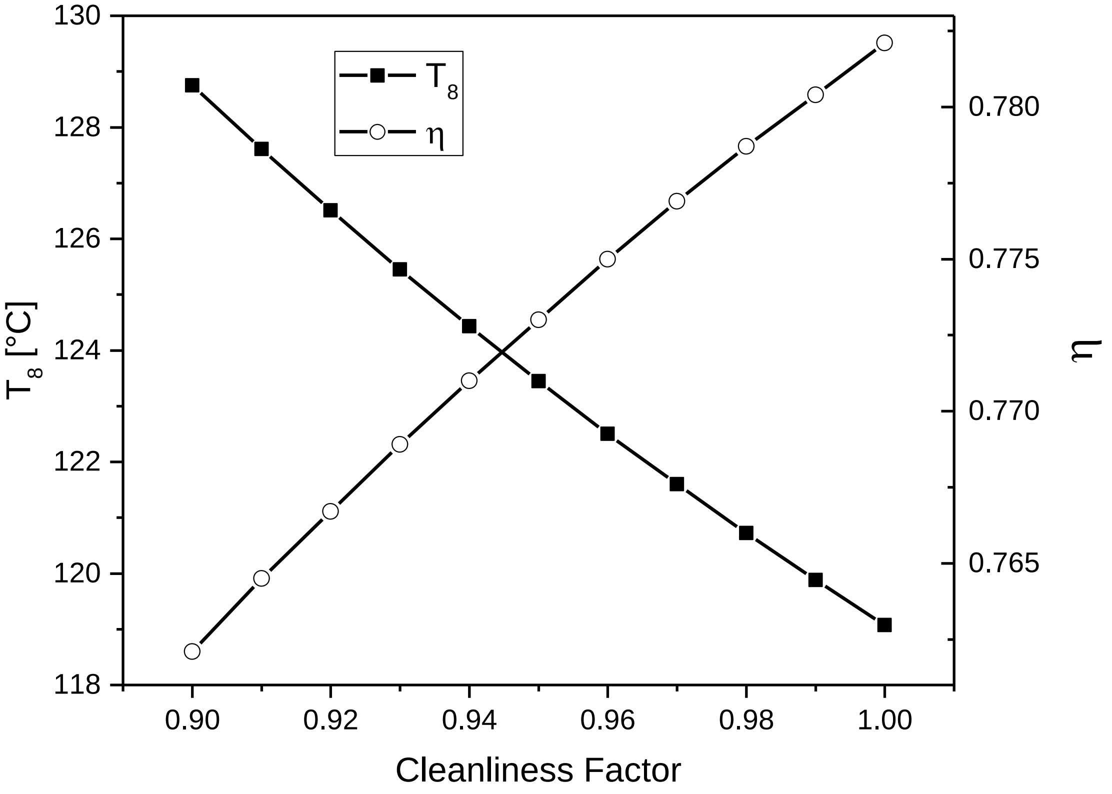

Figure 4-22 Effect of Cleanliness Factor (CF) on OTSG T_8 and η.

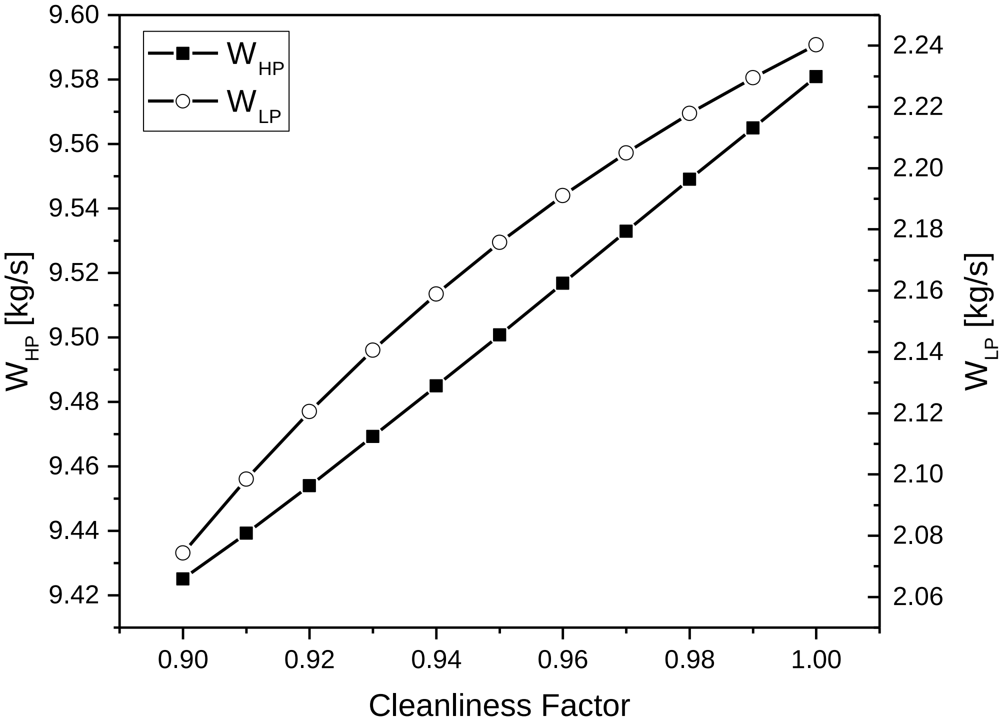

Figure 4-23 Effect of CF on W_{HP} and W_{LP}.

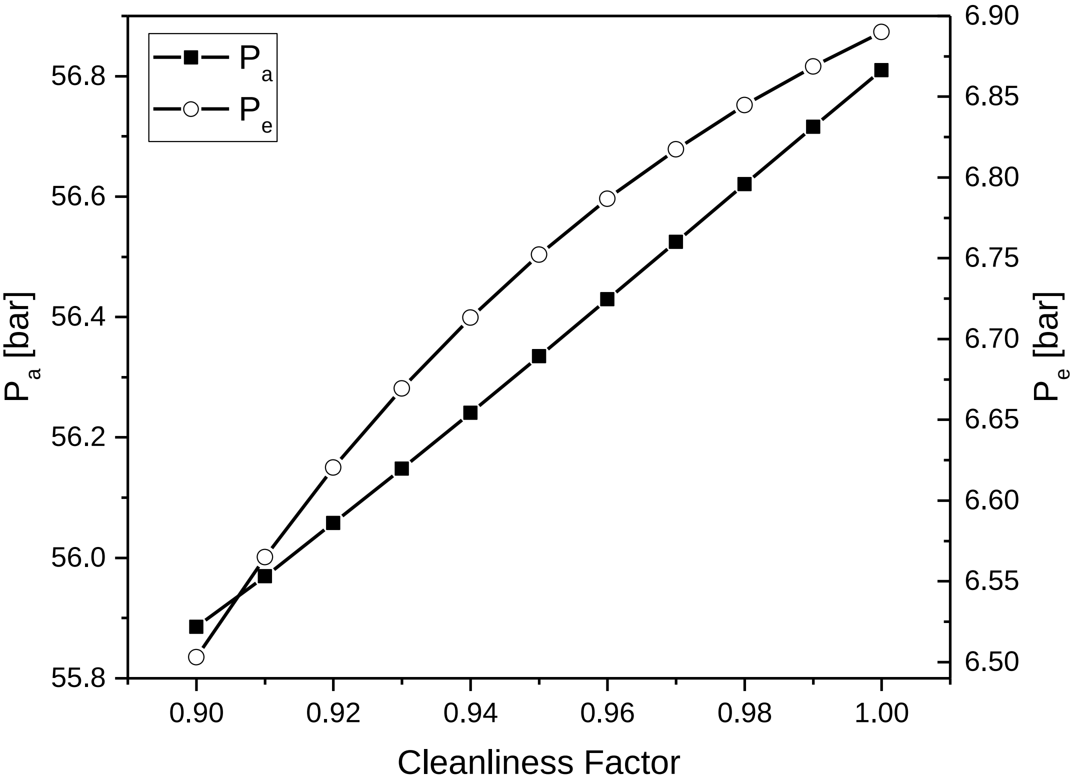

Figure 4-24 Effect of CF on P_a and P_e.

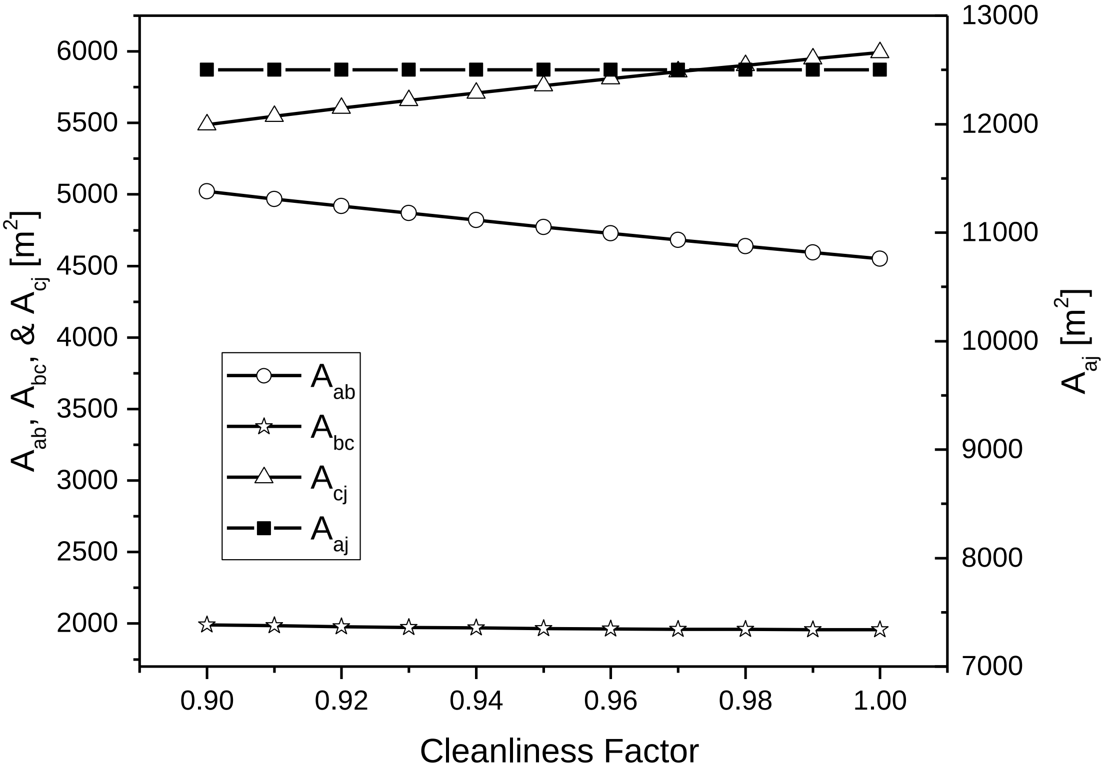

Figure 4-25 Effect of CF on OTSG HP Heat Transfer Area.

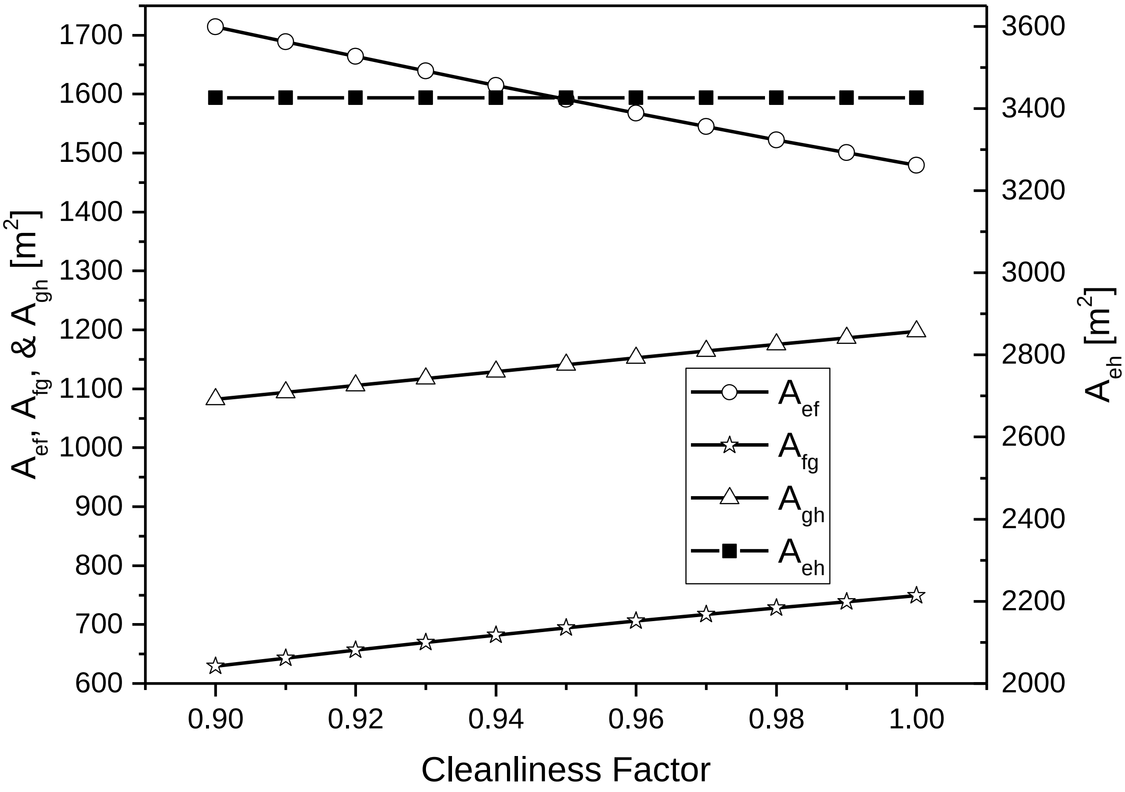

Figure 4-26 Effect of CF on OTSG LP Heat Transfer Area.

4.2.2 Diagnostic System Testing

To test the effectiveness of the introduced diagnostic method, three cases of fouling represented by three different values of Cleanliness Factor were used. The fouling was implanted into the OTSG performance model to simulate the gas path measurements of the degraded OTSG. Such simulated measurements are assumed the observable information for the gas path diagnostics of the OTSG. It also is assumed that the GT exhaust gas and ST non-dimensional flow capacity is kept unchanged for both the clean and degradation conditions. The HP steam temperature is a function of the OTSG inlet gas temperature (i.e. upstream GT exhaust temperature) in the OTSG control scheme so that it will remain the same for both the clean and degraded OTSG. The LP steam temperature T_{e} is controlled in a way that a constant temperature difference between T_4 and T_{e} is always kept. Meanwhile, the steam pressure is adjusted through a sliding pressure control for both the clean and degraded conditions. Consequently, the degradation of OTSG will result in changes of six available OTSG gas path measurements W_{HP}, W_{LP}, P_a, P_e, T_8, and T_{e}, as shown in Table 4-6.

Table 4-6 OTSG Measurement Set $\vec{z}$.

Parameter	Unit	Meanings
W_{HP}	kg/s	HP mass flow rate
W_{LP}	kg/s	LP mass flow rate
P_a	bar	HP steam pressure
P_e	bar	LP steam pressure
T_8	℃	Stack temperature
T_e	℃	Steam temperature at point e

By using the non-linear GPA method described in Section 3.5.2.2, the CF of the OTSG due to its fouling for all the three diagnostics test cases are predicted using the simulated measurements as shown in Table 4-7 to Table 4-9. By comparing the predicted degradation and the implanted degradation as shown in Table 4-10 and Figure 4-27, it can be seen that the relative prediction errors are less than 0.002%, indicating that the predictions are satisfactory.

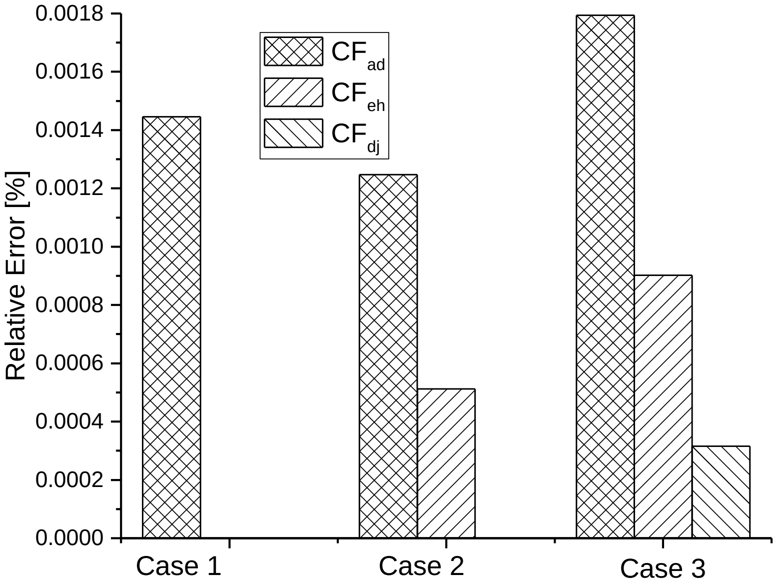

Figure 4-27 Relative Error of CF.

Table 4-7 Diagnostic Results of Measurements for Case 1.

Parameter	Measured	Predicted	Relative Error [%]
W_{HP}	9.22473387	9.22479377	0.000649346
W_{LP}	2.453645882	2.453610889	0.001426190
P_a	54.69788248	54.69823766	0.000649346
P_e	7.747149443	7.747005561	0.001857223
T_8	123.9364454	123.9356101	0.000673975
T_e	271.9247826	271.9224384	0.000862077

Table 4-8 Diagnostic Results of Measurements for Case 2.

Parameter	Measured	Predicted	Relative Error [%]
W_{HP}	9.453623163	9.453634343	0.000118269
W_{LP}	2.034236981	2.034262242	0.001241773
P_a	56.05507715	56.05514345	0.000118269
P_e	6.459224934	6.459283114	0.000900724
T_8	128.6827705	128.6817266	0.000811220
T_e	275.0086902	275.0068144	0.000682088

Table 4-9 Diagnostic Results of Measurements for Case 3.

Parameter	Measured	Predicted	Relative Error [%]
W_{HP}	9.375231204	9.375260252	0.000309833
W_{LP}	2.089872651	2.0899069	0.001638787
P_a	55.59025354	55.59042578	0.000309833
P_e	6.625260442	6.625333705	0.001105816
T_8	129.6693843	129.6675278	0.001431718
T_e	274.1289839	274.1260619	0.001065922

Table 4-10 Comparison of Implanted and Predicted Degradations for Three Diagnostic Test Cases.

Diagnostics Case 1

OTSG Section	Implanted CF	Predicted CF	Iterative Steps	Relative Error [%]
a–d	0.85	0.850012289	18	0.001445722

Diagnostics Case 2

OTSG Sections	Implanted CF	Predicted CF	Iterative Steps	Relative Error [%]
a–d	0.85	0.850010605	19	0.0012476505
e–h	0.9	0.900004608		0.0005119673

Diagnostics Case 3

OTSG Sections	Implanted CF	Predicted CF	Iterative Steps	Relative Error [%]
a–d	0.85	0.850015251	18	0.0017942337
e–h	0.9	0.900008115		0.0009016297
d–j	0.95	0.950002997		0.0003154215

As in real applications, the true degradations are never available to OTSG users. To assess the quality of the diagnostic results, the predicted degradations are implanted back into the OTSG model, and the measurement parameters of the degraded OTSG were simulated and compared with the actual values of the measurement parameters as shown in Table 4-7 to Table 4-9. It can be seen that the predicted measurements agree very well with the actual measurements. This indicates more practically that the predicted OTSG degradations are satisfactory.

Figure 4-28 shows the convergence process indicated by the decreasing of the relative errors in RSM defined by Eq. (3-116) for the above three diagnostic cases where convergence was achieved within 20 iterations. The calculation time for the three cases are 2.97, 3.709, and 4.089 seconds respectively using a desktop computer (Intel(R) Core(TM) i7-4790 CPU of 3.6 GHz and 16 GB RAM). All the above results prove that the non-linear GPA is a fast and effective method for OTSG fouling diagnostics.

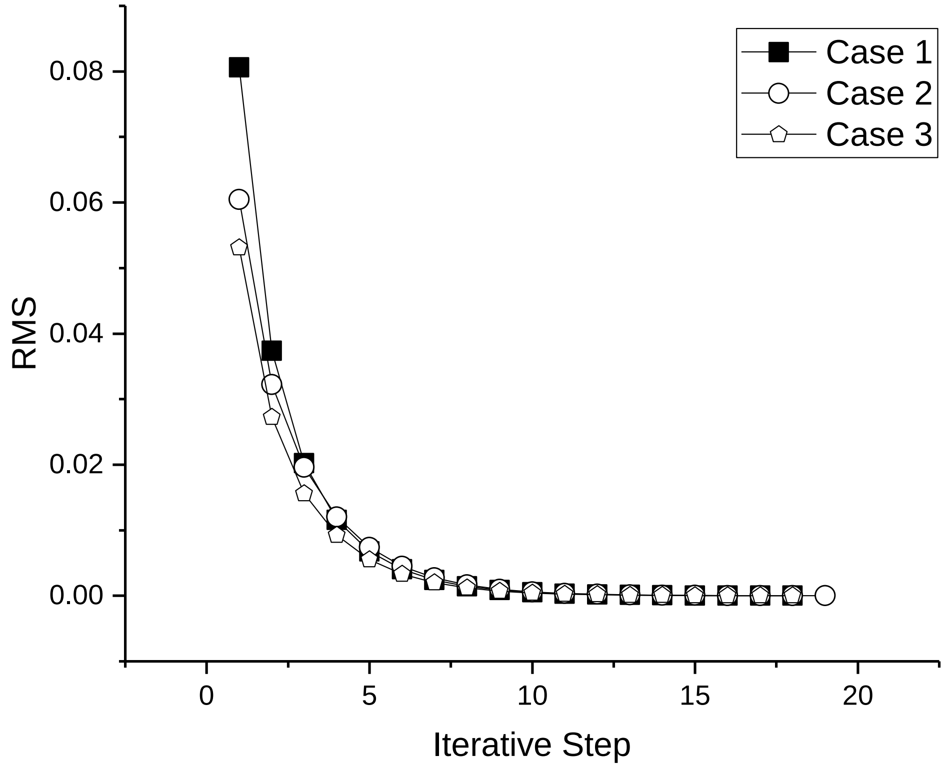

Figure 4-28 Convergence Procedure of Three Diagnostic Cases.

4.2.3 Effect of Measurement Noise

Measurement noise has a negative impact on diagnostic results. The maximum measurement noise simulated in this study are shown in Table 3-5 [186], and the measurement noise was randomly generated within the maximum noise. To assess the impact, ten sets of noisy samples of OTSG gas path measurements based on Test Case 3 are selected and used by the GPA for the prediction of the implanted fouling. An example of the noisy measurement T_8 is shown in Figure 4-29 where the 11th point shows the post filtering values of the measurement from the previous 10 noisy points by the average filter and the 12th point shows the true value (Table 4-9). The predictions of all three CF of the OTSG are shown in Figure 4-30, where the first 10 points illustrate the diagnostic results from 10 sets of noisy measurements, the 11th point shows the diagnostic result using preprocessed measurement, and the last point shows the implanted degradation. The relative errors of the diagnostic predictions using the 10 sets of noisy measurements and 1 set of preprocessed measurements are shown in Figure 4-31.

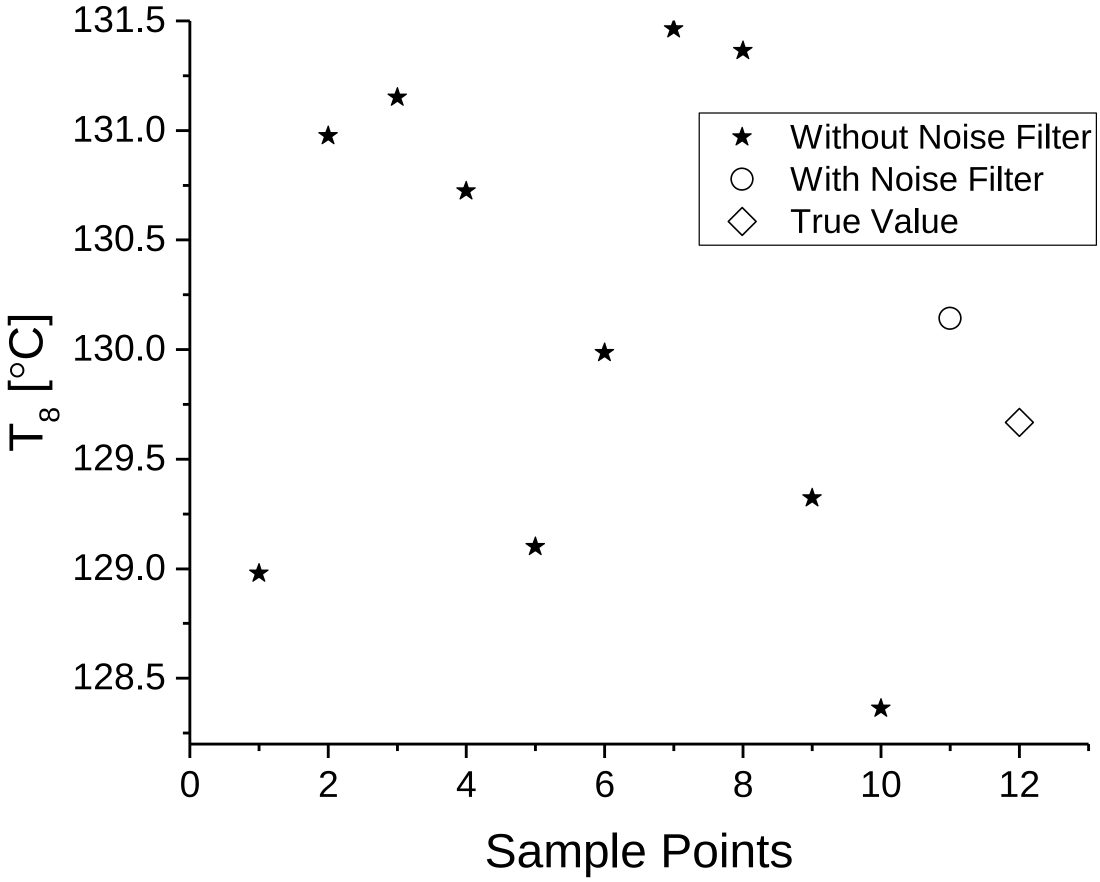

Figure 4-29 Measurement Samples of T_8 with Measurement Noise, Post-filtered Measurement and True Value.

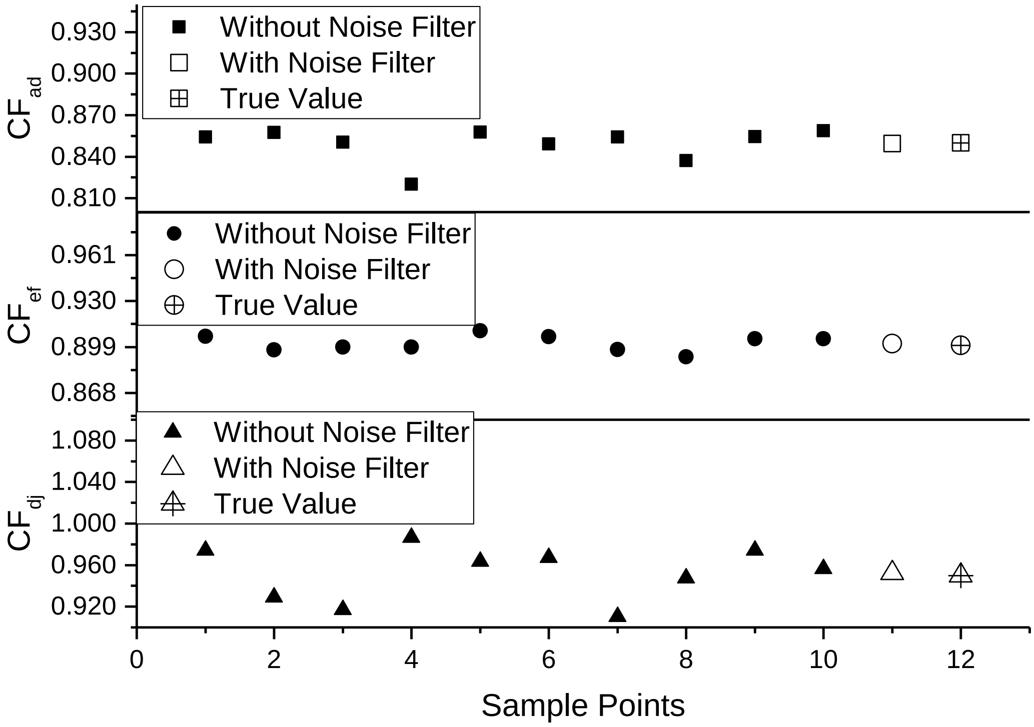

Figure 4-30 Diagnostic Results CF using Noisy Measurements.

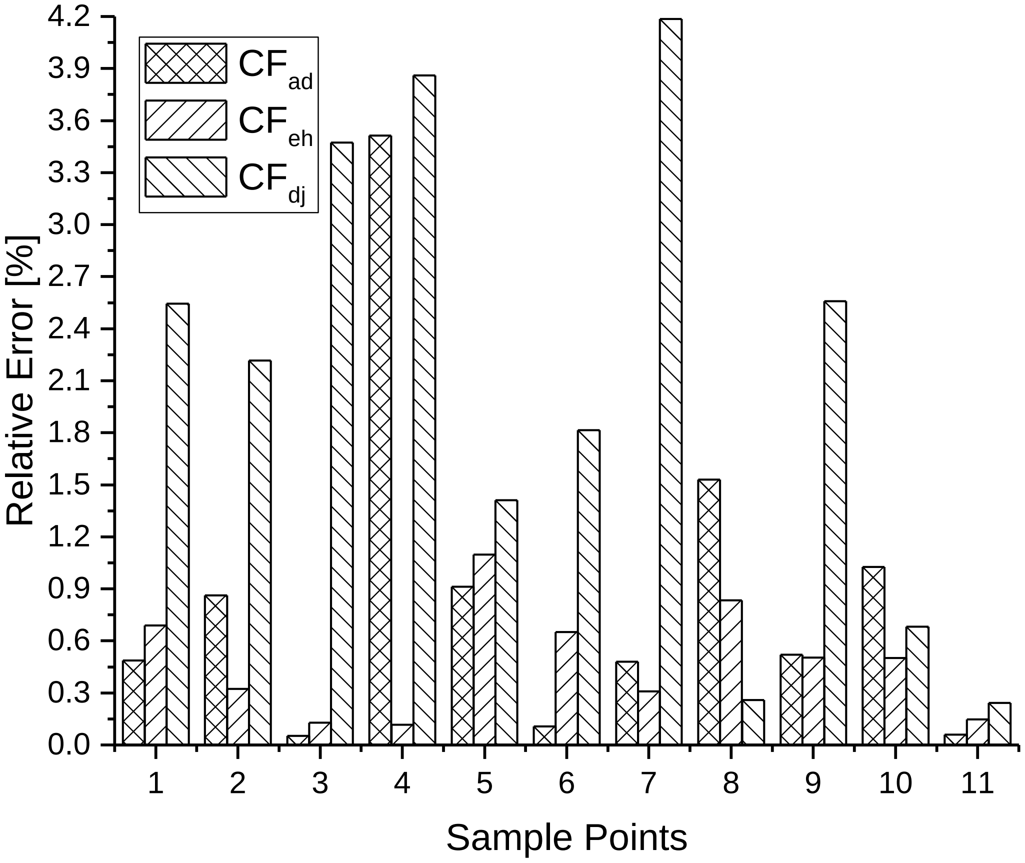

Figure 4-31 Relative Error of CF.

A comparison of the average prediction errors between Case 3 using the measurement without noise (Table 4-10) and Figure 4-31 shows that the measurement noise does increase the prediction errors of the Cleanliness Factors. However, the most significant prediction errors for all the CF are relatively small and acceptable, with the maximum error less than 4.2% at the seventh point for CF_{dj}. In addition, the diagnostic result using the preprocessed measurements has improved diagnostic accuracy, with a maximum relative error of the CF less than 0.3% for CF_{dj}. Figure 4-32 gives a comparison between the average relative error obtained through Eq. (3-118) for the 10 sets of noise samples and the preprocessed sample. Figure 4-33 shows that the number of iterations to achieve a converged solution using the noisy measurements has doubled compared with those using the measurements without noise. However, the increase of the calculation time is not significant and is quite acceptable for off-line diagnostic applications.

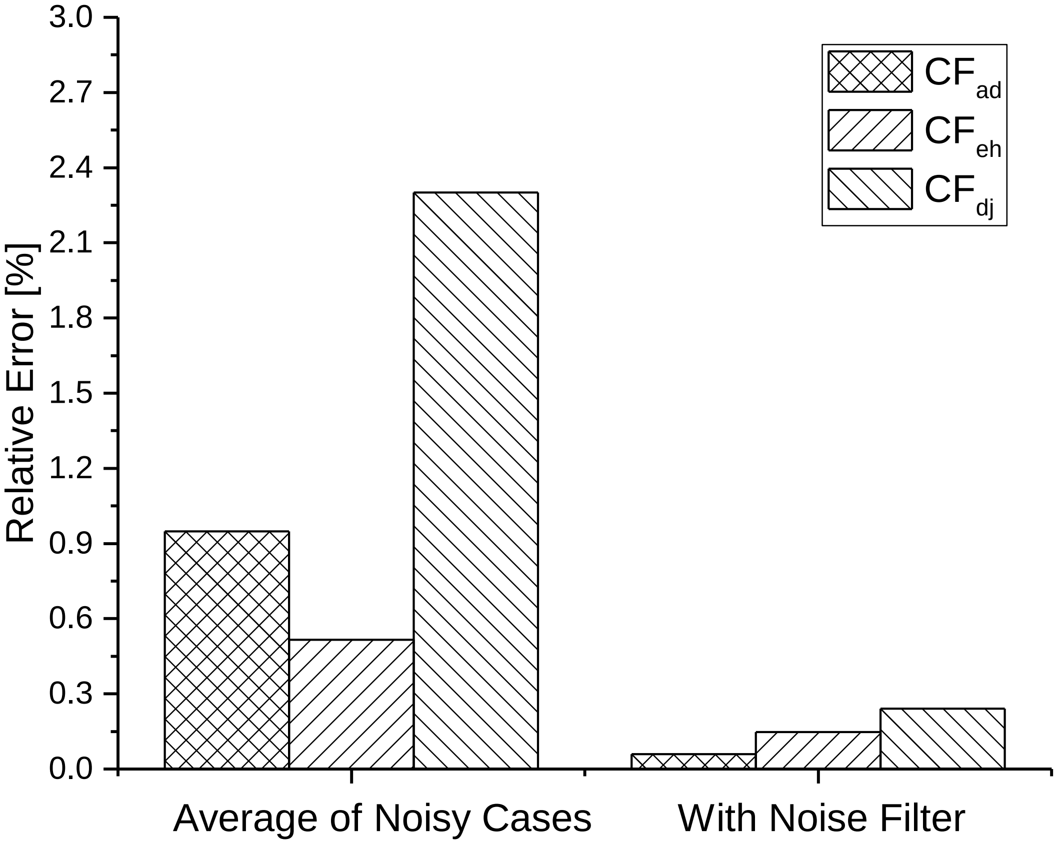

Figure 4-32 Comparison of Relative Error between Ten Noisy Measurement and Post-filtering Measurement.

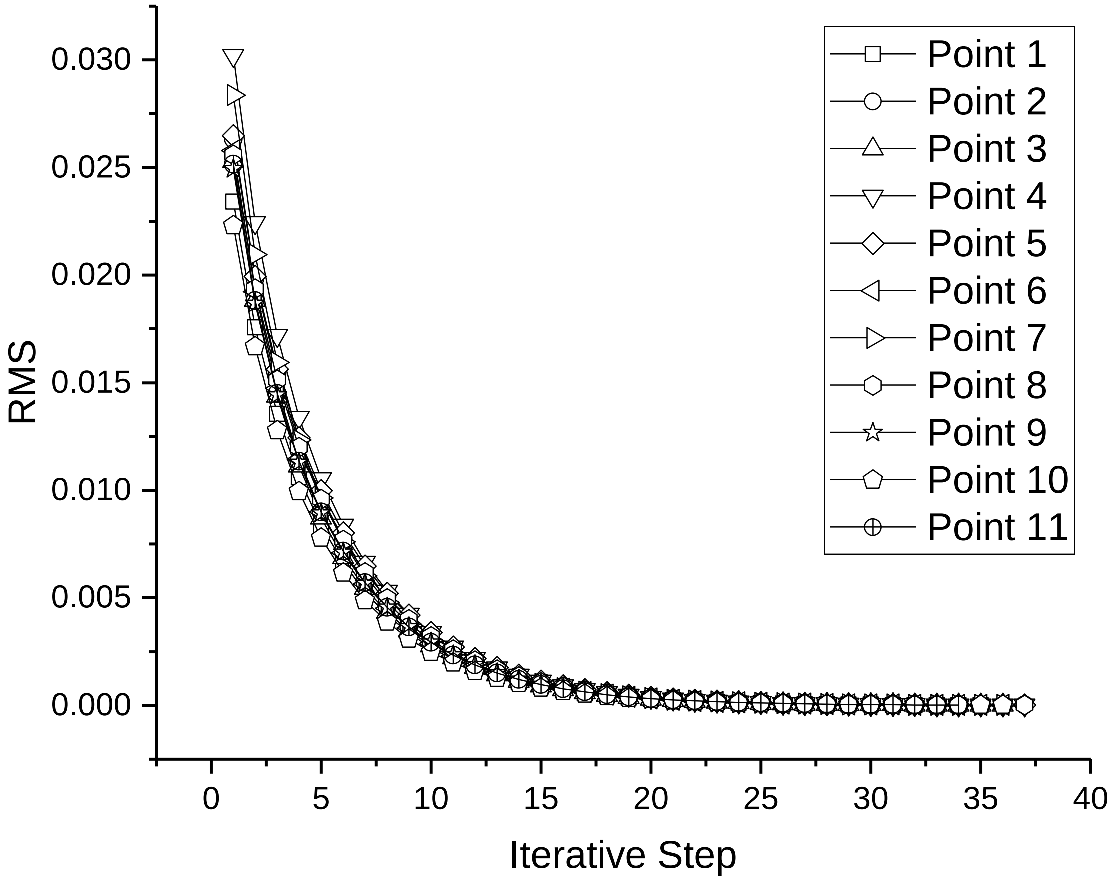

Figure 4-33 Convergence Processes of 11 Diagnostic Points.

4.2.4 Diagnostic Analysis Applied to Real Power Plant Measurements

The CCGT power plant where the OTSG is operated in was constructed at MU in 2003 and has been operating since then. The OTSG has been used to recover the energy from the GT exhaust gas in the form of steam with high pressure and temperature driving an ST. The gas path measurements of the CCGT are recorded every five minutes for condition monitoring. To demonstrate the application of the developed diagnostic method, ten sets of steady-state OTSG measurements are randomly selected to analyse the fouling of the OTSG. Due to confidentiality reason, only the range of OD input parameters is given in Table 4-11.

Table 4-11 Range of Operating Conditions for 10 OD Points.

Parameter	Unit	Range
T_1	℃	508.8 – 512.9
T_{amb}	℃	14.4 – 17.0
Ambient Pressure	bar	1.00 – 1.01
Relative Humidity	%	58.40 – 74.4
W_{exh}	kg/s	75.49 – 80.44
Gas Turbine Power	MW	28.06 – 28.45
T_j	℃	43.7 – 46.14
T_h	℃	43.7 – 46.14

Figure 4-34 shows the predicted diagnostic results of the three CF, with the first 10 points representing the predicted degradations corresponding to the 10 sets of measurements, and the 11th point showing the averaged value for the ten sets of predicted CF. To test the consistency of the predictions, the averaged CF are implanted back into the OTSG performance model to simulate the gas path measurements of the degraded OTSG. The relative errors between the simulated measurements and the measured values of the measurement parameters of the ponits are showed in Figure 4-35 to Figure 4-40. It is clearly shown that the maximum relative errors are less than 1.18% with implanted degradation and are less than 10.61% without considering the degradation. Meanwhile, the average relative errors calculated with Eq. (3-120) for all ten points with and without implanted degradations are showed in Figure 4-41 indicating that the predicted fouling provides correct and consistent results.

Although the predicted CF are difficult to validate quantitatively, it indicates the severity of the fouling happening in the OTSG. The maintenance engineers could use the information to track the fouling and arrange condition-based maintenance actions based on the predicted severity of the fouling.

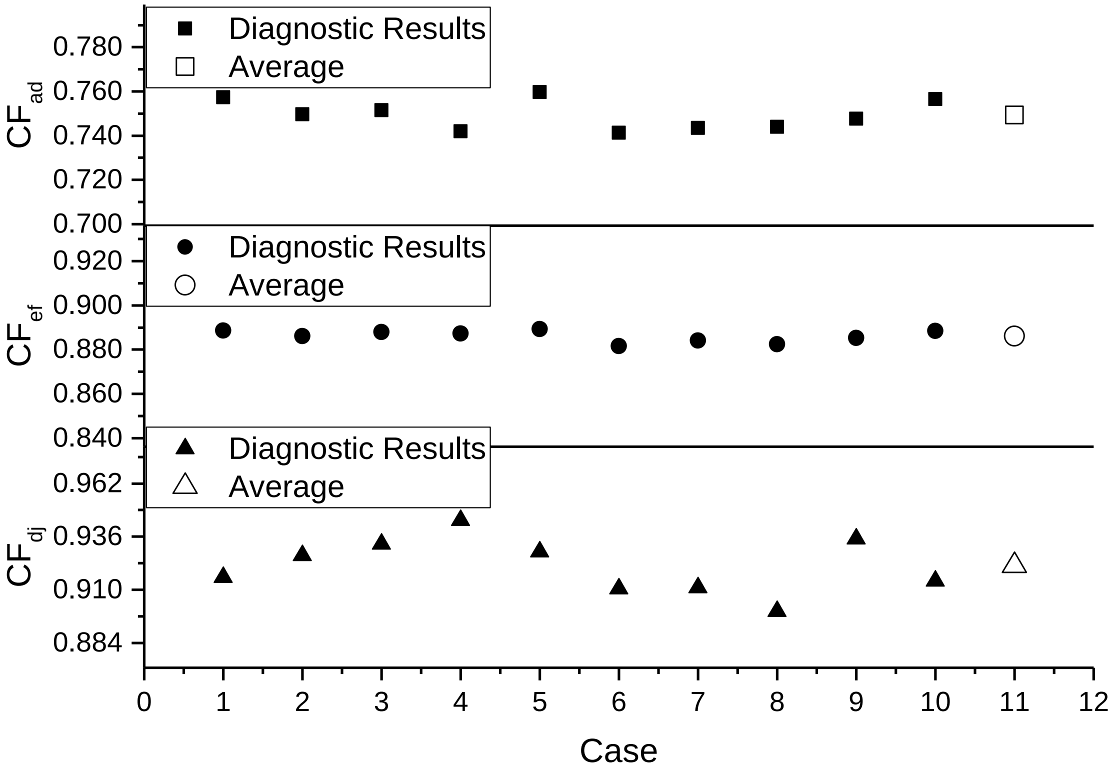

Figure 4-34 Predicted CF and Averaged Value.

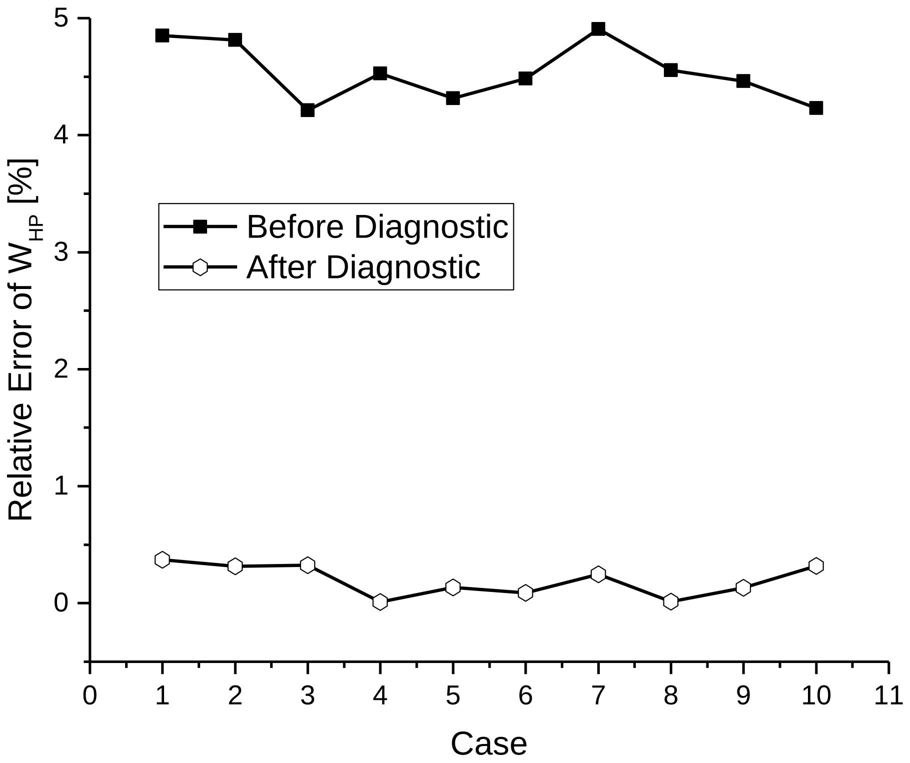

Figure 4-35 Relative Prediction Error of W_{HP} with and without Implanted Degradation.

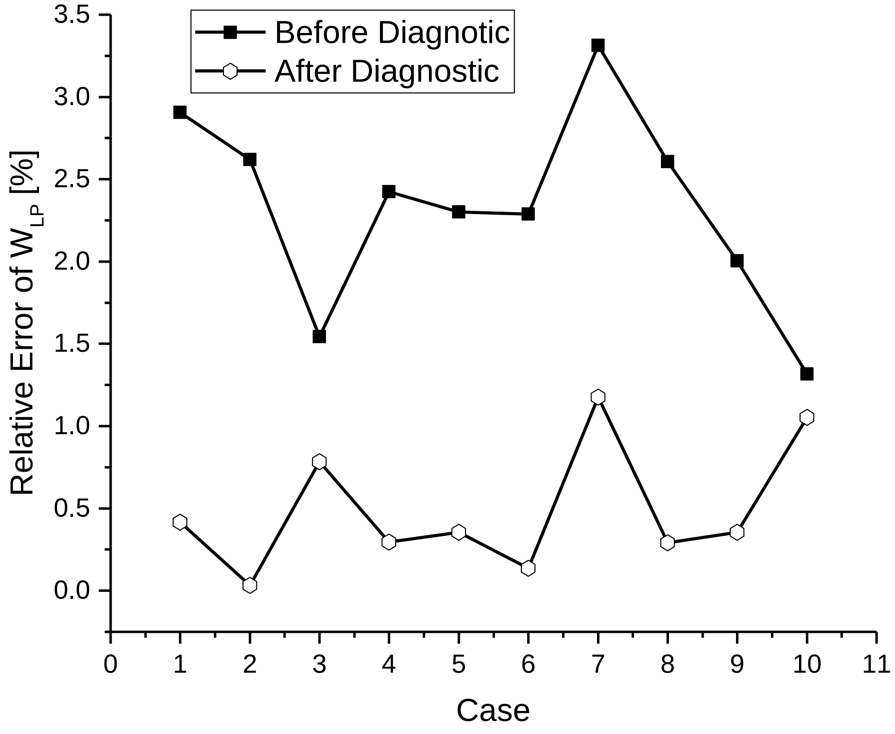

Figure 4-36 Relative Prediction Error of W_{LP} with and without Implanted Degradation.

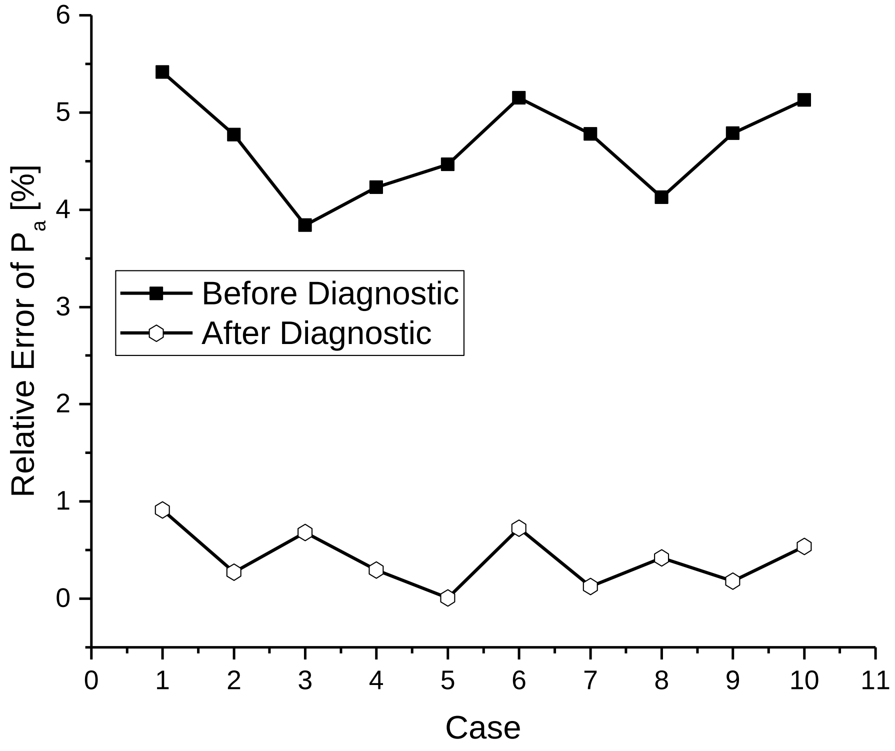

Figure 4-37 Relative Prediction Error of P_a with and without Implanted Degradation.

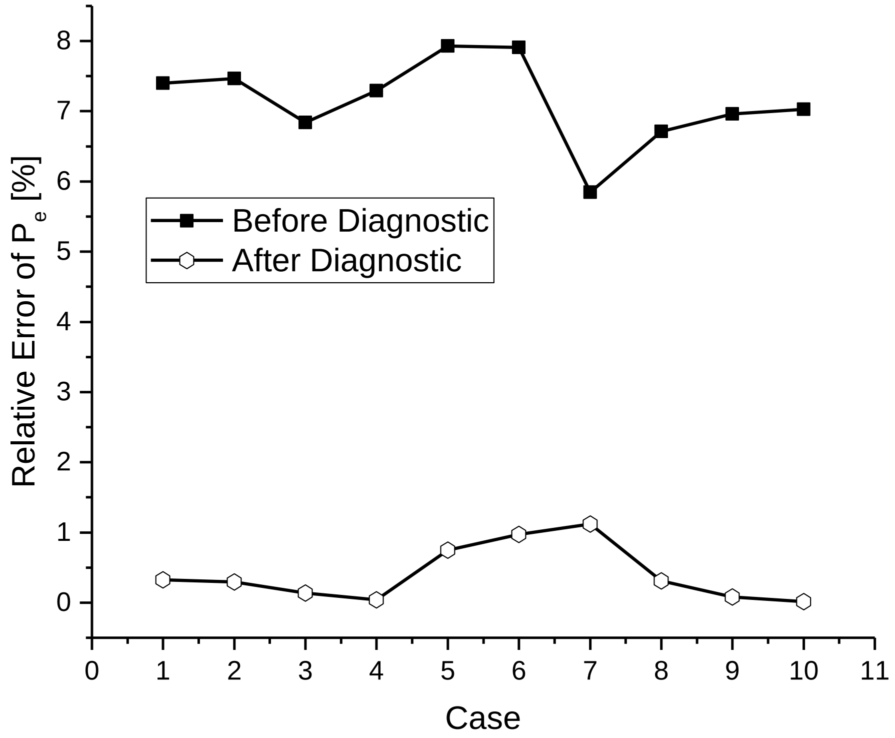

Figure 4-38 Relative Prediction Error of P_e with and without Implanted Degradation.

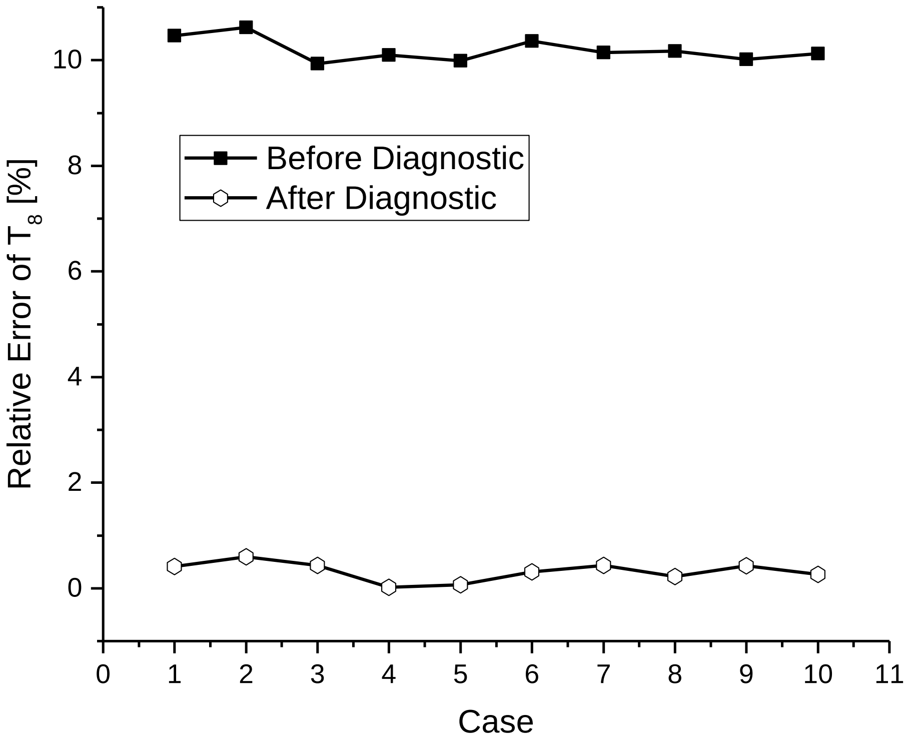

Figure 4-39 Relative Prediction Error of T_8 with and without Implanted Degradation.

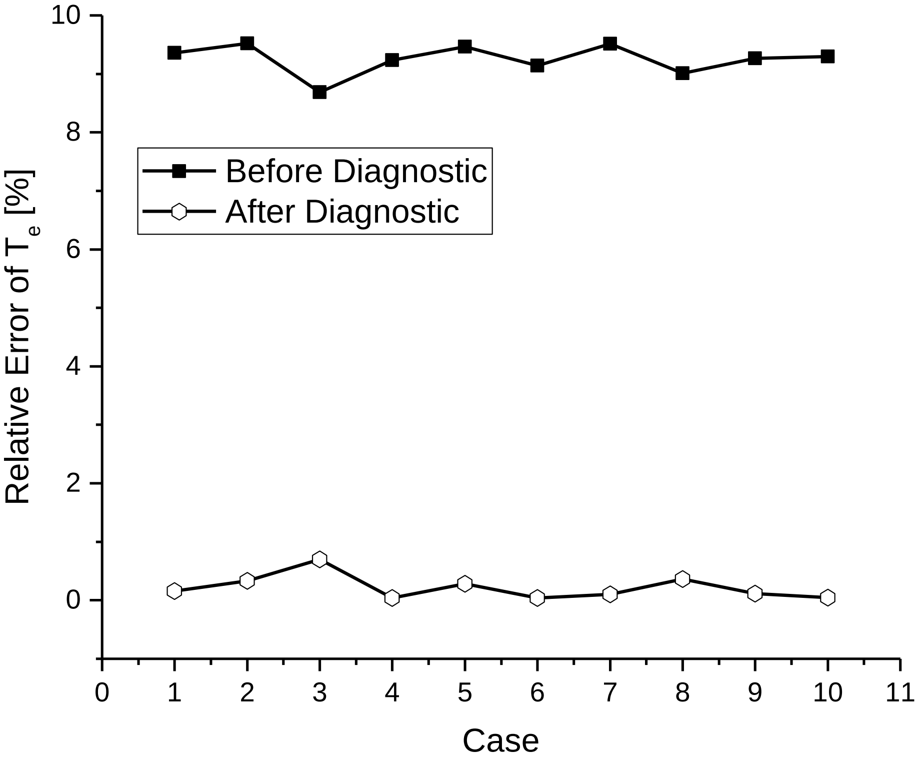

Figure 4-40 Relative Prediction Error of T_e with and without Implanted Degradation.

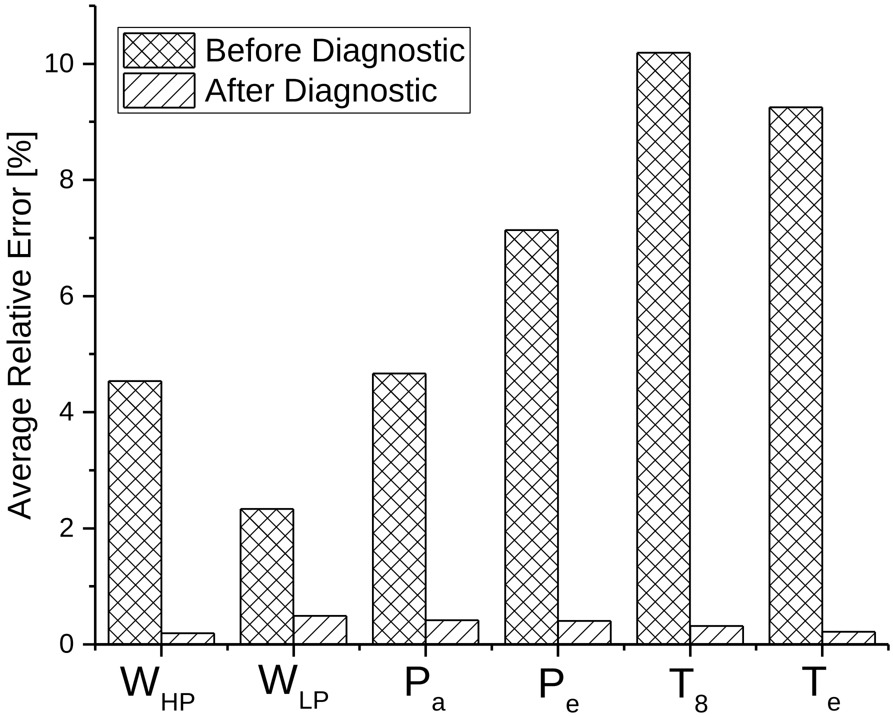

Figure 4-41 Comparison of Relative Errors with and without Implanted Predicted Fouling.

4.3 Decision Support of CCGT Power Plant

4.3.1 CCGT Specification

The GTs in concern are two aero-derived dual shaft industrial engines similar to the GE LM2500+ SAC. The GT includes 17 compressor stages with seven rows of variable guide vanes. The HP and LP turbines comprise two and six stages respectively. The GT specification is shown in Table 4-12.

Table 4-12 GT DP Specification [175]**.**

Symbol	Parameter	Value	Units
PO_{GT}	Power Output	32	MW
PR	Pressure Ratio	23.1	-
N	Power Turbine Speed	6100	rpm
T_{exh}	Exhaust Gas Temperature	498	℃
W_{exh}	Exhaust Gas Mass Flow Rate	89.09	kg/s

The heat recovery boilers at issue are two dual-pressure OTSGs manufactured by IST that the detailed information is mentioned in section 4.1.1.

The ST of interest is similar to a dual-pressure ST designed by Man Turbomachinery and includes an admission steam path. The ST comprises 19 HP stages and 14 LP stages. The ST specification is showed in Table 4-13.

Table 4-13 Steam Turbine DP Specification [175]**.**

Symbol	Parameter	Value	Units
PO_{ST}	Power Output	23	MW
N	Turbine Speed	4818	rpm
x	Exhaust Steam Wetness	11.7	%
P_{cond}	Exhaust Steam Pressure	0.06	bar

As shown in Figure 3-28, three generators connected with two GTs, and one ST respectively. Hence, the rated power of CCGT power plant is 87 MW. The sensitivity study of the CCGT power plant related to the performance, emission, lifing, and economics is presented in Appendix B that the range of x-axis is the same as the GT power setting range (22 - 32 MW) for optimisation.

4.3.2 Typical Day Operation

The typical island power demand DM_{island} and the total demand DM_{total} for both island and island plus grid are shown in Figure 4-42, and Figure 4-43 shows the typical system selling price SSP and ambient temperature T_{amb} profile. Each point represents half an hour time interval (48 points for a day).

The power plant should, itself, satisfy the island's demand, but if it can't, then electricity is purchased from the UK grid and delivered via the cable with no middle price difference assumed. Thus, when the power demand of island is lower than 45 MW, that demand could be satisfied by one of three ways: supply by the island's power plant alone; supply by cable only; and the combination of power plant and cable. Supply by cable only is outside the scope for this study and will not be further discussed.

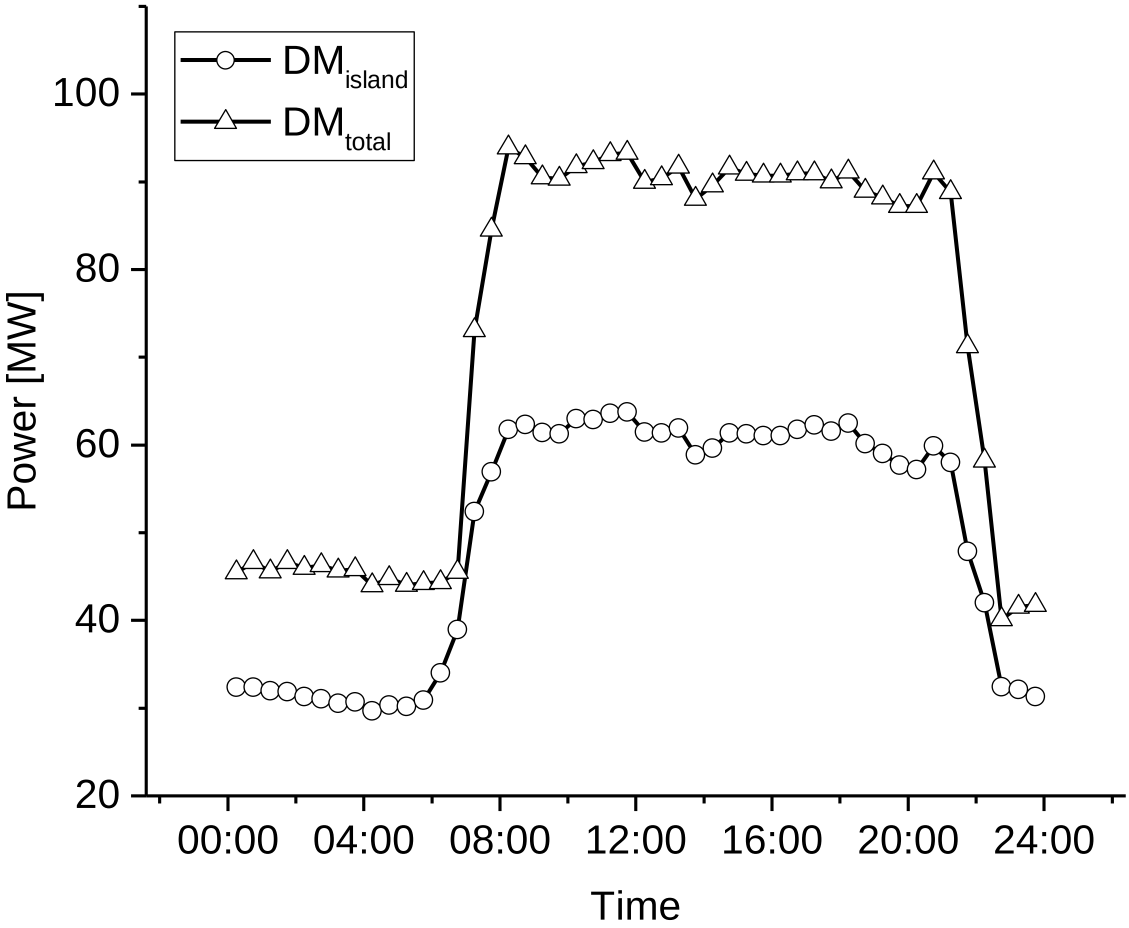

Figure 4-42 Typical Day Load Profile.

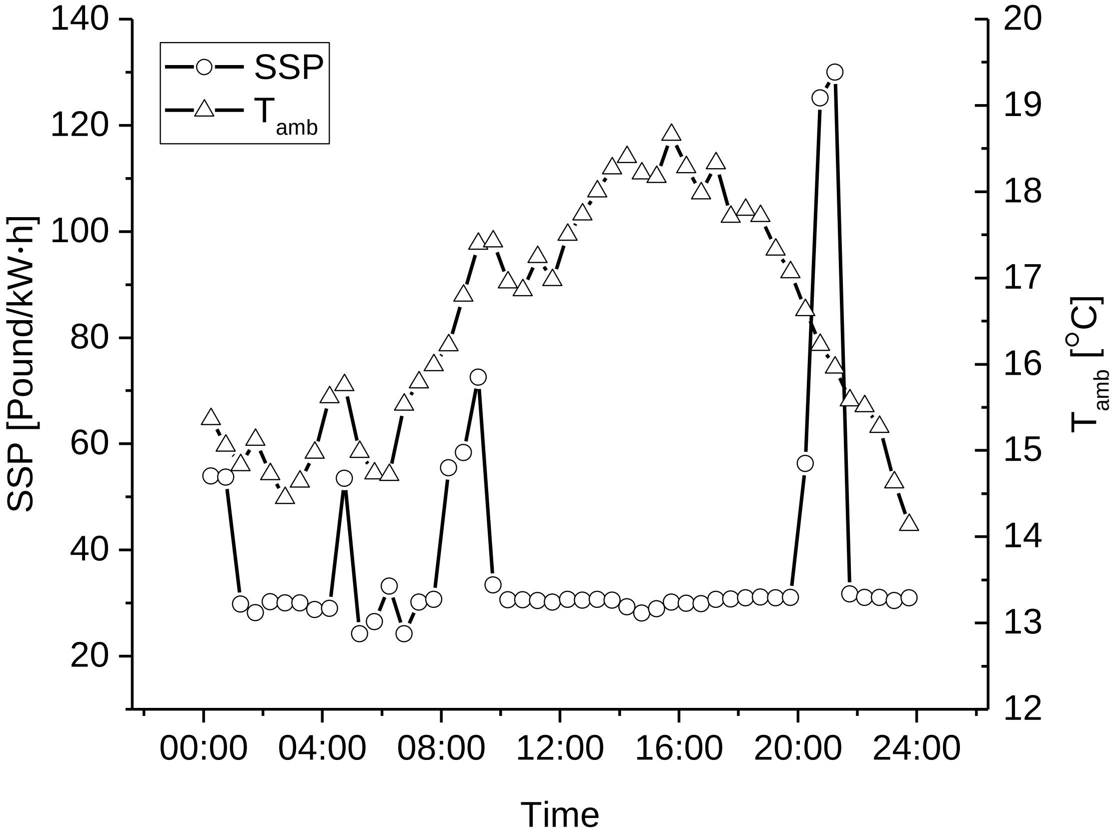

Figure 4-43 Typical Day System Buying (SSP) and Ambient Temperature (T_{amb}) Profile.

If the island demand is higher than the cable capacity and lower than the CCGT power plant capacity. Then, the island power could be supplied by the CCGT only, or by a combination of CCGT and cable. Since the island's demand is less than CCGT capacity, then the power plant could also sell electricity to the UK grid via the cable, provided the grid needed that electricity. If the power plant can cover the island's demand independently and has available capacity for the cable, the allowed maximum power generated by power plant will be the sum of the power demanded on the island, and that supplied to the cable (DM_{total}). If more power is generated than DM_{total} the power plant is unlikely to receive payment for the excess power.

If the island power demand is higher than the CCGT capacity, there is only one way to deal with this situation. The CCGT and cable will supply the power for the island simultaneously.

The challenge is to suggest an operating schedule (engine power settings, engine configurations and cable transmission capacity) for the power plant under different situations (engine health conditions, ambient conditions, electricity price, fuel price, and so on), to provide decision support during daily operation.

4.3.3 Gas Turbine Engine without Degradation

The optimisation result for a typical day from 00:00 to 24:00 (48 time intervals - 30 mines per interval) using the developed graphical user interface software is shown in Appendix C. The results could be summarised in two categories: only operating a single GT with the relevant steam cycle, and operating both GTs with relevant steam cycles. The following will explain the two different optimisation results separately.

Initially, it is assumed the two GTs are entirely the same when without degradation, ignoring any differences in the manufacture, assembly, and site environment. Meanwhile, the two OTSGs are also assumed equally at a clean state.

4.3.3.1 Single Gas Turbine with Corresponding Steam Cycle

The selected example of the operating interval is between 00:00 - 00:30. The power demand of the island is quite low and can be satisfied by one GT and the corresponding steam cycle. The total demand (island demand plus electricity supplied to UK grid via the cable) is 45.45 MW. If two GTs were operated at their lower boundary (22 MW) with the corresponding steam cycle, the CCGT power output could be higher than the DM_{total}. Hence, the power plant should operate only one GT and the corresponding steam cycle. The power plant trading team could forecast power demand and SSP with low prediction error in advance.

Figure 4-44 showed the derived PF and GT power setting from the optimisation system. It is clear to see that the optimised result is the same as discussed above; operating only one GT with the steam cycle for the whole PF that GT7 power output, PO_{GT7}, equals to zero and GT6 power output, PO_{GT6} is between 22 MW and 32 MW. Because, when the CCGT power output is higher than the total demand, the cable transmission load will satisfy the constraint and the result will be filtered automatically. Meanwhile, the base load engine GT6 could operate between 22 MW and 32 MW. If the power generated is less than the island power demand, the electricity will be imported via the cable. If the power generated is more than the island demand, the electricity will be sold through the cable to the UK.

Table 4-14 Operation Condition between 00:00 and 00:30.

Parameter	Value	Unit
Island Demand	32.37	MW
Cable Demand	13.08	MW
Total Demand	45.45	MW
SSP	53.95	$£/(kW \cdot h)$

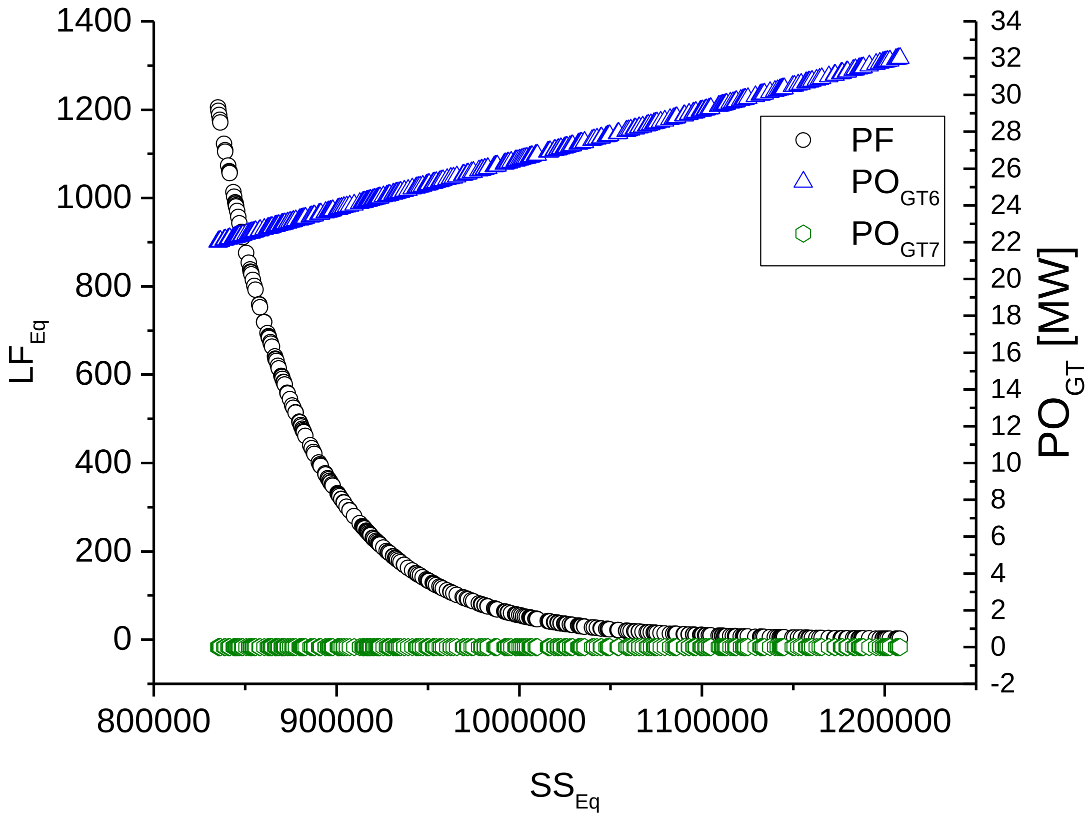

Figure 4-44 PF Searched by MCGA.

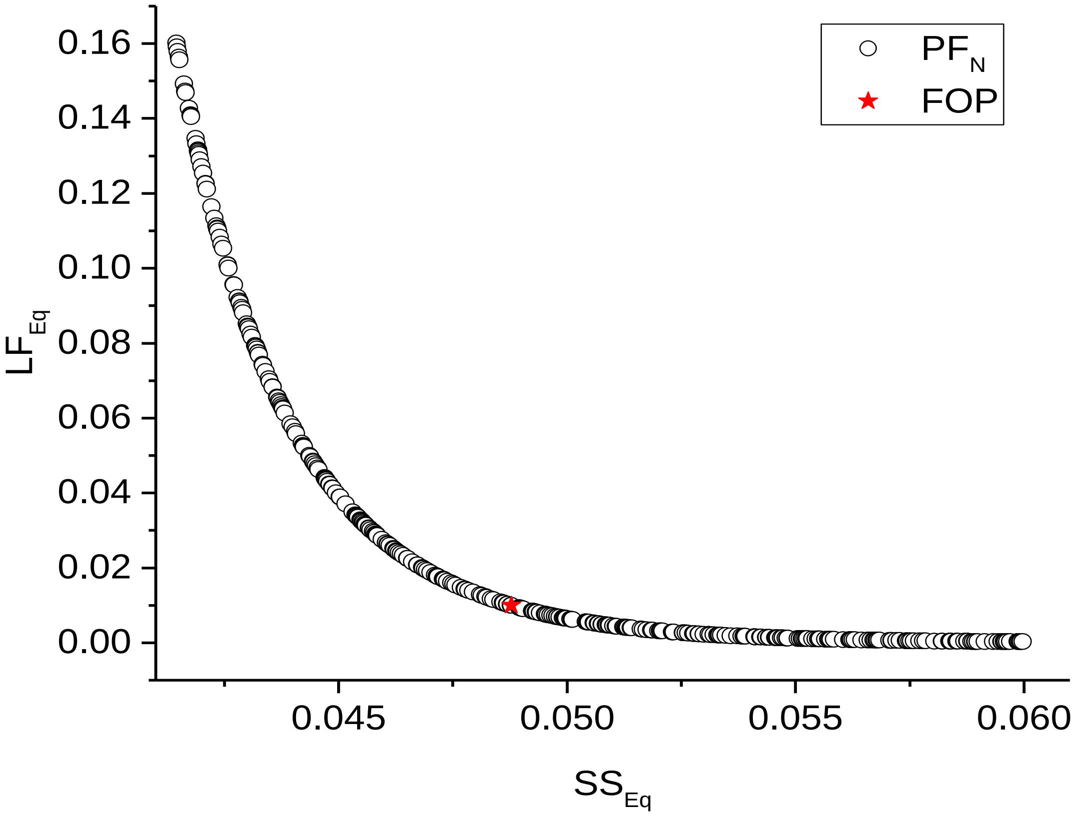

Figure 4-45 Normalised PF (PF_N) and Final Operating Point (FOP).

After the optimisation results are obtained from the MCGA, it is difficult for the power plant operator to decide the operation point directly. Then, the MCDM model is used to determine the final operation point (FOP). The normalised PF (PF_N) will be obtained based on Eq. (3-139) and detailed explanation see Section 3.9.3. Finally, the FOP could be found by cumulative distance and normalised weighted vector that is showed in Figure 4-45.

4.3.3.2 Two Gas Turbines with Corresponding Steam Cycle

The second example operating interval is selected between 11:30 and 12:00, just before mid-day. As can be seen in Table 4-15, the rated CCGT power output is between the island demand and total demand. Hence, the power plant could generate enough power to satisfy the island demand and sell electricity to the UK grid, or it could meet part of the demand via the cable. The maximum allowed CCGT power output may not be the same as the rated power; the power could vary with ambient conditions and engine health state. If the LP turbine inlet temperature is higher than the constrained value, the results will be filtered even the GT power setting is less than 32 MW which could happen at high T_{amb} or/and serious GT degradation.

Table 4-15 Operation Condition between 11:30 and 12:00.

Parameter	Value	Unit
Island Demand	63.75	MW
Cable Demand	29.55	MW
Total Demand	93.30	MW
SSP	30.15	$£/(kW \cdot h)$

Before discussing the results from MCGA, it is necessary to demonstrate the cases study in Table 4-16. When comparing case 1 and case 2, we have the same total GT power output, and the closer the two GT power settings the larger the LCF_{Eq} and SS_{Eq} for the two engines combined. If we change the conditions of case 2 to case 3 by slightly increasing both GT power settings, we see that both LCF_{Eq} and SS_{Eq} are still greater than for case 1. So, case 1 is eliminated by case 2, and case 3 in MCGA by PF selection. If we compare case 2 and case 3, the LCF_{Eq} of case 2 is better than the case 3, however, the SS_{Eq} of case 2 is less than the case 3. Therefore, neither case will be eliminated by the comparison.

If we now reduce the power outputs of both GTs to give case 4 and compare cases 3 and 4, the result is again that neither will be eliminated. We now turn off GT7 and vary the output of GT6 to obtain cases 5-7. Comparing cases 4 and case 5, the SS_{Eq} of case 4 is more than for case 5, but, the LCF_{Eq} of the latter is greater than the former, so case 5 cannot be eliminated. Similarly case 4 is not able to eliminated case 6 as the LCF_{Eq} of case 6 is better than case 4. Finally, if we compare case 4 and case 7, we see that case 7 will be eliminated by case 4.

This means that for the specific condition of only a single engine with corresponding steam cycle, the optimum operation (PF) will also be obtained through MCGA by a limited operating range. Those cases are eliminated that are the non-optimal solutions, and the remaining are the set of PF.

Table 4-16 Case Study of Different Operating Conditions.

Case No.	PO_{GT6} [MW]	PO_{GT7} [MW]	PO_{ST8} [MW]	SS_{Eq}	LCF_{Eq}
Case 1	30.00	28.00	19.264	1179143.83	3.58
Case 2	29.00	29.00	19.266	1179170.40	4.21
Case 3	29.25	29.25	19.427	1189263.77	3.62
Case 4	22.00	22.00	14.884	898553.73	459.09
Case 5	22.00	0.00	7.442	449256.87	918.19
Case 6	22.50	0.00	7.890	463730.08	629.95
Case 7	23.00	0.00	7.748	469189.13	436.45

The PF obtained using MCGA shows a discontinuity with SS_{Eq}, see Figure 4-46. This is because the line on the left of the plot refers to operating only a single GT and corresponding steam cycle and operating only a single GT with low power setting, gives a relatively low value to the SS_{Eq} when compared with dual GTs. Hence, there is a discontinuity for the PF when switching from one to two GTs.

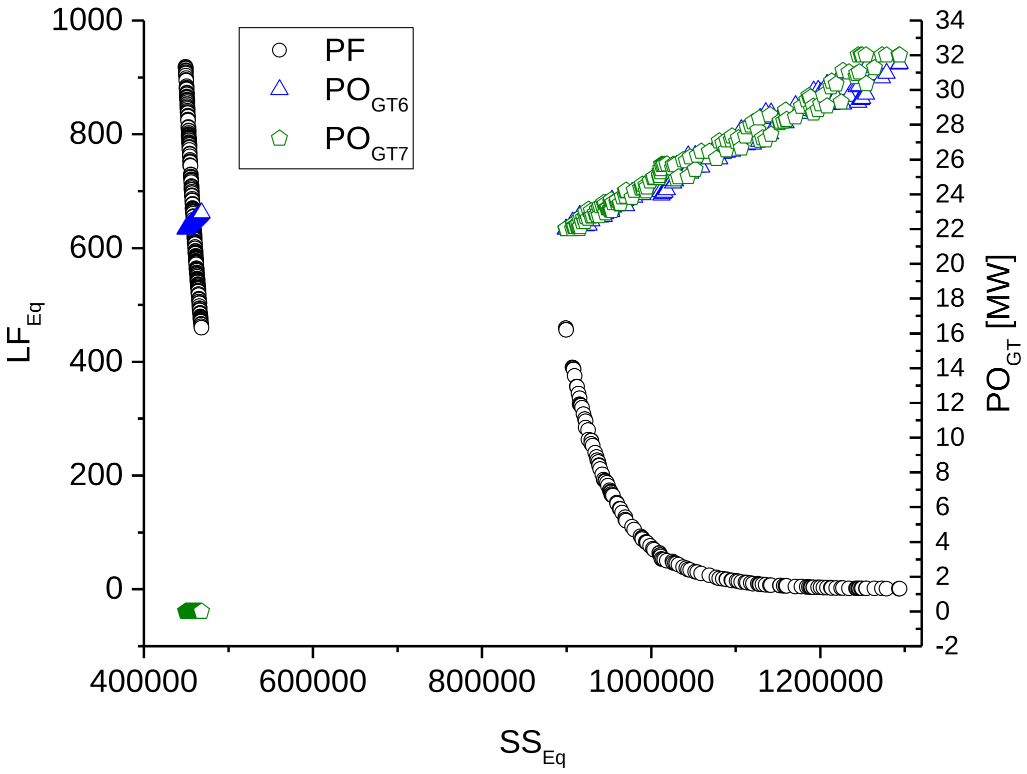

Figure 4-46 PF Searched by MCGA.

Figure 4-46 also shows the power setting when the two GT outputs are close to each other, which demonstrates the second objective of obtaining minimum life consumption for two engines by suitable power allocation. Meanwhile, the variable (GT power setting) shows the same characteristic as discussed in the previous paragraph, see Table 4-16. The FOP selection is shown in Figure 4-47 based on MCDM, and detailed explanation see Section 3.9.3.

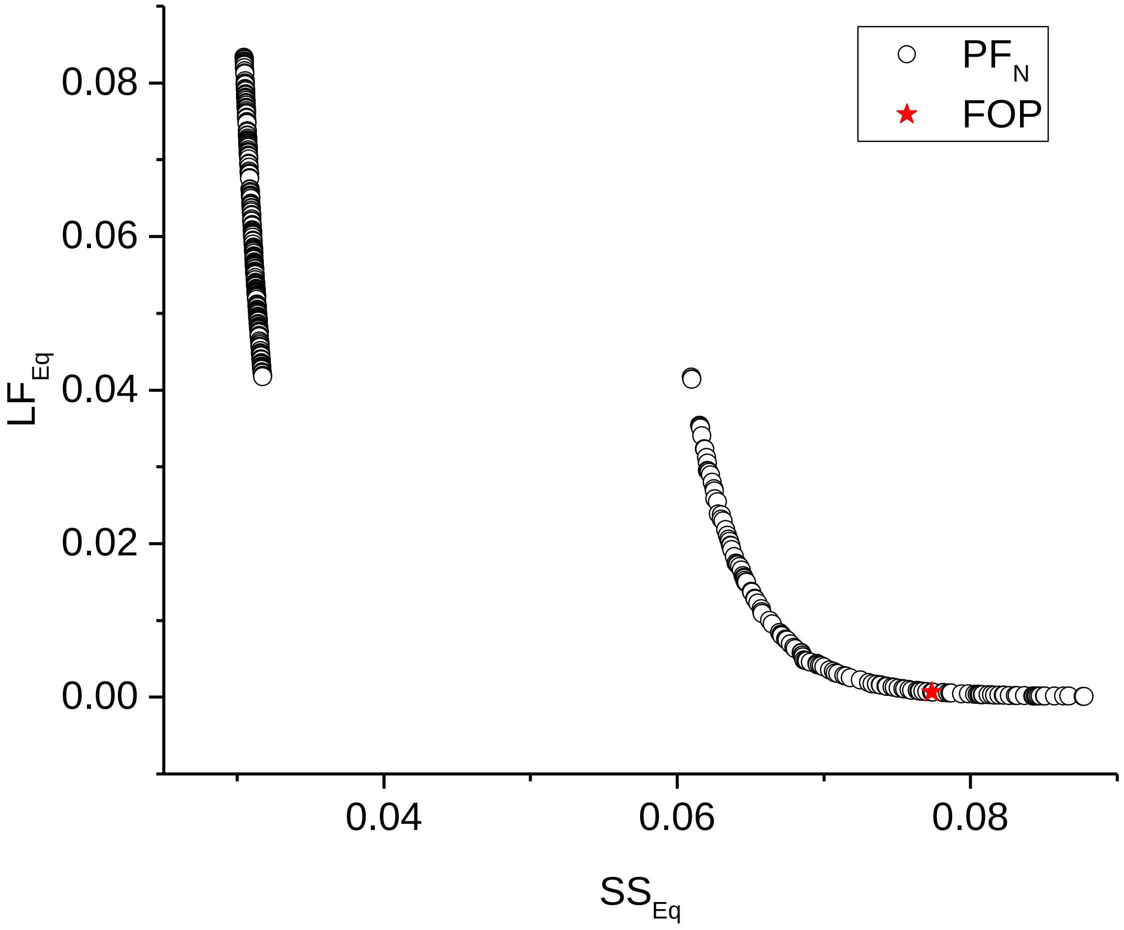

Figure 4-47 PF_N and FOP.

4.3.3.3 Typical Day Optimisation without Degradation

The Section 4.3.3.1 and 4.3.3.2 presented an analysis of two results obtained from Appendix C, and each case suggested a final operation point. The final decision for the operation points for a typical day is shown in Figure 4-48. It was found that there were two time intervals (06:30-07:00, and 22:00-22:30) during which the power plant should import electricity from the grid to help satisfy the island’s demand.

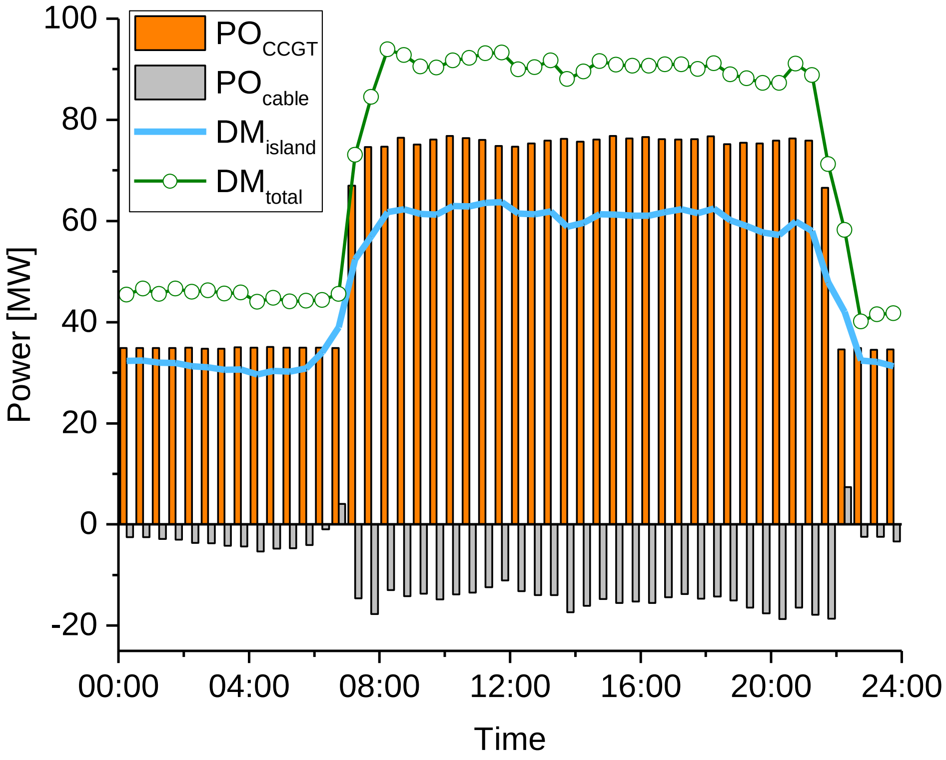

Figure 4-48 Suggested Trading Schedule without Degradation.

Figure 4-49 shows the SS_{Eq} for the suggested operation point as obtained by MCDM. It was found that the SS_{Eq} has a very similar overall trend when compared with the SSP in Figure 4-43, and the PO_{CCGT} will effect the amplitude of SS_{Eq} as well that $Income$ is dominated in Eq. (3-136).

In the early morning and late evening, the power plant will operate with only a single GT and corresponding steam cycle. Hence, the LCF_{Eq} will be higher than the values obtained when operating two GTs, see Figure 4-50. However, there are two exceptions; at times earlier than 07:00 (before the 15th point on the plot), the power plant operates only a single GT with the corresponding steam cycle at relatively high power setting. At 07:00-07:30 (the 15th point) the second GT and its steam cycle come on stream due to the increased power demand. This demand can be shared by two GTs at relatively low power settings but that reduces the GT life consumption. Subsequently, the power demand increases further and that requires the GT to run at relatively high power setting. At 21:30-22:00 (the 44th point) we see a reduction of power demand but the power plant is still able to operate both GTs and corresponding steam cycle, though at relatively low power settings. After this point, the power plant will shut down the peak load engine and run a single GT and corresponding steam cycle at relative high power setting.

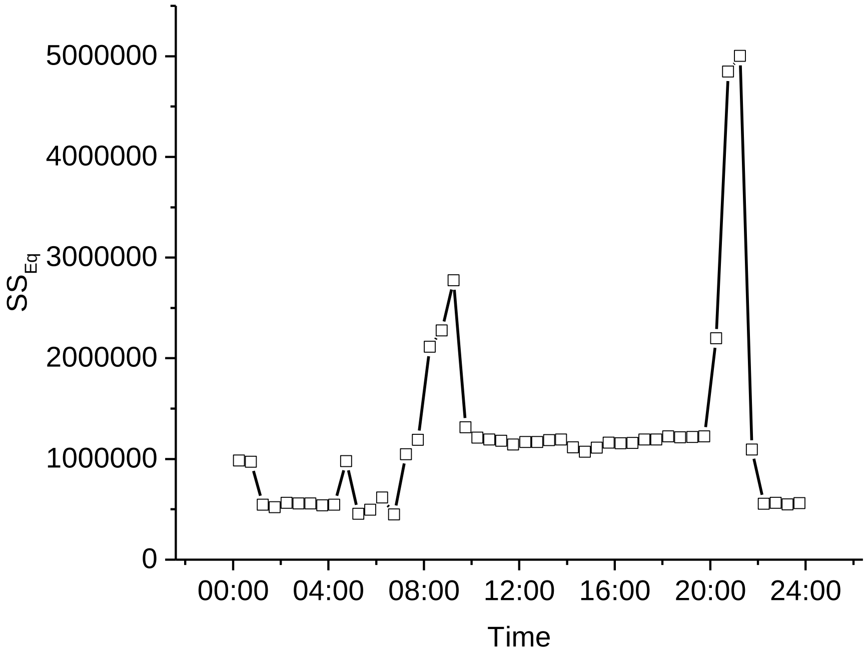

Figure 4-49 SS_{Eq} for Typical Day Operation.

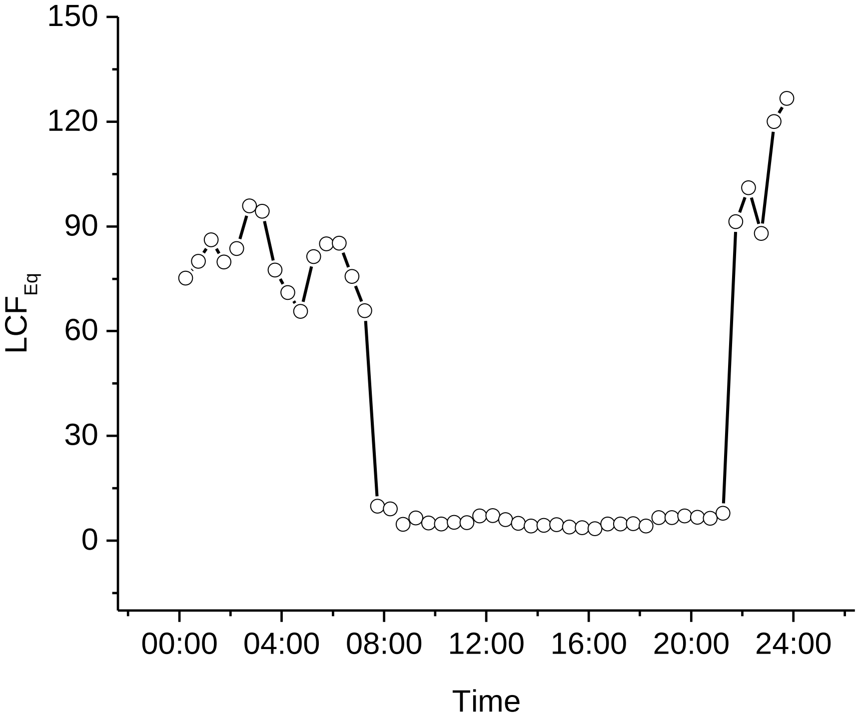

Figure 4-50 LCF_{Eq} for Typical Day Operation.

4.3.4 Gas Turbine Engine under Degradation

As discussed above, the power plant will operate a single GT and corresponding steam cycle in the early morning and late at night even though two GTs are available. Hence, even though the two GTs were installed at the same time. The healthy condition tends to be different; thus, the same power setting will consume different creep life for two GTs. Figure 4-51 shows the effect on creep factor of degradation level for the same ambient conditions and power settings. Assuming GT compressor (efficiency, pressure ratio, and flow capacity) deteriorated from 1 to 0.9. It was found that the GT creep life consumption increased exponentially with degradation level.

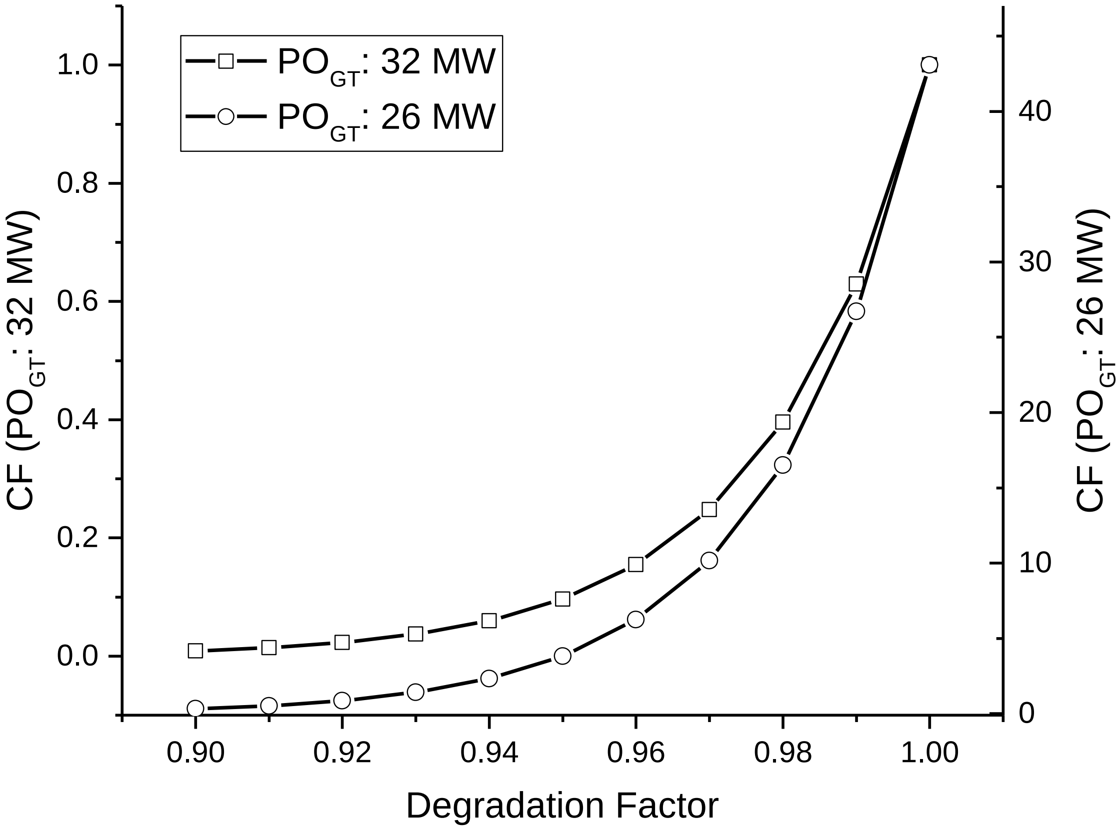

Figure 4-51 Effect on Creep Factor of GT Degradation Factor.

Therefore, it is necessary to propose an algorithm to guide the power plant operation when the two GTs have different health conditions. It is not as easy as a clean state, when the GT power settings would be equal, as discussed above and demonstrated by the PF in Section 4.3.3. The healthier engine should be run harder relative to the more degraded engine, because the creep life changes with

GT power setting for the same health condition (Figure-Apx B-6). This was a primary reason for proposing the optimisation system for power plant operation. A lower power setting to extend the engine creep life will compensate for faster life consumption caused by engine degradation. The GT6 is assumed under the degraded condition, and the implanted degradation is as shown in Table 4-17.

Table 4-17 Assumed GT6 Engine Degradation.

Component	Degradation Parameter	Level [%]
Compressor	Efficiency	-2.0
Compressor	Flow Capacity	-2.0
Compressor	Pressure Ratio	-2.0
HP Turbine	Efficiency	-1.5

4.3.4.1 Typical day Optimisation with Degradation

The single operation point analysed in Section 4.3.3.1 and 4.3.3.2 will not be repeated here. Figure 4-52 shows the PF, PO_{GT6}, and PO_{GT7} found by MCGA search and is clear that the GT7 tends to operate at a higher power setting when compared with GT6. This is one of the significant benefits for the proposed decision support platform; that the power split between different engine units is suggested. Figure 4-53 shows the FOP selection from normalised PF by a weighted factor.

Figure 4-54 shows the operational results suggested by MCGA. Meanwhile, the FOP is still decided by the weighting factor and PF together. That does not mean the CCGT power output should always be less under deteriorated conditions, because of the LCF_{Eq} is only one objective, and SS_{Eq} should not be ignored. The suggested operation points are always a comprise between spark spread and life consideration as determined by the predefined weighting factor.

The SS_{Eq} and LCF_{Eq} are showed in Figure 4-55 and Figure 4-56 respectively for both clean and the degraded condition. It was found that the SS_{Eq} is very close for both the clean and degraded conditions, see Figure 4-55. For LCF_{Eq}, the life consumption is much greater under the degraded condition when compared with the clean state in the early morning and late at night. This is because only GT6 and corresponding steam cycle are running, hence it is not possible to reduce the GT6 power setting by using power from the GT7 engine set.

For those points, both GTs are operating with the corresponding steam cycle, the LCF_{Eq} maintains the same level with the clean state, and that demonstrated the benefit of developing a decision support framwork. The LCF_{Eq} is close for the two conditions (clean and degraded) except at 07:00-07:30 (the 15th point) and 21:30-22:00 (the 44th point) when the two GTs operate at a relatively low power setting. According to Figure-Apx B-6, the life fraction change is relative small at a low power setting. Hence, even if the GT7 is operated at a higher power setting than the GT6, the effect of total life consumption by power allocation is much less than when compared to a high power setting.

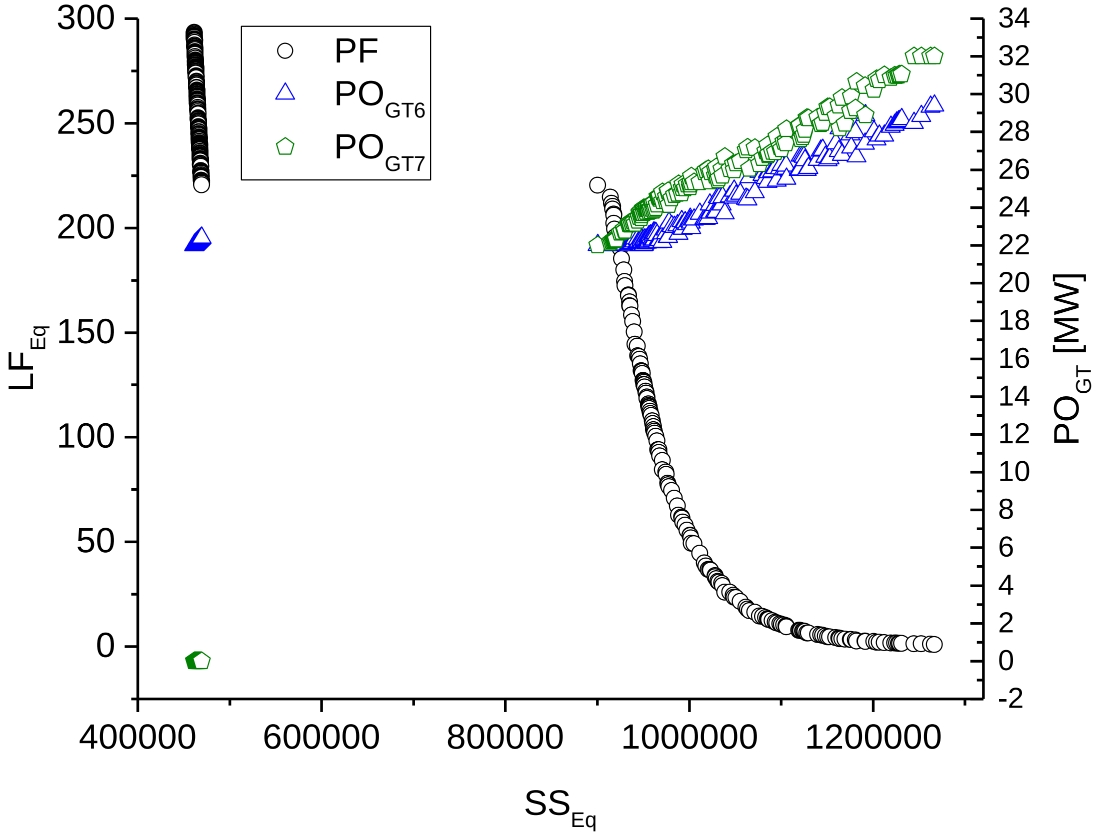

Figure 4-52 PF Found by MCGA Search.

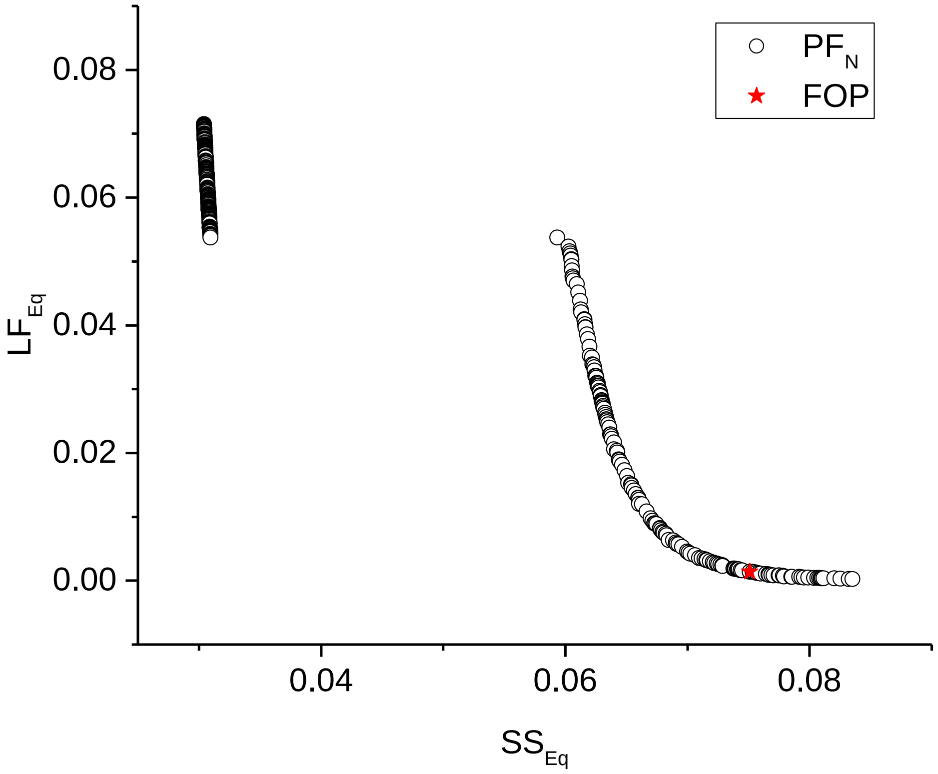

Figure 4-53 FOP Selection from PF_N.

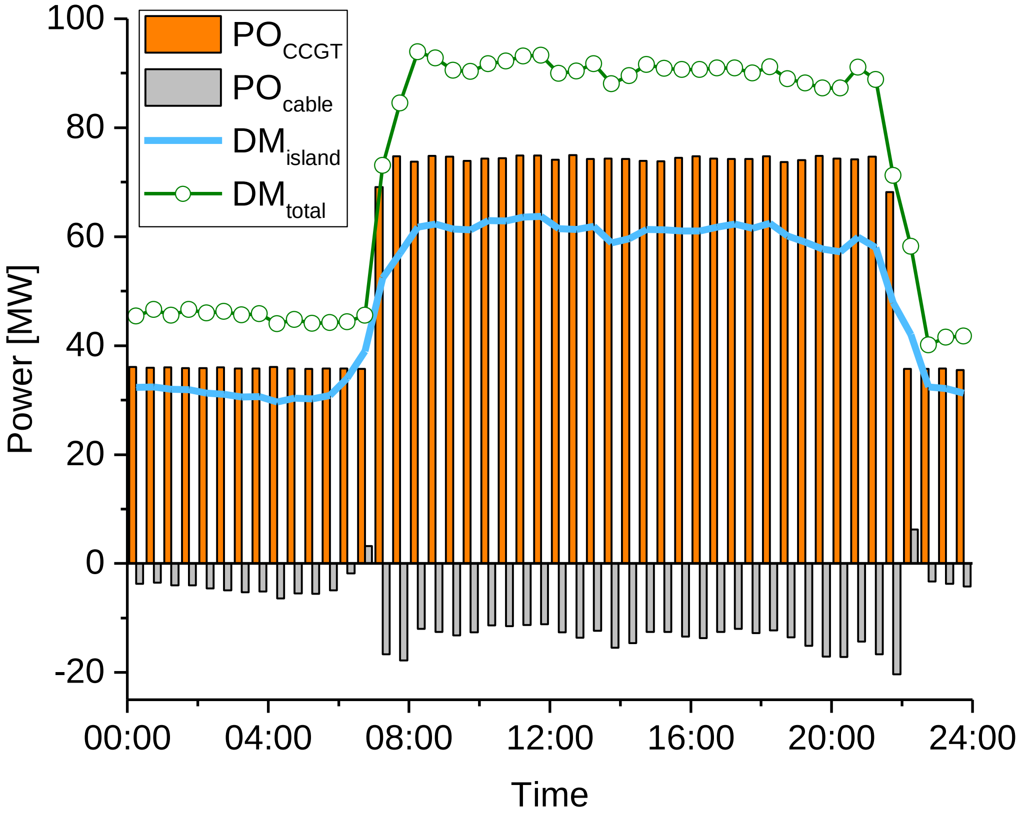

Figure 4-54 Suggested Trading Schedule under Degradation.

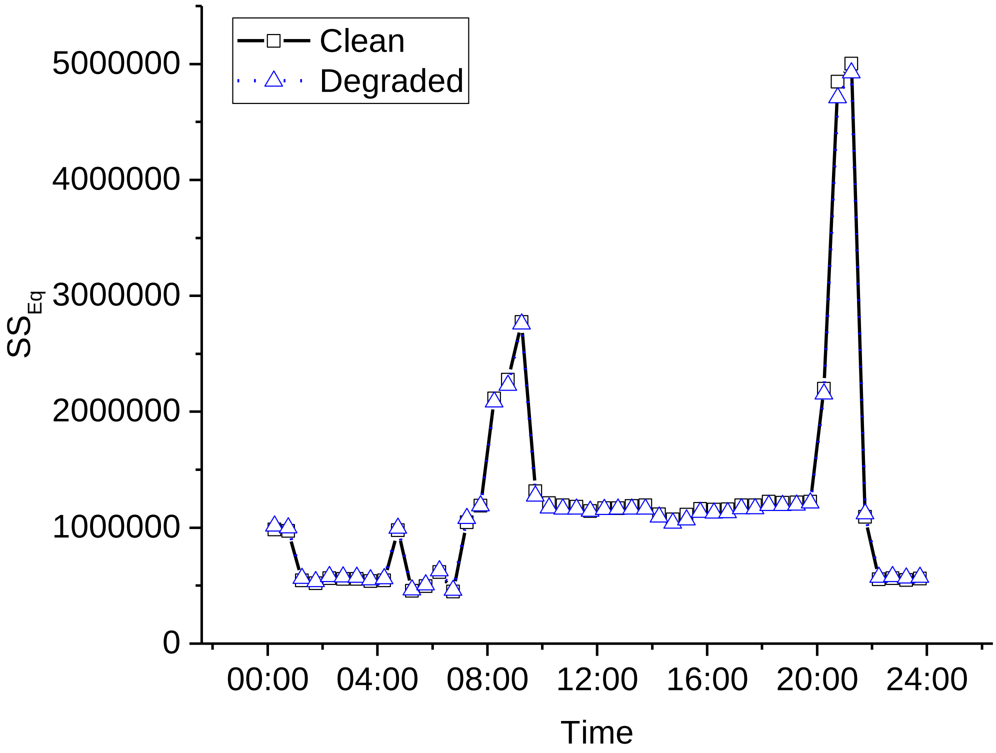

Figure 4-55 SS_{Eq} under Suggested Typical Day Operation.

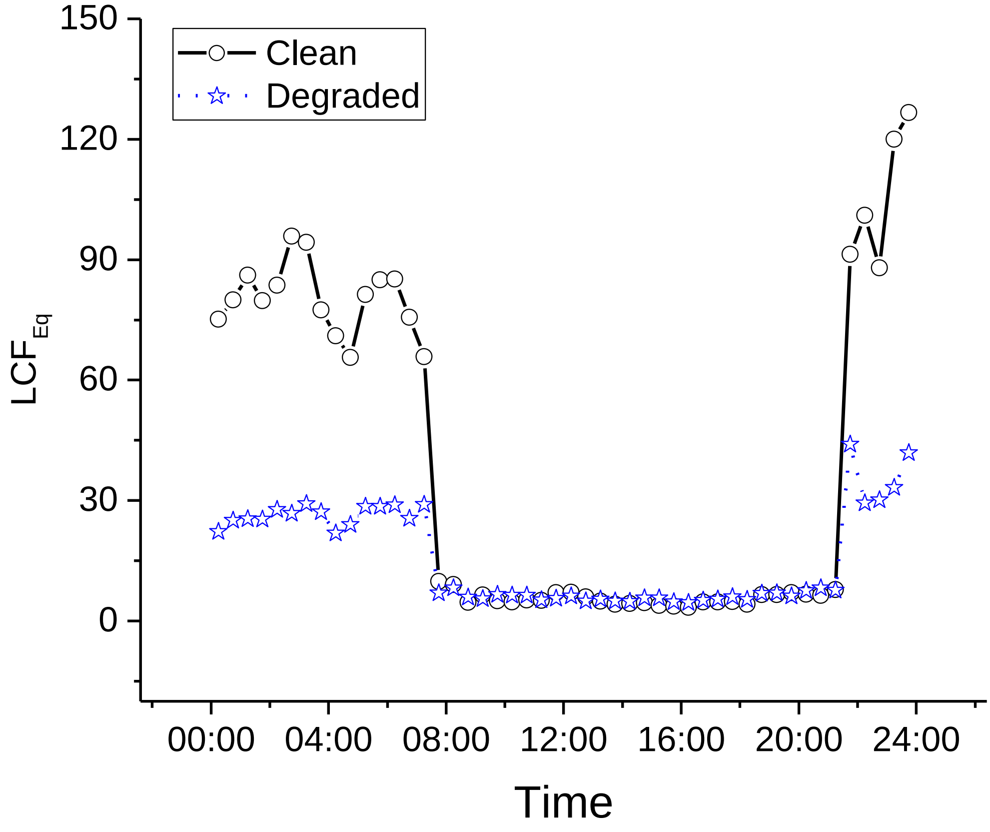

Figure 4-56 LCF_{Eq} under Suggested Typical Day Operation.

4.3.5 Comparison between Optimised and Original Operations

As mentioned before, the original operation of the CCGT power plant is keeping the power setting of two GTs the same when both engines in service. It is necessary to compare the origin operation with optimal operation. The SS_{Eq} is kept the same for original operation scheme and optimal operation suggested by the decision-making system. Figure 4-57 showed through GTs power allocation, the LCF_{Eq} is increased when maintaining the same SS_{Eq}. Figure 4-58 showed the enhancement of LCF_{Eq} in percentage and the average improvement is 9.81% for all those dual GTs in operation for the typical day. It is evident that the operation optimisation system could help achieving high economic benefit without over consuming the gas turbine hot section life.

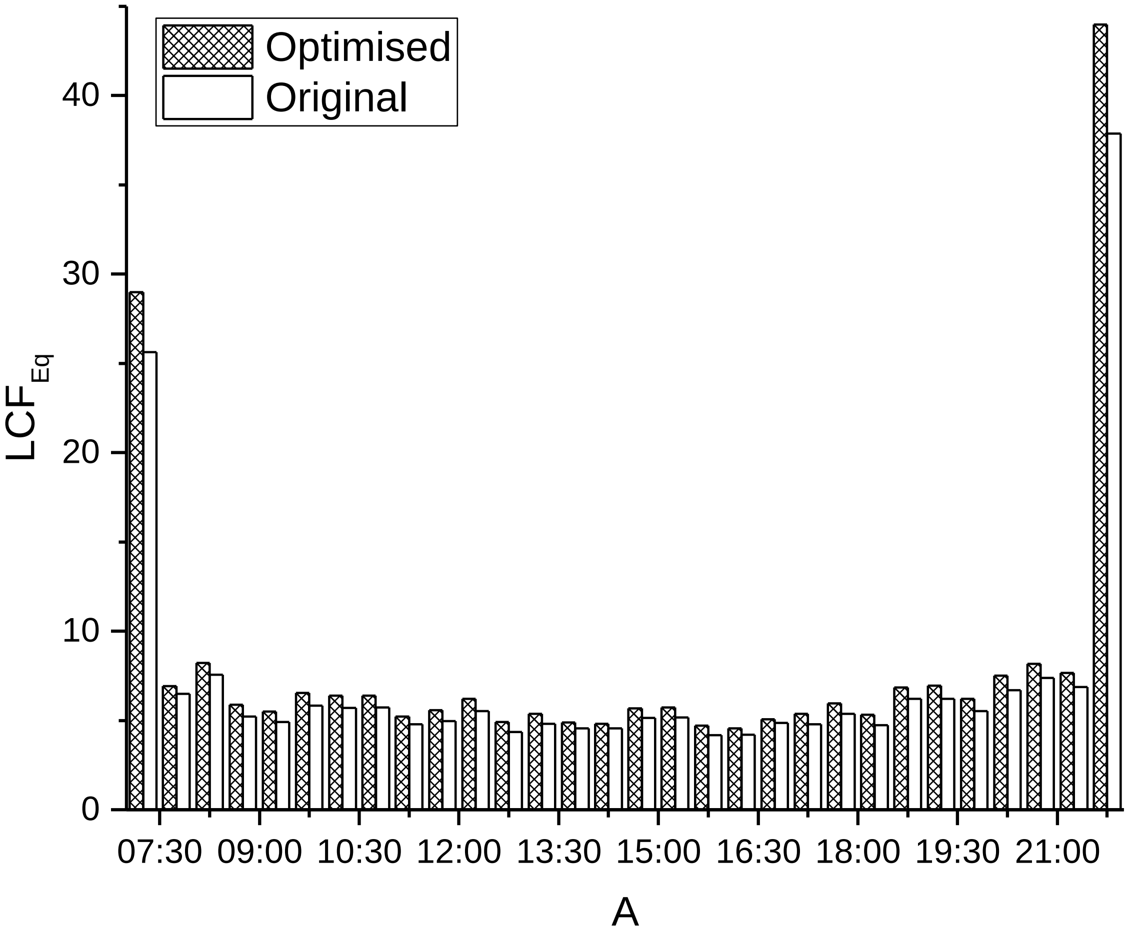

Figure 4-57 Comparison between Optimised and Original Operation in LCF_{Eq}.

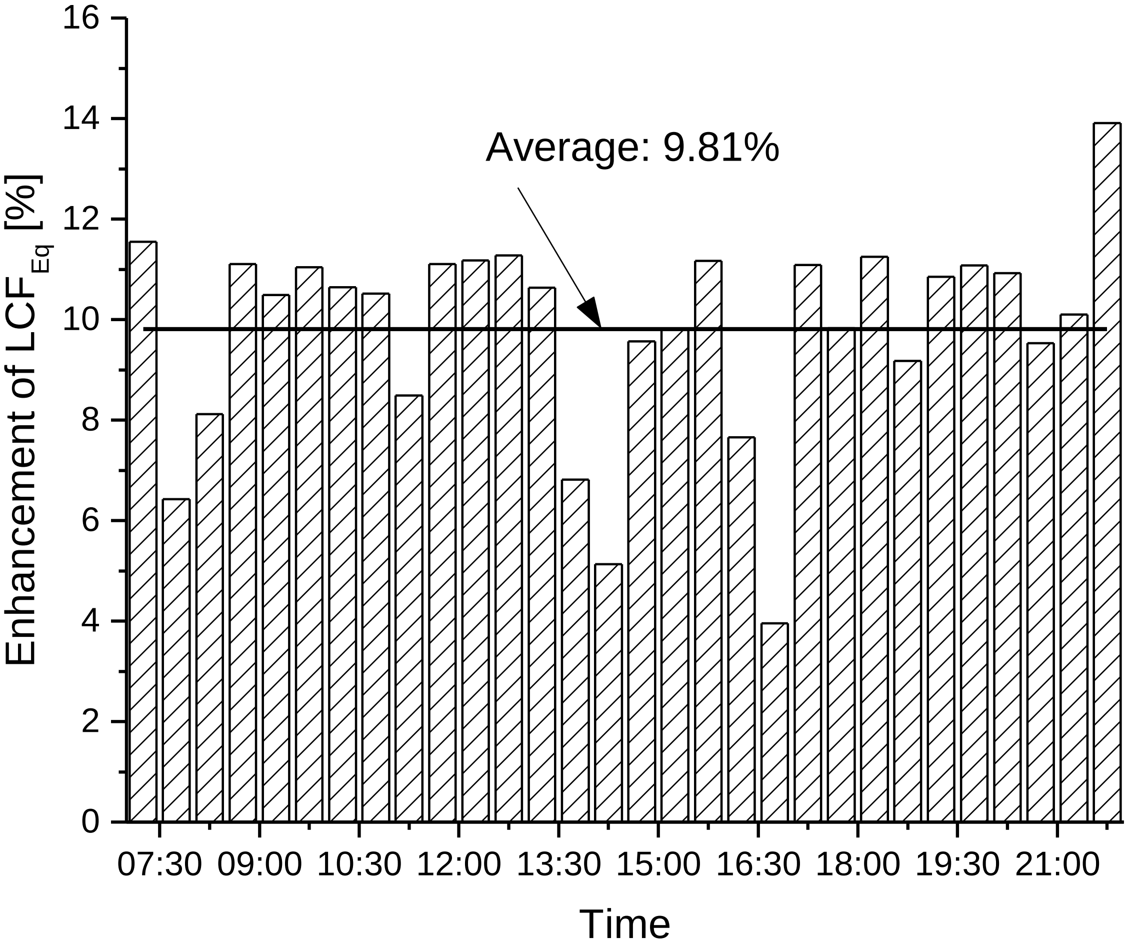

Figure 4-58 Enhancement of LCF_{Eq} in Percentage.

4.3.6 Conclusions

Actually, the power plant operator could decide whether to operate a single or dual GT with corresponding steam cycles by analysing the power demand. Power splitting between GTs under clean state conditions is also easy to decide, requiring equal power allocation. In such circumstances, the MCGA appears unnecessary for obtaining the PF for power distribution. Only the MCDM is needed to apply the FOP selection from a sensitivity analysis of power plant thermoeconomic and lifing.

However, when the two GTs are in different health states, the power split should not be by equal distribution of power. It is better to run the healthier engine at a relatively higher power setting to avoid over-consuming the engine life of the more severely degraded engine, and so obtain a larger LCF_{Eq}. Hence, the decision support framework combines the MCGA and MCDM with thermoeconomic and lifing models. Moreover, different health states for engine units is the real-life scenario in power plants where one is the base load engine set, and the other is the peak load engine set. The base load engine tends to degrade more than the peak load engine over the same calendar time, since the base load engine will be operated for a longer time. The case of a GT engine without degradation was used to test the decision-support framework developed here.

It is necessary to emphasise that the optimisation system is applied for each time interval (half an hour) and it is not to optimise the whole day operation directly. Meanwhile, it is assumed steady-state operation in each time interval that does not need to consider the low cycle fatigue during optimisation. The low cycle fatigue is related to load changing that requires the taking into all-time intervals during daily operation, which is beyond the scope of the optimisation system. In addition, as showed in Figure 4-48 and Figure 4-54, the base load engine operated 18 hours longer than the peak load engine set for the typical day. Besides, Figure 3-29 showed the effect of low cycle fatigue on GT hot section life consumption is less than 15%. Hence, even the peak load engine operated with daily shut down, but the total life consumption considered creep-fatigue interaction of the base load engine unit is still faster than the peak load engine set.

The operational condition and state of power plant engines will vary with time. It is necessary to propose a universal framework that can handle the operation of both single and dual engine units automatically, rather than the plant operator making a manual judgement on plant loads. Meanwhile, based on the decision support framework, the decisions regarding total power output and power splitting could be model-based, rather than experience-based. It is necessary to emphasise that the PF obtained means that no able to find a solution could be better than both two objectives at the same time. It is essential to be aware that the MCGA is trying to approach the best solutions. This means the MCDM is selected from the best solution sets. However, like the iteration stopping criteria, the iteration will terminate when the relative error less than a pre-set threshold.

The MCGA is similar; generation will stop when the stopping rule is satisfied. Hence, the final PF is the set of optimal solutions found by MCGA in the specified and limited evolution that no guarantees PF are the actual best solutions. Moreover, the more potent of MCGA will get closer results to the ideal PF in the same generation.

5 Conclusions

The primary objectives of this study were threefold:

- To develop a reliable thermodynamic performance simulation model for parallel dual-pressure once-through steam generator (OTSG).
- To propose a gas path diagnostic system to quantify the fouling level of OTSG.
- To establish a techno-economic methodology for decision support of combined cycle gas turbine (CCGT) power plant operation optimisation that taking into account life usage and economic benefits.

5.1 Once-through Steam Generator Performance Simulation

In this study, a novel algorithm for the design point (DP) and off-design (OD) thermodynamic performance simulation of a parallel dual-pressure OTSG is presented. It considers dual pressure parallel circuits and moving boundaries between the economiser, evaporator, and superheater of both the high pressure and low pressure steam circuits. The new method has been applied to the simulation and prediction of the performance of an OTSG installed in a CCGT power plant located at Manx Utilities, Isle of Man, United Kingdom. A comparison between the predictions and the OTSG field data show that the proposed method offers accurate prediction of the OTSG performance with maximum average prediction error for individual measurements being less than 0.8%, 1.5% and 3.2%, for design point, dual-pressure operation at off-design and single-pressure operation at off-design respectively.

The proposed simulation method can help in the construction of OTSG simulations to predict the likely performance of new or existing dual pressure OTSG systems with parallel circuit configurations under both DP and OD operating conditions including consideration of moving boundaries between the economiser, evaporator, and superheater. The proposed simulation is also able to model the impact of prime mover part load, and downstream ST erosion on the OTSG performance.

5.2 OTSG Performance Diagnosis

The present study has introduced an effective non-linear gas path analysis (GPA) diagnostic method using gas path measurements from the OTSG as inputs to predict the fouling of the OTSG as determined by the change in a parameter defined as the Cleanliness Factor (CF).

The application of the diagnostic method in three test cases showed that the relative prediction errors of the implanted fouling are within 0.002% for CF and this solution can be obtained within 20 iterations if measurement noise is not a factor. Measurement noise has a negative impact on GPA predictions, with prediction errors of 4.2% and 0.3% for raw noisy data and pre-processed measurements respectively. Such prediction errors are regarded as small and acceptable for engineering applications. Application of the method to real field data obtained from an OTSG in a CCGT power plant operated by Manx Utilities, indicates that the method is able to provide useful information concerning OTSG fouling. Such diagnostic information can usefully contribute to guide condition-based maintenance of the OTSG. Theoretically, this approach could be applied to the diagnostic analysis of different types of OTSGs.

5.3 Operation Optimisation of CCGT Power Plant

This study has also established a decision support framework for thermo-economic and lifing optimisation of a CCGT power plant for daily power plant operation that changes control of the operation from experience-based to model-based. The proposed universal decision support platform for plant operation optimisation can accommodate the operation of both single and dual engine units automatically, rather than the plant operator making a personal judgement on plant loads. The decision support framework included a combined cycle performance model, gas turbine (GT) high-pressure turbine life model, emission model, economic model, optimiser, and decision-making model. The framework was applied to the CCGT power plant at Manx Utilities and recommended optimal operation schedules to the power plant operator. Concrete results have been suggested for a typical day's operation to decide the total power output and power split between the turbines for varying power demand, and GT engine health states, ambient conditions, and electricity price. It suggests running the healthier engine at a relatively higher power output to stop over-consumption of the engine life of the more severely degraded engine. Comparison between original operation (the same power setting for two GTs) and optimal operation (power allocation) showed an average enhancement of 9.81% in equivalent life consumption factor (LCF_{Eq}) for maintaining the same equivalent spark spread (SS_{Eq}). The decision support framework considered of thermoeconomic and lifing that is the outcome of this project is able to significantly assist the future operation of CCGT plants generating electricity for domestic and industrial consumption.

5.4 Overall Conclusion

The objectives of this study for both academic and industrial concerns have been achieved. A novel parallel dual-pressure OTSG performance model has been successfully developed. The established OTSG gas path diagnostic system can be applied to support the OTSG condition monitoring. The proposed decision support platform for power plant operation optimisation could help the plant operator to decide total power generation and guide the division of power between GTs during daily operation.

6 Future Work

This research has generated many questions that need further investigation. These are listed below.

6.1 Dynamic Model for the CCGT

The objective of this study was to develop a steady state simulation model for CCGT performance optimisation. An obvious development would be to extend the model to include the transient behaviour of the CCGT power plant. This would extend knowledge of plant dynamic operation behaviour. The development of a dynamic model for the CCGT will be extremely useful for modelling the start-up and shutdown behaviour of the power plant. Such a model would also be useful for power plant system design.

6.2 Adiabatic Flame Temperature Calculation

It was assumed air is comprised of only O_2 and N_2 for flame temperature calculation. This could be improved by considering the actual air composition, as listed in Table 3-1. Also, the fuel was considered as methane only, which is a simplification of the real natural gas composition. A more realistic composition of the fuel gas could be used for future flame calculations.

6.3 Lifing Model

A natural progression of this work would be to analyse the lifing of the low-pressure turbine and burner. Meanwhile, the OTSG lifing due to dry-running at the start and shut down could also be usefully explored. A further study could assess the different failure mechanisms effects on hot section component life.

6.4 OTSG Leakage Prediction

The issue of OTSG leakage is intriguing, and could be usefully explored in further research. The current OTSG model requires heat balance between the hot path and cold path. If the leakage happens inside the OTSG, the cold flow will pass through the tube inner to the outer in a radial direction. Under such conditions, the inlet mass flow rate of each path will not be equal to the outlet. The leakage would change the OTSG performance. This would be a fruitful area for further work.

6.5 Optimal Cleaning Schedules

The thermal shock of dry running the GT exhaust gas through the OTSG while the HP and LP paths have no feed water could be used for fouling mitigation at the fume side of the OTSG tube. However, the dry-run operation for a steam generator is limited by consideration of the life of OTSG tubes. It is suggested that applying the developed OTSG diagnostic system could optimise OTSG cleaning schedules.

6.6 CCGT Cooling Cycle Optimisation

The power plant auxiliary equipment consumes about 3.4% of CCGT total power output. The lower the condenser pressure, the higher the ST power output, but the higher the consumption of power by the auxiliaries for the cooling cycle. Therefore, there is a degree of trade-off between auxiliary power consumption and plant efficiency. The cooling cycle could be affected by the ambient conditions, and the states of health of both condenser and air-cooled heat exchanger. At a specific operating condition, there will be an optimum set point for condenser pressure, so that the CCGT efficiency is maintained without the excessive use of power by the auxiliaries.

6.7 Integration Heat Pump for Natural Gas De-icing

The ST exhaust steam energy is absorbed by condenser cooling water, and the heat is released externally by the air-cooled heat exchanger. The power plant is concerned to recover a portion of this heat through the heat pump and the heat the will be used for de-icing pipes and other equipment when transferring high-pressure natural gas to the much lower gas pressure required for the turbines. Further investigations are needed to analyse the feasibility of improving power plant efficiency by the heat pump.

6.8 Steam Turbine Corrosion

Further research could usefully explore the ST corrosion phenomenon that is a risk to safe operation and a cause of economic loss. It is necessary to propose an algorithm to quantify the effect of condenser setting point on ST corrosion for operational guidance.

REFERENCES

1. Lefebvre AH. Gas Turbine Combustion. 3rd edn. CRC press; 2010. 560 p.
2. Energy Information Association. International energy outlook 2009. Washington; 2009.
3. Muhammed MS. Exergoeconomic analysis and optimization of combined cycle power plants with complex configuration. UNIVERSITY OF BELGRADE; 2015.
4. MacMillan WL. Development of a modular-type computer program for the calculation of gas turbine off-design performance. PhD Thesis. Cranfield University; 1974.
5. Li Y., Singh R. An Advanced Gas Turbine Gas Path Diagnostic System - PYTHIA. Munich: International Symposium of Air Breathing Engines (ISABE); 2005.
6. Nalianda D. Impact of Environmental Taxation Policies on Civil Aviation - A Techno-Economic Environmental Risk Assessment. PhD Thesis. Cranfield University; 2012. Available at: DOI:004
7. Lefebvre AH. Fuel effects on gas turbine combustion-liner temperature, pattern factor, and pollutant emissions. Journal of Aircraft. 1984. pp. 887–898. Available at: DOI:10.2514/3.45059
8. Goodger EM. An Overview of Heat Engines and Their Fuels. Landfall Press; 2014.
9. Goodger EM. Comubstion Stoichiometry & Temperatures Using Open Office Excel Spreadsheet Computing. Landfall Press; 2012.
10. Goodger EM. Combustion Stoichiometry & Temperatures Using Open Office Excel Spreadsheet Computing. Cranfield, Bedford, UK; 2012.
11. Ghafir Abdul F.M. Performance Based Creep Life Estimation for Gas Turbines Application. Cranfield University; 2011.
12. Manassaldi JI., Arias AM., Scenna NJ., Mussati MC., Mussati SF. A discrete and continuous mathematical model for the optimal synthesis and design of dual pressure heat recovery steam generators coupled to two steam turbines. Energy. 2016; 103: 807–823. Available at: DOI:10.1016/j.energy.2016.02.129
13. Franco A., Russo A. Combined cycle plant efficiency increase based on the optimization of the heat recovery steam generator operating parameters. International Journal of Thermal Sciences. 2002; 41(9): 843–859. Available at: DOI:10.1016/S1290-0729(02)01378-9
14. Kehlhofer R., Rukes B., Hannemann F., Stirnimann F. Combined-Cycle Gas & Steam Turbine Power Plants. 3rd edn. Pennwell Books; 2009. 434

p.

15. Mucino M. CCGT Performance Simulation and Diagnostics for Operations Optimisation and Risk Management. Cranfield University; 2007.

16. Todd DS. Multiple criteria genetic algorithms in engineering design and operation. University of Newcastle upon Tyne; 1997.

17. Hwang C-L., Yoon K. Multiple Attribute Decision Making Methods and Applications A State-of-the-Art Survey. 1st edn. Berlin: Springer-Verlag Berlin Heidelberg; 1981. 269 p.

18. Pilidis P. Digital simulation of Gas Turbine Performance. PhD Thesis. University of Glasgow; 1983.

19. Sugiyama N. Generalized high speed simulation of gas turbine engines. 1990; : GT270 8p.

20. Sanghi V., Lakshmanan BK., Sundararajan V. Digital Simulator for Steady-State Performance Prediction of Military Turbofan Engine Introduction. Journal of Propulsion and Power. 1998; 14(1): 74–81. Available at: DOI:10.2514/2.5252

21. Wang C. Transient Performance Simulation of Gas Turbine Engine Integrated with Fuel and Control Systems. Cranfield University; 2016.

22. Kurzke J. Advanced user-friendly gas turbine performance calculations on a personal computer. New York, US: ASME International Gas Turbine and Aeroengine Congress and Exposition; 1995. p. 8. Available at: DOI:10.1115/95-GT-147

23. GasTurb. Gas turbine performance. 2017. Available at: http://www.gasturb.de/%0A (Accessed: 14 August 2018)

24. Parker KI., Guo T. Development of a Turbofan Engine Simulation in a Graphical Simulation Environment. Nasa Tm. 2003; (August 2003): 212543. Available at: DOI:Rept-1, E-13718

25. Liu Y., Frederick DK., DeCastro JA., Litt JS., Chan WW. User ' s Guide for the Commercial Modular Aero- User ' s Guide for the Commercial Modular Aero-Propulsion System Simulation (C-MAPSS). 2012.

26. Parker KI., Melcher KJ. The Modular Aero-Propulsion System Simulation (MAPSS) Users ' Guide. 2004.

27. NASA. Modular Aero-Propulsion System Simulations - MAPSS, C-MAPSS, C-MAPSS40k. Intelligent Control and Autonomy Branch. Available at: https://www.grc.nasa.gov/WWW/cdtb/software/mapss.html (Accessed: 14 August 2018)

28. Netherlands Aerospace Centre D. Gas Turbine Simulation Program. Available at: https://www.gspteam.com/ (Accessed: 14 August 2018)

29. Janikovic J. Gas turbine transient performance modeling for engine flight path cycle analysis. 2010; U617280. Available at: http://search.proquest.com/docview/1651897146?accountid=14987%5Cn http://linker.westminster.ac.uk/sfx_wmin?url_ver=Z39.88-2004&rft_val_fmt=info:ofi/fmt:kev:mtx:dissertation&genre=dissertations+&+theses&sid=ProQ:ProQuest+Dissertations+&+Theses:+UK+&+Ireland

30. Apostolidis A., Sampath S., Laskaridis P., Singh R. Webengine: a web-based gas turbine performance simulation tool. San Antonio, Texas, USA: ASME Turbo Expo Turbine Technical Conference and Exposition; 2018. pp. 1–11.

31. Escher, P.C. and Singh R. An object-oriented diagnostics computer program suitable for industrial gas turbines. Switzerland: In 21st (CIMAC) International Congress of Combustion Engines; 1995. pp. 15–18.

32. Li Y. Gas Turbine Diagnostics Course Notes. 2013.

33. U. S. Environmental Protection Agency. Calculations and References for Greenhouse Gas Equivalencies. US Environment Protection Agency. 2011. Available at: https://www.epa.gov/energy/ghg-equivalencies-calculator-calculations-and-references (Accessed: 24 August 2016)

34. Mohamed W. Techno-Economic, Environmental and Risk Analysis (TERA) for Power Generation. Cranfield University; 2013. Available at: DOI:10.1017/CBO9781107415324.004

35. Pervier H. Emissions Modelling for Engine Cycle and Aircraft Trajectory Optimisation. Cranfield University; 2013.

36. MIT web course notes for Propulsion. Thermodynamics and Propulsion: Generating Heat. MIT. Available at: http://web.mit.edu/16.unified/www/SPRING/propulsion/notes/notes.html (Accessed: 25 August 2016)

37. Conference WI., Transfer M. Recent advances in heat and mass transfer. Literary Licensing, LLC. 2012; : 412.

38. Edwards T. Advancements in Gas Turbine Fuels From 1943 to 2005. Journal of Engineering for Gas Turbines and Power. 2007; 129(2007): 13–20. Available at: DOI:10.1115/1.2364007

39. Incropera FP., DeWitt DP., Bergman TL., Lavine AS. Fundamentals of Heat and Mass Transfer. 6th edn. John Wiley & Sons; 2006.

40. IV JHL., V JHL. A Heat Transfer Textbook: Fourth Edition. 3rd edn. Dover Publications; 2000.

41. Odgers J., Kretschmer D. The Prediction of Thermal NOX in Gas Turbines. International Journal of Turbo and Jet Engines. 1985; 5(1–4). Available at: DOI:10.1515/TJJ.1988.5.1-4.225

42. Lewis GD. A New Understanding of NOx Formation. Tenth International

Symposium on Air-Breathing Engines; 1991. pp. 625–629.

43. Røkke NA., Hustad JE., Berg S. Pollutant Emissions From Gas Fired Turbine Engines in Offshore Practice: Measurements and Scaling. ASME 1993 International Gas Turbine and Aeroengine Congress and Exposition. 1993; : V03AT15A021-V03AT15A021. Available at: DOI:10.1115/93-GT-170

44. Rizk NK., Mongia HC. Emissions Predictions of Different Gas Turbine Combustors. 32nd Aerospace Sciences Meeting & Exhibit . 1994; (AIAA 94-01 18). Available at: DOI:doi:10.2514/6.1994-118

45. Tsalavoutas a., Kelaidis M., Thoma N., Mathioudakis K. Correlations Adaptation for Optimal Emissions Prediction. Volume 3: Turbo Expo 2007. 2007; : 545–555. Available at: DOI:10.1115/GT2007-27060

46. Kyprianidis KG., Nalianda D., Dahlquist E. A NOx Emissions Correlation for Modern RQL Combustors. Energy Procedia. 2015; 75(March 2017): 2323–2330. Available at: DOI:10.1016/j.egypro.2015.07.433

47. Samaras C. Emissions Estimation from Industrial Gas Turbines Combustors. Power. Cranfield University; 2010.

48. Celis C. Evaluation and optimisation of environmentally friendly aircraft propulsion systems. Cranfield University; 2010. Available at: DOI:10.1017/CBO9781107415324.004

49. Vervisch L., Hauguel R., Domingo P., Rullaud M. Three facets of turbulent combustion modelling: DNS of premixed V-flame, LES of lifted nonpremixed flame and RANS of jet-flame. Journal of Turbulence. 2004; 5. Available at: DOI:10.1088/1468-5248/5/1/004

50. Maidhof S., Janicka J. Numerical Modelling of Gas Turbine Combustion Chambers. AGARD, Fuels and Combustion Technology for Advanced Aircraft Engines; 1993.

51. Alizadeh S. Flowfield prediction of nox and smoke production in aircraft engines. Cranfield Institute of Technology; 1993.

52. Marini A., Bucchieri L., Peschiulli A. CFD Aerodynamic and Reactive Study of an Innovative Lean. System. 2010; : 1–11.

53. Meloni R. Pollutant Emission Validation of a Heavy-Duty Gas Turbine Burner by CFD Modeling. Machines. 2013; 1(3): 81–97. Available at: DOI:10.3390/machines1030081

54. Pierre G. Combustion CFD turbulence-chemistry interactions. 2016.

55. Rizk NK., Mongia HC. Semianalytical Correlations for NOx, CO, and UHC Emissions. Journal of Engineering for Gas Turbines and Power. 1993; 115(3): 612. Available at: DOI:10.1115/1.2906750

56. Allaire DL. A Physics-Based Emissions Model for Aircraft Gas Turbine

Combustors. Master Thesis. Massachusetts Institute of Technology; 2006.

57. Marchand MD. Multi-Dimensional Carbon Monoxide Emissions Predictor for Preliminary Gas Turbine Combustor Design Optimization. Cranfield University; 2013.

58. McGuirk J. 3D combustor predictions: a comparison of equilibrium and laminar flamelet chemistry models. In AGARD conference proceedings; 1988.

59. Frassoldati A., Cuoci A., Faravelli T., Ranzi E., Colantuoni S., Martino P Di., et al. Fluid Dynamics and Detailed Kinetic Modeling of Pollutant. Glasgow, UK: ASME Proceedings; 2010. pp. 451–459.

60. Nkoi B. Techno-economic studies of environmentally friendly brayton cycles in the petrochemical industry. Cranfield University; 2014.

61. Quintero RFC. Techno-Economic and Environmental Risk Assessment of Innovative Propulsion Systems for Short-Range Civil Aircraft. Cranfield University; 2008. Available at: https://dspace.lib.cranfield.ac.uk/bitstream/1826/3748/1/Colmenares_Quintero_Thesis_2009.pdf

62. Coutinho A. Performance and emission optimisation of novel aero-engine concepts. Cranfield University; 2002.

63. Zhang Q. Preliminary Design of a Low Emission Aero-Derived Gas Turbine Combustor. Cranfield Univeristy; 2011.

64. Maccapani M. A Techno – Economical and Environmental Study of Stationary Gas Turbines for LNG Applications. Cranfield Univeristy; 2011.

65. Khan RSR. TERA for Rotating Equipment Selection. Cranfield Univeristy; 2012.

66. Eshati S., Abu A., Laskaridis P., Haslam A. Investigation into the effects of operating conditions and design parameters on the creep life of high pressure turbine blades in a stationary gas turbine engine. Mechanics and Mechanical Engineering. 2011; 15(3): 237–247.

67. Mohamed W., Eshati S., Pilidis P., Ogaji S., Laskaridis P., Nasir a. A method to evaluate the impact of power demand on HPT blade creep life. 2011; 4: 1–9. Available at: DOI:10.1115/GT2011-45092

68. Larson FR., Miller J. A time-temperature relationship for rupture and creep stresses. Transactions of ASME; 1952. pp. 765–775.

69. Jaffe LD., Swartz B. Time-Temperature Relations in Tempering Steels. Watertown Arsenal Laboratory. 1945. Available at: DOI:10.2214/AJR.09.3938

70. Bueno L de O., Sordi VL., Marino L. Constant load creep data in air and vacuum on 2.25Cr-1Mo steel from 600 °C to 700 °C. Materials Research.

2005; 8(4): 401–408. Available at: DOI:10.1590/S1516-14392005000400008

71. Oluyede EO., Phillips JN. Fundamental Impact of Firing Syngas in Gas Turbines. Montreal, Canada: In ASME Turbo Expo: Power for Land, Sea, and Air (pp. 175-182); 2012. pp. 1–8.

72. Vaezi M., Soleymani M. Creep life prediction of Inconel 738 gas turbine blade. Journal of Applied Sciences. 2009; 9(10): 1950–1955. Available at: DOI:10.3923/jas.2009.1950.1955

73. Abdul Ghafir MF., Li YG., Singh R., Huang K., Feng X. Impact of Operating and Health Conditions on Aero Gas Turbine: Hot Section Creep Life Using a Creep Factor Approach. Volume 3: Controls, Diagnostics and Instrumentation; Cycle Innovations; Marine. 2010; : 533–545. Available at: DOI:10.1115/GT2010-22332

74. Eshati S., Abu A., Laskaridis P., Khan F. Influence of water-air ratio on the heat transfer and creep life of a high pressure gas turbine blade. Applied Thermal Engineering. Elsevier Ltd; 2013; 60(1–2): 335–347. Available at: DOI:10.1016/j.applthermaleng.2013.06.061

75. Ogiriki EA., Li YG., Nikolaidis T. Prediction and Analysis of Impact of TBC Oxidation on Gas Turbine Creep Life. Proceedings of ASME Turbo Expo: Power for land, Sea and Air; 2015. pp. 1–13. Available at: DOI:10.1115/GT2015-42177

76. Sahoo B., Panigrahi SK., Satpathy RK. Creep Life Degradation and Microstructure Degeneration in a Low-Pressure Turbine Blade of a Military Aircraft Engine. Journal of Failure Analysis and Prevention. Springer US; 2017; 17(3): 529–538. Available at: DOI:10.1007/s11668-017-0271-x

77. Schmidt N., Grauer F., Simon A., Geers P., Staudacher S., Vogeler K. The Effect of Turbine Blade Pre-Design on Three-Dimensional Thermal and Mechanical Stress Distribution Resulting in Component Creep Life. 2018 Joint Thermophysics and Heat Transfer Conference. 2018; : 1–12. Available at: DOI:10.2514/6.2018-4079

78. Wikipedia the free encyclopedia. Heat recovery steam generator. 2018. Available at: https://en.wikipedia.org/wiki/Heat_recovery_steam_generator (Accessed: 10 January 2018)

79. Carazas FJG., Salazar CH., Souza GFM. Availability analysis of heat recovery steam generators used in thermal power plants. Energy. 2011; 36(6): 3855–3870. Available at: DOI:10.1016/j.energy.2010.10.003

80. Ahmadi P., Dincer I. Thermodynamic analysis and thermoeconomic optimization of a dual pressure combined cycle power plant with a supplementary firing unit. Energy Conversion and Management. Elsevier Ltd; 2011; 52(5): 2296–2308.

81. Nadir M., Ghenaiet A. Thermodynamic optimization of several (heat

recovery steam generator) HRSG configurations for a range of exhaust gas temperatures. Energy. Elsevier Ltd; 2015; 86: 685–695. Available at: DOI:10.1016/j.energy.2015.04.023

82. Bassily AM. Modeling, numerical optimization, and irreversibility reduction of a triple-pressure reheat combined cycle. Energy. 2007; 32(5): 778–794. Available at: DOI:10.1016/j.energy.2006.04.017

83. Plis M., Rusinowski H. A mathematical model of an existing gas-steam combined heat and power plant for thermal diagnostic systems. Energy. Elsevier Ltd; 2018; 156: 606–619. Available at: DOI:10.1016/j.energy.2018.05.113

84. Oko COC., Njoku IH. Performance analysis of an integrated gas-, steam- and organic fluid-cycle thermal power plant. Energy. Elsevier Ltd; 2017; 122: 431–443.

85. Bayless PD. a performance model for a helically coiled once-through steam generator tube. Massachusetts Institute of Technology; 1979.

86. Tuyle GJ Van., Lee JC. Linearized Transient Analysis of Nuclear Steam Generators. Nuclear Science and Engineering. 1980; 75(3): 225–242. Available at: DOI:10.13182/NSE80-A19055

87. Tzanos CP. A movable boundary model for once-through steam generator analysis. Nuclear Technology. 1988; 82(1): 5–17.

88. Li H., Huang X., Zhang L. A lumped parameter dynamic model of the helical coiled once-through steam generator with movable boundaries. Nuclear Engineering and Design. 2008; 238(7): 1657–1663. Available at: DOI:10.1016/j.nucengdes.2008.01.009

89. Dumont M. Mathematical modelling and design of an advanced once-through heat recovery steam generator. Computers & Chemical Engineering. 2004; 28(5): 651–660. Available at: DOI:10.1016/j.compchemeng.2004.02.034

90. Ngoma G., Sadiki A., Wamkeue R. Efficient Approach in Modelling and Simulation of Dual Pressure Once-through Heat Recovery Steam Generator. CA, USA: IASTED International Conference Power and Energy Systems; 2003. pp. 218–223.

91. Bott T. Fouling of heat exchangers. Elsevier Science & Technology Books; 1995.

92. Kuppan T. Heat exchanger design handbook. New York: Marcel Dekker, Inc; 2000.

93. Shah RK., Sekulic DP. Fundamentals of heat exchanger design. New Jersey, Canada: John Wiley & Sons; 2003. 972 p.

94. Ganapathy V. Steam Generators and Waste Heat Boilers: For Process and Plant Engineers. 2014. 539 p. Available at: DOI:10.1201/b17519

95. Belmiloudi A. Heat transfer-theoretical analysis, experimental investigations and industrial systems. Vienna: InTech (Open access Publisher); 2011.

96. Walker ME., Safari I., Theregowda RB., Hsieh MK., Abbasian J., Arastoopour H., et al. Economic impact of condenser fouling in existing thermoelectric power plants. Energy. Elsevier; 2012; 44(1): 429–437. Available at: DOI:10.1016/j.energy.2012.06.010

97. Tay S., Yang C. Assessment of the hydro-ball condenser tube cleaning system. 2006.

98. Hans M. VDI Heat Atlas: Fouling of Heat Exchanger Surfaces. VDI Heat Atlas. Stuttgart, Germany: Springer-Verlag; 2010.

99. Muller-Steinhagen H. Heat Exchanger Fouling: Mitigation and Cleaning Techniques. Rugby, Warwickshire, UK: Institution of Chemical Engineers; 2000.

100. Wilson E. A basis for rational design of heat transfer apparatus. 1915.

101. Somerscales EFC. Fouling of heat transfer surfaces: An historical review. Heat Transfer Engineering. 1990; 11(1): 19–36. Available at: DOI:10.1080/01457639008939720

102. Mohanty DK., Singru PM. Use of C-factor for monitoring of fouling in a shell and tube heat exchanger. Energy. Elsevier Ltd; 2011; 36(5): 2899–2904. Available at: DOI:10.1016/j.energy.2011.02.032

103. Chenoweth J. Final report of the HTRI/TEMA joint committee to review the fouling section of the TEMA standards. Heat Transfer Engineering. 1990; 11(1): 73–107.

104. Qureshi BA., Zubair SM. Predicting the impact of heat exchanger fouling in power systems. Energy. Elsevier Ltd; 2016; 107: 595–602. Available at: DOI:10.1016/j.energy.2016.04.032

105. Tian J., Wang Y., Feng X. Simultaneous optimization of flow velocity and cleaning schedule for mitigating fouling in refinery heat exchanger networks. Energy. Elsevier Ltd; 2016; 109: 1118–1129. Available at: DOI:10.1016/j.energy.2016.05.053

106. Sheikh AK., Zubair SM., Younas M., Budair MO. A risk based heat exchanger analysis subject to fouling: Part I: Economics of heat exchangers cleaning. Energy. 2000; 25(5): 445–461. Available at: DOI:10.1016/S0360-5442(99)00081-X

107. Teruel E., Cortés C., Ignacio Díez L., Arauzo I. Monitoring and prediction of fouling in coal-fired utility boilers using neural networks. Chemical Engineering Science. 2005; 60(18): 5035–5048. Available at: DOI:10.1016/j.ces.2005.04.029

108. Bishara E., Abd-Elhady MS., Halim MA. Influence of thermal shock on

fouling of smooth, rough and finned tubes. Energy. Elsevier Ltd; 2015; 93: 354–360. Available at: DOI:10.1016/j.energy.2015.09.063

109. Shlyakhin P. Steam Turbines: Theory and Design. University Press of the Pacific; 2005. 248 p.

110. Yahya SM. Turbine, compressors and fans. 4th edn. Mc Graw Hill India; 2010.

111. Forsthoffer WE. Steam Turbine Best Practices. Forsthoffer's Best Practice Handbook for Rotating Machinery. Butterworth-Heinemann; 2011. pp. 313–346. Available at: DOI:10.1016/B978-0-08-096676-2.10006-2

112. Guo S., Liu P., Li Z. Estimation of exhaust steam enthalpy and steam wetness fraction for steam turbines based on data reconciliation with characteristic constraints. Computers and Chemical Engineering. Elsevier Ltd; 2016; 93: 25–35. Available at: DOI:10.1016/j.compchemeng.2016.05.019

113. Bahadori A., Vuthaluru HB. Estimation of performance of steam turbines using a simple predictive tool. Applied Thermal Engineering. Elsevier Ltd; 2010; 30(13): 1832–1838. Available at: DOI:10.1016/j.applthermaleng.2010.04.017

114. Medina-Flores JM., Picón-Núñez M. Modelling the power production of single and multiple extraction steam turbines. Chemical Engineering Science. 2010; 65(9): 2811–2820. Available at: DOI:10.1016/j.ces.2010.01.016

115. Steag system technologies. Ebsilon Professional. Available at: https://www.steag-systemtechnologies.com/de/produkte/ebsilon-professional/ (Accessed: 20 August 2018)

116. Walsh PP., Fletcher P. Gas turbine Performance. 2004. Available at: DOI:10.1037/023990

117. Seme S., Sredenšek K., Praunseis Z., Štumberger B., Hadžiselimović M. Optimal price of electricity of solar power plants and small hydro power plants – Technical and economical part of investments. Energy. 2018; 157: 87–95. Available at: DOI:10.1016/j.energy.2018.05.121

118. Lukač N., Seme S., Dežan K., Žalik B., Štumberger G. Economic and environmental assessment of rooftops regarding suitability for photovoltaic systems installation based on remote sensing data. Energy. 2016; 107: 854–865. Available at: DOI:10.1016/j.energy.2016.04.089

119. Madlener R., Stoverink S. Power plant investments in the Turkish electricity sector: A real options approach taking into account market liberalization. Applied Energy. Elsevier Ltd; 2012; 97: 124–134. Available at: DOI:10.1016/j.apenergy.2011.11.050

120. Mohamed W., Pilidis P., Nasir A. Economic Evaluation of Industrial Gas

Turbines for Electrical Power Generation. ASME Turbo Expo: Turbine Technical Conference and Exposition; 2012. pp. 1–10.

121. Nasir A., Pilidis P., Ogaji S. A study of the effect of gas turbine emissions on the economics of natural gas pipeline transportation. Proceedings of the 20th International Conference on Nuclear Engineering; 2012. pp. 1–5.

122. Nasir A. Some Economic Implications of Deploying Gas Turbine in Natural Gas Pipeline Networks. International Journal of Engineering and Technology. 2013; 5(1): 141–145. Available at: DOI:10.7763/IJET.2013.V5.528

123. Ku A. That Option Called Power. Available at: http://www.analyticalq.com/energy/exotic/default.htm (Accessed: 20 August 2018)

124. Deng SJ., Oren SS. Electricity derivatives and risk management. Energy. 2006; 31(6–7): 940–953. Available at: DOI:10.1016/j.energy.2005.02.015

125. Poats RS. The spark spread as a measure of wholesale electricity's economic reliability. Proceedings of the IEEE Power Engineering Society Transmission and Distribution Conference. 2002; 2(c): 967–968. Available at: DOI:10.1109/PESW.2002.985149

126. Hsu M. Spark Spread Options Are Hot! The Electricity Journal. 1998; 11(2): 28–39. Available at: DOI:10.1016/S1040-6190(98)00004-9

127. Stephenson P., Paun M. Electricity market trading. Power Engineering Journal. 2001; 15(6): 277–288. Available at: DOI:10.1049/pe:20010602

128. Woo CK. What went wrong in California's electricity market? Energy. 2001; 26(8): 747–758. Available at: DOI:10.1016/S0360-5442(01)00047-0

129. Woo CK., Lloyd D., Tishler A. Electricity market reform failures: UK, Norway, Alberta and California. Energy Policy. 2003; 31(11): 1103–1115. Available at: DOI:10.1016/S0301-4215(02)00211-2

130. Termraz H., Salama M., Chikhani A. Review of electric load forecasting methods. Ieee. 1997; 1: 289–292. Available at: DOI:10.1109/CCECE.1997.614846

131. Breipohl A. Electricity price forecasting models. 2002 IEEE Power Engineering Society Winter Meeting. Conference Proceedings (Cat. No.02CH37309). 2002; 2(c): 963–966. Available at: DOI:10.1109/PESW.2002.985148

132. Holland JH. Adaptation in Natural and Artificial Systems. Ann Arbor MI University of Michigan Press. 1975; Ann Arbor: 183. Available at: DOI:10.1137/1018105

133. Metropolis N., Rosenbluth AW., Rosenbluth MN., Teller AH., Teller E. Equation of State Calculations by Fast Computing Machines. The Journal of Chemical Physics. 1953; 21(6): 1087–1092. Available at:

DOI:10.1063/1.1699114

134. Kirkpatrick S., Gelatt CD., Vecchi MP. Optimization by simulated annealing. Science Magazine. 1983; 220(4598): 671–680.

135. Dorigo M., Maniezzo V., Colorni A. The ant system: An autocatalytic optimizing process. TR91-016, Politecnico di Milano. Milano; 1991; : 1–21. Available at: http://lis.nsysu.edu.tw/exam/doctor/mana/infom/infom_93.pdf

136. Tian Y., Song J., Yao D., Hu J. Dynamic vehicle routing problem using hybrid ant system. Proceedings of the 2003 IEEE International Conference on Intelligent Transportation Systems. 2003; 2: 970–974. Available at: DOI:10.1109/ITSC.2003.1252630

137. Eberhart R., Kennedy J. A new optimizer using particle swarm theory. MHS'95. Proceedings of the Sixth International Symposium on Micro Machine and Human Science. : 39–43. Available at: DOI:10.1109/MHS.1995.494215

138. Storn R., Price K. Differential Evolution – A Simple and Efficient Heuristic for global Optimization over Continuous Spaces. Journal of Global Optimization. 1997; 11(4): 341–359. Available at: DOI:10.1023/A:1008202821328

139. Arias-Montano A., Coello CAC., Mezura-Montes E. Multiobjective Evolutionary Algorithms in Aeronautical and Aerospace Engineering. IEEE Transactions on Evolutionary Computation. 2012; 16(5): 662–694. Available at: DOI:10.1109/TEVC.2011.2169968

140. Curry HB. The method of steepest descent for non-linear minimization problems. Quarterly of Applied Mathematics. 1944; 2(3): 258–261.

141. Glover F. Future paths for integer programming and linkes to artificial intelligence. Computers & Operations Research. 1986; 13(5): 533–549. Available at: DOI:http://dx.doi.org/10.1016/0305-0548(86)90048-1

142. Dalton J. Optimisation Lectures. Newcastle; 2014.

143. Saaty TL. Share Facebook Twitter Pinterest <Embed> Buy New $30.00 Qty: Only 3 left in stock (more on the way). Ships from and sold by Amazon.com. Gift-wrap available. Add to Cart Buy Now Turn on 1-Click ordering for this browser This item ships to United Kingdom. L. RWS Publications; 2001.

144. Sen P., Yang J-B. Design decision making based upon multiple attribute evaluations and minimal preference information. Mathematical and Computer Modelling. 1994; 20(3): 107–124. Available at: DOI:10.1016/0895-7177(94)90034-5

145. Ho W., Xu X., Dey PK. Multi-criteria decision making approaches for supplier evaluation and selection: A literature review. European Journal of Operational Research. Elsevier B.V.; 2010; 202(1): 16–24. Available at:

DOI:10.1016/j.ejor.2009.05.009

146. Pohekar SD., Ramachandran M. Application of multi-criteria decision making to sustainable energy planning - A review. Renewable and Sustainable Energy Reviews. 2004; 8(4): 365–381. Available at: DOI:10.1016/j.rser.2003.12.007

147. Stewart T. A critical survey on the status of multiple criteria decision making theory and practice. International Journal of Management Science. 1992; 20(5): 569–586. Available at: DOI:10.1016/0305-0483(92)90003-P

148. Henning D a G. MODEST--An energy-system optimisation model applicable to local utilities and countries. Energy. 1997; 22(12): 1135–1150.

149. Yokoyama R., Shinano Y., Wakayama Y., Wakui T. Multiobjective Optimal Design of a Gas Turbine Cogeneration Plant by a Revised Hierarchical Optimization Method. Charlotte, North Carolina, USA: ASME Turbo Expo 2017: Turbomachinery Technical Conference and Exposition; 2018.

150. Assavapokee T., Realff MJ., Ammons JC. Min-max regret robust optimization approach on interval data uncertainty. Journal of Optimization Theory and Applications. 2008; 137(2): 297–316. Available at: DOI:10.1007/s10957-007-9334-6

151. Koroneos C., Michailidis M., Moussiopoulos N. Multi-objective optimization in energy systems: The case study of Lesvos Island, Greece. Renewable and Sustainable Energy Reviews. 2004; 8(1): 91–100. Available at: DOI:10.1016/j.rser.2003.08.001

152. Pasaoglu G., Garcia NP., Zubi G. A multi-criteria and multi-expert decision aid approach to evaluate the future Turkish power plant portfolio. Energy Policy. Elsevier Ltd; 2018; 119(May): 654–665. Available at: DOI:10.1016/j.enpol.2018.04.044

153. Attala L., Facchini B., Ferrara G. Thermoeconomic optimization method as design tool in gas-steam combined plant realization. Energy Conversion and Management. 2001; 42(18): 2163–2172. Available at: DOI:10.1016/S0196-8904(00)00129-1

154. Pelster S., Favrat D., von Spakovsky MR. The Thermoeconomic and Environomic Modeling and Optimization of the Synthesis, Design, and Operation of Combined Cycles With Advanced Options. Journal of Engineering for Gas Turbines and Power. 2001; 123(4): 717. Available at: DOI:10.1115/1.1366323

155. Valdés M., Durán MD., Rovira A. Thermoeconomic optimization of combined cycle gas turbine power plants using genetic algorithms. Applied Thermal Engineering. 2003; 23(17): 2169–2182. Available at: DOI:10.1016/S1359-4311(03)00203-5

156. Möller BF., Obana M., Assadi M., Mitakakis A. Optimisation of HAT-Cycles - With and Without CO2 Capture. Proceedings of ASME Turbo Expo, Viena,

Austria. 2004; (ASME Pape No. GT2004-53734): 1–8. Available at: DOI:10.1115/GT2004-53734

157. Casarosa C., Donatini F., Franco A. Thermoeconomic optimization of heat recovery steam generators operating parameters for combined plants. Energy. 2004; 29(3): 389–414. Available at: DOI:10.1016/S0360-5442(02)00078-6

158. Aref P., Pilidis P., Ogaji S., Lorenzo G Di., Adams M. Development of A Framework For Thermoeconomic Optimization of Combined Cycle Power Plants. 46th AIAA Joint Propulsion Conference. 2010; (July). Available at: DOI:10.2514/6.2010-6624

159. Brighenti GD., Orts-gonzalez PL., Sanchez-de-leon L., Zachos PK. Design Point Performance and Optimization of Humid Air Turbine Power Plants. Applied Sciences. 2017; 7(4): 413. Available at: DOI:10.3390/app7040413

160. Yokoyama R., Ito K. b., Matsumoto Y. Optimal multistage expansion planning of a gas turbine cogeneration plant. Journal of Engineering for Gas Turbines and Power. 1996; 118(4): 803–809. Available at: DOI:Doi 10.1115/1.2816996

161. Kaya A., Keyes MA. Methods of energy efficient control and optimization for combined-cycle cogeneration. Energy Conversion and Management. 1992; 33(4): 225–233. Available at: DOI:10.1016/0196-8904(92)90112-A

162. Bojić M., Stojanović B. MILP optimization of a CHP energy system. Energy Conversion and Management. 1998; 39(7): 637–642. Available at: DOI:10.1016/S0196-8904(97)00042-3

163. Nikolaidis T., Pachidis V. Gas Turbine Performance Simulation Lecture Note. 2016.

164. NASA. NASA computer program for calculating of the Chemical Equilibrium with Applications. NASA Glenn Research Center, Cleveland, OH.;

165. McKinney JS. Simulation of turbofan engine, part 1-description of method and balancing technique. 1967.

166. Fishbach LH., Koenig RW. GENENG II — A Program for Calclating Design and Off-Design Performance of Two- and Three-Spool Turbofans With As Many As Three Nozzles. 1972.

167. Li YG., Pilidis P., Newby MA. An Adaptation Approach for Gas Turbine Design-Point Performance Simulation. Journal of Engineering for Gas Turbines and Power. 2006; 128(4): 789. Available at: DOI:10.1115/1.2136369

168. Li YG., Ghafir MFA., Wang L., Singh R., Huang K., Feng X. Nonlinear Multiple Points Gas Turbine Off-Design Performance Adaptation Using a Genetic Algorithm. Journal of Engineering for Gas Turbines and Power. 2011; 133(7): 071701. Available at: DOI:10.1115/1.4002620

169. Demirbas A. Methane Gas Hydrate. Springer; 2010.

170. Stull DR., Prophet H. JANAF thermochemical tables. 2nd edn. Washington, DC: National Bureau of Standards; 1971.

171. Gomes EEB., Pilidis P. Gas Turbine Life Cycle Assessment and Preliminary Risk Analysis. Volume 5: Turbo Expo 2007. 2007; : 1157–1165. Available at: DOI:10.1115/GT2007-27972

172. Laskaridis P. Mechanical Design of Turbomachinery. Bedford; 2016.

173. Eshati S., Ghafir MFA., Laskaridis P., Li YG. Impact of Operating Conditions and Design Parameters on Gas Turbine Hot Section Creep Life. Glasgow, UK: ASME Turbo Expo Power for Land, Sea, and Air; 2016.

174. Torbidoni L., Horlock JH. A New Method to Calculate the Coolant Requirements of a High-Temperature Gas Turbine Blade. Journal of Turbomachinery. 2005; 127(1): 191. Available at: DOI:10.1115/1.1811100

175. Manx Utilities. Welcome to Pulrose Power Station. Pulrose Power Station. 2018. Available at: https://www.manxutilities.im/media/1138/welcome-to-pulrose-power-station.pdf (Accessed: 7 August 2018)

176. Klaus G. VDI Heat Atlas: Heat Transfer to Finned Tubes. VDI Heat Atlas. Duisburg, Germany: Springer-Verlag; 2010.

177. Dechamps P. Modeling the transient behavior of combined cycle plants. Hague, Netherlands: ASME International Gas Turbine and Aeroengine Congress and Exposition; 1994.

178. Gnielinski V. Forced convection in ducts. Bell KJ etal (eds) HEDH–heat exchanger design handbook. Washington: Hemisphere & VDI; 1983.

179. Matthias K. VDI Heat Atlas: Saturated Flow Boiling. Karlsruhe, Germany: Springer-Verlag; 2010.

180. Wagner WK. Properties of water and steam/IAPWS-IF97. Berlin, Germany: Springer-Verlag; 1997.

181. Li Y-G. Aero Gas Turbine Flight Performance Estimation Using Engine Gas Path Measurements. Journal of Propulsion and Power. 2015; 31(3): 851–860. Available at: DOI:10.2514/1.B35381

182. Cooke DH. On Prediction of Off-Design Multistage Turbine Pressures by Stodola’s Ellipse. Journal of Engineering for Gas Turbines and Power. 1985; 107(3): 596. Available at: DOI:10.1115/1.3239778

183. Lakshminarasimha a. N., Boyce MP., Meher-Homji CB. Modeling and Analysis of Gas Turbine Performance Deterioration. Journal of Engineering for Gas Turbines and Power. 1994; 116(1): 46. Available at: DOI:10.1115/1.2906808

184. Tahan M., Tsoutsanis E., Muhammad M., Abdul Karim ZA. Performance-

based health monitoring, diagnostics and prognostics for condition-based maintenance of gas turbines: A review. Applied Energy. Elsevier Ltd; 2017; 198: 122–144. Available at: DOI:10.1016/j.apenergy.2017.04.048

185. Stamatis A., Mathioudakis K., Smith M., Papailiou K. Gas turbine component fault identification by means of adaptive performance modeling. Proceedings of the ASME Turbo Expo. 1990; 5. Available at: DOI:10.1115/90-GT-376

186. Dyson RJ., Doel D. CF-80 condition monitoring – the engine manufacturing's involvement in data acquisition and analysis. AIAA Paper; 1984.

187. Blinstrub J., Li YG., Newby M., Zhou Q., Stigant G., Pilidis P., et al. Application of Gas Path Analysis to Compressor Diagnosis of an Industrial Gas Turbine Using Field Data. Volume 3A: Coal, Biomass and Alternative Fuels; Cycle Innovations; Electric Power; Industrial and Cogeneration. 2014; Available at: DOI:10.1115/GT2014-25330

188. Kim P. Kalman filter for beginners: with MATLAB examples. A-JIN; 2011.

189. Newby MA. Gas Turbine techno economics - application of a gas turbine model for optimising techncial and economic decisions for a CCGT power generation plant. Cranfield Univeristy; 2007.

190. Newby M., Stigant G. CCGT Operation Discussion. Manx Utilities; 2018.

191. WorldBank. State and Trends of Carbon Pricing. Washington, DC: World Bank. 2015. 1-135 p. Available at: DOI:10.1596/978-1-4648-0268-3

192. Dalton J. Genetic Search Algorithms. Newcastle upon Tyne; 2007.

193. Manne JR. Swarm Intelligence for Multi-Objective Optimization in Engineering Design. 4th editio. Information Resources Management Association, USA; 2018.

194. Goldberg DE. Genetic Algorithm in Search, Optimization, and Machine Learning. Boston, MA, USA: Addison-Wesley Longman Publishing Co; 1989. 412 pp p.

195. Fonseca CM., Fleming PJ. Genetic Algorithms for Multiobjective Optimization: Formulation, Discussion and Generalization. Proceedings of the Fifth International Conference. 1993; 93(July): 416–423. Available at: DOI:citeulike-article-id:2361311

196. Sen P., Yang JB. Multiple-criteria decision-making in design selection and synthesis. Journal of Engineering Design. 1995; 6(3): 207–230. Available at: DOI:10.1080/09544829508907914

197. Gomes EEB., Pilidis P., Polizakis a. L. Generation Schedule Optimisation for Gas Turbine Power Systems. Volume 2: Turbo Expo 2007. Montreal, Canada: ASME Turbo Expo; 2007. pp. 989–998. Available at: DOI:10.1115/GT2007-27934

198. EGBIGENIBO GENUINE SATURDAY. Hot section components life usage analyses for industrial gas turbines. Cranfield University; 2015.

199. Innovative Steam Technologies. IST-2015-Manx-Electricity-Authority. 2005. Available at: https://otsg.com/ist-uploads/2015/04/2015-Manx-Electricity-Authority.pdf (Accessed: 7 August 2017)

200. Hamid E. Performance Simulation of Combined Cycle Gas & Steam Turbine Power Plant. Cranfield University; 2011.

APPENDICES

Appendix A Pythia-Turbomatch Bricks

The explanation of Turbomatch bricks is referred to [163].

INTAKE	Intake component
COMPRE	Compressor
BURNER	Main combustor
MIXEES	Mixed at a constant area when one inlet flow is much smaller than the other
TURBIN	Turbine
DUCTER	Duct
NOZCON	Convergent nozzle
HETCOL	Cold side of heat exchanger
HETHOT	Hot side of heat exchanger

Appendix B Sensitivity Analysis

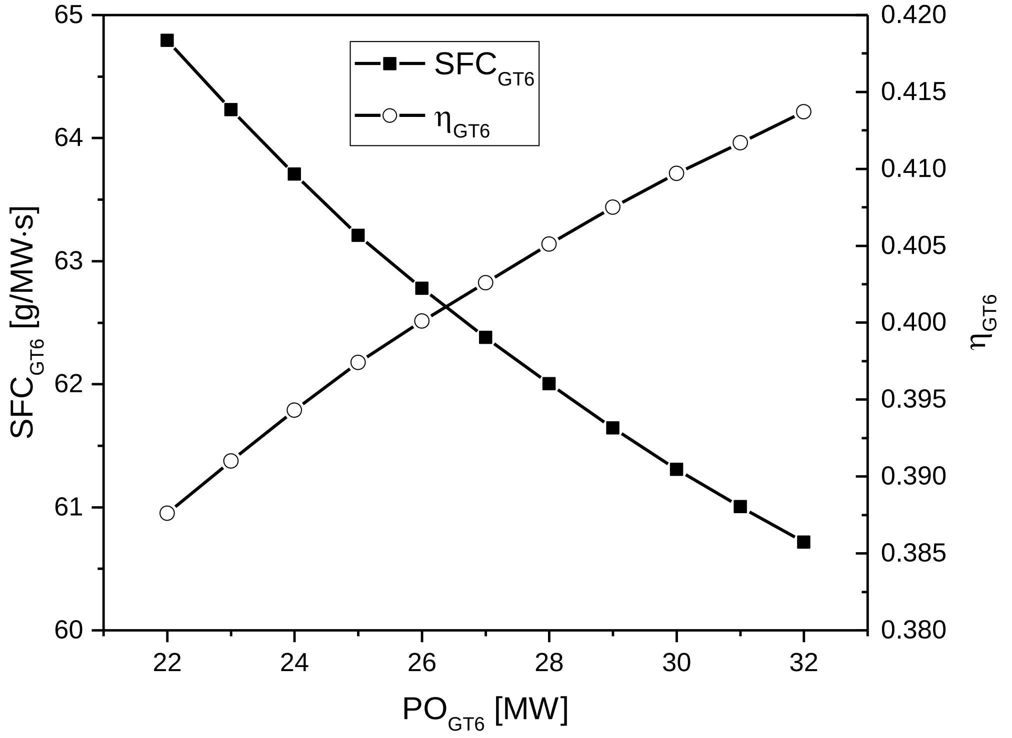

Figure-Apx B-1 Effect of Gas Turbine Power Output PO_{GT} on Specific Fuel Consumption (SFC) and Thermal Efficiency η_{GT}.

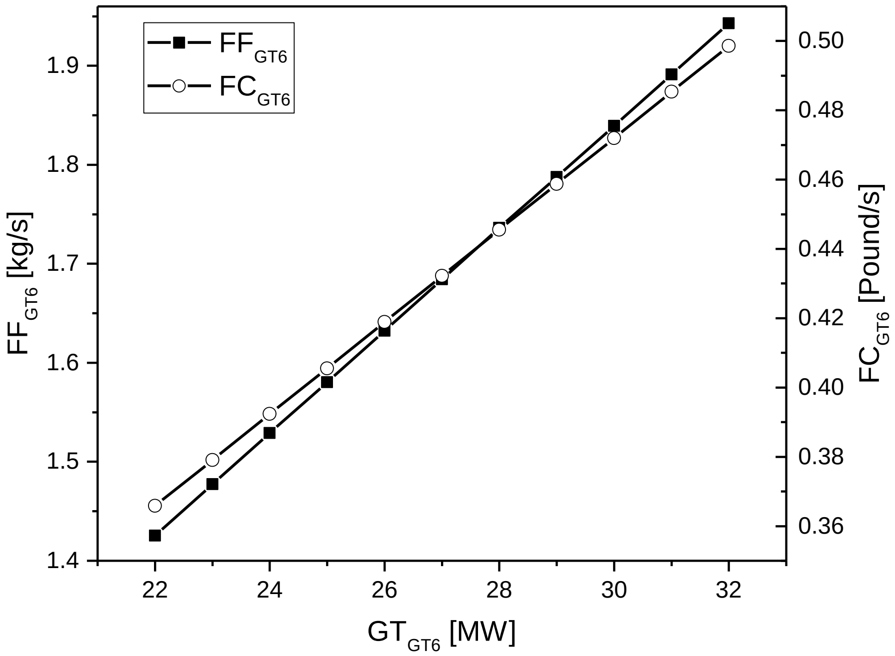

Figure-Apx B-2 Effect of Gas Turbine Power Output PO_{GT} on Fuel Flow (FF) and Fuel Cost (FC).

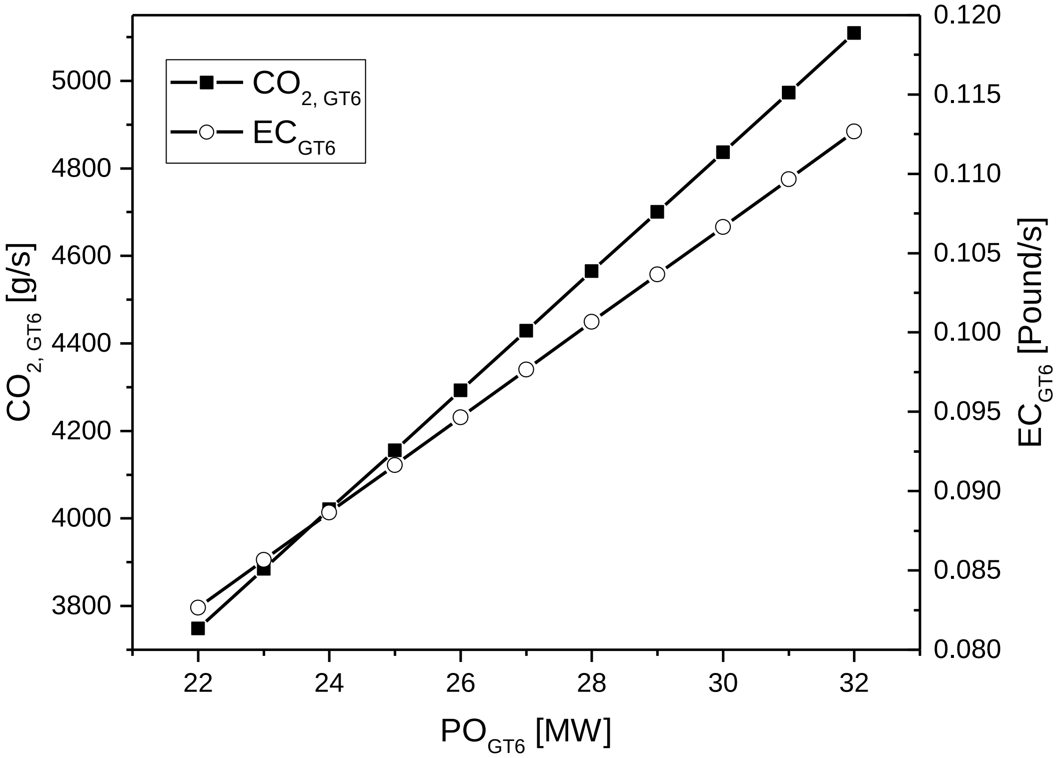

Figure-Apx B-3 Effect of Gas Turbine Power Output PO_{GT} on CO_2 Flow Rate and Emission Cost (EC).

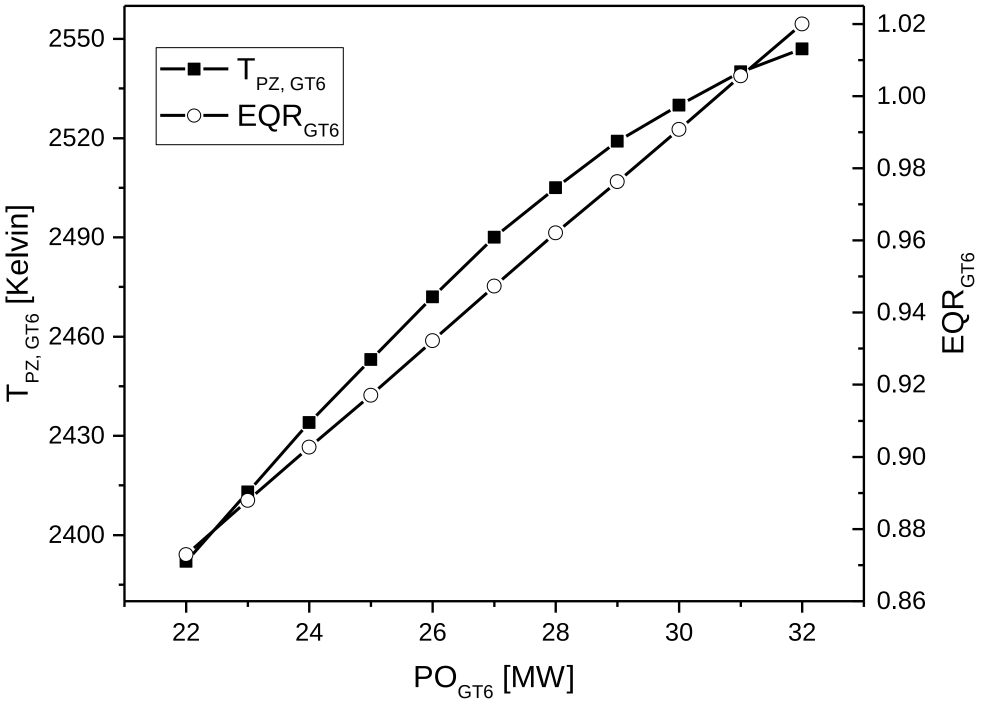

Figure-Apx B-4 Effect of Gas Turbine Power Output PO_{GT} on Primary Zone Flame Temperature T_{PZ} and Equivalence Ratio (EQR).

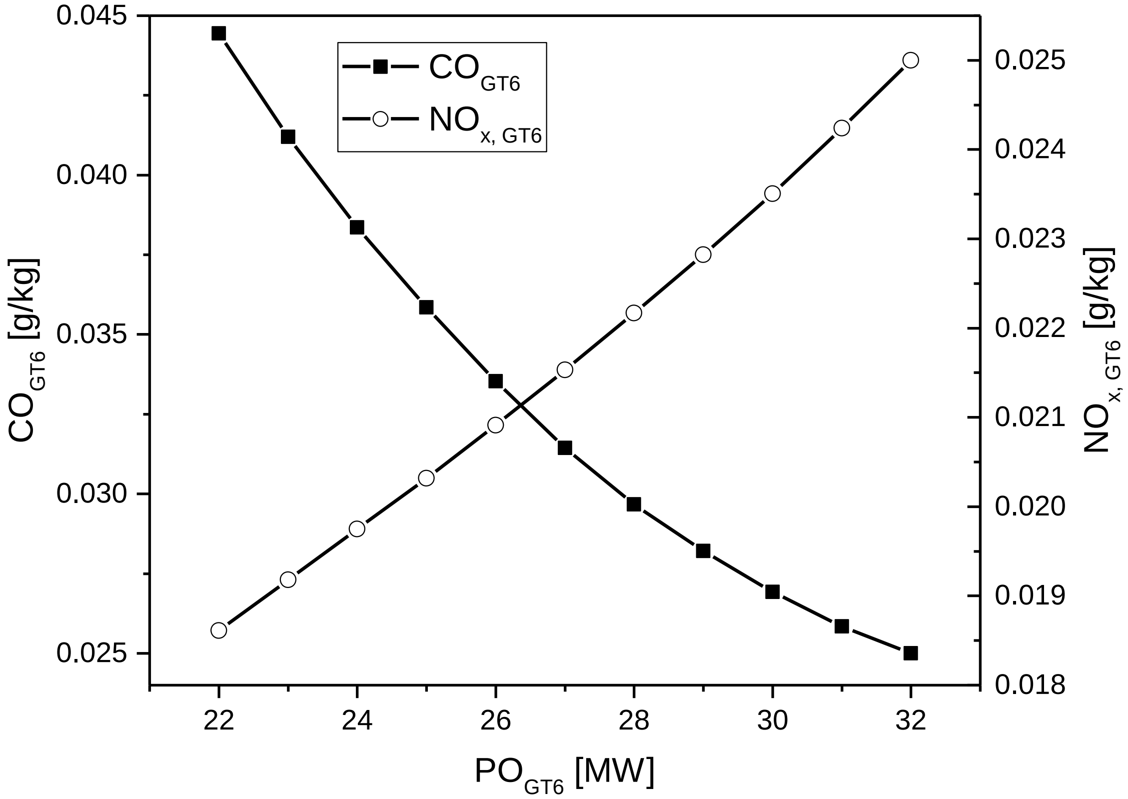

Figure-Apx B-5 Effect of Gas Turbine Power Output PO_{GT} on CO and NO_x.

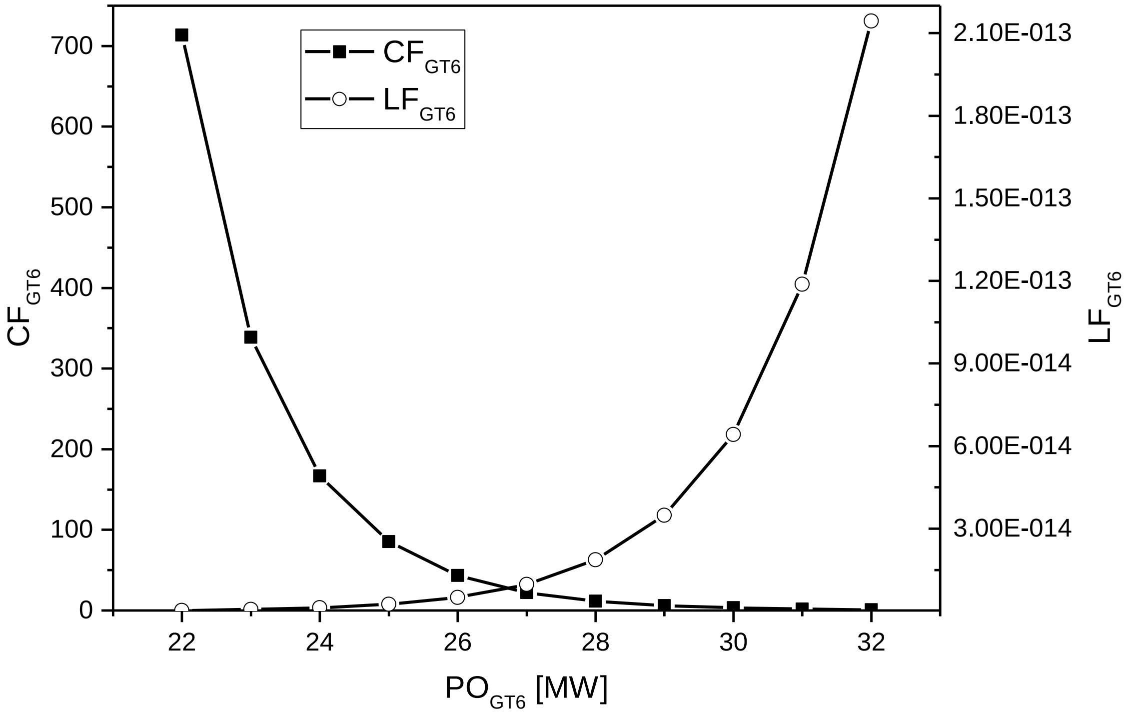

Figure-Apx B-6 Effect of Gas Turbine Power Output PO_{GT} on Creep Factor CF and Life Fraction LF.

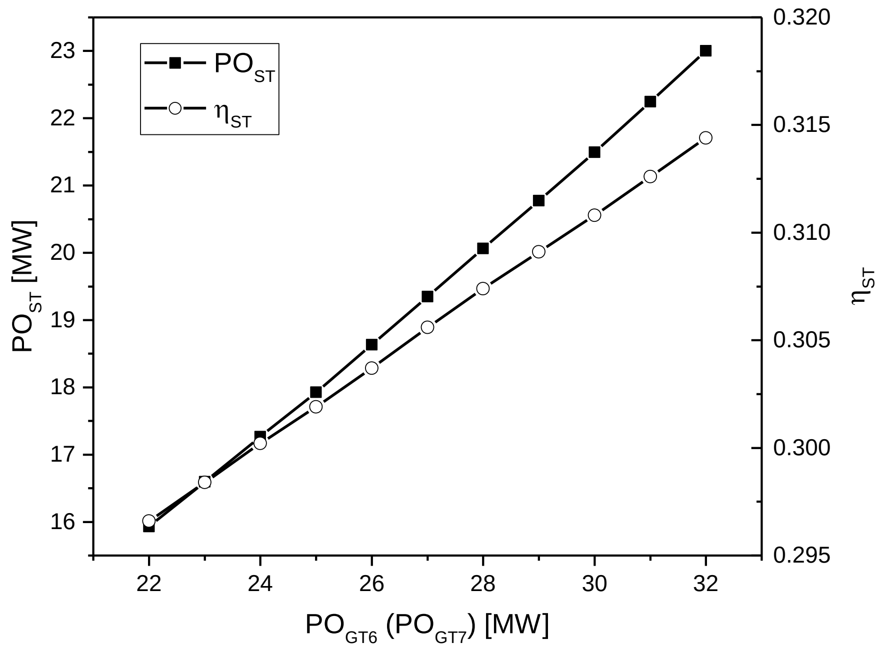

Figure-Apx B-7 Effect of Gas Turbine Power Output PO_{GT} on Steam Turbine Power Output PO_{ST} and Steam Turbine Efficiency η_{ST}.

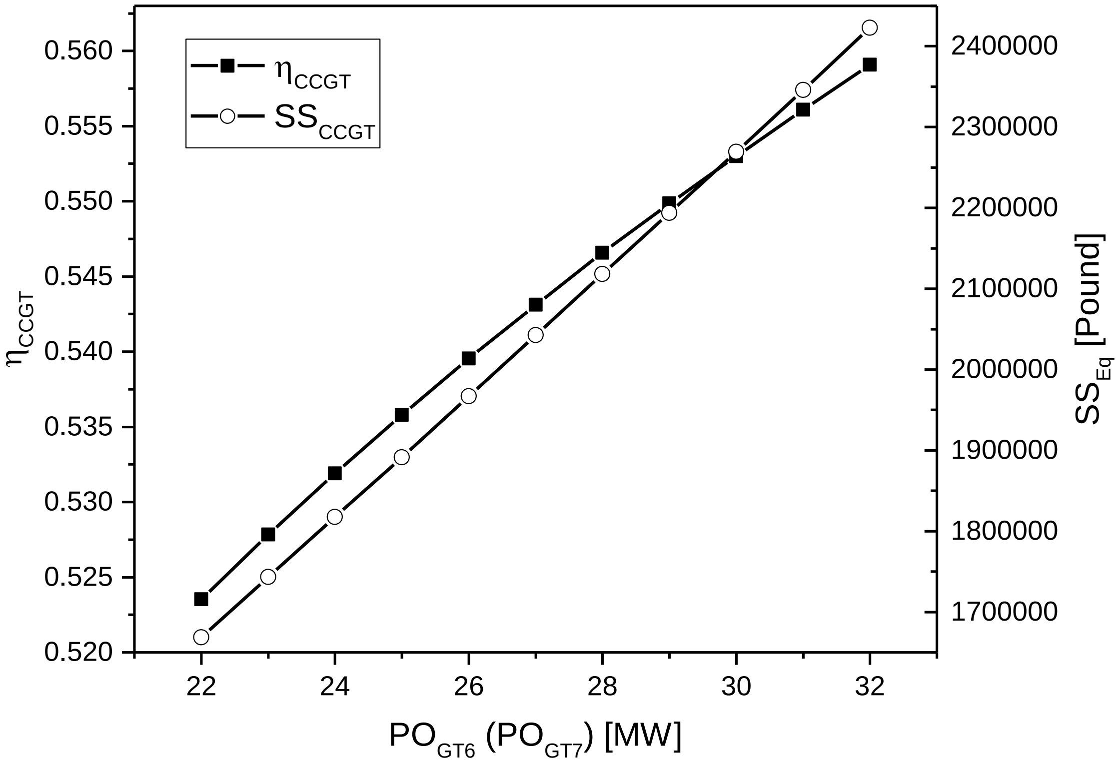

Figure-Apx B-8 Effect of Gas Turbine Power Output PO_{GT} on CCGT Efficiency η_{CCGT} and Equivalent Spark Spread SS_{CCGT}.

Appendix C Optimisation Results without Degradation

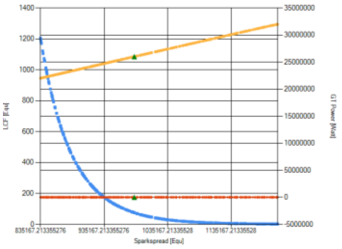

00:00-00:30

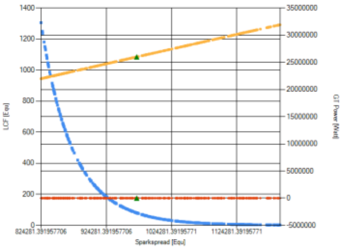

00:30-01:00

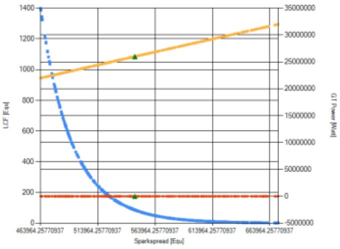

01:00-01:30

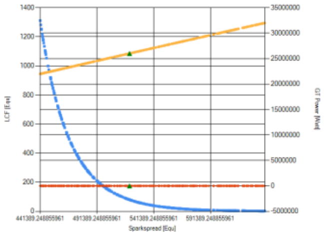

01:30-02:00

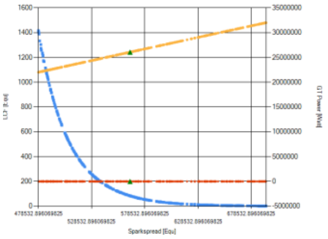

02:00-02:30

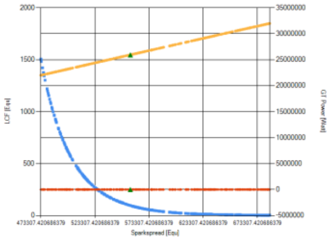

02:30-03:00

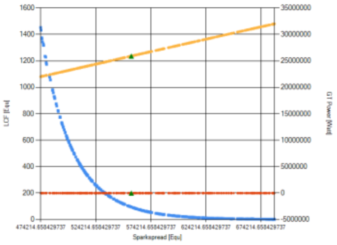

03:00-03:30

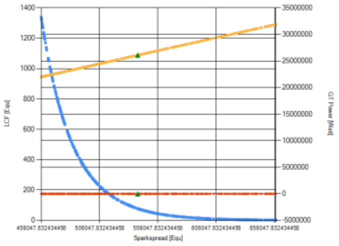

03:30-04:00

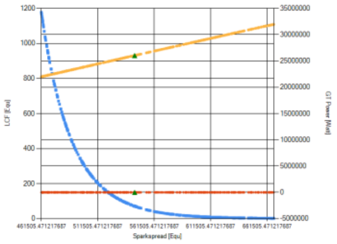

04:00-04:30

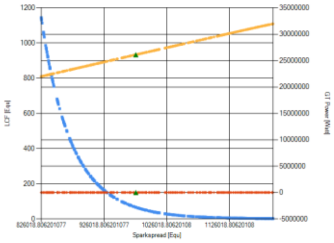

04:30-05:00

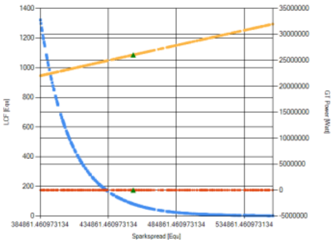

05:00-05:30

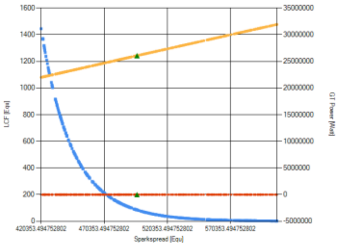

05:30-06:00

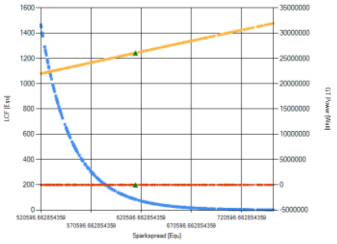

06:00-06:30

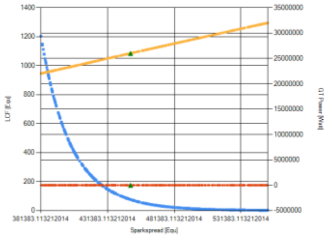

06:30-07:00

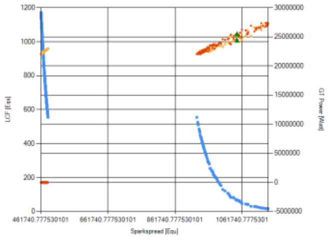

07:00-07:30

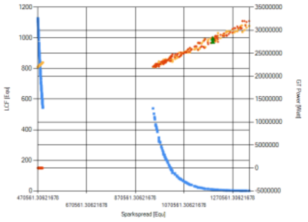

07:30-08:00

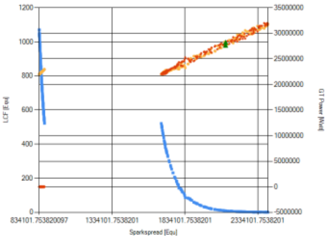

08:00-08:30

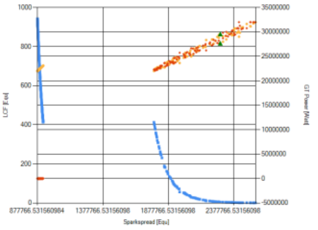

08:30-09:00

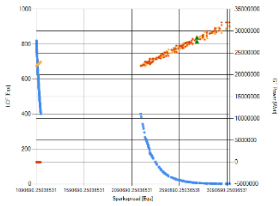

09:00-09:30

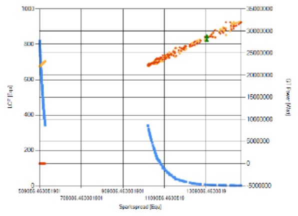

09:30-10:00

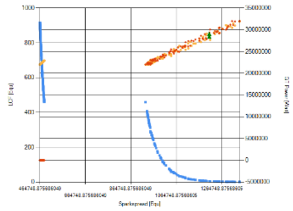

10:00-10:30

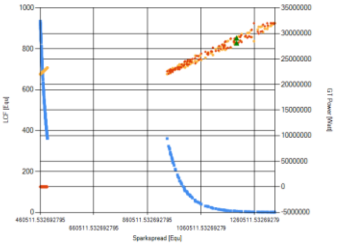

10:30-11:00

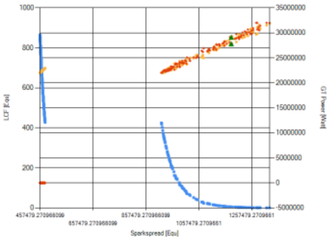

11:00-11:30

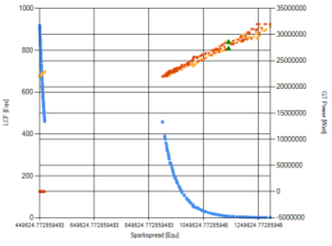

11:30-12:00

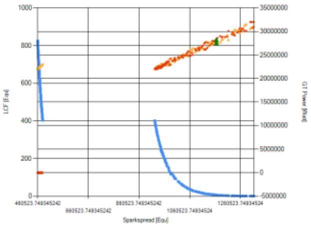

12:00-12:30

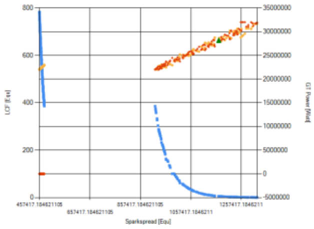

12:30-13:00

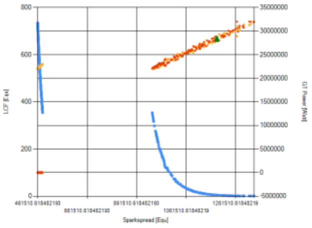

13:00-13:30

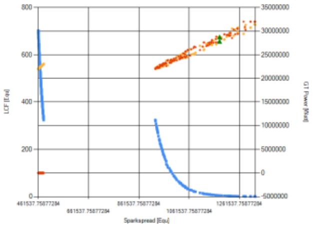

13:30-14:00

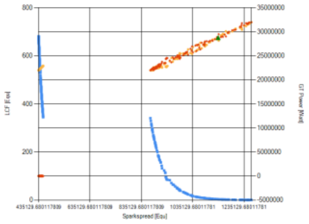

14:00-14:30

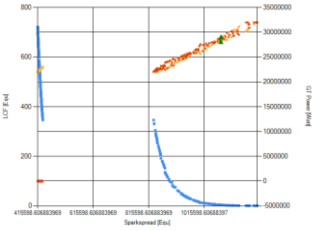

14:30-15:00

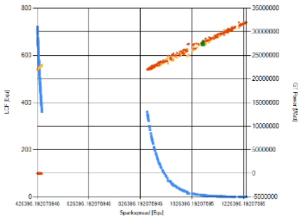

15:00-15:30

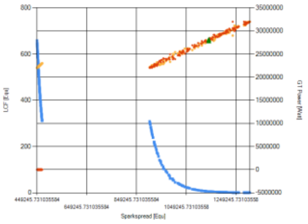

15:30-16:00

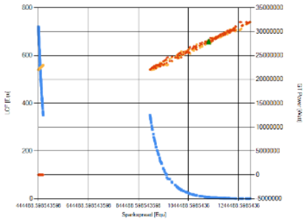

16:00-16:30

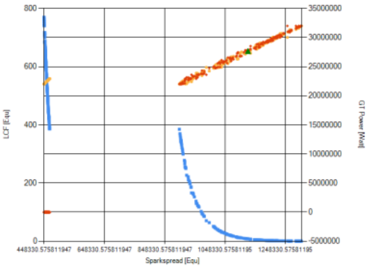

16:30-17:00

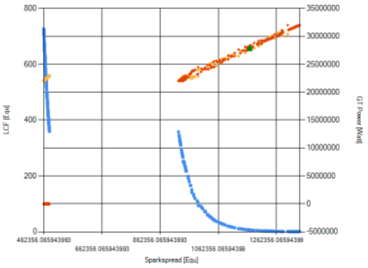

17:00-17:30

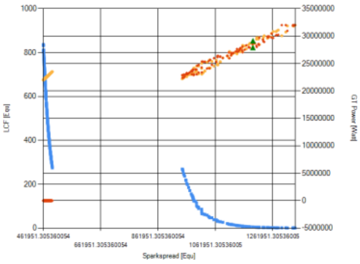

17:30-18:00

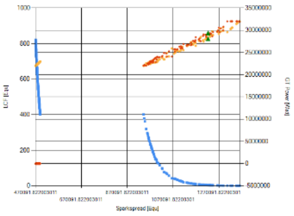

18:00-18:30

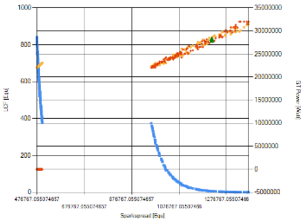

18:30-19:00

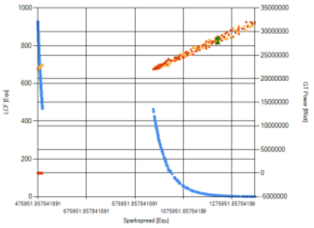

19:00-19:30

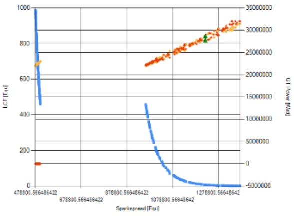

19:30-20:00

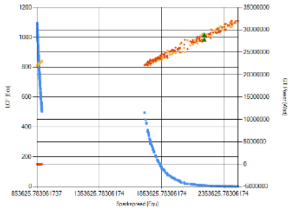

20:00-20:30

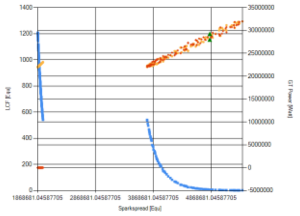

20:30-21:00

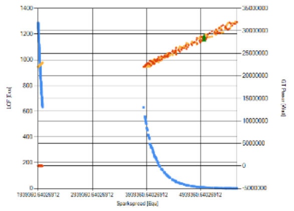

21:00-21:30

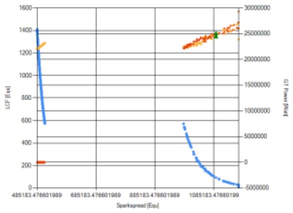

21:30-22:00

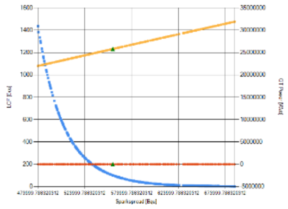

22:00-22:30

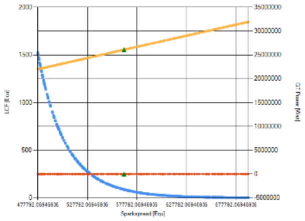

22:30-23:00

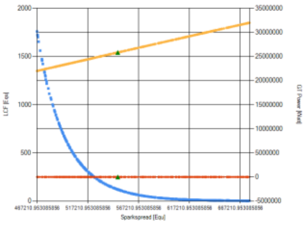

23:00-23:30

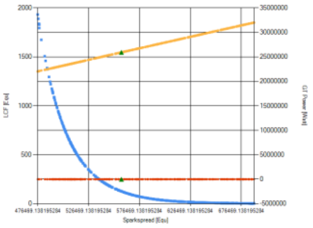

23:30-24:00

Appendix D Optimisation Results under Degradation

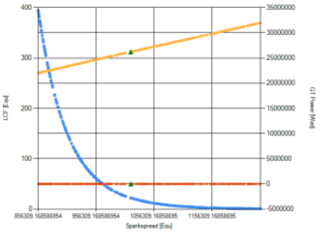

00:00-00:30

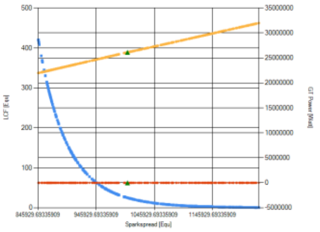

00:30-01:00

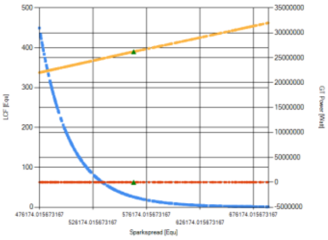

01:00-01:30

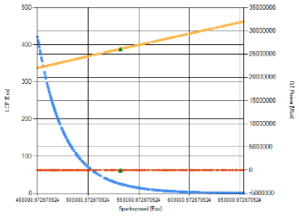

01:30-02:00

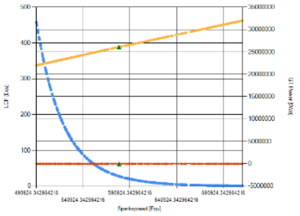

02:00-02:30

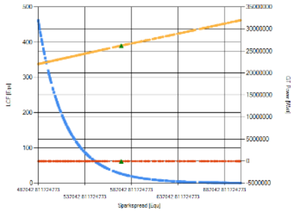

02:30-03:00

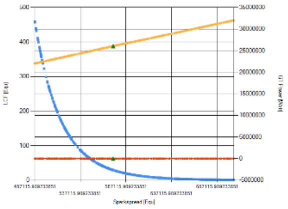

03:00-03:30

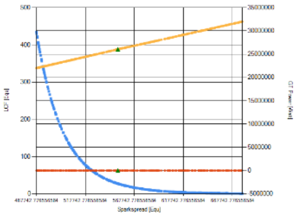

03:30-04:00

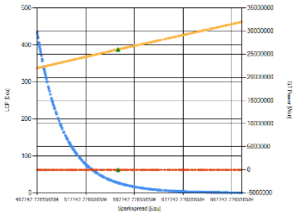

04:00-04:30

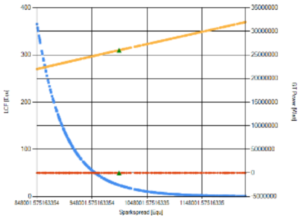

04:30-05:00

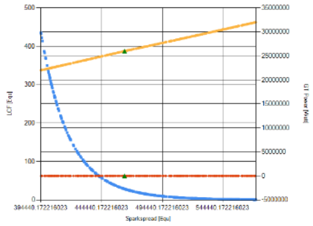

05:00-05:30

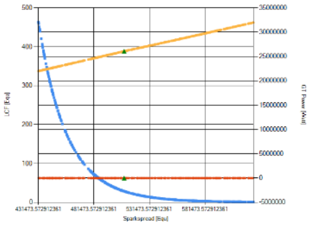

05:30-06:00

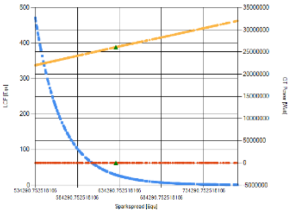

06:00-06:30

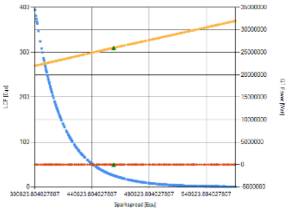

06:30-07:00

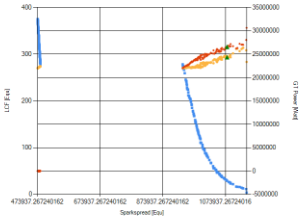

07:00-07:30

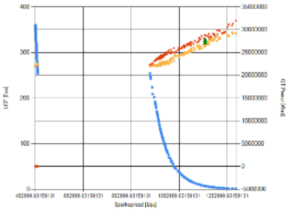

07:30-08:00

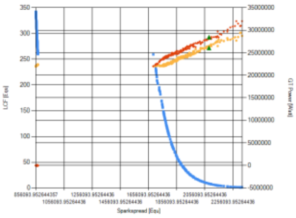

08:00-08:30

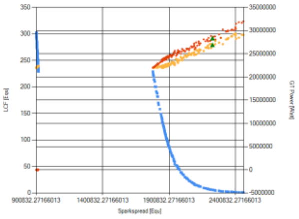

08:30-09:00

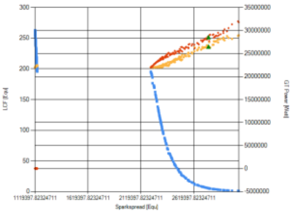

09:00-09:30

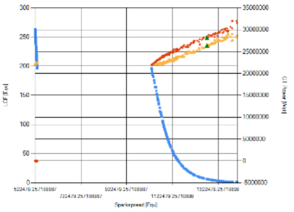

09:30-10:00

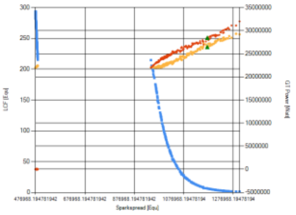

10:00-10:30

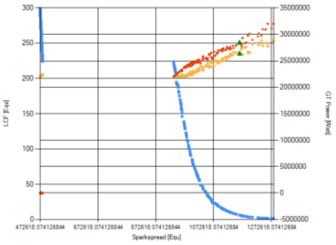

10:30-11:00

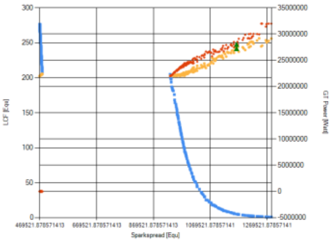

11:00-11:30

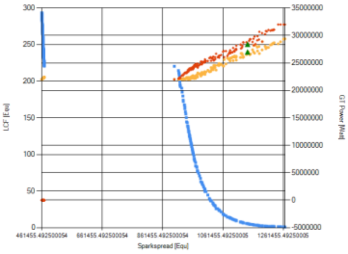

11:30-12:00

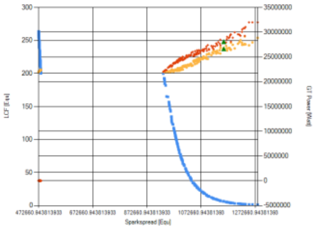

12:00-12:30

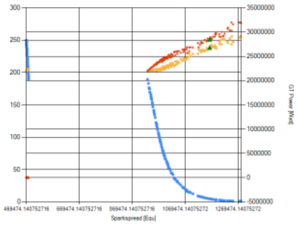

12:30-13:00

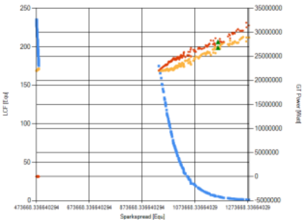

13:00-13:30

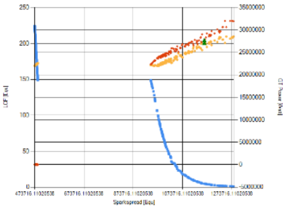

13:30-14:00

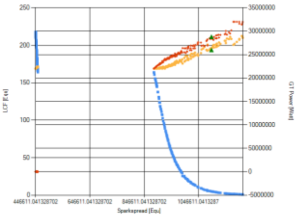

14:00-14:30

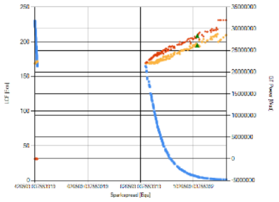

14:30-15:00

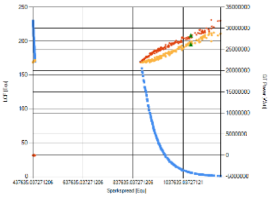

15:00-15:30

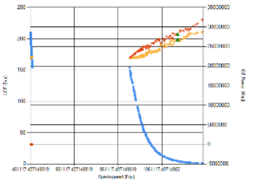

15:30-16:00

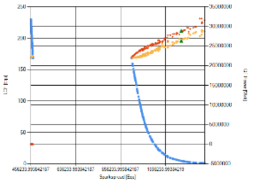

16:00-16:30

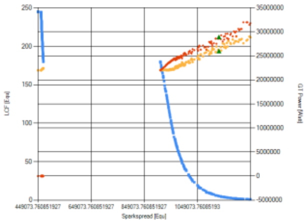

16:30-17:00

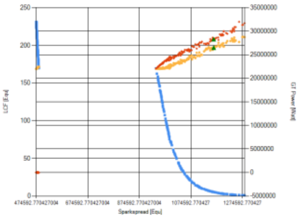

17:00-17:30

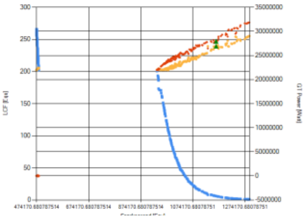

17:30-18:00

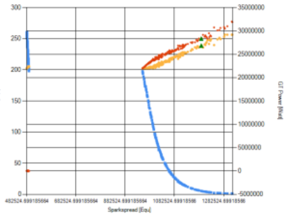

18:00-18:30

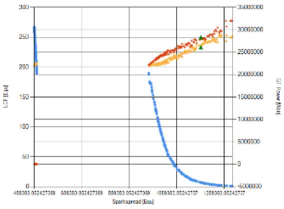

18:30-19:00

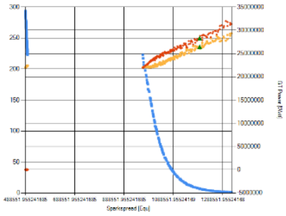

19:00-19:30

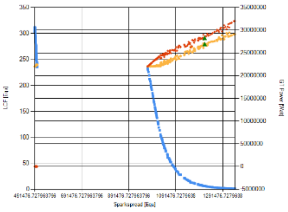

19:30-20:00

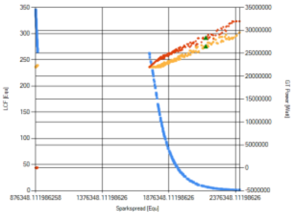

20:00-20:30

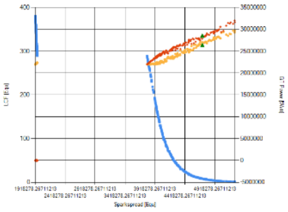

20:30-21:00

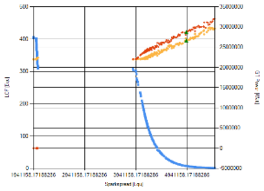

21:00-21:30

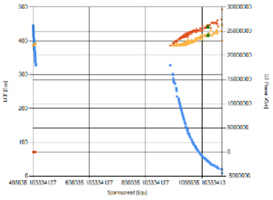

21:30-22:00

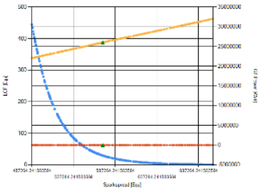

22:00-22:30

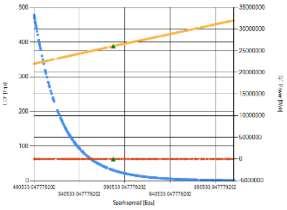

22:30-23:00

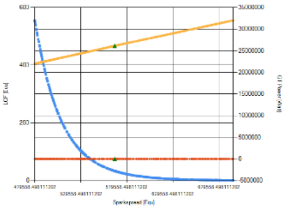

23:00-23:30

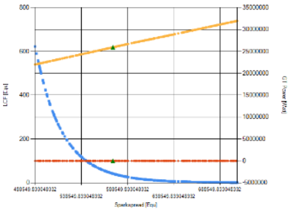

23:30-24:00

Appendix E Main Interfaces

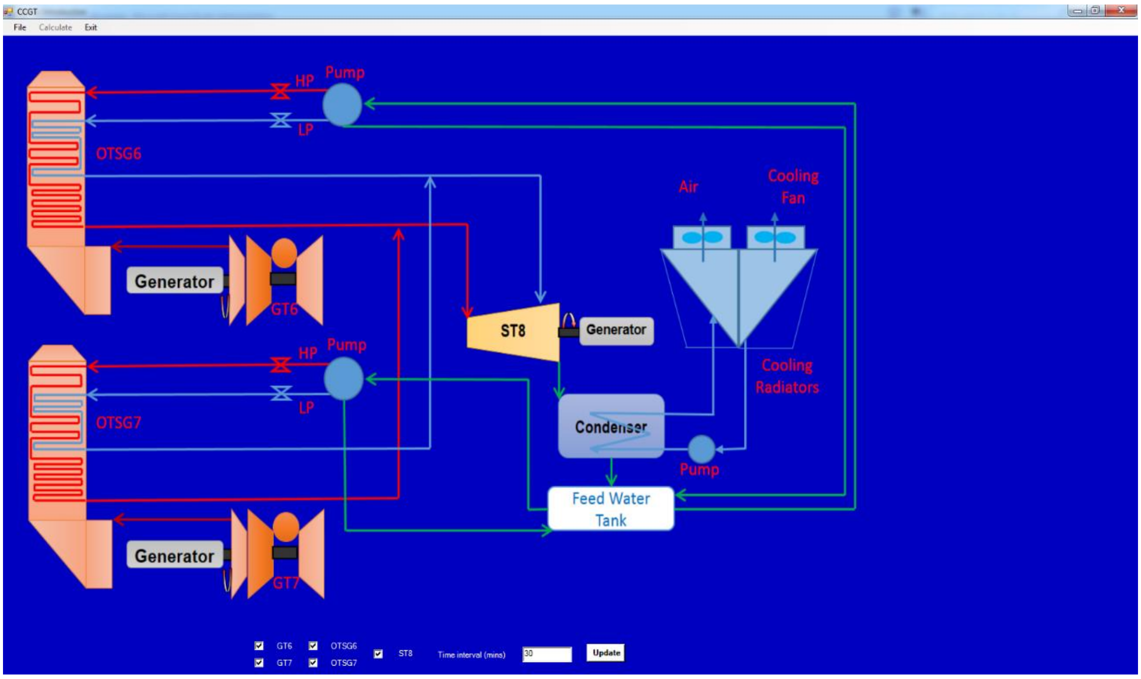

☑ GT6 ☑ OTSG6 ☑ ST8
☑ GT7 ☑ OTSG7

Time interval (mins) 30

Figure-Apx E-1 Start Interface.

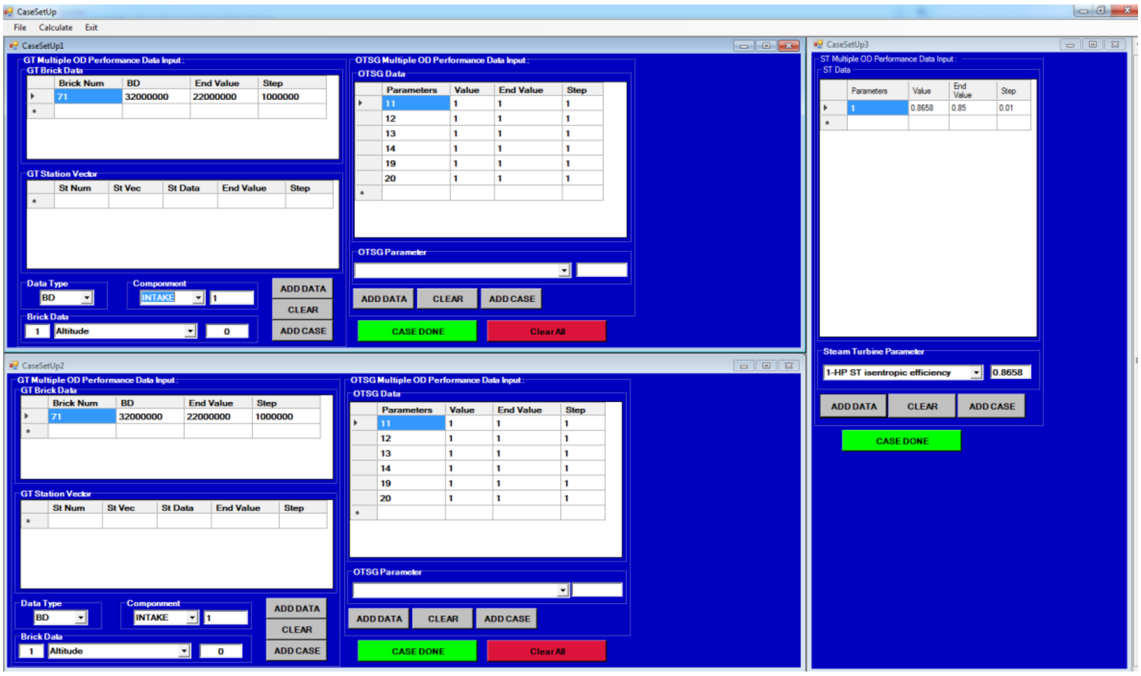

CaseSetUp1

GT Multiple OD Performance Data Input :

GT Brick Data

Brick Num	BD	End Value	Step
71	32000000	22000000	1000000

GT Station Vector

St Num	St Vec	St Data	End Value	Step

Data Type: BD

Compponent: INTAKE 1

Brick Data: 1 Altitude 0

OTSG Multiple OD Performance Data Input :

OTSG Data

Parameters	Value	End Value	Step
11	1	1	1
12	1	1	1
13	1	1	1
14	1	1	1
19	1	1	1
20	1	1	1

OTSG Parameter

CaseSetUp2

GT Multiple OD Performance Data Input :

GT Brick Data

Brick Num	BD	End Value	Step
71	32000000	22000000	1000000

GT Station Vector

St Num	St Vec	St Data	End Value	Step

Data Type: BD

Compponent: INTAKE 1

Brick Data: 1 Altitude 0

OTSG Multiple OD Performance Data Input :

OTSG Data

Parameters	Value	End Value	Step
11	1	1	1
12	1	1	1
13	1	1	1
14	1	1	1
19	1	1	1
20	1	1	1

OTSG Parameter

CaseSetUp3

ST Multiple OD Performance Data Input :

ST Data

Parameters	Value	End Value	Step
1	0.8658	0.85	0.01

Steam Turbine Parameter: 1-HP ST isentropic efficiency 0.8658

Figure-Apx E-2 CCGT Off-design Performance Simulation Setting.

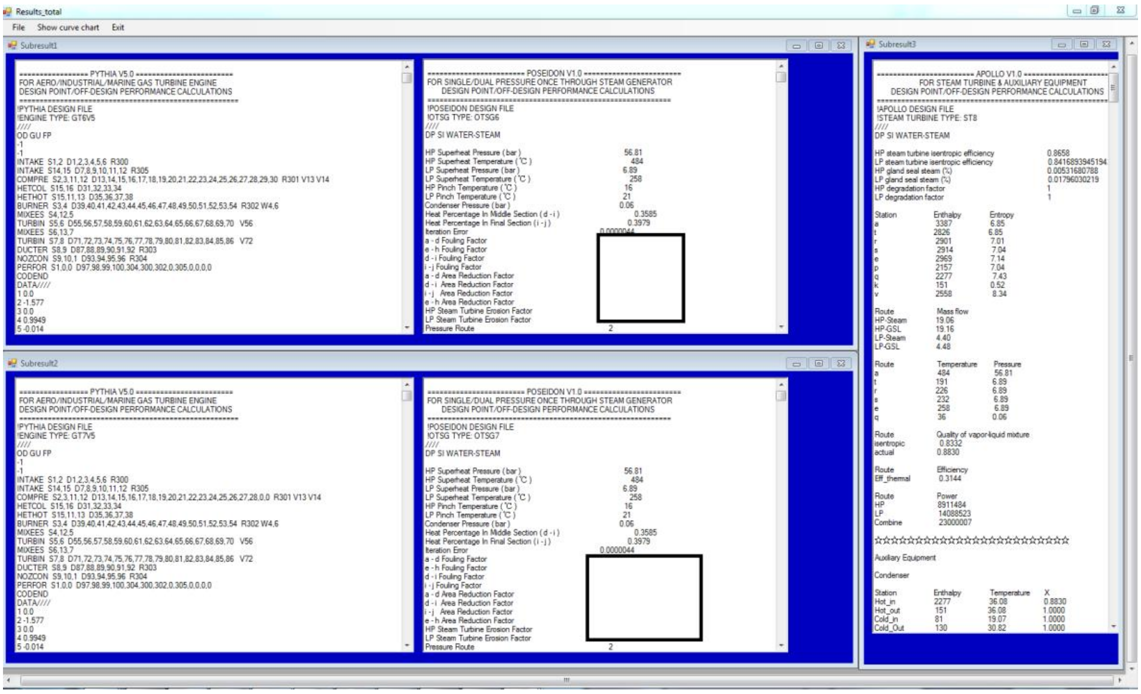

```
================= PYTHIA V5.0 =======================
FOR AERO/INDUSTRIAL/MARINE GAS TURBINE ENGINE
DESIGN POINT/OFF-DESIGN PERFORMANCE CALCULATIONS
=====================================================
!PYTHIA DESIGN FILE
!ENGINE TYPE: GT6V5
////
OD GU FP
-1
-1
INTAKE  S1,2  D1,2,3,4,5,6  R300
INTAKE  S14,15  D7,8,9,10,11,12  R305
COMPRE  S2,3,11,12  D13,14,15,16,17,18,19,20,21,22,23,24,25,26,27,28,29,30  R301 V13 V14
HETCOL  S15,16  D31,32,33,34
HETHOT  S15,11,13  D35,36,37,38
BURNER  S3,4  D39,40,41,42,43,44,45,46,47,48,49,50,51,52,53,54  R302 W4,6
MIXEES  S4,12,5
TURBIN  S5,6  D55,56,57,58,59,60,61,62,63,64,65,66,67,68,69,70   V56
MIXEES  S6,13,7
TURBIN  S7,8  D71,72,73,74,75,76,77,78,79,80,81,82,83,84,85,86   V72
DUCTER  S8,9  D87,88,89,90,91,92  R303
NOZCON  S9,10,1  D93,94,95,96  R304
PERFOR  S1,0,0  D97,98,99,100,304,300,302,0,305,0,0,0,0
CODEND
DATA////
1 0.0
2 -1.577
3 0.0
4 0.9949
5 -0.014
```

```
======================== POSEIDON V1.0 ========================
FOR SINGLE/DUAL PRESSURE ONCE THROUGH STEAM GENERATOR
     DESIGN POINT/OFF-DESIGN PERFORMANCE CALCULATIONS
===============================================================
!POSEIDON DESIGN FILE
!OTSG TYPE: OTSG6
////
DP SI WATER-STEAM

HP Superheat Pressure ( bar )                          56.81
HP Superheat Temperature ( ℃ )                          484
LP Superheat Pressure ( bar )                          6.89
LP Superheat Temperature ( ℃ )                          258
HP Pinch Temperature ( ℃ )                             16
LP Pinch Temperature ( ℃ )                             21
Condenser Pressure ( bar )                            0.06
Heat Percentage In Middle Section ( d - i )               0.3585
Heat Percentage In Final Section ( i - j )               0.3979
Iteration Error                                    0.0000044
a - d Fouling Factor                               [redacted]
e - h Fouling Factor
d - i Fouling Factor
i - j Fouling Factor
a - d Area Reduction Factor
d - i  Area Reduction Factor
i - j   Area Reduction Factor
e - h Area Reduction Factor
HP Steam Turbine Erosion Factor
LP Steam Turbine Erosion Factor
Pressure Route                                       2
```

```
================= PYTHIA V5.0 =======================
FOR AERO/INDUSTRIAL/MARINE GAS TURBINE ENGINE
DESIGN POINT/OFF-DESIGN PERFORMANCE CALCULATIONS
=====================================================
!PYTHIA DESIGN FILE
!ENGINE TYPE: GT7V5
////
OD GU FP
-1
-1
INTAKE  S1,2  D1,2,3,4,5,6  R300
INTAKE  S14,15  D7,8,9,10,11,12  R305
COMPRE  S2,3,11,12  D13,14,15,16,17,18,19,20,21,22,23,24,25,26,27,28,0,0  R301 V13 V14
HETCOL  S15,16  D31,32,33,34
HETHOT  S15,11,13  D35,36,37,38
BURNER  S3,4  D39,40,41,42,43,44,45,46,47,48,49,50,51,52,53,54  R302 W4,6
MIXEES  S4,12,5
TURBIN  S5,6  D55,56,57,58,59,60,61,62,63,64,65,66,67,68,69,70   V56
MIXEES  S6,13,7
TURBIN  S7,8  D71,72,73,74,75,76,77,78,79,80,81,82,83,84,85,86   V72
DUCTER  S8,9  D87,88,89,90,91,92  R303
NOZCON  S9,10,1  D93,94,95,96  R304
PERFOR  S1,0,0  D97,98,99,100,304,300,302,0,305,0,0,0,0
CODEND
DATA////
1 0.0
2 -1.577
3 0.0
4 0.9949
5 -0.014
```

```
======================== POSEIDON V1.0 ========================
FOR SINGLE/DUAL PRESSURE ONCE THROUGH STEAM GENERATOR
     DESIGN POINT/OFF-DESIGN PERFORMANCE CALCULATIONS
===============================================================
!POSEIDON DESIGN FILE
!OTSG TYPE: OTSG7
////
DP SI WATER-STEAM

HP Superheat Pressure ( bar )                          56.81
HP Superheat Temperature ( ℃ )                          484
LP Superheat Pressure ( bar )                          6.89
LP Superheat Temperature ( ℃ )                          258
HP Pinch Temperature ( ℃ )                             16
LP Pinch Temperature ( ℃ )                             21
Condenser Pressure ( bar )                            0.06
Heat Percentage In Middle Section ( d - i )               0.3585
Heat Percentage In Final Section ( i - j )               0.3979
Iteration Error                                    0.0000044
a - d Fouling Factor                               [redacted]
e - h Fouling Factor
d - i Fouling Factor
i - j Fouling Factor
a - d Area Reduction Factor
d - i  Area Reduction Factor
i - j   Area Reduction Factor
e - h Area Reduction Factor
HP Steam Turbine Erosion Factor
LP Steam Turbine Erosion Factor
Pressure Route                                       2
```

```
======================== APOLLO V1.0 ========================
              FOR STEAM TURBINE & AUXILIARY EQUIPMENT
    DESIGN POINT/OFF-DESIGN PERFORMANCE CALCULATIONS
=============================================================
!APOLLO DESIGN FILE
!STEAM TURBINE TYPE: ST8
////
DP SI WATER-STEAM

HP steam turbine isentropic efficiency               0.8658
LP steam turbine isentropic efficiency               0.8416893945194
HP gland seal steam (%)                              0.00531680788
LP gland seal steam (%)                              0.01796030219
HP degradation factor                                1
LP degradation factor                                1

Station          Enthalpy        Entropy
a                 3387            6.85
t                2826            6.85
r                 2901            7.01
s                 2914            7.04
e                2969            7.14
p                2157            7.04
q                2277            7.43
k                151             0.52
v                2558            8.34

Route            Mass flow
HP-Steam         19.06
HP-GSL           19.16
LP-Steam         4.40
LP-GSL           4.48

Route            Temperature     Pressure
a                 484             56.81
t                191             6.89
r                226             6.89
s                 232             6.89
e                 258             6.89
q                 36             0.06

Route            Quality of vapor-liquid mixture
isentropic        0.8332
actual           0.8830

Route            Efficiency
Eff_thermal       0.3144

Route            Power
HP               8911484
LP                14088523
Combine           23000007

☆☆☆☆☆☆☆☆☆☆☆☆☆☆☆☆☆☆☆☆☆☆☆☆☆☆☆☆☆☆

Auxiliary Equipment

Condenser

Station          Enthalpy        Temperature     X
Hot_in           2277            36.08           0.8830
Hot_out          151             36.08           1.0000
Cold_in          81              19.07           1.0000
Cold_Out         130             30.82           1.0000
```

Figure-Apx E-3 CCGT Off-design Performance Simulation Results.

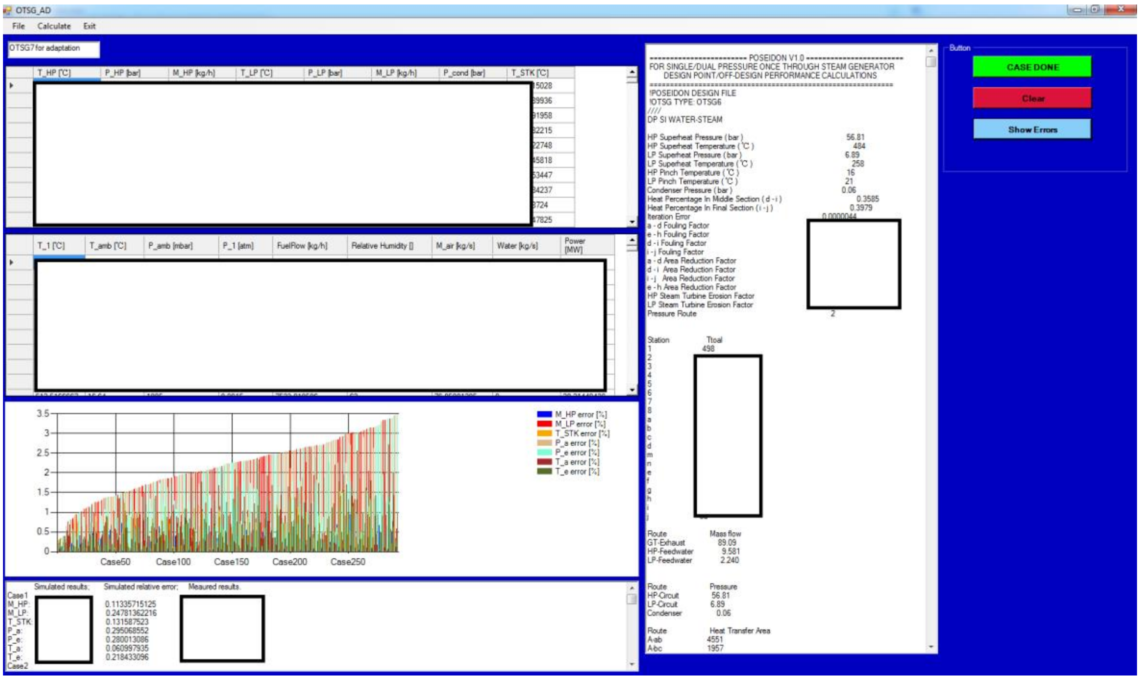

OTSG7 for adaptation

```
T_HP [℃]   P_HP [bar]   M_HP [kg/h]   T_LP [℃]   P_LP [bar]   M_LP [kg/h]   P_cond [bar]   T_STK [℃]
[redacted]                                                                                 5028
                                                                                           9936
                                                                                           1958
                                                                                           2215
                                                                                           2748
                                                                                           5818
                                                                                           3447
                                                                                           4237
                                                                                           3724
                                                                                           7825

T_1 [℃]   T_amb [℃]   P_amb [mbar]   P_1 [atm]   FuelFlow [kg/h]   Relative Humidity []   M_air [kg/s]   Water [kg/s]   Power [MW]
[redacted]
```

```
        Simulated results:   Simulated relative error:   Meaured results:
Case1
M_HP:   [redacted]           0.11335715125               [redacted]
M_LP:                        0.24781362216
T_STK:                       0.131587523
P_a:                         0.295068552
P_e:                         0.280013086
T_a:                         0.060997935
T_e:                         0.218433096
Case2
```

```
======================== POSEIDON V1.0 ========================
FOR SINGLE/DUAL PRESSURE ONCE THROUGH STEAM GENERATOR
     DESIGN POINT/OFF-DESIGN PERFORMANCE CALCULATIONS
===============================================================
!POSEIDON DESIGN FILE
!OTSG TYPE: OTSG6
////
DP SI WATER-STEAM

HP Superheat Pressure ( bar )                          56.81
HP Superheat Temperature ( ℃ )                          484
LP Superheat Pressure ( bar )                          6.89
LP Superheat Temperature ( ℃ )                          258
HP Pinch Temperature ( ℃ )                             16
LP Pinch Temperature ( ℃ )                             21
Condenser Pressure ( bar )                            0.06
Heat Percentage In Middle Section ( d - i )               0.3585
Heat Percentage In Final Section ( i - j )               0.3979
Iteration Error                                    0.0000044
a - d Fouling Factor                               [redacted]
e - h Fouling Factor
d - i Fouling Factor
i - j Fouling Factor
a - d Area Reduction Factor
d - i  Area Reduction Factor
i - j   Area Reduction Factor
e - h Area Reduction Factor
HP Steam Turbine Erosion Factor
LP Steam Turbine Erosion Factor
Pressure Route                                       2


Station          Ttoal
1                498
2                [redacted]
3
4
5
6
7
8
a
b
c
d
m
n
e
f
g
h
i
j

Route            Mass flow
GT-Exhaust         89.09
HP-Feedwater        9.581
LP-Feedwater        2.240


Route            Pressure
HP-Circuit        56.81
LP-Circuit       6.89
Condenser          0.06

Route            Heat Transfer Area
A-ab             4551
A-bc             1957
```

Figure-Apx E-4 OTSG Performance Validation System.

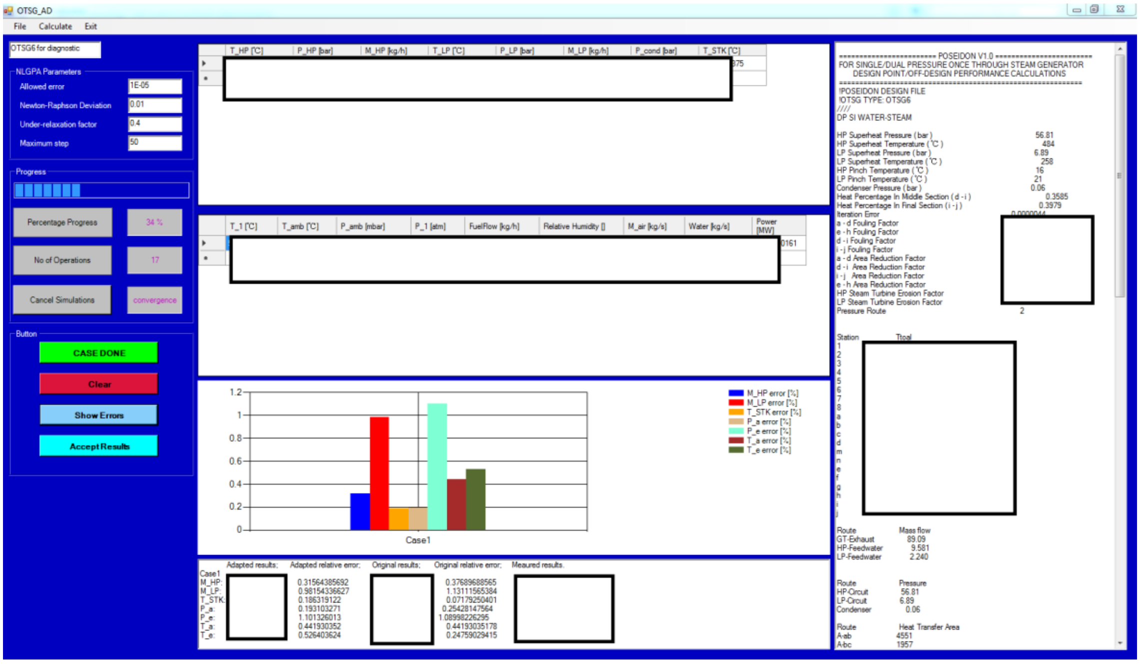

OTSG6 for diagnostic

Allowed error: 1E-05
Newton-Raphson Deviation: 0.01
Under-relaxation factor: 0.4
Maximum step: 50

Percentage Progress: 34 %
No of Operations: 17
Cancel Simulations: convergence

T_HP [°C]	P_HP [bar]	M_HP [kg/h]	T_LP [°C]	P_LP [bar]	M_LP [kg/h]	P_cond [bar]	T_STK [°C]
[redacted]							375

T_1 [°C]	T_amb [°C]	P_amb [mbar]	P_1 [atm]	FuelFlow [kg/h]	Relative Humidity []	M_air [kg/s]	Water [kg/s]	Power [MW]
[redacted]								0161

```
======================== POSEIDON V1.0 ========================
FOR SINGLE/DUAL PRESSURE ONCE THROUGH STEAM GENERATOR
     DESIGN POINT/OFF-DESIGN PERFORMANCE CALCULATIONS
==============================================================
!POSEIDON DESIGN FILE
!OTSG TYPE: OTSG6
////
DP SI WATER-STEAM

HP Superheat Pressure ( bar )                    56.81
HP Superheat Temperature ( °C )                    484
LP Superheat Pressure ( bar )                    6.89
LP Superheat Temperature ( °C )                    258
HP Pinch Temperature ( °C )                      16
LP Pinch Temperature ( °C )                      21
Condenser Pressure ( bar )                      0.06
Heat Percentage In Middle Section ( d - i )           0.3585
Heat Percentage In Final Section ( i - j )          0.3979
Iteration Error                                0.0000044
a - d Fouling Factor                        [redacted]
e - h Fouling Factor
d - i Fouling Factor
i - j Fouling Factor
a - d Area Reduction Factor
d - i  Area Reduction Factor
i - j  Area Reduction Factor
e - h Area Reduction Factor
HP Steam Turbine Erosion Factor
LP Steam Turbine Erosion Factor
Pressure Route                                2

Station        Ttoal
1          [redacted]
2
3
4
5
6
7
8
a
b
c
d
m
n
e
f
g
h
i
j

Route          Mass flow
GT-Exhaust       89.09
HP-Feedwater       9.581
LP-Feedwater       2.240

Route          Pressure
HP-Circuit       56.81
LP-Circuit       6.89
Condenser          0.06

Route          Heat Transfer Area
A-ab           4551
A-bc           1957
```

Case1	Adapted results;	Adapted relative error;	Original results;	Original relative error;	Meaured results.
M_HP:	[redacted]	0.31564385692	[redacted]	0.37689688565	[redacted]
M_LP:		0.98154336627		1.13111565384	
T_STK:		0.186319122		0.07179250401	
P_a:		0.193103271		0.25428147564	
P_e:		1.101326013		1.08998226295	
T_a:		0.441930352		0.44193035178	
T_e:		0.526403624		0.24759029415	

Figure-Apx E-5 OTSG Diagnostic System.

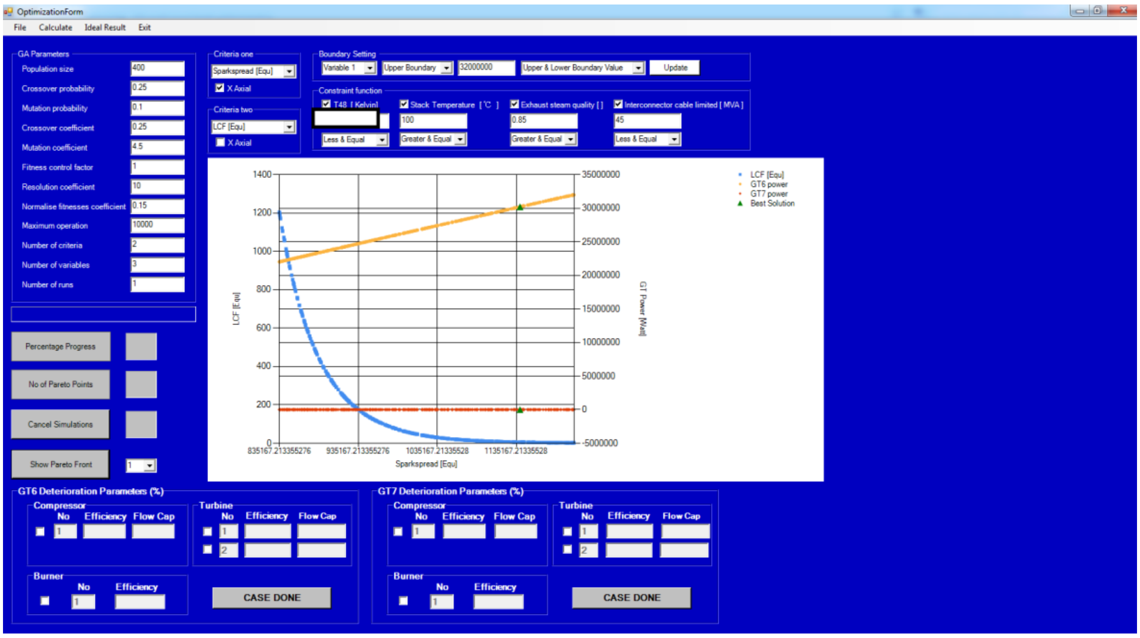

Population size: 400
Crossover probability: 0.25
Mutation probability: 0.1
Crossover coefficient: 0.25
Mutation coefficient: 4.5
Fitness control factor: 1
Resolution coefficient: 10
Normalise fitnesses coefficient: 0.15
Maximum operation: 10000
Number of criteria: 2
Number of variables: 3
Number of runs: 1

Criteria one: Sparkspread [Equ] ☑ X Axial
Criteria two: LCF [Equ] ☐ X Axial

Boundary Setting: Variable 1 | Upper Boundary | 32000000 | Upper & Lower Boundary Value

Constraint function:
☑ T48 [Kelvin] [redacted] Less & Equal
☑ Stack Temperature [°C] 100 Greater & Equal
☑ Exhaust steam quality [ ] 0.85 Greater & Equal
☑ Interconnector cable limited [MVA] 45 Less & Equal

Show Pareto Front: 1

GT6 Deterioration Parameters (%): Compressor ☐ No 1; Turbine ☐ No 1, ☐ No 2; Burner ☐ No 1
GT7 Deterioration Parameters (%): Compressor ☐ No 1; Turbine ☐ No 1, ☐ No 2; Burner ☐ No 1

Figure-Apx E-6 Decision Support System.